THÈSE DE DOCTORAT

DE L'UNIVERSITÉ PSL

Préparée à l'Ecole Supérieure de Physique et de Chimie Industrielles de la ville de Paris (ESPCI Paris)

Quantitative detection of damage in soft materials using mechano-fluorescence

Détection quantitative de l'endommagement moléculaire, par mécano-fluorescence, dans les matériaux mous

Soutenue par
Juliette SLOOTMAN
Le 20 septembre 2019

Ecole doctorale n° ED 397
Physique et chimie des matériaux

Spécialité
Chimie des Matériaux

Composition du jury :

Annie, COLIN Professeur, ESPCI Paris	*Présidente*
Laurent, CHAZEAU Professeur, INSA Lyon	*Rapporteur*
Kees, STORM Professeur, Eindhoven University of Technology	*Rapporteur*
Robert, GÖSTL Research group leader, Leibniz Institute for Interactive Materials	*Examinateur*
Jutta, RIEGER Chargé de recherche, Sorbonne Université CNRS	*Examinatrice*
Costantino, CRETON Directeur de recherche, ESPCI Paris CNRS	*Directeur de thèse*

ESPCI PARIS | PSL

Table of contents

Chapter 2: Synthesis and characterization of mechano-fluorescent and non mechano-fluorescent single and multiple network elastomers

Chapter 3: Detection and mapping of bond scission in multiple network elastomers using confocal microscopy

Chapter 4: Bond scission in single network elastomers

Chapter 5: Bond scission in the filler of multiple network elastomers

Remerciements

J'adresse tout d'abord mes remerciements aux personnes qui ont accepté de juger mon travail et qui ont montré de l'intérêt pour mon sujet de recherche : Annie Colin, Jutta Rieger, Robert Göstl ainsi que les rapporteurs de mon mémoire Kees Storm et Laurent Chazeau. Leurs retours et discussions ont été très enrichissants.

Je tiens à remercier chaudement Costantino Creton, qui m'a offert l'opportunité de travailler sur ce sujet de recherche passionnant. Il m'a confié ce sujet pluridisciplinaire en me faisant confiance pour développer les compétences et connaissances nécessaires et je lui en suis reconnaissante. Au cours de ces trois ans, il m'a beaucoup appris, guidé et permis de prendre du recul.

J'aimerais remercier les personnes qui m'ont aidée lors des étapes de chimie organique de synthèse de mécanophore : Nadège Pantoustier et Nicolas Sanson ainsi que Christophe Meyer (LCO) et Jessica Clough, Robert Göstl et Rint Sijbesma (Tu/e Eindhoven). Je souhaite également remercier Bruno Bresson pour son aide pour les différents montages avec la Deben ainsi que pour les images MEB. Merci à Artem Kovalenko et à Sandrine Ithurria (LPEM) pour leur aide sur la caractérisation de fluorescence.

Travailler sur un projet ERC était une réelle chance de collaborer et de partager avec d'autres thésards et post-docs. Je tiens à remercier, tout particulièrement Josh Yeh pour son aide précieuse sur l'analyse d'image. Cette thèse n'aurait pas la même dimension sans l'aide de Josh qui m'a permis de gravir une marche et de pousser les résultats jusqu'à une quantification fiable. Chaque membre de l'équipe ERC m'a énormément apporté et je leur en suis reconnaissante.
J'aimerais remercier, en particulier, Pierre Millereau et Yinjun Chen qui m'ont formée et transmis leur savoir et surtout leur savoir-faire. J'en profite pour souhaiter bon courage à Victoria Waltz pour la suite, je suis sûre qu'elle donnera un bel avenir à la mécanochimie !

Merci à ceux qui m'ont accompagnée dans la vulgarisation scientifique : Alba, Anne-Cha, Miléna et Cécile qui ont participé à Pint of Science et Guylaine, Anne-Cha, Gaëlle et Ludo avec qui j'ai pris plaisir à monter des ateliers pour la Fête de la Science.

Plus personnellement, j'aimerais remercier toutes les personnes qui m'ont donné le sourire et ont égayé mon quotidien. Ces trois années m'ont permis de faire de très belles rencontres et j'en garderai d'excellents souvenirs. Merci à Mehdi, Miléna et Giorgia, partager votre bureau a été un plaisir (et un soutien moral entre writting buddies !). Merci au 3ème étage et anciens du 3ème, en particulier, Raphaëlle, Mélanie, Bruno et Xavier, pour les déjeuners, le badminton, les potins… Merci aux compagnons de « petite bière ? » ou de « pause thé ? » qui rendent la thèse beaucoup plus agréable. Plus particulièrement, merci à Paul, d'abord de m'avoir encouragée à postuler à cette thèse, mais aussi pour ces trois années d'amitié. Ensuite Ludo, avec qui j'ai adoré travailler, j'ai énormément appris et apprécié nos discussions aussi bien professionnelles que personnelles. Un grand frère de thèse sur qui j'ai toujours pu compter.

Résumé en français
Détection quantitative de l'endommagement moléculaire par mécano-fluorescence, dans les matériaux mous

1   Contexte, objectif et stratégie

Un pneu, un ligament de synthèse, de l'électronique flexible, tous ces matériaux sont mous mais doivent être aussi résistants. Pourtant, dès leur première utilisation des microfissures se créent. Tout l'enjeu est d'empêcher ces fissures, invisible à l'œil nu, de se propager. Imaginez un joint plastique pour l'aéronautique incolore qui devient fluorescent quand il est usé, mais avant qu'il ne soit trop tard. C'est la stratégie que nous avons adoptée, reposant sur la mécano-chimie (utilisation d'une force mécanique pour déclencher une réaction chimique). Au-delà de cette application directe, ces matériaux, dans lesquels l'activation de fluorescence traduit l'endommagement, nous permettent de mieux comprendre les conditions d'amorçage et de propagation d'une fracture. Notre approche multi-échelle est entièrement nouvelle et relie les ruptures de liaisons chimiques à l'échelle moléculaire à la fracture macroscopique de l'échantillon. J'ai synthétisé en cinq étapes la molécule activable mécaniquement, appelé un mécanophore. J'ai intégré ce mécanophore dans des élastomères modèles. J'ai effectué ensuite des tests mécaniques de fracture combinés à une analyse par microscopie de fluorescence qui m'ont permis de répondre à plusieurs questions présentées ci-dessous.

2   Cartographie quantitative de l'endommagement moléculaire

Comment et combien de liaisons casse-t-on dans des matériaux renforcés par un mécanisme de réseau sacrificiel ?

Nous avons d'abord travaillé sur des caoutchoucs modèles, contenant des liaisons sacrificielles : en cassant, ces liaisons dissipent de l'énergie [1]. Ce mécanisme de renforcement a déjà été mis en évidence de manière qualitative grâce à la mécano-chimie. Un mécanophore (qui émet de la lumière lorsqu'il se casse) a été introduit dans ces matériaux et de la lumière a été détectée en pointe de fissure. Le caractère éphémère du signal et l'imprévisibilité de la fissure, empêche une analyse à fort grossissement et une calibration du signal. J'ai sélectionné un nouveau mécanophore de type adduit de Diels-Alder. J'ai adapté la voie de synthèse, en collaboration avec *Eindhoven University of technology* [2]. Cette molécule utilise l'énergie mécanique pour déclencher une réaction de rétro Diels-Alder qui donne lieu à une activation de fluorescence (comme représenté schématiquement Figure 1.a). La fluorescence est stable et intense ; elle permet donc une analyse par microscopie confocale. Ce mécanophore est chimiquement intégré lors de la synthèse. Le chapitre 2 présente la synthèse du mécanophore et des matériaux mécano-fluorescents utilisé dans l'étude. Les matériaux, mécano-fluorescents ou de référence,

sont ensuite caractérisé. J'ai montré que les propriétés à petites et grandes déformations des matériaux mécano-fluorescent sont inchangé par rapport aux matériaux de référence.

J'ai calibré le signal lumineux en incorporant une molécule de référence (représentée Figure 1.a) possédant la même fluorescence que le mécanophore activé dans des chaines de polymère. La méthode que j'ai développée, et qui est détaillée dans le chapitre 3, a permis d'observer et de quantifier directement et à un fort niveau de grossissement la rupture des liens sacrificiels lors de la fissuration. Des exemples d'image en 3D, à différents grossissements, reconstituées à partir de microscopie confocale sont représentés Figure 1.b et 1.c.
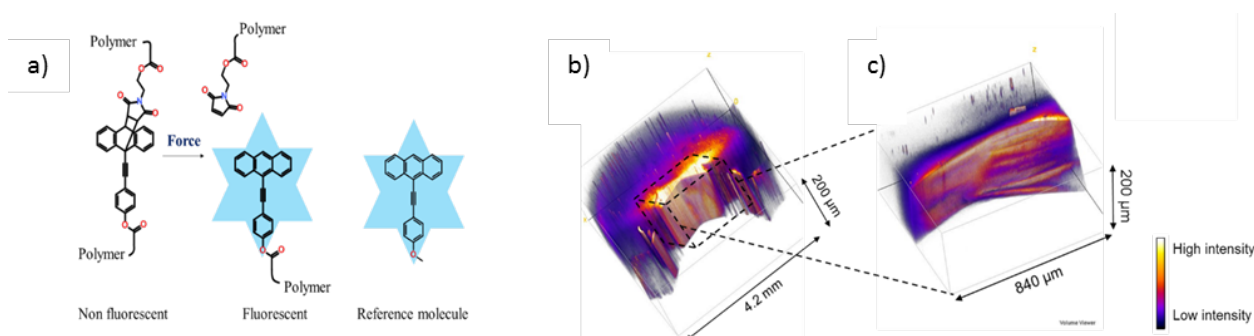
Figure 1. a) Schéma d'activation du mécanophore et molécule de référence. Reconstruction 3D de la pointe de fissure à faible b) et plus fort grossissement c) (le signal fluorescent correspond à l'endommagement moléculaire).

3   Fracture de la matière molle, un phénomène 3D

Pour casser un élastomère, faut-il casser des liaisons chimiques dans un volume ou uniquement un plan moléculaire ?

Cette nouvelle méthode a également permis de mettre en évidence des résultats complètement nouveaux, présentés dans le chapitre 4. Il y a cinquante ans, Lake et Thomas ont proposé une théorie majeure de la fracture [3]. Celle-ci présente la propagation de fissure comme une rupture de liaisons chimique sur un plan moléculaire uniquement, soit une dizaine de nm. Cette théorie, très utilisée, permet de prédire le bon ordre de grandeur de l'énergie nécessaire pour propager une fracture, pourtant son sens physique est discutable. Nous sommes les premiers à montrer que, dans un réseau élastomère simple, les ruptures de liaison sont 5 à 20 fois supérieures à la prédiction de Lake et Thomas et surtout ont lieu dans un zone d'épaisseur supérieure à 10 µm autour d'un plan de la fissure, valeur qui est supérieure de trois ordres de grandeur à la dimension de la maille. Ces résultats remettent en question de façon claire une théorie bien établie et permettront certainement des avancées théoriques importantes.

4 Dépendance de la viscoélasticité et de la rupture de liaison

La rupture de liaisons est-elle dépendante de la vitesse et de la température dans les caoutchoucs ?

Les mécanismes de dissipation d'énergie en pointe de fissure sont, dans les modèles actuels [4, 5], considérés comme provenant de deux origines : d'une part la dissipation viscoélastique (dépendante de la vitesse et de la température) et d'autre part la rupture de liaison (supposée indépendante de la vitesse et de la température). Nous avons montré que cette séparation ne peut pas être faite si simplement car la rupture de liaison dépend de la vitesse et de la température. En effet, nous avons effectué des tests mécaniques de propagation de fissure à différentes vitesses et différentes températures et la quantité de liaisons cassées augmente avec la vitesse de propagation ou avec une réduction de la température. Le couplage entre viscoélasticité et endommagement moléculaire a été étudié pour les réseaux simple élastomère dans le chapitre 4 et pour différents réseaux multiples d'élastomère dans le chapitre 5.
L'endommagement moléculaire dans un réseau simple de poly acrylate de methyl augmente avec la vitesse de propagation et avec une température décroissante (s'approchant de la Tg). La comparaison, à une même distance de la température de transition vitreuse, d'un réseau simple de poly acrylate d'ethyl et de methyl a montré que l'endommagement moléculaire est plus localisé dans le poly acrylate d'ethyl. Malgré les expériences et analyses, il est difficile de conclure avec certitude sur l'origine de cette intéressante observation.
Une plus faible dépendance en température et vitesse est attendue pour les réseaux multiples comparé aux réseaux simples. Des fissures ont été propagées à différentes vitesses et différentes températures dans des réseaux doubles et triples de poly acrylate d'ethyl et de methyl. Quand le second réseau est fait de poly acrylate d'ethyl, et les tests effectués à au moins 30 °C au-dessus de la Tg, l'énergie de fracture et l'endommagement moléculaire sont faiblement dépendant de la vitesse et de la température. Cependant, quand le second réseau est viscoélastique, comme fait de poly acrylate de methyl à des températures proches de la Tg, l'énergie de fracture et l'endommagement moléculaire sont fortement dépendant de la température et de la vitesse. Cette dépendance s'amoindrit avec le pré-étirement du premier réseau.
De ces analyses, nous avons mis en évidence une compétition entre deux phénomènes : l'énergie dissipée intrinsèquement par la friction moléculaire (viscoélasticité classique) et l'énergie dissipée par la rupture non corrélée de chaines de polymère, facilité par la friction moléculaire. Selon les conditions, un phénomène domine l'autre. Il est important de gardé en tête que ces deux phénomènes sont couplés. Cet argument est applicable aussi bien aux réseaux simples qu'aux réseaux multiples d'élastomère mais les ordres de grandeur sont différents.

5 Conclusion

Pendant ma thèse, j'ai mis au point une méthode de cartographie de l'endommagement moléculaire, en 3D, à fort grossissement mais surtout de manière quantitative. Cette nouvelle méthode est la première permettant d'estimer le nombre de liaisons cassées dans un élastomère

simple ou dans des systèmes renforcés. J'ai mis en évidence des résultats nouveaux et inattendus : contrairement à des théories couramment acceptées et utilisées, cet endommagement ne se limite pas à un plan moléculaire et dépend de la vitesse et de la température. Cette méthode peut être adaptée à d'autres systèmes comme des hydrogels ou des élastomères chargés. Plus généralement, la méthode que j'ai développée est un nouvel outil essentiel pour la compréhension et la modélisation multi-échelle des mécanismes de dissipation en pointe de fissure. Ces modèles pourraient guider les choix des chimistes, pour l'instant empiriques, afin de créer de nouveaux matériaux avec une meilleure résistance à la fracture pour des applications biomédicales ou bien de haute technologie.

6   Références

1.   Ducrot, E., et al., *Toughening Elastomers with Sacrificial Bonds and Watching Them Break.* SCIENCE, 2014. **344**(6180): p. 186-9.
2.   Göstl, R. and Sijbesma R.P., *π-extended anthracenes as sensitive probes for mechanical stress.* Chem. Sci., 2016. **7**(1): p. 370-375.
3.   Lake, G.J. and Thomas A.G., *The Strength of Highly Elastic Materials.* Proceedings of the Royal Society of London. Series A, Mathematical and Physical Sciences, 1967. **300**(1460): p. 108-119.
4.   Gent, A.N., *Adhesion and Strength of Viscoelastic Solids. Is There a Relationship between Adhesion and Bulk Properties?* Langmuir, 1996. **12**(19): p. 4492-4496.
5.   Zhao, X., *Multi-scale multi-mechanism design of tough hydrogels: building dissipation into stretchy networks.* Soft Matter, 2014. **10**(5): p. 672-87.

List of symbols

C_∞ Characteristic ratio

E Young's modulus

E_e Contribution of the entanglement of the Young's modulus

E_x Contribution of the crosslinks of the Young's modulus

ϕ Quantum yield

$\phi_{act.DACL}$ Average fraction of mechanophore activation up to the distance L_{damage}

ϕ_{SN} Volume fraction of first network in multiple network elastomers

Γ Fracture energy

Γ_0 Intrinsic fracture energy

Γ_{damage} Contribution of chains scission in fracture energy

Γ_{exp} Macroscopically measured fracture energy

L_{damage} Length over which damage is detected

λ Stretch ratio

$\dot{\lambda}$ Stretch rate

λ_0 Level of pre-stretching of the filler network

λ_{break} or λ_c Stretch ratio at crack propagation

M_0 Molecular weight of the monomer

M_e Molecular weight between entanglements

M_x Molecular weight between crosslinks

N_x Number of C-C bonds between cross-links

v_x Density of cross-links

σ_N Nominal Stress

Σ Areal density of chains

Σ_{exp} Areal density of broken chains

$\bar{\Sigma}$ Normalized areal density of broken chain

ρ Polymer network density

U_b Bond energy

U Energy that is stored per bond when the strand breaks

List of abbreviations

BDA	1,4-butanediol diacrylate (cross-linker)
DACL	Diels-Alder Adduct Cross-Linker (mechanophore cross-linker)
DN	Double network elastomer
EA	Ethyl Acrylate (monomer)
HMP	2-hydroxy-2-methylpropiophenone (UV initiator)
LSCM	Laser Scanning Confocal Microscope
MA	Methyl Acrylate (monomer)
MN	Multiple network elastomer
PSF	Point spread function
QN	Quadruple network elastomer
SN	Single network elastomer
TN	Triple network elastomer

List of materials

Molar percentages are relative to moles of monomer.

Single network composition

Name	Monomer	[HMP] (mol%)	[BDA] (mol%)	[DACL] (mol%)	[Total Cross-linker] (mol%)	[DACL] (mol.m^{-3})
SNEA	EA	1.16	0.50	0	0.5	0
DASNEA	EA	1.16	0.48	0.02	0.5	2.2
SNMA	MA	1.16	0.43	0	0.43	0
DASNMA	MA	1.16	0.41	0.02	0.43	2.8
SNMA$_{0.2}$	MA	1.16	0.22	0	0.22	0
DASNMA$_{0.2}$	MA	1.16	0.20	0.02	0.22	2.8

Multiple networks composition

Multiple networks are noted BBCC(z)
BB: EA or MA for Ethyl Acrylate or Methyl Acrylate monomers in the filler network
CC: EA or MA for the monomer of the matrix
(z): the prestretching λ_0

'DA' written before the network in which the mechanophore is incorporated:
- DABBCC(z): contains the Diels-Alder adduct mechanophore in the filler network
- BBDACC(z): contains the Diels-Alder adduct mechanophore in the second network

Name	Type of MN	Filler monomer	Matrix monomer	ϕ_{SN}	λ_0	[DACL] (mol/m^3)	Network containing DACL
EAEA(1.6)	DN	EA	EA	0.2	1.6	0	/
DAEAEA(1.6)	DN	EA	EA	0.2	1.6	0.5	1st
EADAEA(1.6)	DN	EA	EA	0.2	1.6	0.9	2nd
DAMAEA(1.5)	DN	MA	EA	0.3	1.5	0.9	1st
MAMA(1.6)	DN	MA	MA	0.3	1.6	0	/
DAMAMA(1.6)	DN	MA	MA	0.3	1.6	0.7	1st
EAEA(2.4)	TN	EA	EA	0.07	2.4	0	/
DAEAEA(2.3)	TN	EA	EA	0.07	2.3	0.2	1st
EADAEA(2.5)	TN	EA	EA	0.07	2.5	0.3	2nd
MAMA(2.3)	TN	MA	MA	0.08	2.3	0	/
DAMAMA(2.3)	TN	MA	MA	0.08	2.3	0.2	1st
EAEA(3.1)	QN	EA	EA	0.03	3.1	0	/
DAEAEA(3.1)	QN	EA	EA	0.03	3.1	0.08	1st
EADAEA(3.2)	QN	EA	EA	0.03	3.2	0.1	2nd

Introduction

General introduction and motivation of the manuscript

Background: Incomplete fracture picture

Soft and stretchable materials are irreplaceable in engineering applications such as large amplitude actuators, flexible electronics or soft prosthesis. However, their range of use is limited by their mechanical strength and more precisely by the propagation of a crack initiated by a defect. Therefore, initiation, propagation of a crack and dissipative mechanisms implicated at the crack tip are crucial phenomena to understand.

Currently, it is not possible to predict the fracture toughness or large strain mechanical properties of a soft material from its molecular composition or structure. If these predictions were possible thanks to modeling, the chemists would have precious guidance to design novel soft and high strength materials for biomedical and high-tech applications. The current inaccuracy of the predictions can be attributed to the lack of comprehensive picture on mechanisms of dissipation in front of the propagating cracks. In fact, proper investigation tools to elucidate the mechanisms that dissipate energy in all their complexity are still missing.

Dissipative mechanisms in elastomers are of three general types: friction between monomers, relaxation of pendant polymer chains and fracture of stretched chains by bond breakage (*1, 2*). Today's picture of crack propagation and dissipative mechanisms can be summarized by the drawing given in Figure 1. The molecular bond breakage is generally associated to a small zone at the very crack tip (black damage zone in Figure 1). In the Lake-Thomas model, currently used, this area is limited to a mesh size (*1*). Viscoelastic dissipation is commonly considered to occur in a much broader volume of linear deformations (grey region in Figure 1). However, chain scission is probably coupled to viscoelastic dissipation and likely occurs in a broad region where non-linear deformation occurs (red hatched region). Up to now, energy dissipation is still a black box.
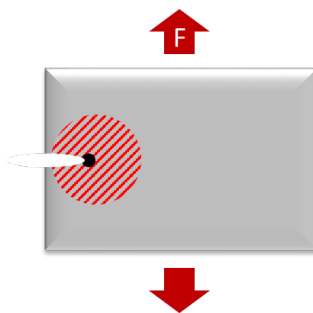
Figure 1: Schematic representation of a crack tip and dissipative zones

Context: an ERC program

This PhD work was included in a larger program funded by the European Research Council (ERC). The overall objective of the ERC project is to understand fracture of soft materials by linking the molecular structure with the meso-structure (at 50-100 µm scale). Its final goal is to build multi-scale and physically based molecular models predicting the fracture energy of soft materials based on their architecture. To do so different soft reinforced materials are under investigation in the ERC project, such as hydrogels with physical and chemical crosslinks, nanocomposite elastomers or multiple network elastomers. Only the last reinforced material is under discussion in this thesis.

PhD Objectives

This PhD project focuses on the analysis of one specific dissipative mechanism, namely chain scission. Indeed, the characterization of molecular damage in soft materials is the core of the thesis. This study can be defined by different objectives:

1. Developing and optimizing an investigation tool to examine chains scission at the crack tip.
2. Building a methodology up in order to get robust and quantitative results on chain scission.
3. Improving the comprehensive picture of fracture in multiple network elastomers.
4. Analyzing the coupling between viscoelasticity and molecular damage in single and multiple network elastomers.

Strategy

The key point to achieve the first and second objectives is the detection of bond scission. Thanks to the so-called mechano-chemistry, it is possible to trigger, by mechanical force, chemical reactions. These chemical reactions can include bond breakage that can lead to detectable change in the material optical properties such as color change, light emission or fluorescence activation. Mechanophores have already been used to investigate molecular damage but, due to practical limitations, up to now, no quantitative information on molecular damage has been obtained. In addition, the resolution was limited. Among all mechanophores described in the literature, a π-extended anthracene mechano-fluorochrome, developed by R. Göstl and R. P. Sijbesma (*3*) attracted our interest. Thanks to a high quantum yield and good stability, fluorescence can be observed at high magnification and in 3D using a confocal microscope. For these reasons, the strategy adopted to map molecular damage in 3D was using a confocal microscope to detect elastomers labeled with mechano-fluorescent probes. The calibration of the fluorescence signal by a calibration molecule (with the same fluorescence as the activated mechanophore) seems a promising strategy to quantify the molecular damage. This quantitative information will be helpful to achieve objectives 3 and 4.

Methodology

The first set of model materials investigated are multiple network elastomers. They are a combination of a highly pre-stretched network called the filler network, diluted in a loosely cross-linked network called the matrix network. This combination of a high extensibility (from the matrix) and a high but fragile stiffness (from the filler) toughens the overall material by breaking the bonds of the filler network at a much lower macroscopic extension than what is needed to break the sample. These model materials are ideal candidates for our study as they are transparent, tough and their reinforcement mechanism is based on sacrificial bond breakage. The last point means that a lot of molecular damage (from the filler network) is expected to occur in front of the crack tip and its detection should be easier than for simple networks where bond scission is more localized (*4*).

The second set of materials investigated are simple elastomer networks. This basic case is less favorable but the amount of molecular damage in a cross-linked elastomer is still a crucial and open question.

The mechanophore will be introduced in the material structure. These mechano-fluorescent materials will be analyzed using a confocal macroscope that can be combined with a tensile test device.

Scientific challenges

Using these model materials and experimental tools, this PhD work will address specific scientific questions:

1. *How many sacrificial bonds break in multiple network elastomers and how does the level of pre-stretching of the filler network influence this amount of molecular damage?*
   In fact, the fracture toughness of multiple network elastomers increases non-linearly with the level of pre-stretching of the filler network (*5*). If the optimum volume and amount of sacrificial bond breakage is found (if any) it will provide precious guidance to their design.

2. *How many bonds break and how localized near the crack plane is the detected molecular damage after a crack propagation in a single network?*
   Lake and Thomas considered the rupture of a molecular plane to estimate the intrinsic fracture energy (*1*). At ambient conditions, the molecular damage is probably larger than a monolayer. However, this damage is missing in models because of a lack of knowledge.

3. *How is the damage zone affected by the applied strain rate and by the temperature during crack propagation in a single network? And in multiple network elastomers?*
   Strain rate and temperature are known to influence viscoelasticity but we do not know if these parameters have an influence on molecular damage. The coupling between viscoelasticity and molecular damage (if any) is not taken into account in current models.

Manuscript structure

To address these questions, the manuscript is structured as follows:

In Chapter 1, an overview of fracture and bond scission theories related to mechano-chemistry, is given. The choice of a specific mechanophore is detailed. Having in mind the Lake-Thomas theory and the selected mechano-fluorescent molecule behavior are essential to fully assess what follows.

In Chapter 2, materials used in the manuscript are introduced. The 5-step synthesis of the mechano-fluorescent molecule is presented. The 1-step synthesis of the calibration molecule, used to calibrate the fluorescence signal, is also indicated. The preparation of reference (non-mechanofluorescent) and mechano-fluorescent single and multiple networks are detailed. These materials are then characterized by uniaxial extension, dynamic mechanical analysis and rheology. The influence of the mechanophore introduction in the network structure on small and large deformation properties is analyzed.

Chapter 3 is a key chapter and contains the most challenging part of the work. The new investigation tool is presented. All along this chapter, methodologies are illustrated by the example of multiple networks with different levels of pre-stretching of the filler network. The 3D mapping of molecular damage is obtained. Crack initiation is qualitatively analyzed. The best strategy for quantification is discussed. The 'post mortem' quantitative methodology, adopted for Chapter 4 and Chapter 5, is detailed: its work flow, assumptions, limitations and outputs.

Chapter 4 is a results chapter dedicated to single networks. Molecular damage in single networks is observed and quantified. In order to study the coupling between viscoelastic dissipation and molecular damage, cracks are propagated at different rates and different temperatures. Evolution of molecular damage with these parameters is discussed.

Chapter 5 is a results chapter dedicated to multiple network elastomers. Cracks are propagated at different rates and different temperatures in multiple network elastomers with different levels of filler network pre-stretching and with different polymers. The

coupling of viscoelasticity and molecular damage in multiple network elastomers is discussed.

A concluding part summarizes the main achievements of this PhD work and presents a discussion and an attempt of a comprehensive picture of fracture in single and multiple network elastomer and the coupling of viscoelasticity and damage.

References

1.   G. J. Lake, A. G. Thomas, The Strength of Highly Elastic Materials. *Proceedings of the Royal Society of London. Series A, Mathematical and Physical Sciences* **300**, 108-119 (1967).
2.   C. Creton, M. Ciccotti, Fracture and adhesion of soft materials: a review. *Rep Prog Phys* **79**, 046601 (2016).
3.   R. Göstl, R. P. Sijbesma, π-extended anthracenes as sensitive probes for mechanical stress. *Chem. Sci.* **7**, 370-375 (2016).
4.   E. Ducrot, Y. Chen, M. Bulters, R. P. Sijbesma, C. Creton, Toughening Elastomers with Sacrificial Bonds and Watching Them Break. *Science* **344**, 186-189 (2014).
5.   P. Millereau, U. P. E. M. CURIE, Ed. (2017).

Chapter 1

Fracture in soft materials and mechano-chemistry

Chapter 1: Fracture in soft materials and mechano-chemistry

Introduction

This chapter is a complement to the general introduction. Its objective is to present a state of the art and to introduce concepts that are useful for the understanding of the following chapters.

A first section is dedicated to fracture. Bulk cohesion of a material is ensured by chemical bonds (*1*) and bonds breakage results in macroscopic fracture. For that reason, fracture will be discussed at all its characteristic lengths: from the bulk material (cm scale) to the extension of polymer strands forming the network ($\sim$ nm scale) up to bond breakage ($\sim$ Å scale).

A second section focuses on the existing strategies to reinforce soft materials in order to resist fracture. Multiple network elastomers are introduced.

A last section presents mechano-chemistry and its use to detect bond scission.

1   Top down approaches of fracture of a simple elastomer

1.1   Bulk material failure: Fracture Mechanics

In all this manuscript, fracture energy, noted Γ, will be used to characterize fracture toughness. It is defined as the energy per unit area necessary to propagate a crack (*2*). Material failure occurs by the propagation of preexisting defects when the strain energy release rate at the crack tip, G, exceeds the fracture energy Γ (*2*).

1.1.1   Linear elastic fracture mechanics (LEFM)

It is useful to describe briefly crack propagation in an elastic solid before moving to soft materials that are more complicated. Linear elastic fracture mechanism (LEFM) describes well crack propagation in a rigid and brittle solid (such as glass or ceramic). The material is homogeneous, isotropic and linear elastic. The propagation is assumed isothermal and

quasi-static. The objective of the LEFM theory is to predict crack propagation conditions. We consider a notch of length c in a material under traction, as represented in Figure 1. The major assumption of the LEFM is that the bulk material behavior remains linearly elastic everywhere except in a very small region around the crack tip. This area is schematically collapsing into a linear crack front spanning an interface.
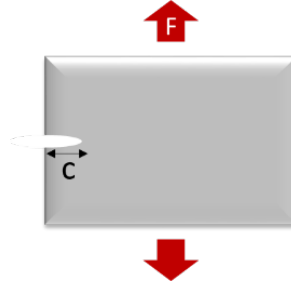
Figure 1: Schematic representation of a crack propagation test

In 1921, Griffith gave a first energetic picture of crack propagation (*3*). The growth of a crack corresponds to a conversion of mechanical energy into a thermodynamic energy cost per area unit to create two new surfaces, Eq 1.

$$\Gamma = 2\gamma$$
Eq 1.

where γ represents the solid surface energy.

By minimizing total energy, a strain energy release rate, G, in J.m^{-2}, is defined by Eq 2.

$$G = \frac{\partial Uw}{\partial A} - \frac{\partial Uel}{\partial A}$$
Eq 2.

Where A is the surface created by crack propagation, Uw is the external work, Uel represents variations of the elastic energy. In this theory the crack propagation condition is given by Eq 3.

$$G \geq G_c = 2\gamma$$
Eq 3.

In 1957, Irwin developed a model for the stress field, σ, at the crack tip induced by the external load and by the crack tip itself (*4*). The crack tip acts as a stress concentrator. He expressed a singularity at the crack tip in the form of an inverse square root dependence of the stress on the distance r from the crack tip, Eq 4., represented in Figure 2.

$$\sigma(r) \sim \frac{K}{\sqrt{r}} \qquad\qquad \text{Eq 4.}$$

Where K (Pa.m$^{1/2}$) is the loading parameter called the stress intensity factor
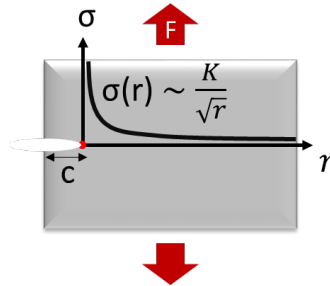
Figure 2: Stress singularity at the crack tip according to Irwin model:

In this theory, the crack propagation condition is given by Eq 5.

$$K \geq K_c \qquad\qquad \text{Eq 5.}$$

where K_c is called the fracture toughness and is a material property.

1.1.2 Limitations

LEFM is valid provided that all inelastic or nonlinear processes are limited to a small size, generally known as small scale yield condition (red dot in Figure 2). In soft dissipative matter, almost all soft materials, this assumption does not hold anymore, as the energy dissipation is not limited to a very small region, as represented in Figure 3 (*1*). In this extended region, the non-linear finite deformations and modifications of the viscoelastic dissipation have to be taken into account.
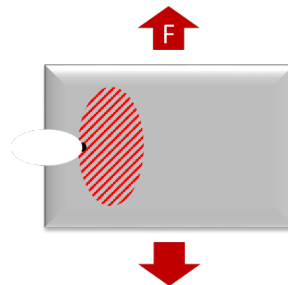
Figure 3: Schematic representation of the large nonlinear zone in soft materials (red hatch)

Energetic approaches are also limited by the difficulty to separate fracture energy in two contributions of energy dissipation: one due to fracture propagation the other due to macroscopic material deformation.

13

In fact, soft materials deform extensively and non-linearly before failing and their structure changes during deformation so that failure depends crucially on how the individual bonds are loaded as a function of the macroscopic strain and how they transfer stress to each other when they break. For that reason, it is important to get to a smaller length scale and to consider the network structure.

1.2 Polymer network mechanics

1.2.1 Polymer network structure

We consider an ideal rubber made of polymer chains attached at both ends by covalent bonds. Flexible polymer chains are composed of n+1 backbone atoms, named A_i with $0 \leq i \leq n$. In a first assumption, the chain experiences a free motion (*5*). The conformation can be described as a free walk of n segments with a length l. Each segment is described by a vector $\vec{r_i}$, called the bond vector, going from an atom A_i to an atom A_{i+1}. As represented in Figure 4, the end-to-end vector of the chain $\vec{R}$ is defined as the sum of all n bond vectors in the chain $\vec{r_i}$, Eq 6.
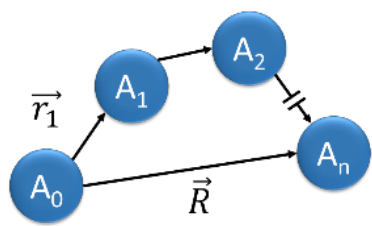
$$\vec{R} = \sum_{i=1}^{n} \vec{r_i}$$
<div align="right">Eq 6.</div>

Figure 4 : Schematic representation of a flexible polymer chain

In the simple case, we consider a polymer chain experiencing a random motion without preferred direction. As the average end-to-end vector is zero, a more relevant end-to-end distance can be defined, Eq 7., as the mean-square end-to-end distance, Eq 7.

$$\langle R^2 \rangle^{1/2} = n^{1/2} l$$
<div align="right">Eq 7.</div>

In real chains, the segments are not exactly randomly oriented relative to each other. The characteristic ratio C_∞ takes this correlation into account (for infinite number of

monomers), Eq 8. This ratio depends on the monomer used and represents the average rigidity or the flexibility of the bonds.

$$\langle R^2 \rangle^{1/2} = C_\infty^{1/2} n^{1/2} l \qquad\qquad \text{Eq 8.}$$

As the end-to-end distance is shorter than the fully extended chain nl, we can assume that the chain is retracted on itself.

This chain explores different conformations but they do not have an equal probability to be reached. We consider A_0, to be fixed as the origin of a Cartesian coordinate system. A_n, the other end, has a certain probability to be in a small volume element in the vicinity of a particular position (x, y, z). This probability, calculated by Kuhn (1934, 1936) and by Guth and Mark (1934), corresponds to a Gaussian function (6). In other words, the chain conformation follows a Gaussian statistic, as represented Figure 5.
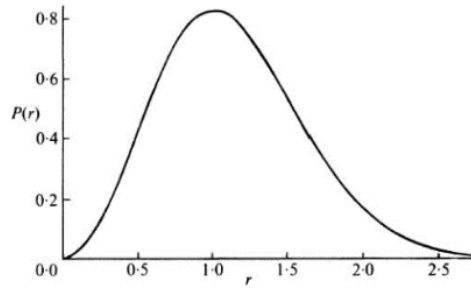
Figure 5: Distribution function of chain conformation following a Gaussian statistic

The distribution function is defined by Eq 9.

$$P(r) = constant \times r^2 e^{(-b^2 r^2)} \qquad\qquad \text{Eq 9.}$$

where $r^2 = x^2 + y^2 + z^2$ and $b^2 = \frac{3}{2} n l^2$

1.2.2 Polymer network deformation

Polymer networks have the ability to reversibly deform and come back to their original state. This phenomenon, called rubber elasticity, is due to entropic elasticity of the network strand. Rubber elasticity was first described by Kuhn, Wall and Flory in their affine network model(6). The main assumption of this model is an affine deformation: the relative deformation of each network strand is the same as the macroscopic relative deformation imposed on the overall network. For an affine deformation, the end-to-end

vector is modified from $\vec{R_0}(R_{x,0}, R_{y,0}, R_{z,0})$ to $\vec{R}(R_x, R_y, R_z)$ in the deformed state. Projections along x, y and z directions are given by Eq 10.,Eq 11. and Eq 12.

$$R_x = \lambda_x R_{x,0} \qquad\qquad \text{Eq 10.}$$

$$R_y = \lambda_y R_{y,0} \qquad\qquad \text{Eq 11.}$$

$$R_x = \lambda_z R_{z,0} \qquad\qquad \text{Eq 12.}$$

The strain energy density W of a cross-linked material can be estimated by the sum of the entropic elasticity of the elastic chains and can be estimated as a function of the three principal stretches, Eq 13.(*1*)

$$W = \frac{v_x k_b T}{2}(\lambda_x^2 + \lambda_y^2 + \lambda_z^2 - 3) \qquad\qquad \text{Eq 13.}$$

Where v_x is the density of cross-links.

For incompressible materials, Eq 14. has to be verified

$$\lambda_x \, \lambda_y \, \lambda_z = 1 \qquad\qquad \text{Eq 14.}$$

When considering an uniaxial extension test ($\lambda = \lambda_x$ and $\lambda_y = \lambda_z = {1}/{\sqrt{\lambda}}$), the value of the nominal stress σ_N can be predicted by deriving the strain energy density function relative to the uniaxial stretch λ, Eq 15.

$$\sigma_N = v_x k_b T \left(\lambda - \frac{1}{\lambda^2}\right) \qquad\qquad \text{Eq 15.}$$

The coefficient relating the stress and the deformation is the shear modulus G, defined by Eq 16.

$$G = v_x k_b T = \frac{\rho R T}{M_x} \qquad\qquad \text{Eq 16.}$$

Where ρ is the network density, R the gas constant and M_x the average molecular weight between crosslinks.

The Young's modulus, E, is another coefficient used to measure the stiffness of a material, defined by Eq 17.

$$E = 2(1 + v)G \qquad\qquad \text{Eq 17.}$$

Where v the Poisson's ratio. For rubbers v ≈ 0.5 and E = 3G, and the Young's modulus can be estimated by Eq 18.

$$E = 3\nu_x k_b T = \frac{3\rho RT}{M_x} \qquad\qquad \text{Eq 18.}$$

At small strain, the entanglement points act as temporary crosslink points. The Young's modulus can be estimated by the sum of two contribution: the first one from crosslinks E_x and the second one from entanglement E_e, as defined in Eq 19.

$$E = E_x + E_e = \frac{3\rho RT}{M_x} + \frac{3\rho RT}{M_e} \qquad\qquad \text{Eq 19.}$$

Where M_e is the average molecular weight between entanglements.

Rubinstein and Panyukov have developed a molecularly based slip-tube model for non-linear elasticity of entangled polymer networks. The model will be presented and used to fit data in Chapter 2.

Gaussian theory can describe what happens at low extension. But at higher extension, when the distance between the two ends of the chain or two cross-linked points approaches the fully extended length, Gaussian treatment is not sufficient (6). The stiffening of an individual chain is well described by the Langevin function, however the stiffening of an elastic material cannot be easily predicted simply from the density of crosslinks (1). Unfortunately, non-Gaussian theories are less (or not) simple and general as the Gaussian one.

In 1996, Gent proposed an empirical model containing a parameter to take into account the finite extensibility of the polymer chain (7). In his model, the nominal stress σ_N is predicted by Eq 20.

$$\sigma_N = \nu_x k_b T \frac{\left(\lambda - \frac{1}{\lambda^2}\right)}{\left(1 - \frac{J_1 - 3}{J_m}\right)} \qquad\qquad \text{Eq 20.}$$

Where J_1 is the first invariant defined by Eq 21. and J_m is the maximum allowable value of $J_1 - 3$.

$$J_1 = \lambda_x^2 + \lambda_y^2 + \lambda_z^2 \qquad\qquad \text{Eq 21.}$$

This model is in good agreement with experiments as long as the effect of entanglement is not dominant.

1.3 Polymer strand loading

The experimental mechanical characterization of a single polymer chain has been carried out using an AFM tip (*8-10*). Typical force-displacement plots of the stretching of a single chain are obtained by attaching a polymer chain on an AFM tip and recording the force while pulling. One example is given in Figure 6, made by Oesterhelt *et al.* with a poly(ethylene glycol) polymer chain (*9*).

1. At a force value around a few pN the chain unfolds. The response is not specific to the properties of the monomer/repeat unit but is characteristic of the statistical behavior of an ideal chain (polymer entropic restoring forces). Initially these entropic forces are well approximated by the so-called Gaussian approximation and the force-displacement plot is linear.

2. At hundreds of pN, the entropic force becomes non-linear and finally at very high forces the elasticity becomes increasingly enthalpic, as explained by bond distortion.

This distinction is schematically represented in Figure 7, where the red shaded area under the force *vs* end-to-end distance represents the total work done to extend the polymer chain and the area shaded by black lines corresponds to the enthalpic contribution only (*11*).
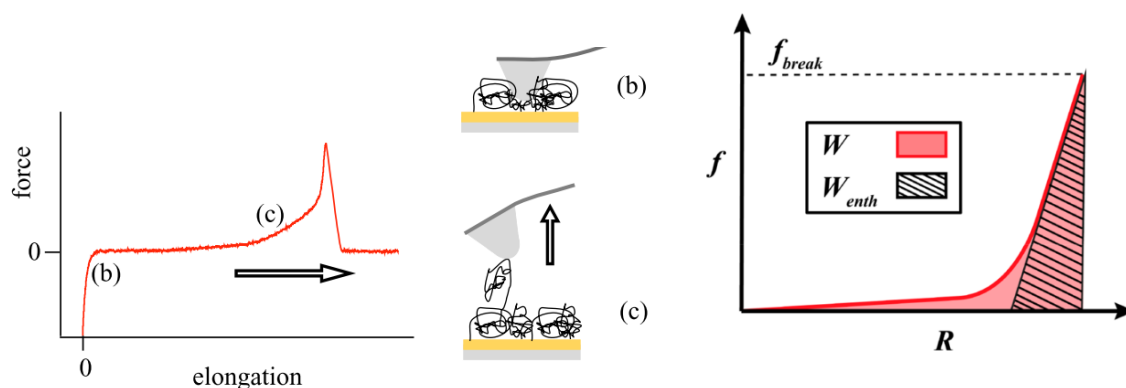
Figure 6: Schematic of a single molecule force spectroscopy experiment, upon retraction of the cantilever the polymer chain is stretched while force and elongation are recorded

Figure 7: Work done to extend a polymer chain (W) is the area under the force vs. end-to-end distance curve. The enthalpic part is the area shaded by black lines.

The multi-scale interpretation of the elastic response of the polymer chain is summarized in Figure 8 (*9*). Once the chain's finite extensibility is reached, the stress is applied on bonds, which are deformed up to their scission.
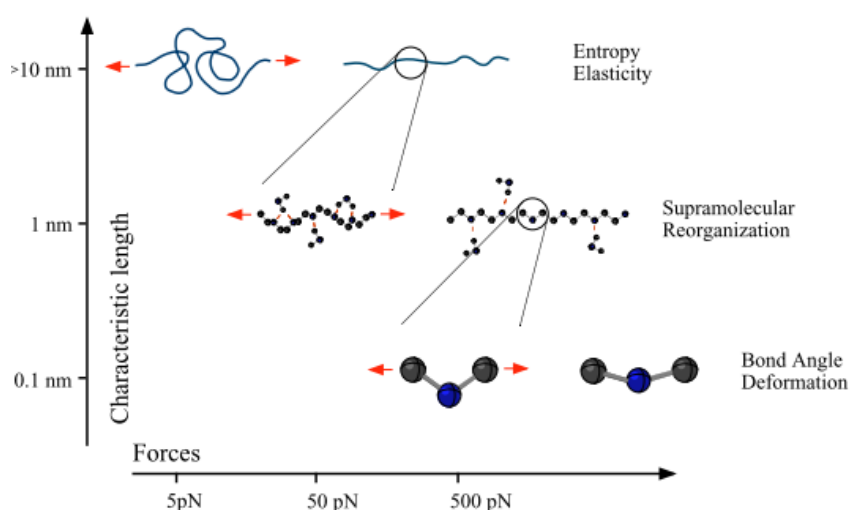
Figure 8: Schematics of hierarchy of elastic responses in PEG

1.4 Bond scission: a chemical reaction

From a chemical point of view, bond scissions are chemical reactions. To trigger a chemical reaction, which is a concerted motion of atoms that converts reactant(s) into product(s), a certain amount of energy is needed. The so-called activation energy ΔE_{act} corresponds to the energetic gap between reactants and the transition state. The potential

energy surface of a reaction and the activation energy associated $\Delta E_{A(0)}$ are represented in blue in Figure 9 (*12*).
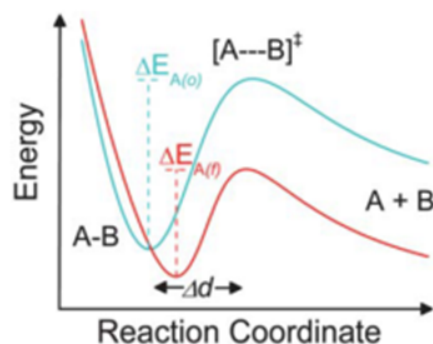
Figure 9: Representation of the potential energy surface of a reaction in the absence of coupled force (blue) and in the presence of a coupled force (red)

Stretching a molecule or a polymer chain modifies the potential energy landscape of a reaction and thus can lower the activation energy (*13*). The potential energy surface and the associated activation $\Delta E_{A(f)}$ of a reaction coupled with the force are represented in red in Figure 9. $\Delta E_{A(f)}$ is lower than $\Delta E_{A(0)}$ and thus the reaction is facilitated by the force applied. The term mechano-chemistry was suggested to qualify all the reactions accelerated by mechanical force (*13*). A following section (Section 3) presents in more details mechano-chemistry.

In the simplest model, the mechanically induced reduction in the activation energy ΔE_A is proportional to the magnitude of the applied force F and the geometry change that is aligned with the applied force during the reaction. The change in activation energy $\Delta(\Delta E_A)$ is therefore proportional to F through Δd, the difference in geometry of the transition state vs. that of the reactant projected along the vector of applied force:

$$\Delta(\Delta E_A) = F \cdot \Delta d$$

Mechanical force necessary to rupture a single covalent bond in a polymer chain depends on the orientation of the force applied compared with the bond orientation. When the force is coupled to the reaction, the activation energy is lowered but still exists. Mechano-chemical activation only enhances thermo-chemical activation.

Lengthening a carbon-carbon bond (C-C bond) will lower the activation energy of the homolytic fission (also called homolysis) of this C-C bond. In fact, the homolysis reaction,

presented in Figure 10, is accelerated by mechanical force. The lengthening of the C-C bond occurs only if the force is coupled to the bond-breaking process.

Figure 10: Schematic representation of a homolytic scission of a C-C bond

From here, the question of the definition of the bond strength arises. Evan Evans and Ken Ritchie proposed a definition of bond strength as the force that produces the most frequent failure in repeated tests of breakage (*14*).

The mechanical strength of a covalent bond has been calculated based on the density functional theory (DFT) by Beyer (*15*). He used a kinetic model to calculate the bond rupture rate of different atom-atom bonds as a function of the applied force. The calculated bond rupture probability densities (nN^{-1}) as a function of force F (nN) is given in Figure 11. He found a value around 4 nN for the carbon-carbon bond.
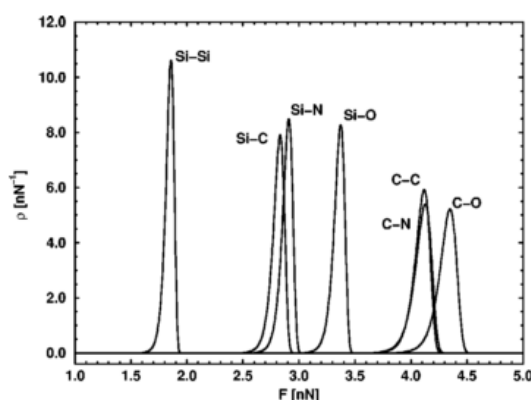
Figure 11: Evolution of the calculated bond rupture probability density ρ (in nN^{-1}) with the force F (in nN)

The bond strength depends on the rate at which the load is applied. The bond survival time diminishes with increasing loading rate. Evan Evans and Ken Ritchie checked this result experimentally for weak bonds. They investigated the interaction between biotin, a coenzyme, and streptavidin, a protein. The affinity of streptavidin for biotin is the strongest noncovalent biological interaction known. Figure 12 represents the force histograms obtained from tests of single biotin-streptavidin bonds (*16*). A shift in peak location and increase in width with increase in loading rate can be noticed.
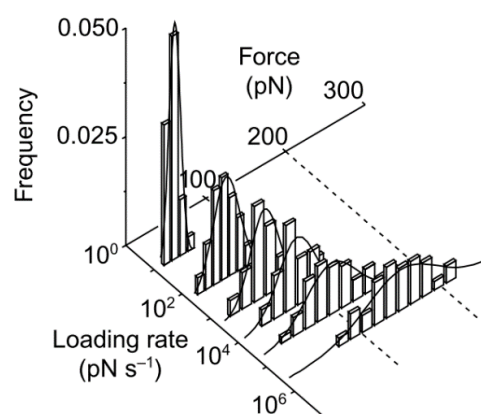
Figure 12: Force histograms from tests of single biotin-streptavidin bonds

Currently, the results have not been proven experimentally for covalent bonds because of practical limitations. Conceptually the phenomenon is the same; the difference is the energy involved, which is much higher in carbon-carbon bonds dissociation than in weak bonds.

Homolytic scission seems to be the main mechano-degradation mode for many polymers, for which the formation of neutral mechano-radicals can be experimentally shown (*17*). However, other reactions such as heterolytic cleavage or oxidative degradation cannot be completely excluded. Furthermore, chemical environment of the rupturing bond also influences the mechanical force. It would be an oversimplified picture to consider chain rupture as only homolysis with a unique value of activation energy associated.

1.5   Polymer network fracture: Lake and Thomas model

In 1967, Lake and coworkers developed a molecular model of fracture. From experiments, they exhibited a minimum tearing energy Γ_0 , ranging between 50 and 100 J.m^{-2}, at which "mechanic-oxidative" cut growth occurs in a large range of elastomers (*18*). This minimum amount of mechanical energy corresponds to the energy required to produce new surface by mechanical rupture of chains occurring in absence of viscoelastic dissipation (at high temperature far from the Tg of the rubber or with oil swollen rubber). This value does not correlate with the viscoelastic behavior of the material and varies only relatively slightly with chemical structure.

They approximate a value of Γ_0 for an ideal network without heterogeneities, imperfections and entanglement. Their estimate relies on two assumptions:

1. Only chains lying across the path of the crack break, as represented in the drawing in Figure 13 (red polymer strands).
2. The total bond energy of each bond of the stretched strand (length of chain between cross-links) is irreversibly lost.
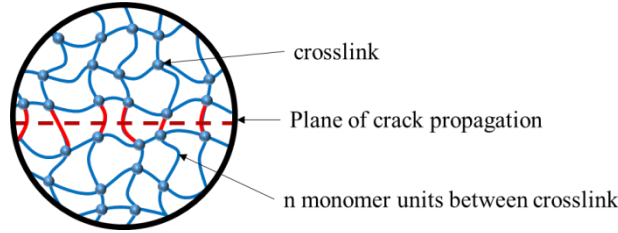
Figure 13: Schematic representation of Lake Thomas theory, red strands cross the crack plane

In this model, secondary forces are ignored and the minimum energy to break a strand is proportional to the chain length, corresponding to the number of C-C bonds between cross-links, N_x, in that chain. From these two assumptions, Γ_0 can be estimated by Eq 22.

$$\Gamma_0 = N_x U_b \Sigma \hspace{4cm} \text{Eq 22.}$$

Where U_b is the bond energy, 350 kJ.mol^{-1} for a carbon-carbon bond and Σ is the areal density of chain crossing the plane of the crack.

For a homogeneously cross-linked network , in the affine network model (*5*), Σ is given by Eq 23.

$$\Sigma \sim v_x \langle R_0{}^2 \rangle^{1/2} \sim v_x C_\infty{}^{1/2} N_x{}^{1/2} l \hspace{3cm} \text{Eq 23.}$$

Where v_x is the density of cross-links, $\langle R_0{}^2 \rangle^{1/2}$ the end-to-end distance, C_∞ the characteristic ratio and l the segment length (as presented in Section 1.2.1.).

By combining Eq 22. and Eq 23., Γ_0 can be estimated by Eq 24.

$$\Gamma_0 \sim U_b \, v_x \, C_\infty{}^{1/2} \, N_x{}^{3/2} l \sim \frac{U_b l \, \rho}{M_0} C_\infty{}^{1/2} N_x{}^{1/2} \hspace{2cm} \text{Eq 24.}$$

Where ρ is the monomer density and M_0 is the molar mass of the monomer.

Increasing the cross-linking density has two opposite effects. On one hand, increasing the cross-linking density reduces the number of chain bonds between cross-links, which

decreases the fracture energy. On the other hand, increasing the cross-linking density increases the number of chains lying across the path of the crack and increases the fracture energy. These two factors do not cancel out and are taken into account in the $N_x^{1/2}$ term.

This model is useful and broadly used for two reasons:

1. It gives a right order of magnitude of Γ_0 (1-100 J.m^{-2}).
2. It explains a classic and non-intuitive trend: a more cross-linked network is more brittle, as Γ_0 scale with $N_x^{1/2}$.

Very recently, S. Craig and co-worker suggested an adjustment to the Lake-Thomas model (*11*) relying on molecular details of chain extension and force-coupled bond dissociation. As they estimated the intrinsic fracture toughness, they kept the first assumption that only chains lying across the path of the crack break. They adjusted the second assumption regarding the energy dissipated per chain scission. In their model, because at that point no better models were available, Lake and Thomas estimated this energy by the total bond energy of each bond of the stretched strand. With the adjustement, Eq 22. is replaced by Eq 25., where U is the energy that is stored per bond when the strand breaks which is different from the bond dissociation energy.

$$\Gamma_0 = N_x \, U \, \Sigma \hspace{4cm} \text{Eq 25.}$$

Thanks to the recent advances in covalent polymer mechanochemistry, the estimation of U, different from U_b, seems more accurate. Indeed, they consider that the energy that is required to break one strand is the area under the force-extension curve of a representative elastically active strand in the polymer network that is stretched until it breaks (represented by the red area in Figure 7). By normalizing by the number of bonds, they quantify the energy stored per bond at fracture. Force extension curves were reported from single-molecule force spectroscopy experiment (presented in Section 1.2) and were modeled by the modified freely jointed chain model (*9*). From their model, they estimated U at 60 kJ.mol^{-1} for a typical hydrocarbon polymers. This value is well below the typical carbon-carbon bond dissociation energy (U_b = 350 kJ.mol^{-1}). In their model, they also highlighted the two contributions of U: one entropic (from chain elongation) and one enthalpic (from bond distortion).

1.6   Limitation of current molecular models

Γ_0 calculated by the Lake and Thomas theory corresponds to the intrinsic fracture toughness of polymer networks, meaning the energy required to fracture a single layer of polymer chains alone. Lake and Thomas theory can predict results for materials at high temperature, far from Tg and at low velocity, when the viscous effects are minimized. However, out of these conditions, other dissipative mechanisms are not negligible.

As early as 1972, Gent and Schultz (*19*) proposed to define the adhesion energy Γ as the sum of two contributions:

1. Γ_0, the intrinsic (chemical) strength of the interface that can be estimated by the Lake-Thomas model
2.   A function $f(v, T)$, usually much larger than unity, representing viscoelastic energy dissipation in front of the crack tip, propagating at a speed v and a temperature T.

The fracture energy is then given by Eq 26.(*20*).

$$\Gamma = \Gamma_0\big(1 + f(v, T)\big) \qquad\qquad \text{Eq 26.}$$

This approach was then used to analyze both adhesion tests (*21*) and fracture tests (*22*).

The second contribution, described by the factor $f(v, T)$, comes from the viscoelastic dissipation in the polymer in the linear viscoelastic region in front of the tip. From Persson's work, this contribution can be estimated theoretically from the linear viscoelastic properties of the polymer (*20, 23, 24*).

However, if Γ_0 is defined by the energy required to fracture a single layer of polymer chains and $f(v, T)$ is estimated by linear viscoelasticity, all highly non-linear processes such as cavity formation, stringing, chain pull-out and bond breaking are ignored.

In an interesting review on soft and tough material design, X. Zhao suggested a different general expression of the fracture toughness, given in Eq 27. (*24*)

$$\Gamma = \Gamma_0 + \Gamma_D \qquad\qquad \text{Eq 27.}$$

Where Γ_D is the contribution from dissipation in the so-called process zone, defined by the volume where significant mechanical dissipation is induced. The energy dissipation

mechanisms include fracture of polymer chains, domain transformations, cavity formation, stringing, chain pull-out or reversible cross-links. Currently, these contributions cannot be accurately calculated theoretically.

Figure 14 is a summarizing drawing representing a crack tip: at the very crack tip, bond breakage of a single layer of polymer chains occur (in black) and in the process zone, bulk dissipation occurs (in red hatching).
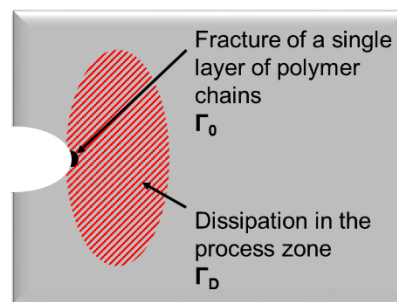
Figure 14: Schematic representation of a crack and the process zone (red hatch)

2 How to resist fracture: Reinforced soft matter

2.1 Soft and tough materials design

In the previous section, different models of fracture have been presented. The strategies to design fracture-resistant materials are now introduced. To mitigate crack propagation, the forces applied on the polymer strands at the crack tip, for a given macroscopic load of the sample, have to be reduced. In other words, high stresses concentrated at the crack tip have to be relaxed. This relaxation of the concentrated stress can be achieved by energy dissipation between the loading point (far from the crack) and the crack tip (*2*). Indeed, fracture energy, stress at break and stiffness can be enhanced by introduction of dissipative mechanisms into an extensible network.

X. Zhao presented different strategies for tough hydrogels in a review (*25*). The design principles he presented can be applied for elastomers. In general, soft and tough materials should combine mechanisms for high stretchability and for mechanical energy dissipation.

The mechanisms to achieve high stretchability include interpenetration of long-chain networks, hybrid physical and chemical cross-links and high functionality crosslinks. In fact, the average limiting extensibility of the polymer chain itself is a hard limit. Long strands or low cross-link density, are essential.

The mechanisms to create energy dissipation upon stretching are, among others, fracture of polymer chains, reversible cross-links, and domain transformation (*24, 25*). Another major bulk energy dissipation mechanism in elastomers, which is not present in hydrogels, is molecular friction. However, increasing the viscoelastic character of the elastomer through molecular friction only works over a limited temperature range (*23*).

A first strategy to increase energy dissipation consists in incorporating a stiffer dispersed phase (like ionic bonds or nanocrystals) that can only be deformed above a certain stress level. One example is the ionically and covalently cross-linked network developed by Suo (*26*). The unzipping of ionic cross-links is the major dissipation mechanism in these tough hydrogels.

A second strategy is the introduction of dynamic bonds in order to minimized local heterogeneities during deformation. This is the strategy used in sliding gels (*27*) or in dual cross-linked gels (*28, 29*).

A third strategy is the introduction of sacrificial bonds that break because they are overloaded relative to the main bonds. This last strategy will be discussed in details in the next section.

2.2   Multiple networks

2.2.1   Multiple networks design

2.2.1.1 *First Gong's double network hydrogels*

As discussed earlier in this Chapter (Section 1.5), stretched chains store energy. This energy is dissipated once bonds are broken. In 2003, Gong and her group take advantage of this irreversible dissipative mechanism to design new tough hydrogels, called double networks (DN) gels (*30*). A small fraction of sacrificial bonds breaks because they are overloaded relatively to the bonds of the main stretchable network. As the reinforcement mechanism by sacrificial bond scissions is not viscoelastic, they developed strain rate independent soft and tough hydrogels. In fact, fracture energy shows a weak dependence on crack propagation velocity in tearing experiments (*31*).

Double network hydrogels are a combination of a diluted and highly cross-linked first network in a concentrated and loosely cross-linked second network. Figure 15 is a schematic representation of the combination of the different networks with a picture of a sample (*32*). Thanks to this strategy, they were able to synthetize relatively stiff (0.3 MPa) hydrogels containing 90 wt% of water with a high fracture energy: 10^2 to 10^3 J/m^2 (while standard hydrogels range about 1 J/m^2). After trying several combinations of polymers, the best system appeared to be a polyelectrolyte poly(2-acrylamide-2-methylpropanesulfonic acid) (PAMPS) as the first swollen network and poly(acrylamide) (PAAm) as the second network. The first and the second network are interconnected to transfer the strain: a DN gel cannot be toughened by an un-cross-linked isolated second network (*33*).
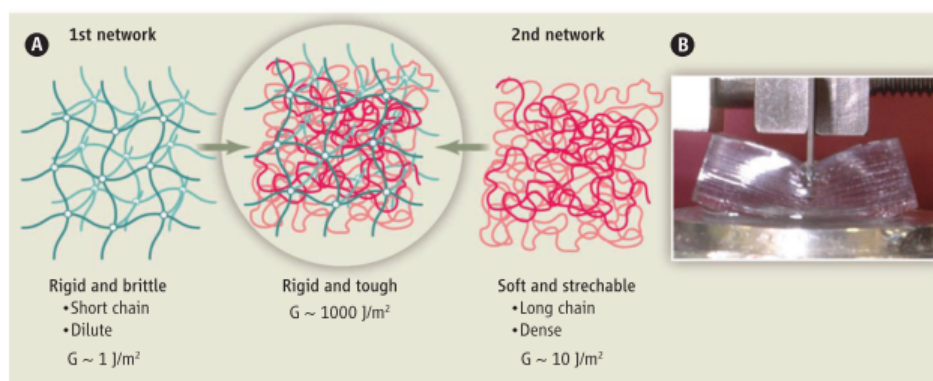
Figure 15: Schematic representation of double network composition with the rigid network in green and the soft network in pink (a). Picture of a DN tough gel (b)

2.2.1.2 Multiple network elastomers

Inspired by Gong's DN hydrogel, Etienne Ducrot, a PhD who graduated from our group, adapted the multiple step sequential free-radical polymerization from hydrogels to elastomers (*34*). In 2014, he synthesized multiple (also called inter-penetrated) network elastomers made of acrylate. Their schematic representation is similar to the one given in Figure 15 for gels: they are a combination of a stiff and highly cross-linked first network diluted in a loosely cross-linked second network. Short chains of the first network fracture under deformation while long chains of the second network maintain high elasticity. By repeating the swelling polymerization steps, he not only synthesized double networks but also triple and quadruple networks.

Multiple network elastomers are strongly reinforced in stiffness and toughness compared with simple (and brittle) elastomers. Young's moduli up to 4 MPa and fracture energies up to 9 kJ.m^{-2} were obtained (only 50 J.m^{-2} for acrylate single networks).

These values are comparable with those obtained for filled elastomers. However, multiple networks remain fully transparent while elastomers filled with carbon black are not, which precludes some applications.

Also, the reinforcement mechanism, by scission of sacrificial bonds does not rely on viscoelastic dissipation meaning that the mechanical properties improvements are not limited to a narrow window of temperature.

Since then, mechanical properties have been investigated. The two important parameters controlling properties have been identified:

1. The maximum extensibility of the first network, described by the level of pre-stretching λ_0, defined by Eq 28.

$$\lambda_0 = \frac{d_{total}}{d_{SN}} = \left(\frac{V_{total}}{V_{SN}}\right)^{1/3} = \left(\frac{m_{total}}{m_{SN}}\right)^{1/3} \qquad \text{Eq 28.}$$

With d_{total} and d_{SN} characteristic distances such as the thickness, the length or the width of the final material and the first network respectively. V_{SN} and V_{total} are the volume of the first network and of the final material respectively. m_{SN} and m_{total} are the weight of the first network and of the final material respectively.

2. The volume fraction, ɸ, of first network defined and Eq 29.

$$\phi_{SN} = \frac{V_{SN}}{V_{total}} \sim \frac{m_{SN}}{m_{total}} \qquad \text{Eq 29.}$$

If the two networks have the same density, the volume fraction is equal to the weight fraction. Otherwise, density has to be taken into account (or the volume fraction can be approximated by the weight fraction).

2.2.2 Sacrificial bonds in multiple network elastomers
2.2.2.1 Pseudo-Mullins effect

The Mullins' effect is a stretch dependent damage mechanism first identified for filled rubbers and defined by a considerable softening only observed at elongations less than the previous value of maximum stretch. While at higher elongations that the previous maximum stretch the stress-strain curve is relatively unaffected (*35*). The phenomenon is commonly observed in filled rubber and natural rubber.

After carrying out systematic loading and unloading experiments on DN hydrogels, a kind of Mullins' effect was reported (*36*). A large hysteresis was observed during the first loading cycle while no hysteresis appeared during a second softened loading-unloading cycle (elastic behavior). One major difference with the classic Mullins' effect observed for filled elastomers is the absence of recovery with time for the DN gel. As the dissipative

phenomenon is irreversible, the initial hysteresis can be attributed to the fracture of covalent bonds in the first network. As soon as it is deformed, some of the shorter strands break. This continuous fracture of bonds does not lead to macroscopic fracture of the material even if many microscopic (or molecular) cracks are created within the material. Micro-cracks coalescence is prevented by the second network bridges but also because the stress concentration is averaged by the softening of the material in a large plasticized zone.

Multiple network elastomers also experience this pseudo-Mullins' effect and the same interpretation is given. Multiple network elastomers only dissipate energy in the first cycle and then subsequent cycles are very elastic, in contrast with conventional elastomers that always display some viscoelastic dissipation in steady state cycles (*2*). As shown in Figure 16, each n-th cycle follows a different path when λ of the n-th cycle exceeds the maximum value of the (n-1) cycle (*34*).
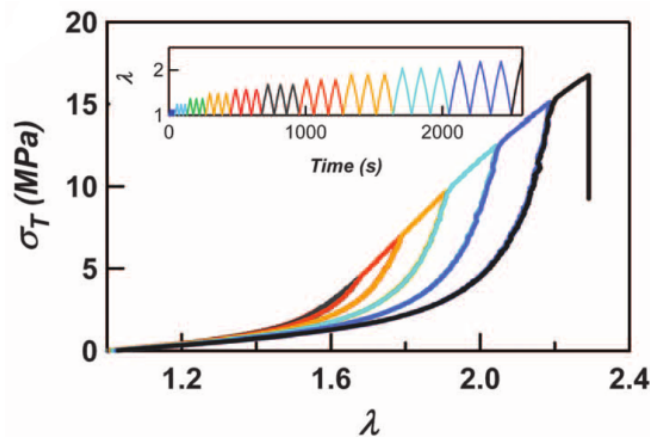
Figure 16: Stress-strain curve of a triple network elastomer submitted to a step-cycle loading.

2.2.2.2 Necking phenomenon

During elongation of DN hydrogels, Gong's group noticed the apparition and growth of constricted zones, this phenomenon is called necking or yielding (*37*). Figure 17 represents the stress-strain curve of a DN gel; where the necking corresponds to the plateau starting at the point C up to point E. Pictures of the sample illustrate the phenomenon. They investigated necking in DN hydrogels and proved that the Young's

modulus of the necked region of a PAMPS/PAAm gel is much lower than in the un-necked region (0.015 MPa compared to 0.1 MPa).

They suggested the following scenario. During stretching of the sample, the first network breaks into fragments. Fragmentation has two consequences on the material reinforcement. First, the fragmentation dissipates energy. Then, first network fragments act as clusters, which are ultra-multifunctional crosslinking point for the second network. These cross-linked points are not chemical, the molecular weight between "cross-link" can evolve by chain sliding. Furthermore, clusters can break into smaller fragments. These two adjustments allowed a better strain distribution (*38, 39*). The fragmentation of the filler network in isolated clusters is questionable and is discussed later in this chapter by Yinjun Chen's work on elastomers.
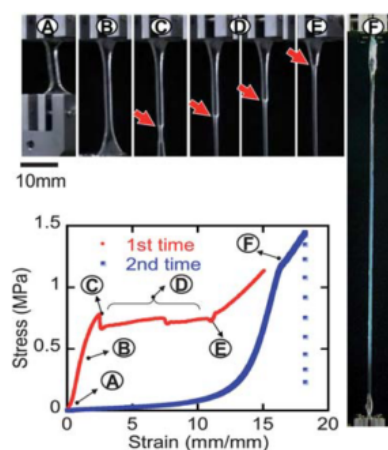

Figure 17: Stress-strain curve of DN gel under uniaxial elongation with pictures illustrating the necking process (arrows showing the necking front)

What is sure is that the necking corresponds to a large dissipation of energy at the two necking fronts, attributed to the comprehensive breakage of first network's chains. The yield stress appears to be dependent on the details of the structure of the first network and especially on its areal density of strands normal to the tensile direction (*40*). Yield stress is an increasing linear function of the surface chain density of the first network. The yield stress decreases with the swelling of the first network and the pre-stretching of its chains. Looking at the hysteresis loop, it was found that permanent damage appears before necking (*39*). The presence of a large hysteresis in the first loading unloading cycle reports for structural modifications such as first network internal fracture. This result means that bond scissions occur before necking.

Necking was also observed in multiple network elastomers with a high enough level of pre-stretching of the first network ($\lambda_0 > 3$), as shown in Figure 18 (*40, 41*). Necking in multiple network elastomers will be discussed in more details in a following section (Section 3.4.2).
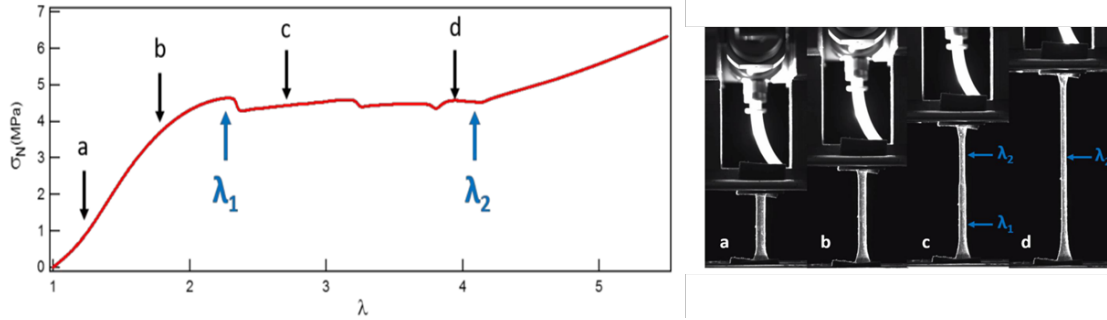

Figure 18: Stress-strain curve of a sample presenting a yield stress and recorded pictures describing the macroscopic state of the sample as the elongation increases

Thanks to direct observations, using a conventional optical microscope (Figure 19a) and a high-low image captured using a color 3D violet laser scanning microscope (Figure 19b), Gong's group was able to estimate the size of a (swollen) necked zone around crack tips in double-network gels (*42*). The estimate of the thickness of the damage zone, about 220 μm, is in good agreement with predictions from models described in a next section (several hundred micrometers). They also found that there is a proportionality relationship between the thickness of the necked zone and the fracture energy.

Figure 19: Visualization of the necked zone by optical microscopy (a) and high-low image (b)

2.2.3   Structure-properties relationship

2.2.3.1 Level of pre-stretching and dilution of the first network

In 2016, Gong's group investigated model DN gels with various swelling ratio (pre-stretching and dilution). They showed that all normalized stress-deformation ratio curves collapse on the same curve. Meaning, the strain hardening and necking occur at the same

normalized deformation (*43*). They found that the yield point of DN gels is determined by the finite extensibility of the first network chains and the yield stress (in the stretching direction) is determined by the areal density of the first network. The effect of the second network on the yield point is negligible.

Similar results were obtained for multiple network elastomers. During his PhD in our group, Pierre Millereau decoupled the level of pre-stretching of the first network from its dilution (*40*). He highlighted that the number of polymerization was not essential. The level of pre-stretching is the determinant parameter. Figure 20 represents stress strain curves of multiple network with different level of pre-stretching of the first network (*41*).
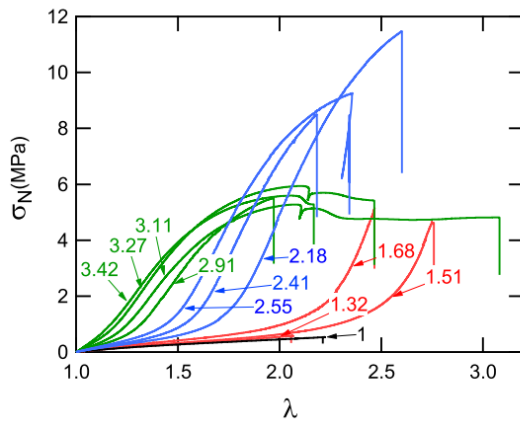

Figure 20: Stress-strain curves of uniaxial extension of different multiple network made of polyethyl acrylate, λ_0 value of is written by each curve The color corresponds to the number of polymerization steps: black, one; red, two; blue, three; and green, four.
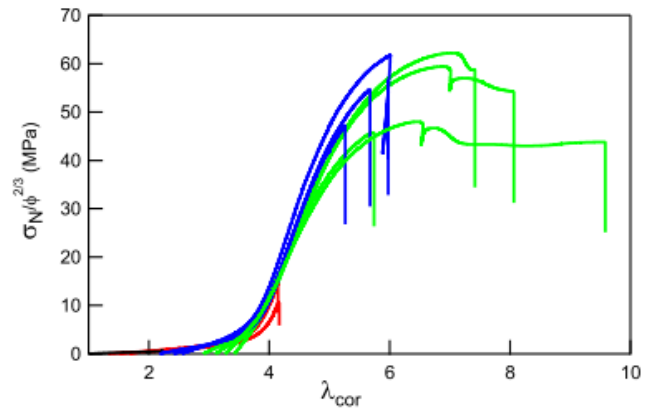
Figure 21: Master curve of nominal stress renormalized by $\phi^{2/3}$ as a function of λ_{cor} for different multiple network made of polyethyl acrylate. The color corresponds to the number of polymerization steps: black, one; red, two; blue, three; and green, four.

He classified multiple network elastomers behaviors in uniaxial extension as a function of their level of pre-stretching (*40*):

- Type 1: Low λ_0 gave a brittle fracture at relatively low strain
- Type 2: $1.5 < \lambda_0 < 2$ a hardening phenomenon was observed in large strain leading to a much higher stress at break
- Type 3: $2 < \lambda_0 < 3$ the hardening phenomenon was followed by a softening phenomenon
- Type 4: $\lambda_0 > 3$ the material displayed a yield stress with necking appearing macroscopically.

He also showed that the Young's modulus of the material increased with an increase of the degree of pre-stretching of the first network, λ_0, (non-linear increase of E with λ_0).

During his work, P. Millereau also proved that the strain hardening was governed by the first network and that the dilution of the polymer by a solvent does not affect this phenomenon. The more pre-stretched the first network, the earlier it reaches its maximum elongation and thus strain hardens.

By taking into account the dilution of the volume density of strands of the first network (by a factor $\phi_{SN}^{2/3}$) and the pre-stretching of the first network ($\lambda_{cor} = \lambda \lambda_0$), P. Millereau proved that all curves fall on a master curve, as shown in Figure 21.

From his work, a new picture arose: multiple network elastomers can be seen as molecular composites. In fact, multiple networks are composed of a stiff and continuous internal phase that is synthesized first and a second phase that acts as a highly extensible but incompressible matrix (*41*). Therefore, multiple networks appear as good models for filled elastomers. From now on, the first network will be referred to as the filler network and the second, third and fourth will be referred to as matrix networks.

In conclusion, the filler network properties are essential for the multiple network properties. In fact, the initial modulus is controlled by both networks but as the material is stretched the stress is carried increasingly by the minority network (*2*). Furthermore, the elongation where hardening appears is mainly or even exclusively controlled by the first network.

2.2.3.2 The matrix

By adding solvent, P. Millereau compared multiple networks with the same level of pre-stretching of the filler network but different quantities of matrix network (*40*). He proved that the amount of second network plays a crucial role, and lack of the matrix network leads to the early failure of the sample.

The filler network and the matrix network are not fully decoupled. Indeed, intermolecular chain transfer reactions are likely to occur during the second and third polymerization, as represented in Figure 22 (*44*). These transfer reactions effectively loosely connect the networks with each other. Connections affect the stress transfer between the networks (*34*).
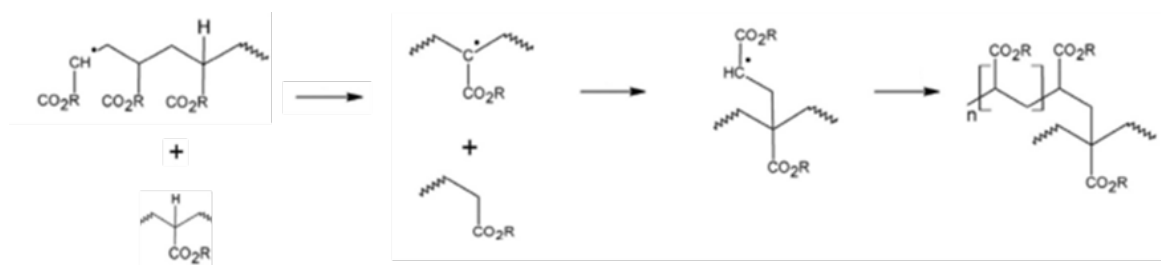
Figure 22: Intermolecular transfer reaction in the radical polymerization

By using a methacrylate monomer instead of an acrylate, P. Millereau replaced the labile H in the alpha position of the acrylate function by a methyl function. By removing this specific H, the transfer reactions between filler and matrix networks are suppressed. From the differences in mechanical properties, he concluded that the transfer reactions may play an important role to transfer the stress from highly stretched network to the other less stretched one. This result was confirmed using mechano-chemistry by an other PhD student of our group, Yinjun Chen (details in a following section).

2.2.4 Models of damage and crack propagation in multiple networks

2.2.4.1 Damage in uniaxial extension

A first phenomenological model on damage in double network hydrogels was developed by X. Wang and W. Hong (*45*). They introduced two variables to take into account the gradual damage in DN hydrogels. The first variable is related to the fraction of the intact polymer chains in the first network (and decreases with the fracture of the 1st network) and the second is related to the stretching limit of the damaged phase (and results from the pullout of the second network). The model describes well the Mullins' effect and the necking phenomenon (presented in Section 2.2.2).

Several models were then developed on multiple network elastomers. A constitutive model describing the multiple network elastomers was developed by McMeeking and co-workers (*46*). In their model, the first network is subject to limits on their chain extensibility and thus experience stiffening. The strain in the first network is used to determine when it breaks. A damage parameter is introduced describing the fraction of chains of the first network that have failed. Their model captures the damage-induced softening and the Mullins' effect.

Very recently, S. Lavoie and co-workers developed a continuum model for progressive damage in multiple network elastomers (*47*). They consider the pre-stretching of the first network and its effect on subsequent deformation. Following P. Millereau work, the multiple network is modeled as a molecular composite: the filler network is modeled as a polydisperse network of breakable polymer chains with non-linear chain elasticity and the matrix networks are modeled using the generalized neo-Hookean model. This model fits well uniaxial extension and cycling loading results obtained by P. Millereau.

In 2018, Vernerey *et al.* proposed a model of fracture of multiple network elastomer based on statistical damage mechanics (*48*). Their approach connects molecular structure (chain length, density etc.) to damage at the macroscopic scale. They start from a Gaussian chain distribution $\phi(r)$.

1. At low strain, the deformation applied macroscopically to the network stretches the Gaussian chain distribution without affecting its overall area.
2. At higher level of deformation, chain rupture tends to decrease the number of chains with a large end-to-end distance, as represented in Figure 23.

They consider a simple chain failure criterion at a critical length. From polymer chain mechanics, they defined two values: a probability, $P(r)$, of failure of a chain (that experiences an end-to-end distance r) and a 'global damage measure', D.
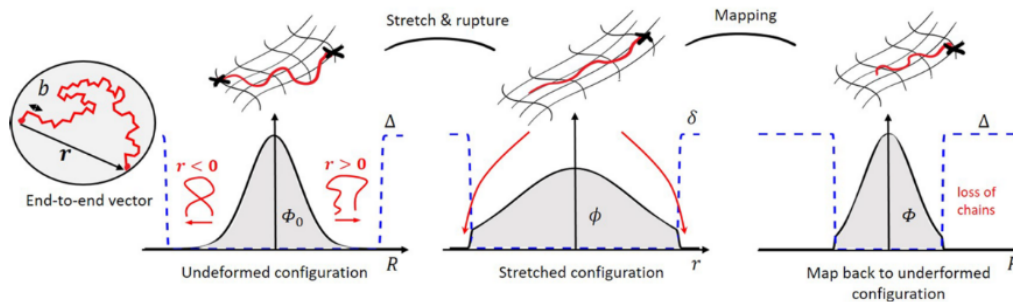

Figure 23: Illustration of the evolution of chain distribution with elongation

They fitted the results obtained by E. Ducrot for multiple network elastomers (*34*). Figure 24 corresponds to the modeling of a triple network elastomer. Figure 24a shows the good matching of the stress-strain curve between experimental data (circles) and their modeling (blue curve). Figure 24b is the modeling of the stress-strain curve experienced by the 1st network in blue, the second network in black and the third network in green. Figure 24c represents the evolution of the chain distribution at different level of

macroscopic elongation for each network. Figure 24c is the modeling of damage (%) vs. elongation for each network. From their modeling, they predict that the first network bares the load and is damaged while the second or third networks are loaded and damaged in a very limited way.
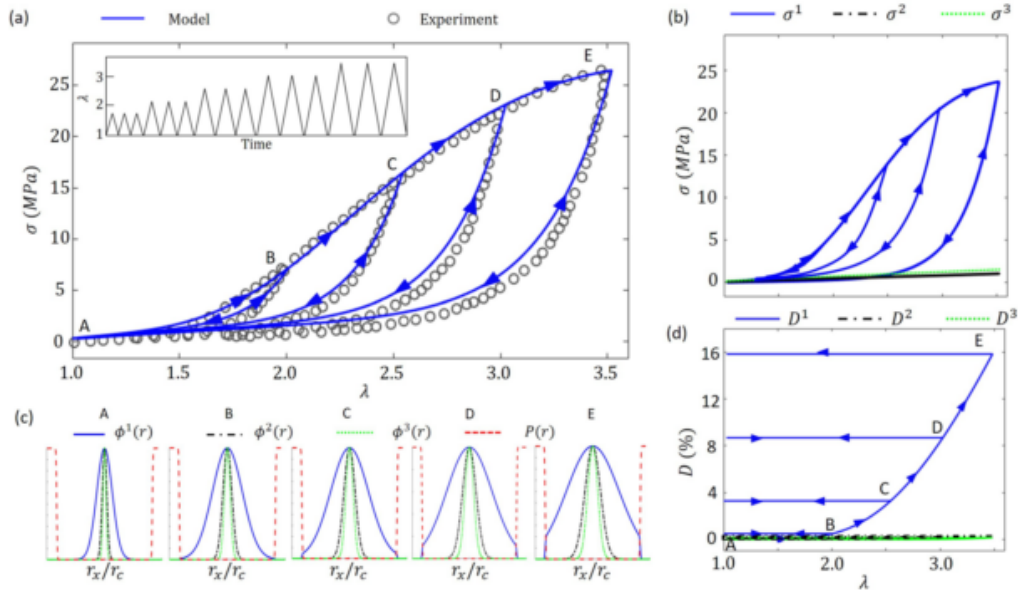

Figure 24 : Matching between Vernerey's model and Ducrot's experimental measurement on the strain stress curve of TN(a). Modeling of the stress-deformation relationship of each individual network (b). Snapshots of the evolution of distribution of ϕ(r) during loading (c). Modeling of damage- deformation relationship of each network (d).

This model has an interesting point of view: it presents a statistical approach to describe the damage based on internal molecular structure. However, this model can be improved as it uses fitting parameters. Moreover, the history of the sample is not taken into account, rendering this model unsuitable for fitting and explaining fatigue experiment.

Y. Higuchi and coworkers studied the damage during uniaxial extension of DN gels using a coarse-grained molecular dynamics simulation (*49*). They investigated the effects of the network ratio, chain length, and first and second network structures on the mechanical properties. Their simulation is in good qualitative agreement with experiments. From the modeling they found that:

- better mechanical properties are achieved with a low concentration of the highly cross-linked first network diluted in a loosely cross-linked second network (with a long chain length between cross linking).
- The Young's modulus is determined by the stretched first network.

They proposed a fracture process at the molecular level. Snapshots of modeling of the DN gel fracture process in given in Figure 25:

- At low strains, the first network (in blue) is stretched and bonds are broken
- Then, interconnection between first and second network (yellow) enhances further bond breaking in the first network while preventing the breakage of the gel.
- Finally, the bond breaking in the first network stops and only the bond breaking in the second network occurs
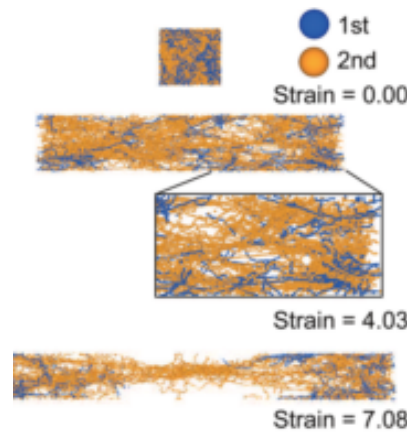

Figure 25: Modeling of the fracture process of DN gel (20% 1st network, 80% 2nd network)

2.2.4.2 Theories on fracture

2.2.4.2.1 Finite element

In 2015, X. Zhao and co-workers proposed a finite element model based on the experimental data that accounts for the synergistic contribution of the intrinsic fracture energies Γ_0 and dissipative fracture toughness Γ_D (represented in Figure 14) (*50*). In order to calculate Γ_0, they considered a triangle cohesive-zone model governed by the maximum nominal stress (the measured failure stress of the material under pure-shear tension) and maximum nominal separation (calculated based on the experimentally measured Γ_0). Γ_D was modeled by the Mullins' effect. This model illustrates well the enhancement of fracture toughness by incorporation of stiff sacrificial bonds in long stretchy polymer network.

In 2007, two mechanical models explaining DN hydrogel reinforcement were proposed by Brown (*51*) and Tanaka (*52*). Both models assumed the formation of a damaged zone in front of the crack tip. At a critical yield stress, chains of the first network break. The energy is dissipated to form the damage zone and the fracture of the damage zone is then controlled by the strain energy stored in that zone (*2*). The difference between models comes from the estimation of the energy needed to propagate the crack in the damaged network (*53*). Both models are presented below.

2.2.4.2.2 Brown's model

Brown's model is based on the Lake-Thomas concepts of energy dissipation by the failure of a polymer strands crossing the crack plane. The particular double network microstructure causes a large enhancement of the number of strands that have to be broken. The assumptions of his model are:

- At a stress σ_a, chains of the first network progressively break and create a damaged zone (with a lower modulus E_2) at the crack tip
- σ_a is directly proportional to the toughness of the first network alone (lower yield stress for more cross-linked first network)

He proposed a two-step crack propagation process:

1. First, the failure occurs in the highly cross-linked and pre-stretched first network. The second network bridges multiple micro-cracks created within the first network. The overall DN gel does not break but a damaged zone is created around the crack tip. This damage zone has a much reduced elastic modulus dominated by the cross-link density of the second network. A micro-crack can be seen, schematically, as represented in Figure 26 where *a* is the length of the crack, Δb the size of the crack held by the second network and σ the external stress applied.

2. Then, the crack propagates in the second network, as represented in Figure 27. The material is composed of an undamaged zone, modulus E_1, mainly controlled by the first network and a damaged zone where the first network is partially broken, modulus E_2. The region around the crack is supposed to be a strip of

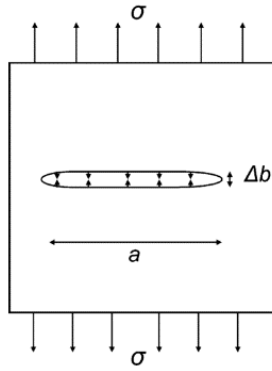material where the first network has broken up by the formation of numerous cracks.

Figure 26: Schematic representation of a crack in the first network, in Brown's model
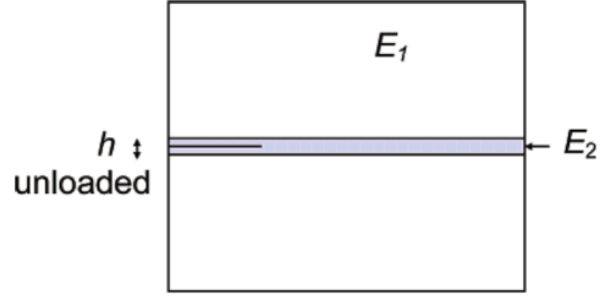
Figure 27: Schematic representation of the damaged zone around the crack, in Brown's model

From these assumptions, Brown extracted a prediction of the global toughness of the DN gels, given by Eq 30..

$$\Gamma_{\text{global}} = \frac{4\ \Gamma_1\ \Gamma_2}{(\lambda_m - 1)E_2\ \Delta b} \qquad\qquad \text{Eq 30.}$$

Where Γ_1 and Γ_2 are the fracture energies of each network taken individually, and λ_m is the maximal macroscopic elongation of the second network and Δb is the crack opening (represented in Figure 26). The results obtained using this model are consistent with experimental data. Compared to just the second network, the energy dissipated in the formation of the damaged zone is found to increase the toughness by a factor of about 40 times.

2.2.4.2.3 Tanaka's model

At approximately the same time as Brown, Tanaka proposed a local damage model for DN gels (*52*). His phenomenological model considers that the DN gel locally yields to become a softer material. The necking is supposed to be triggered by the first network fragmentation inside the second network, which holds the sample together. His model rests on different assumptions listed below and illustrated in Figure 28.

- The yielding occurs around the crack tip at a critical condition characterized by a threshold stress. This threshold value corresponds to the critical tensile stress, σc, where gels undergo macroscopic necking in uniaxial extension.

- There is a sharp boundary between the damaged and the undamaged zone. The size of the damage zone can be characterized by only one spatial scale h, represented in Figure 28.

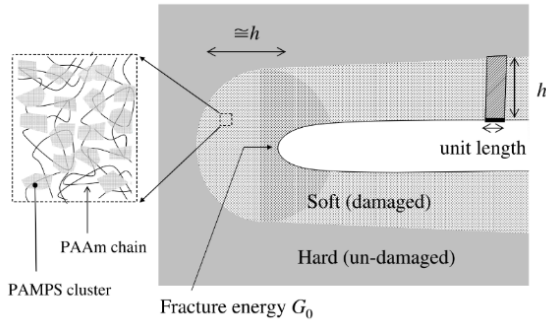- The damage zone behaves as a very soft and purely elastic material with intrinsic fracture energy Γ_0

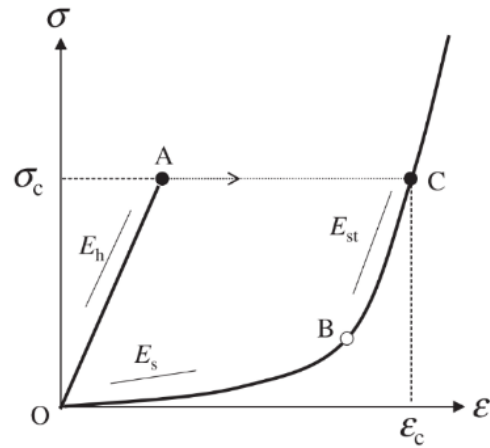*Figure 28: Schematic representation of the structure of crack, in Tanaka's model*

Figure 29: Assumed stress-strain curve for undamaged and damaged zones, in Tanaka's model

The sample's mechanical properties can be described by the stress strain curve given in Figure 29. The first loading of the sample (OAC curve), creates a soft zone when reaching the critical stress σc (point A). The material is then damaged and becomes softer (OBC curve). The large amount of energy dissipated by the yielding (the area defined by OACB) increases the effective fracture energy Γ_{global} by an enhancement factor, defined in Eq 31.

$$\frac{\Gamma_{global}}{\Gamma_0} \sim \frac{E_{st}}{\sigma_c} \varepsilon_c$$

Eq 31.

Where E_{st} is the stiffened modulus and ε_c the strain at the softening point.

The characteristic length of the damage zone can be defined as:

$$h = \frac{\Gamma_0}{U(\sigma_c)}$$

Eq 32.

where Γ_0 is the fracture energy of the damage zone, $U(\sigma_c)$ is the elastic energy density (in J.m^{-3}) for the uniform stretching with critical stress σ_c, a reasonable choice for $U(\sigma_c)$ is given in Eq 33.

$$U(\sigma_c) = \frac{\sigma_c{}^2}{E_{st}}$$

Eq 33.

By combining Eq 31.,Eq 32.and Eq 33., the effective fracture energy is given by Eq 34.

$$\Gamma_{\text{global}} = \Gamma_0 + \sigma_c \varepsilon_c h$$

Eq 34.

This equation is also in good agreement with the values obtained for DN gels when taking the fracture energy of a single loosely crosslinked network as an approximation of Γ_0.

Brown's and Tanaka's models are regarded as the most promising ones even if they are quite simplified. Yet the models are not able to explain or predict the onset of crack propagation quantitatively. Better molecular models need to be developed. Molecular information, and more precisely bond scission detection, is necessary to that purpose. Next section is dedicated to mechanochemistry: a smart strategy to visualize molecular information.

3   Using mechano-chemistry to visualize bond scission

3.1   Principle

As presented earlier (Section 1.4), stretching a polymer chain can lower the activation energy of a chemical reaction, Figure 9. The reaction can be a homolytic scission of a carbon-carbon bond but can also be a cycloreversion, a ring opening reaction or various other types of reaction. The term mechano-chemistry was suggested to qualify all the reactions accelerated by mechanical force (*13*). Mechanophore is the name given to mechanically active molecules or functional groups. Instead of being destructive, these reactions can be useful, for material reinforcement for example (*54*).

Chemical reactions lead to property changes. Some of them are visible like changes in spectral properties: color or fluorescence. Mechano-chemistry is particularly interesting when the consequences of the chemical reaction are easily detectable. Mechanophores are already broadly used in molecular biology as probe, such as DNA probes (*55*). In mechanics, they can be powerful tools to detect stress, strain or bond scission.

3.2   An overview

Recently, successes in the mechano-chemistry field exploded. This trend is visible in Figure 30 where the number of publications dealing with mechano-chemistry is plotted through years.

Many new mechanophores have been designed and screened. They can be incorporated in polymer chains and their mechano-reactivity is investigated by ultrasound sonication of dilute polymer solutions (*56*). Some reactions lead to polymer chain scission (like homolytic cleavage or cycloreversion) while some others do not (like ring opening reaction).

Different interesting reviews summarized the recent boom in the field of polymer mechano-chemistry (*57-59*). It is not the objective of this section, and only a selection of examples is presented below. They are sorted by the associated optical detection: mechano-chromism, mechano-chemiluminescence and mechano-fluorescence. Actually,

mechano-chemiluminescence and mechano-fluorescence are included in mechano-luminescence. In both case, a photon is emitted. The difference is the origin of this photon emission. Chemi-luminescent molecules reach excited states through chemical reaction, while fluorescent molecules reach excited states through light absorption.
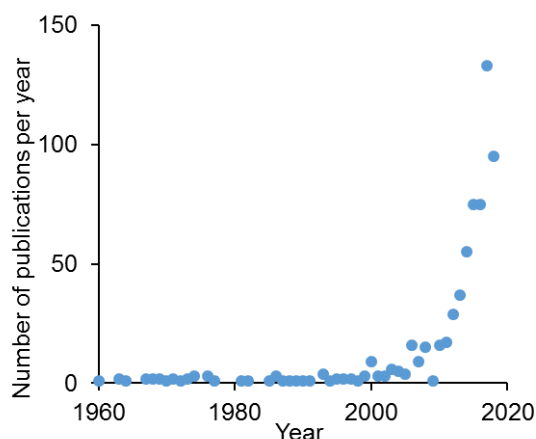

Figure 30: Evolution of the number of publication related to mechano-chemistry over years (generated by PubMed)

3.2.1 Mechanochromism

Mechanochromism refers to the change in absorption triggered by mechanical force. Color changes are directly observed and can be quantified by investigating changes in the absorption spectrum.

Spiropyran (SP) is a popular and well-characterized mechanophore (*60*). Either tensile stretching or irradiation with UV light triggers a reversible 6π electrocycling ring opening of the colorless non-fluorescent spiropyran to a fluorescent red merocyanine, as represented in Figure 31. Hence, this mechanophore experiences both a mechanochromism and mechanofluorochromism. In 2009, J. S. Moore's group created mechanoresponsive polymeric materials by directly linking spiropyran into polymer chains of bulk polymers or by using mechanophores as cross-links (*61*).

Craig's group demonstrated by single molecular force spectroscopy on chain carrying multiple SP groups that the spiropyran was activated when only 240 pN were applied (*62*).

A second color change during material unloading was observed (*63, 64*). The reason is attributed to the different isomers of merocyanine that lead to slight changes in color between the loaded and the unloaded state. This mechanophore was used to map stress in the loading and unloading stage in multiple network elastomers (*65*).

A major specificity of this mechanophore is the reversibility of the conversion. Merocyanine turns back to its spiropyran form after approximately six hours of exposure to fluorescent light (*61*) or forty minutes exposure to ambient light (*66*).

Mechano-chromism leading to chain scission also exists. Among others, three mechanophores: the diarylbibenzofuranone (DABBF), the tetraarylsuccinonitrile (TASN) and the diarylbenzothiophenonyl (DABBT) composed the 'rainbow mechanochromism' developed by K. Ishizuki *et al.* (*67*). They are represented in Figure 32. Homolytic bond scission lead to activation of the primary colors.
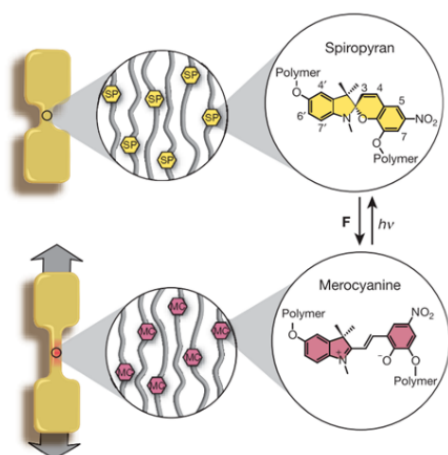

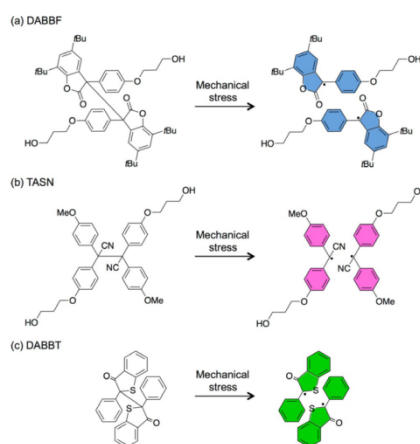*Figure 31: Schematic representation of stress-conversion of spiropyran to coloured merocyanine*

Figure 32: Chemical structure of a) DABBF, b)TASN and c) DABBT before and after applying mechanical stress

3.2.2 Mechanochemiluminescence

Mechano-chemiluminescence refers to generation, facilitated by mechanical force, of a chemiluminescent molecule. These molecules emit photons without the need for additional excitation sources. As mechano-chemiluminophores undergo one reaction before they are consumed, mechanoluminescence gives time resolved and dynamic information. Failure of a material at a molecular scale can be directly read out as a

transient and intense light signal. Mechano-chemiluminescent molecules enable scientists to monitor real time and dynamic information.

Currently, bis(adamantyl) 1,2-dioxetane is the only auto-luminescent system known (*68*). Kopecky and Mumford first synthesized and isolated it in 1969 (*69*). The dioxetane bond is included in a four-membered ring and decomposes into two carbonyl (ketones) moieties, one of which is in a singlet electronically excited state (20 ns of scission). A blue light (420 nm) is emitted while relaxation from the excited moiety to ground state. The molecule and the chemiluminescent reaction associated are represented in Figure 33. Light emission while sonicating solutions of linear polymers or straining of polymer networks containing dioxetane cross-linkers gave evidence of bond scissions (*70*).
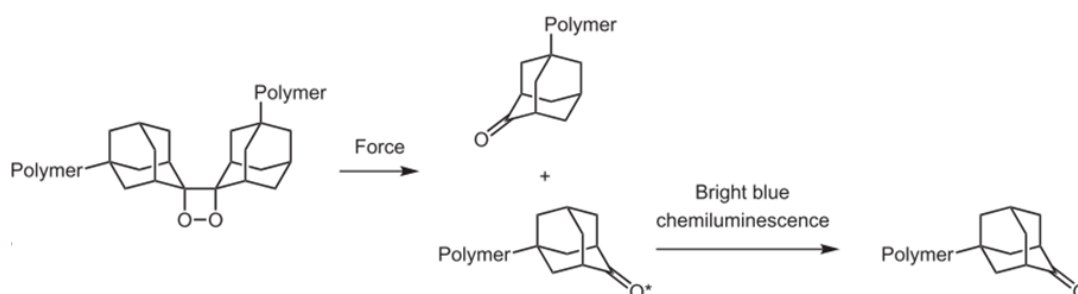

Figure 33: Schematic representation of the mechanically induced decomposition of a polymeric bis(adamantyl) dioxetane

This 1,2-dioxetane is already broadly used to detect bond scission for its many benefits (*70*). Its incorporation does not influence significantly the macroscopic mechanical properties of the polymeric materials. Bis(adamantyl)1,2-dioxetane shows high stability under ambient conditions compared to other dioxetanes.

In particular, R. P. Sijbesma's group showed an important interest in this mechanoluminescent molecule which they introduced in multiple polymer materials. In 2012, they enhanced light emission and tuned wavelength by adding energy acceptors, such as 9,10-diphenylanthracene (DPA). The singlet excited state adamantones transfers energy to the fluorescent acceptor. In 2013, in our group, sacrificial bond breakage in multiple network elastomers was directly demonstrated by incorporating 1,2-dioxetane crosslinkers (*34*) (more details in section 3.4.2). In 2014, dioxetane was incorporated in thermoplastic elastomers containing soft segments and various hard segments in order to interpret chain slippage (*71*). In 2016, dioxetane was also used to highlight and better understand the contribution of bond scission in irreversible stress-softening

phenomenon, known as Mullins' effect, in silica-filled poly(dimethylsiloxane) (PDMS) (*72*). The incorporation of dioxetane in multiple network elastomers was also useful to investigate necking phenomenon (more details in Section 3.4.2) (*41*).

3.3   Mechanofluorescence

Mechano-fluorochromism refers to the change in fluorescence triggered by mechanical force. In the case of fluorescence activation, a fluorescent molecule, called a fluorophore, is generated upon mechanical stimulation.

A change in emission (fluorescence activation or alteration) is usually more sensitive than a change in absorption. For this reason, mechano-fluorescence attracted the interest of several research groups.

First, fluorescence mechanism and photobleaching will be presented, then an overview of mechano-fluorochromes will be given.

3.3.1   Fluorescence

A typical Jablonski diagram to depict fluorescence is represented Figure 34 (*73*).

1. A fluorophore is initially at the singlet ground electronic state S_0.
2. It can reach an excited state by absorbing light (singlet state S_n). The light absorption is a fast process (10^{-15} s). At each electronic energy levels (S_0, S_1, S_2 etc.), the fluorophore can exist at different vibrational energy levels (denoted 0, 1, 2 on the diagram).
3. Usually, the molecule relaxes rapidly (10^{-12} s or less) to the lowest vibrational level S_1. This process is called internal conversion.
4. Then, the fluorophore emits a photon of lower energy when relaxing to the ground state (S_0) by radiative transition.

The quantum yield (ϕ) is defined by the ratio of the number of photons emitted to the number of photons absorbed. It gives an evaluation of the efficiency of photon emission (*74*).
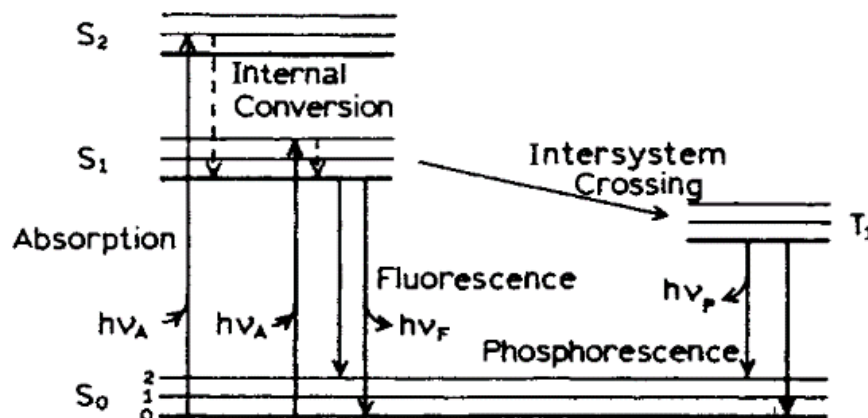

Figure 34: One form of Jablonski diagram

Molecules in the S_1 state can also undergo a spin conversion to the first triplet state T_1. This process, called Intersystem Crossing, is irreversible (transition from T_1 to S_1 is forbidden). Relaxation from T_1 to S_0 corresponds to phosphorescence. Once back to S_0, the fluorophore keeps its ability to fluoresce by absorbing a new photon.

Molecules in excited triplet states are very reactive and may undergo irreversible chemical reactions. For example, they can react with the molecular oxygen in its triplet ground state ($^3O_2$) dissolved in the media (*75*). More generally, all photochemical modifications of fluorophores will result in irreversible loss of its ability to fluoresce. This fading of fluorophore emission during observation is called photobleaching. The sensitivity to photobleaching depends on the molecule. Photostability can be evaluated by the photobleaching quantum efficiency. This value is defined as the ratio between the number of molecules that have been bleached and the total number of photons absorbed during the exposure time. Decreasing the excitation time or lowering the excitation intensity help reducing photobleaching.

Once the fluorochrome is generated and as long as it is not photobleached, it can emit photon after photon absorption. The information can be qualified as 'post-mortem' as opposed to the dynamic information obtained from mechano-chemiluminescence.

The fluorescence is a sensitive measurement. It can fade, but can also be shifted, as it is environment sensitive. For example, a polar solvent can lead to red shift of the emission band (*76*).

3.3.2 Mechanofluorochrome

Spiropyran is not fluorescent while merocyanine is. However, the low fluorescence quantum yield of $\phi < 0.02$ does not render this mechanophore ideal for fluorescence observations.

Anthracene is frequently used as a fluorescent probe in biology. Anthracene dimers are not fluorescent as the π-system is not conjugated anymore. C. Chung's group developed a fluorescent crack sensor based on dimeric anthracene containing polymers, as presented in Figure 35 (*77*). Crack propagation in the material generates the fluorescent anthracene moieties by mechano-chemical cycloreversion of the cyclooctane dimer structure.
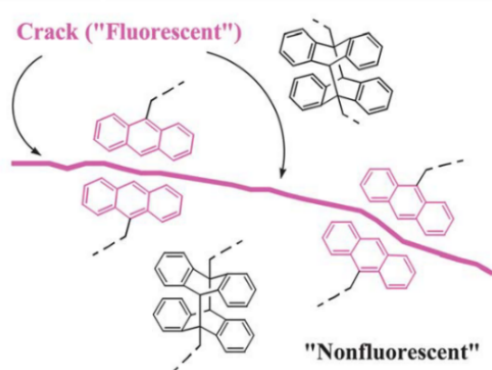

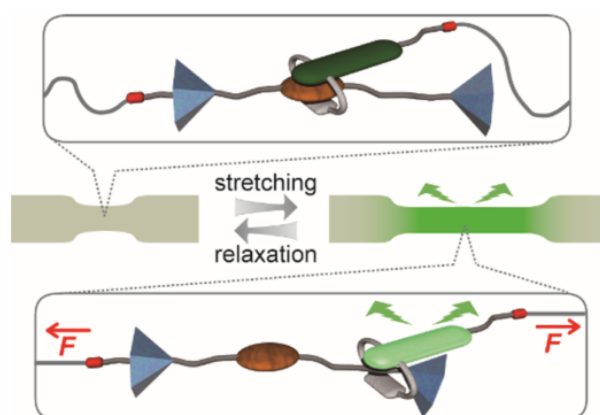*Figure 35: Scematic representation of cycloreversion of anthracene dimers upon crack propagation*

Figure 36: Schematic representation of the fluorescence turn-on while the quencher (in brown) is separated from the fluorochrom(in green)

Fluorescence can also be activated or deactivated by energy transfer between a pair of fluorescent chromophores, a donor and an acceptor called Förster resonance energy transfer (*78*). The distance between the fluorescent molecules or a complex deformation is reported by the fluorescence switching. The energy transfer can also occur between a fluorochrome and a quencher. Y. Sagara *et al.* developed a fluorescent force transducer, represented in Figure 36 (*79*). A fluorophore-carrying macrocycle is combined with a

dumbbell-shape molecule containing a quencher. When they are nearby the fluorescence is quenched. By applying a force, the deformation of the polymer spatially separate the fluorophore from the quencher and the fluorescence is activated. The process is reversible.

3.3.3 Anthracene-maleimide retro Diels-Alder

Anthracene-maleimide Diels-Alder adducts are another class of mechano-fluorochromes reporting for bond scission. Chain breakage is expected through a mechanically facilitated cycloreversion, called a retro Diels-Alder reaction. Fluorescent anthracene is released on one part and maleimide on the other part. A. Boydston's group reported on chain scission rates in linear and three-arm star polymers by incorporating an anthracene-maleimide Diels-Alder adduct mechanophore, as shown in Figure 37 (*80*).
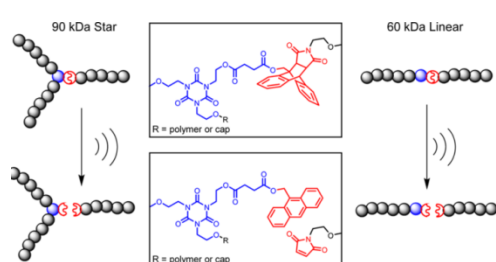

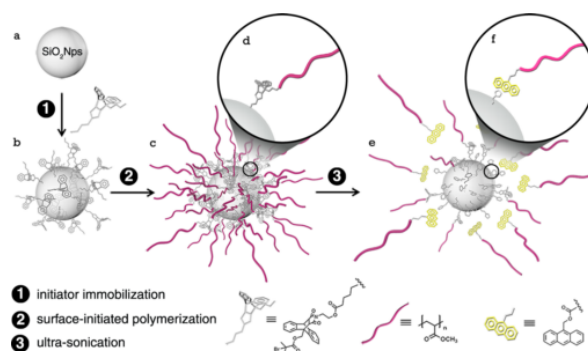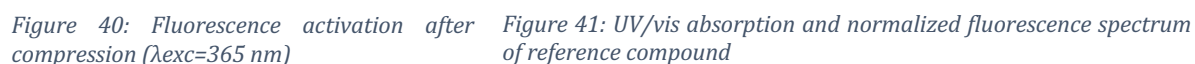*Figure 37: Anthracene-maleimide mechanophore in linear and three-arm polymer*

Figure 38: Anthracene-maleimide mechanophore at the interphase between nanoparticle and polymer

J. Moore group synthesized anthracene-maleimide mechanophore-anchored poly(methyl acrylate) (PMA) grafted silica nanoparticles (*81*). PMA cleavage from the surface releases an anthracene-end-capped PMA that can be detected at 254 nm, as represented Figure 38. The anthracene-maleimide mechanophore was also tested in non-covalent micellar aggregation (*82*).

R. Göstl and R. P. Sijbesma improved the anthracene-maleimide mechanophore system by designing a π-extended anthracene mechanophore (*83*). The mechanically induced retro Diels-Alder reaction, shown in Figure 39, releases a 9π-extended anthracene as fluorophore (instead of bare anthracene). This mechanophore was incorporated in the center of a linear poly(methyl acrylate) and in a crosslinked poly(hexyl methacrylate).

Fluorescence was activated either by sonication or by compression on the acrylate network, as shown in Figure 40.

Figure 39: Retro Diels-Alder reaction on π-extended anthracene mechanophore

Figure 40: Fluorescence activation after compression (λexc=365 nm)

Figure 41: UV/vis absorption and normalized fluorescence spectrum of reference compound

The spectral characteristics of the π-extended anthracenes were investigated by analyzing a reference molecule with the same spectral properties, the 9-((4-anisyl)ethynyl)anthracene. The reference molecule and the UV/vis absorption and fluorescence spectrum are given in Figure 41.

The π-extended anthracenes presents numerous advantages:

- A good sensitivity is obtained by a high quantum yield: $\phi = 0.72$ while only $\phi = 0.27$ for bare anthracene or $\phi < 0.02$ for spiropyran.

- A bathochromic shift in absorption and emission spectra are observed. Excitation of the fluorochrome can be close to visible as the π-extended anthracene absorbs in the visible region of the spectrum. This avoids the generally unwanted irradiation of the material with destructive UV light (~ 200 nm).

- The system activation is irreversible at ambient conditions. The fluorescent signal intensity remains independent of time.

- The π-extended anthracene has a low oxygen sensitivity. $\phi = 0.62$ in air saturated solution. Fluorescence is only mildly susceptible to $^3O_2$ quenching, meaning the fluorochrome has a low sensitivity to photobleaching. This high photostability was already reported for ethynylated anthracenes. For example,

9,10-bis(phenylethynyl) anthracene can emit more than 10^7 photons before photobleaching and possesses a low photobleaching yield of $10^{-9} - 10^{-8}$ (*84*). In fact, the intersystem crossing rate to the triplet state is very low thanks to the large gap between triplet and singlet states.

It is desirable for a fluorescent sensor to emit fluorescence at a long wavelength to enable naked-eye observation. A good bond scission sensor should also have a high quantum yield (*77*) that is verified by the π-extended anthracene Diels-Alder adduct mechanophore. This mechanophore appears as an ideal probe for bond scission.

3.4 Mechanophores already used in multiple networks

3.4.1 Spiropyran

Yinjun Chen, a PhD who graduated from our group, incorporated spiropyran in multiple network elastomers (*65*). Thanks to this mechanophore, he was able to map high stress in multiple network elastomers. The thigh stress was defined by the threshold of spiropyran activation (240 pN), which is lower than the C-C bond (4 nN). He proved that the spiropyran in the filler networks of double network ($\lambda_0 \sim 1.6$), triple network ($\lambda_0 \sim 2.3$), quadruple network ($\lambda_0 > 2.8$) can be activated at the same onset of macroscopic stress (1.5 MPa).

3.4.1.1 Uniaxial extension

Spiropyran was incorporated as a cross-linker in the different networks: either in the first (filler) network, in the second network or in the third network of quadruple networks ($\lambda_0 > 2.8$). Pictures at different levels of elongation during the uniaxial tensile test of these differently labeled quadruple networks are given in Figure 42.

1. When the mechanophore is in the first network, the quadruple network homogenously turns from colorless to blue (homogenous blue visible in Figure 42a). In the necked region, no color change was detectable by naked eyes. Thanks to a color analysis, a slight change was visible from blue to purple in the necked region. This slight secondary color change was attributed to the unloading of a

small fraction of the filler. As the blue color was still visible, the filler was not completely unloaded.

2. He observed a color change in the necked region when the spiropyran was in the second network only (Figure 42b). This color change confirm the stress transmission from first to second network at the necking front.

3. No color change was visible when the spiropyran was in the third network only (Figure 42c).

Based on these different color changes he proposed the following scenario. When a quadruple network is loaded, the stress is initially sustained by the first network. Around the yield point, the filler network starts to fail and the stress is partially transferred from the first network to the second one. At that point, the second network becomes fully stretched and sustains at least an average force per strand of the order of 240 pN. Yet the load supported by the third network is still low (no color) and the broken bits of the filler network are still loaded in the necked area. From his conclusions, it is unlikely that the filler network breaks into separate clusters.
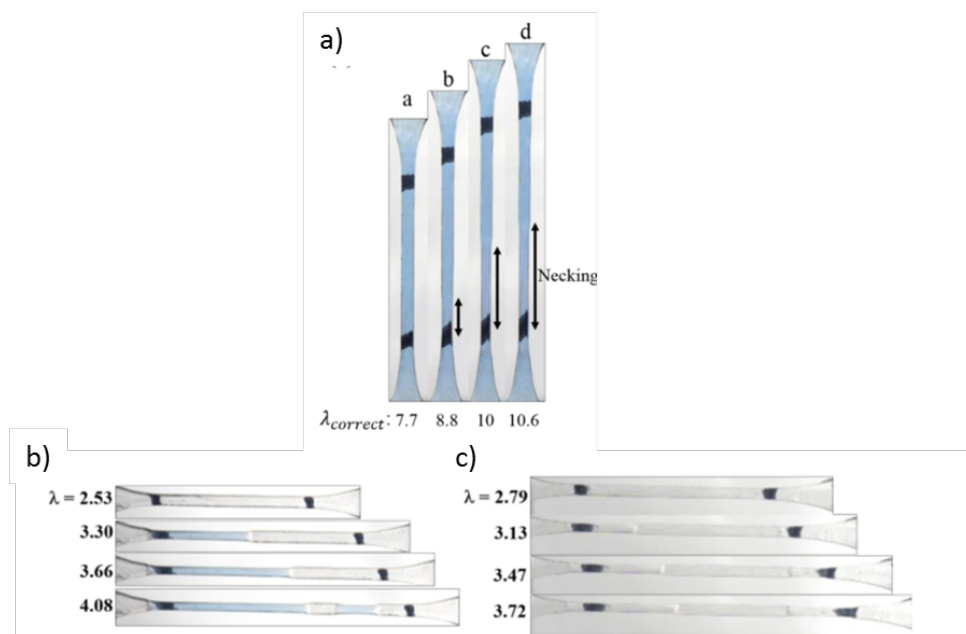
Figure 42: Uniaxial tensile test on quadruple network with the spiropyran incorporated in the first (a), the second (b) and in the third network (c)

He also analyzed the role played by the transfer reactions between the filler and the matrix network in the load transfer. He proved that when the connection between the first and the second network is removed, stress in the first network transfers much less to the

second network and the second network is more extensible. This result confirmed the importance of the limited but existent connection between networks.

3.4.1.2 Crack propagation

After uniaxial extension, Y. Chen performed crack propagation test on mechano-chromic multiple networks. Based on the calibration curve of chromatic change vs. nominal stress, he was able to map the stress around the crack tip during the fracture tests. Figure 43 is an example of the high stress mapping obtained around the crack tip before and during propagation.
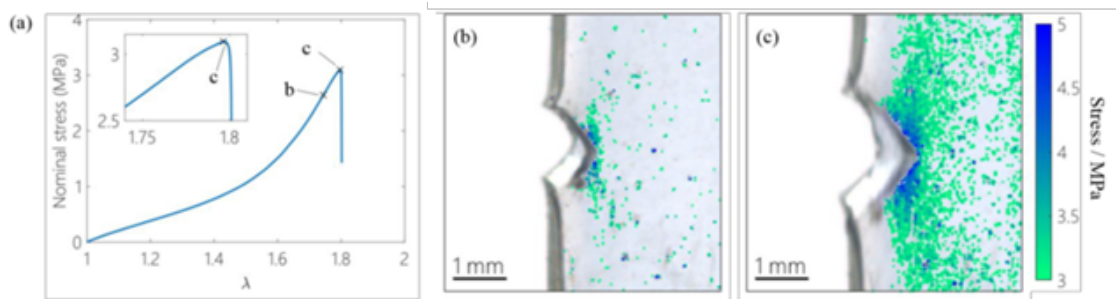
Figure 43: Stress strain curve of a triple network ($\lambda_0 \sim 2.2$). High stress map around the crack tip before b) and during propagation c)

For the first time, he used the second color change of spiropyran, from blue to purple, to map the stress in the unloading process: where the crack propagated and the material was relaxed. The stress distribution was detected by the stress-color map in both loading and un-loading, as shown in Figure 44.
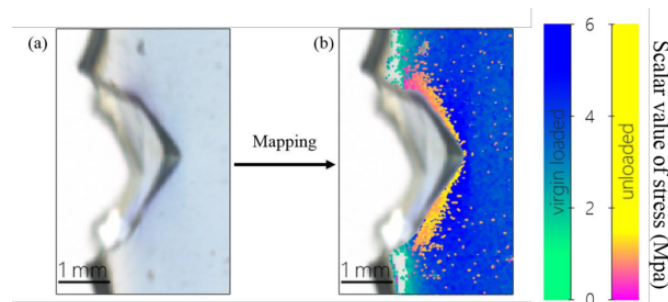
Figure 44: Raw image of a triple network ($\lambda_0 \sim 2.2$) during crack propagation(a) and associated stress-color map of loading (green to blue) and unloading (pink to yellow)

Because of the non-scission nature of spiropyran, it reports for the high stress distribution region but not for the damage zone. In fact, the activation of spiropyran occurred before

the damage of the filler network. Another mechanophore is needed to investigate the damage zone.

3.4.2 Bis-adamantane dioxetane

E. Ducrot was the first one to prepare mechano-chemiluminescent multiple network elastomers (*34, 85*). He incorporated bis-adamantane dioxetane mechanophore as a cross-linker in the filler network of multiple network elastomers. The mechanophore acts as a bond scission probe. Blue light was emitted with bond scission. Incorporation of the mechanophore did not modify the material mechanical properties. He prepared mechano-chemiluminescent multiple networks with different levels of pre-stretching of the filler network (single network SN at $\lambda_0 = 1$; double network DN at $\lambda_0 \sim 1.5$ and triple network TN at $\lambda_0 \sim 2.7$).

3.4.2.1 Uniaxial extension

Stress-strain curves of uniaxial tensile cycles tests of double and triple networks are represented in red in Figure 45, a and b respectively. On the same graphs, the corresponding light emission signal as a function of elongation are indicated in blue. From this experiment, he concluded that irreversible bond breakage only occurs above a certain value of λ, and only for the first cycle. No bond breakages occurred during the subsequent cycles, fully elastic, to the same value of λ.
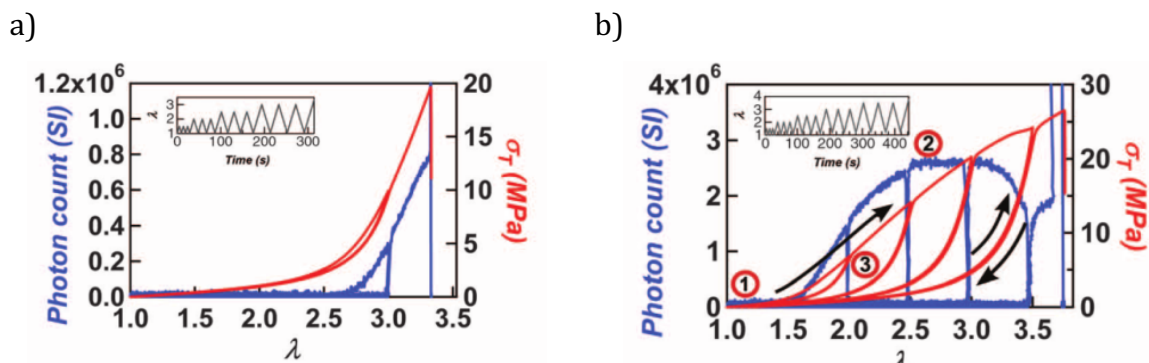
a)   b)

Figure 45: Stress-strain curves of uniaxial tensile cycles test (in red) and corresponding light emission signal (in blue) of DN a) and TN b)

56

P. Millereau used the same strategy and incorporated the same mechanophore in the filler network of a multiple network with a higher level of pre-stretching, $\lambda_0 \sim 3$ (*40, 41*). The mechano-chemiluminescent multiple network was tested in uniaxial extension to investigate the necking phenomenon. The stress-strain curve is represented Figure 46. He recorded images at different levels of stress and strain in order to analyze the luminescent signal.

1. First, at low extension, no mechano-luminescence was detected, meaning no bond scissions were detected (image 1).
2. After the inflexion point, a homogeneous but weak light signal was observed over the entire sample under load (image 2) corresponding to a random scission of highly loaded bonds in the filler network.
3. At the maximum in nominal stress, the signal becomes less intense. A very localized light emission was then detected (image 3) associated to the necking initiation.
4. From that point, two necking fronts moved (images 4 and 5), revealing a more localized failure of bonds (macroscopically and at the molecular level).
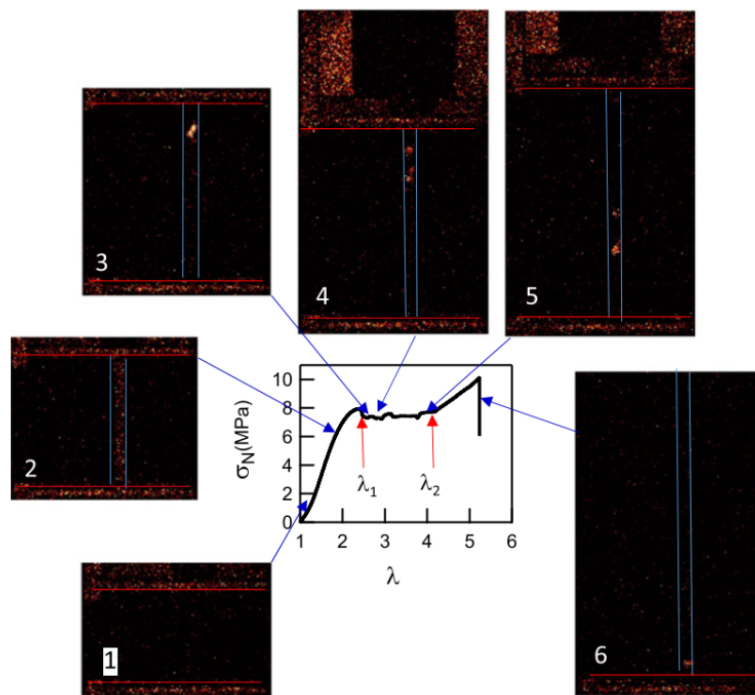

Figure 46: Stress-strain curve of the mechano-chemiluminescent multiple network ($\lambda_0 \sim 3$) and images of luminescent signal emission associated

3.4.2.2 Crack propagation

After uniaxial tensile cyclic tests, E. Ducrot carried out crack propagation tests on the mechano-chemiluminescent materials. The real time observation of the propagation of cracks revealed the presence of a luminescent zone ahead of the crack while it propagated. Figure 47 represents the intensity-colored map obtained. From very small and highly localized in front of the crack tip in a single network, the luminescent zone extended over a large domain when increasing the level of pre-stretching of chains of the filler network (from double to triple networks). An increase in the degree of pre-stretching of the chains of the filler network associated with their decrease in volume fraction led to a much larger dissipative volume ahead of the crack tip and to a tougher material. The stress concentration is reduced at the crack tip and delays the material failure.
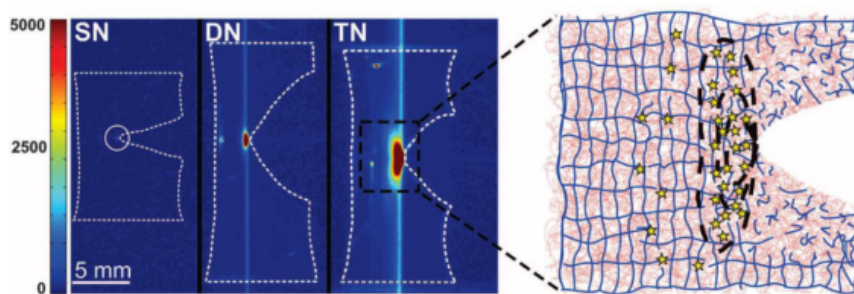
Figure 47: Intensity-colorized images of propagating cracks on notched mechano-chemiluminescent multiple networks (single SN, double DN and triple TN networks)

The combination of multiple network elastomers with mechano-chemistry appears as a promising strategy to investigate fracture mechanics. Indeed, spiropyran and dioxetane have proven their ability to report for stress and for chain scission respectively. Spiropyran does not give information on chain scission but gives a complementary information on stress. As the dioxetane emits light upon breakage, it is a powerful tool for obtaining dynamic information on bond scissions. However, the real time signal is low and not convenient to record. High magnifications cannot be investigated since the location of crack propagation is not predictable. Moreover, signal quantification is difficult because calibration methods are difficult to implement. The quantification of bond breakage using the dioxetane seems limited. Another mechanophore was identified as the most promising bond scission sensor for our purpose: the π-extended anthracene presented in Section 3.3.3.

Conclusions

The linear elastic mechanics of fracture is relatively well understood and modeled. However, when soft and tough materials are under discussion the mechanics becomes more challenging. Indeed, ahead of the crack tip, energy is dissipated in a large volume. Crack initiation and propagation depend on the characteristics of this dissipative zone, and there are still open questions.

In front of the crack tip, in addition to viscoelastic dissipation in the polymer, many non-linear processes occur, such as cavity formation, stringing, chain pull-out and bond scission. This latter point is crucial since bulk strength of the materials is ensured by chemical bonds and bond scission can result in macroscopic fracture. Up to now, there is no molecular model that can predict fracture or crack growth directly from the molecular structure.

Material failure occurs at different length scales: from macroscopic crack propagation, visible to the naked eye, to limited extensibility of polymer strands at the nano-scale, down to bond scission at the angstrom-scale. A multi-scale approach seems necessary to fully interpret fracture.

Therefore, molecular detection of bond scissions appears to be a key parameter to understand failure mechanisms. It is now possible thanks to the recent and fast development of the field of mechano-chemistry. Actually, bond scissions can be detected by incorporating mechanically activable molecules, called mechanophores, into polymer architectures. Mechano-chemistry is fundamentally multiscale: macroscopic stress have consequences at the molecular scale rendering it an ideal tool to investigate fracture at all the characteristic length scales.

Multiple network elastomers are transparent soft and tough molecular composites. They are composed of a rigid filler network diluted in a soft matrix. The toughening mechanism relies on sacrificial bonds. Overloaded bonds of the filler network break and dissipate energy while the matrix prevents the propagation of micro-cracks. The fracture toughness is improved from about 50 J.m^{-2} for a single elastomer to 2000 to 5000 J.m^{-2} for a multiple

network (triple). Focusing on these materials first is a good strategy to investigate bond scissions as their occurrence is enhanced by the toughening mechanism.

Mechano-chemistry has already been used to study bond scissions in multiple network elastomers. A dioxetane mechanophore was introduced in the filler network. As this molecule emits light upon breakage, it is a powerful tool for getting time-resolved information on bond scissions. However, the real time signal remains low and suffers from poor spatial resolution. A precise integration of the luminescence over the whole region is not possible because of the high dynamic range. High magnifications cannot be investigated since the location of the crack propagation is not predictable. Analysis at higher temperature cannot be performed as the bis adamantane dioxetane is activated with temperature. Moreover, signal quantification is difficult because of the difficulty of implementing calibration methods.

Due to these limitations, another mechanophore cross-linker, developed by R. Göstl and R. P. Sijbesma, the π-extended anthracene Diels-Alder adduct, can be incorporated instead. This mechanophore can provide post-mortem bond scission mapping based on stable fluorescence activation induced by bond breakage. By exciting the broken mechanophore at a certain wavelength, it will respond by fluorescent emission. The result will not be dependent on a short time relaxation process. With a quantum yield of 0.72, the fluorescent signal is high and easy to record at high spatial resolution using a fluorescence microscope. The molecule is also stable under UV light and has a low sensitivity to oxygen. Moreover, the fluorescence signal can be calibrated using a calibration molecule having the same fluorescence system. For all these reasons, this mechanophore appears as an ideal candidate for our research.

The comprehensive study we are targeting requires various field of research: from chemistry, to fluorescence and image analysis up to mechanics. Our objective is to map bond scissions using this mechanophore and to get quantitative information during crack initiation and after crack propagation. More precisely our objectives are:

1. Developing and optimizing an investigation tool to examine chains scission at the crack tip.
2. Developing a methodology in order to get robust and quantitative results on chain scission.

3. Improving the comprehensive picture of fracture in multiple network elastomers.

    a. How many sacrificial bonds break in multiple network elastomers?

    b. How does the level of pre-stretching of the filler network influence the molecular damage?

4. Analyzing the coupling between viscoelasticity and molecular damage in single networks

    a. How many bonds break in a single network?

    b. How localized is molecular damage after a crack propagation in a single network?

    c. How does temperature and rate influence the molecular damage in single network?

5. Analyzing the coupling between the matrix viscoelasticity and molecular damage of the filler network of multiple network elastomers.

    a. How does strain rate influence the filler network breakage in multiple network elastomers?

    b. How does temperature influence the filler breakage in multiple network elastomers?

References

1. C. Creton, M. Ciccotti, Fracture and adhesion of soft materials: a review. *Rep Prog Phys* **79**, 046601 (2016).
2. C. Creton, 50th Anniversary Perspective: Networks and Gels: Soft but Dynamic and Tough. *Macromolecules* **50**, 8297-8316 (2017).
3. A. A. Griffith, The Phenomena of Rupture and Flow in Solids. *Philosophical transactions of the royal society a mathematical, physical and engineering sciences* **221**, 163-198 (1921).
4. G. R. Irwin, Analysis of Stresses and Strains near the End of a Crack Traversing a Plate. *Journal of Applied Mechanics* **24**, 351-369 (1957).
5. M. Rubinstein, R. H. Colby, *Polymer Physics*. (2003).
6. L. R. G. Treloar, *The physics of rubber elasticity*. (1975).
7. A. N. Gent, A New constitutive relation for rubber. *Rubber Chemistry and Technology* **69**, 59-61 (1996).
8. J. E. Bemis, B. B. Akhremitchev, G. C. Walker, Single Polymer Chain Elongation by Atomic Force Microscopy. *Langmuir* **15**, 2799-2805 (1999).
9. F. Oesterhelt, M. Rief, H. E. Gaub, Single molecule force spectroscopy by AFM indicates helical structure of poly(ethylene-glycol) in water. *New Journal of Physics* **1**, 6.1-6.11 (1999).

10. M. Grandbois, M. Beyer, M. Rief, H. Clausen-Schaumann, H. E. Gaub, How strong is a covalent bond? *Science* **283**, 1727-1730 (1999).

11. S. Wang, S. Panyukov, M. Rubinstein, S. L. Craig, Quantitative Adjustment to the Molecular Energy Parameter in the Lake–Thomas Theory of Polymer Fracture Energy. *Macromolecules* **52**, 2772-2777 (2019).

12. A. L. Black, J. M. Lenhardt, S. L. Craig, From molecular mechanochemistry to stress-responsive materials. *Journal of Materials Chemistry* **21**, 1655–1663 (2010).

13. T. J. Kucharski, R. Boulatov, The physical chemistry of mechanoresponsive polymers. *Journal of Materials Chemistry* **21**, 8237 (2011).

14. K. R. Evan Evans, Dynamic Strength of Molecular Adhesion Bonds. *Biophysical Journal* **72**, 1541-1555 (1997).

15. M. K. Beyer, The mechanical strength of a covalent bond calculated by density functional theory. *The Journal of Chemical Physics* **112**, 7307-7312 (2000).

16. R. N. Merkel, P.; Leung, A.; Ritchie, K.; Evans, E., Energy landscapes of receptor-ligand bonds explored with dynamic force spectroscopy. *Nature* **397**, 50-53 (1999).

17. J. Sohma, Mechanochemistry of polymers. *Progress in Polymer Science* **14**, 451-596 (1989).

18. G. J. Lake, A. G. Thomas, The Strength of Highly Elastic Materials. *Proceedings of the Royal Society of London. Series A, Mathematical and Physical Sciences* **300**, 108-119 (1967).

19. A. N. Gent, J. Schultz, Effect of Wetting Liquids on the Strength of Adhesion of Viscoelastic Material. *The Journal of Adhesion* **3**, 281-294 (1972).

20. A. N. Gent, Adhesion and Strength of Viscoelastic Solids. Is There a Relationship between Adhesion and Bulk Properties? *Langmuir* **12**, 4492-4496 (1996).

21. A. Ahagon, A. N. Gent, Effect of interfacial bonding on the strength of adhesion. *Journal of Polymer Science - Polymer Physics Edition* **13**, 1285-1300 (1975).

22. A. N. Gent, S.-M. Lai, C. Nah, C. Wang, Viscoelastic effects in cutting and tearing rubber. *Rubber Chemistry and Technology* **67**, 610-618 (1994).

23. B. N. J. Persson, O. Albohr, G. Heinrich, H. Ueba, Crack propagation in rubber-like materials. *Journal of Physics: Condensed Matter* **17**, R1071-R1142 (2005).

24. X. Zhao, Designing toughness and strength for soft materials. *Proc Natl Acad Sci U S A*, (2017).

25. X. Zhao, Multi-scale multi-mechanism design of tough hydrogels: building dissipation into stretchy networks. *Soft Matter* **10**, 672-687 (2014).

26. J. Y. Sun *et al.*, Highly stretchable and tough hydrogels. *Nature* **489**, 133-136 (2012).

27. Y. Okumura, K. Ito, The Polyrotaxane Gel: A Topological Gel by Figure-of-Eight Cross-links. *Advanced Materials* **13**, 485-487 (2001).

28. K. Mayumi, A. Marcellan, G. Ducouret, C. Creton, T. Narita, Stress–Strain Relationship of Highly Stretchable Dual Cross-Link Gels: Separability of Strain and Time Effect. *ACS Macro Letters* **2**, 1065-1068 (2013).

29. N. B. Tito, C. Creton, C. Storm, W. G. Ellenbroek, Harnessing entropy to enhance toughness in reversibly crosslinked polymer networks. *Soft Matter* **15**, 2190-2203 (2019).

30. J. P. Gong, Y. Katsuyama, T. Kurokawa, Y. Osada, Double-network hydrogels with extremely high mechanical strengh. *Advanced Materials* **15**, 1155-1158 (2003).

31. Y. Tanaka *et al.*, Determination of Fracture Energy of High Strength Double Network Hydrogels. *The Journal of Physical Chemistry B* **109**, 11559-11562 (2005).

32.   J. P. Gong, Materials both Tough and Soft. *SCIENCE* **344**, 161-162 (2014).
33.   T. Nakajima *et al.*, True Chemical Structure of Double Network Hydrogels. *Macromolecules* **42**, 2184-2189 (2009).
34.   E. Ducrot, Y. Chen, M. Bulters, R. P. Sijbesma, C. Creton, Toughening Elastomers with Sacrificial Bonds and Watching Them Break. *Science* **344**, 186-189 (2014).
35.   L. Mullins, Softening of rubber by deformation. *Rubber Chemistry and Technology* **42**, 339-362 (1969).
36.   R. E. Webber, C. Creton, Large Strain Hysteresis and Mullins Effect of Tough Double-Network Hydrogels. *Macromolecules* **40**, 2919-2927 (2007).
37.   Y.-H. Na *et al.*, Necking Phenomenon of Double-Network Gels. *Macromolecules* **39**, 4641-4645 (2006).
38.   J. P. Gong, Why are double network hydrogels so tough? *Soft Matter* **6**, 2583 (2010).
39.   T. Nakajima, T. Kurokawa, S. Ahmed, W.-l. Wu, J. P. Gong, Characterization of internal fracture process of double network hydrogels under uniaxial elongation. *Soft Matter* **9**, 1955-1966 (2013).
40.   P. Millereau, Large Strain and Fracture of Multiple Network Elastomers (Doctoral dissertation) UPMC (2017).
41.   P. Millereau *et al.*, Mechanics of elastomeric molecular composites. *Proc Natl Acad Sci U S A*, (2018).
42.   Q. M. Yu, Y. Tanaka, H. Furukawa, T. Kurokawa, J. P. Gong, Direct Observation of Damage Zone around Crack Tips in Double-Network Gels. *Macromolecules* **42**, 3852-3855 (2009).
43.   T. Matsuda *et al.*, Yielding Criteria of Double Network Hydrogels. *Macromolecules* **49**, 1865-1872 (2016).
44.   N. Ballard, J. M. Asua, Radical polymerization of acrylic monomers: An overview. *Progress in Polymer Science* **79**, 40-60 (2018).
45.   X. Wang, W. Hong, Pseudo-elasticity of a double network gel. *Soft Matter* **7**, 8576 (2011).
46.   M. Bacca, C. Creton, R. M. McMeeking, A model for the Mullins effect in multi-network elastomers. *Journal of Applied Mechanics*, (2017).
47.   S. R. Lavoie, P. Millereau, C. Creton, R. Long, T. Tang, A continuum model for progressive damage in tough multinetwork elastomers. *Journal of the Mechanics and Physics of Solids* **125**, 523-549 (2019).
48.   F. J. Vernerey, R. Brighenti, R. Long, T. Shen, Statistical Damage Mechanics of Polymer Networks. *Macromolecules*, (2018).
49.   Y. Higuchi, K. Saito, T. Sakai, J. P. Gong, M. Kubo, Fracture Process of Double-Network Gels by Coarse-Grained Molecular Dynamics Simulation. *Macromolecules* **51**, 3075-3087 (2018).
50.   T. Zhang, S. Lin, H. Yuk, X. Zhao, Predicting fracture energies and crack-tip fields of soft tough materials. *Extreme Mechanics Letters* **4**, 1-8 (2015).
51.   H. R. Brown, A Model of the Fracture of Double Network Gels. *Macromolecules* **40**, 3815-3818 (2007).
52.   Y. Tanaka, A local damage model for anomalous high toughness of double-network gels. *Europhysics Letters (EPL)* **78**, 56005 (2007).
53.   R. Long, C. Y. Hui, Fracture toughness of hydrogels: measurement and interpretation. *Soft Matter* **12**, 8069-8086 (2016).
54.   T. Matsuda, R. Kawakami, R. Namba, T. Nakajima, J. P. Gong, Mechanoresponsive self-growing hydrogels inspired by muscle training. *Science* **363**, 504-508 (2019).

55. S. Beck, H. Koster, Applications of Dioxetane Chemiluminescent Probes to Molecular Biology. *Anal. Chem.* **62**, 2258-2270 (1990).

56. M. M. Caruso *et al.*, Mechanically-Induced Chemical Changes in Polymeric Materials. *Chemical Reviews* **109**, 5755–5798 (2009).

57. Y. Yuan, Y.-l. Chen, Visualized bond scission in mechanically activated polymers. *Chinese Journal of Polymer Science*, (2017).

58. K. M. Wiggins, J. N. Brantley, C. W. Bielawski, Methods for activating and characterizing mechanically responsive polymers. *Chem Soc Rev* **42**, 7130-7147 (2013).

59. A. L. Black, J. M. Lenhardt, S. L. Craig, From molecular mechanochemistry to stress-responsive materials. *J. Mater. Chem.* **21**, 1655–1663 (2010).

60. C. K. Lee *et al.*, Exploiting Force Sensitive Spiropyrans as Molecular Level Probes. *Macromolecules* **46**, 3746-3752 (2013).

61. D. A. Davis *et al.*, Force-induced activation of covalent bonds in mechanoresponsive polymeric materials. *Nature* **459**, 68-72 (2009).

62. G. R. Gossweiler, T. B. Kouznetsova, S. L. Craig, Force-rate characterization of two spiropyran-based molecular force probes. *J Am Chem Soc* **137**, 6148-6151 (2015).

63. H. Zhang *et al.*, Spiropyran as a Mechanochromic Probe in Dual Cross-Linked Elastomers. *Macromolecules* **47**, 6783-6790 (2014).

64. G. R. Gossweiler *et al.*, Mechanochemical Activation of Covalent Bonds in Polymers with Full and Repeatable Macroscopic Shape Recovery. *ACS Macro Letters* **3**, 216-219 (2014).

65. Y. Chen, *Quantitative mapping of stress in soft materials by mechanochemistry 5Doctoral dissertation* UPMC (2018).

66. S. L. Potisek, D. A. Davis, N. R. Sottos, S. R. White, J. S. Moore, Mechanophore-Linked Addition Polymers. *Journal of the American Chemical Society* **129**, 13808-13809 (2007).

67. K. Ishizuki, H. Oka, D. Aoki, R. Goseki, H. Otsuka, Mechanochromic Polymers That Turn Green Upon the Dissociation of Diarylbibenzothiophenonyl: The Missing Piece toward Rainbow Mechanochromism. *Chemistry - A European Journal* **24**, 3170-3173 (2018).

68. Y. Yuan, W. Yuan, Y. Chen, Recent advances in mechanoluminescent polymers. *Science China Materials* **59**, 507-520 (2016).

69. E. W. Meijer, R. Groningen, Ed. (1982).

70. Y. Chen *et al.*, Mechanically induced chemiluminescence from polymers Fincorporating a 1,2-dioxetane unit in the main chain. *Nat Chem* **4**, 559-562 (2012).

71. Y. Chen, R. P. Sijbesma, Dioxetanes as Mechanoluminescent Probes in Thermoplastic Elastomers. *Macromolecules* **47**, 3797-3805 (2014).

72. J. M. Clough, C. Creton, S. L. Craig, R. P. Sijbesma, Covalent Bond Scission in the Mullins Effect of a Filled Elastomer: Real-Time Visualization with Mechanoluminescence. *Advanced Functional Materials*, (2016).

73. J. R. Lakowicz, *Principles of Fluorescence Spectroscopy*. (Springer, 1999).

74. F. A. Villamena, *Fluorescence Technique*. (2017), pp. 87-162.

75. A. Diaspro, G. Chirico, C. Usai, P. Ramoino, J. Dobrucki, *Handbook of Biological Confocal Microscopy*. (2006).

76. A. S. Klymchenko, Y. Mely, Fluorescent environment-sensitive dyes as reporters of biomolecular interactions. *Prog Mol Biol Transl Sci* **113**, 35-58 (2013).

77.   Y.-K. Song *et al.*, Fluorescence sensing of microcracks based on cycloreversion of a dimeric anthracene moiety. *J. Mater. Chem.* **22**, 1380-1386 (2012).

78.   N. Bruns, K. Pustelny, L. M. Bergeron, T. A. Whitehead, D. S. Clark, Mechanical nanosensor based on FRET within a thermosome: damage-reporting polymeric materials. *Angew Chem Int Ed Engl* **48**, 5666-5669 (2009).

79.   Y. Sagara *et al.*, Rotaxanes as Mechanochromic Fluorescent Force Transducers in Polymers. *J Am Chem Soc*, (2018).

80.   D. C. Church, G. I. Peterson, A. J. Boydston, Comparison of Mechanochemical Chain Scission Rates for Linear versus Three-Arm Star Polymers in Strong Acoustic Fields. *ACS Macro Letters* **3**, 648-651 (2014).

81.   J. Li *et al.*, Mechanophore activation at heterointerfaces. *J Am Chem Soc* **136**, 15925-15928 (2014).

82.   H. Li *et al.*, Promoting Mechanochemistry of Covalent Bonds by Noncovalent Micellar Aggregation. *ACS Macro Letters* **5**, 995-998 (2016).

83.   R. Göstl, R. P. Sijbesma, π-extended anthracenes as sensitive probes for mechanical stress. *Chem. Sci.* **7**, 370-375 (2016).

84.   M. Mitsui, Y. Kawano, R. Takahashi, H. Fukui, Photophysics and photostability of 9,10-bis(phenylethynyl)anthracene revealed by single-molecule spectroscopy. *RSC Advances* **2**, 9921 (2012).

85.   E. Ducrot, Innovative tough elastomers: Designed sacrificial bonds in multiple networks (Doctoral dissertation) UPMC (2013).

Chapter 2

Synthesis and characterization of mechano-fluorescent and non mechano-fluorescent single and multiple network elastomers

Introduction

In this chapter, materials' synthesis and properties will be presented. First, the Diels-Alder adduct mechanophore was synthesized. Then, single network and multiple networks reference samples, without mechanophore, were made. Incorporation of the synthesized mechanophore gave mechano-fluorescent samples, single or multiple networks. The mechanophore was integrated either in the filler or in the matrix network. Small-strain rheology and large strain mechanical properties in uniaxial tension were then investigated and compared for both reference and mechano-fluorescent samples.

1 Mechanophore and calibration molecule: synthesis and characterization

1.1 5-steps Diels-Alder adduct mechanophore synthesis

The synthetic procedure of the Diels-Alder adduct mechanophore was adapted from the procedure developed by Robert Göstl and Rint Sijbesma (*1*). Robert Göstl kindly provided details on each step of the procedure. In the first and the last steps, stoichiometry of reactants were adapted to fit laboratory facilities and enhance the yield. The 5-step synthesis is shown schematically in Figure 1. Every step will be detailed in this section. The final product is noted DACL (for Diels-Alder Adduct Cross-Linker). Intermediate species are noted DACL1 to 4.
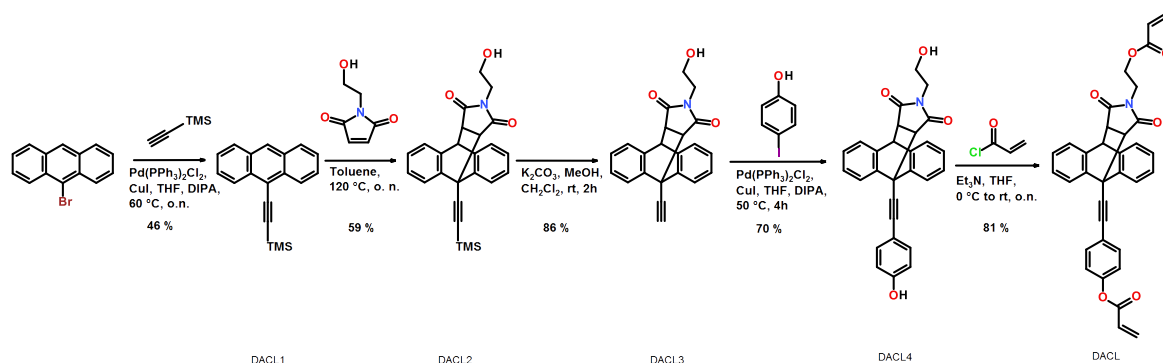
Figure 1: Synthesis of Diels Alder adduct mechanophore

Reagents were purchased from commercial suppliers (TCI Chemicals, VWR, Sigma Aldrich) and used as received. ^{1}H NMR spectra were recorded at 400 MHz and data are reported as follows: chemical shift in ppm from tetramethylsilane as an internal standard, multiplicity (s = singlet, d = doublet, t = triplet, q = quartet, m = multiplet or overlap of nonequivalent resonances), integration. TLC was performed on silica gel plates visualized with $KMnO_4$–K_2CO_3 in water followed by heating.

1.1.1 Step 1: DACL1 synthesis

(Anthracen-9-ylethynyl)trimethylsilane, noted DACL 1, was synthesized by a Sonogashira reaction of TMS-acetylene to 9-bromoanthracene.
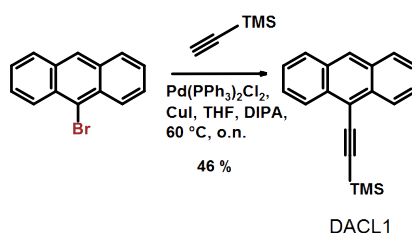
9-bromoanthracene (4.00 g, 15.6 mmol, 1 eq), $Pd(PPh_3)_2Cl_2$ (546 mg, 0.8 mmol, 0.05 eq), and copper(I) iodide (148 mg, 0.8 mmol, 0.05 eq) were dissolved in dry THF (15.5 mL) and degassed with N_2. To this solution were added subsequently TMS-acetylene (6.6 ml, 46.7 mmol, 3 eq) and dry diisopropylamine (15.6 mL) whereupon the solution turned orange and then black. The mixture was stirred at 60 °C under N_2 for 26 h. Afterwards, the solution was cooled down, diluted with CH_2Cl_2, and filtered to remove the insoluble particles. The solvent was evaporated in vacuo and a purification by column chromatography (silica, cyclohexane, 1 % toluene) yielded a red oil that was crystallized

from MeCN in the freezer (-18 °C) to give DACL1 (1.972 g, 7.1 mmol, 45.9 % yield) as yellow needles (1.822 g 1st crop, 0.150 g 2nd crop).

^{1}H NMR (400 MHz, CDCl$_3$) δ (ppm): 8.57 (dd, J = 8.7, 0.8 Hz, 2H), 8.42 (d, J = 8.8 Hz, 1H), 8.00 (d, J = 8.4 Hz, 2H), 7.59 (ddd, J = 8.6, 6.6, 1.2 Hz, 2H), 7.54 – 7.47 (m, 2H), 0.44 (s, 9H).

1.1.2   Step 2: DACL 2 synthesis

13-(2-hydroxyethyl)-9-((trimethylsilyl)ethynyl)-10,11-dihydro-9H-9,10-[3,4]epipyrroloanthracene-12,14(13H,15H)-dione, noted DACL2, was synthesized by a Diels-Alder reaction of N-(2-hydroxyethyl)maleimide and DACL1.
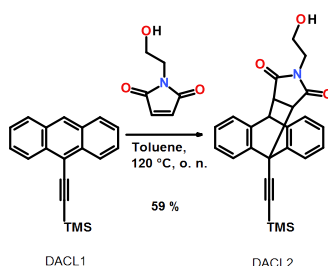
DACL1 (1 g, 3.6 mmol, 1 eq) and *N*-(2hydroxyethyl) maleimide (565 mg, 4.0 mmol, 1.1 eq) were dissolved in toluene (37 mL) and stirred at 110 °C for 21 h. Evaporation of the solvent in vacuo and purification by column chromatography (silica, cyclohexane: EtOAc = 1 : 1) yielded DACL2 (900 mg, 2.2 mmol, 59.4 % yield) as a white solid.

^{1}H NMR (400 MHz, CDCl$_3$) δ (ppm): 7.80 (d, J = 7.3 Hz, 1H), 7.68 (d, J = 7.2 Hz, 1H), 7.38 (d, J = 7.0 Hz, 1H), 7.34 – 7.18 (m, 5H), 4.79 (d, J = 2.7 Hz, 1H), 3.32 (t, J = 5.0 Hz, 2H), 3.29 – 3.21 (m, 2H), 3.15 – 3.01 (m, 2H), 0.41 (s, 9H).

1.1.3   Step 3: DACL 3 synthesis

9-ethynyl-13-(2-hydroxyethyl)-10,11-dihydro-9H-9,10   [3,4]epipyrroloanthracene-12,14(13H,15H)-dione, noted DACL3, was obtained by a deprotection of the TMS group of the acetylene.
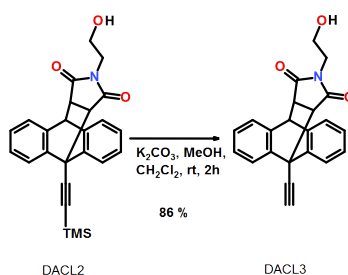
A solution of potassium carbonate (243 mg, 1.8 mmol, 0.8 eq) in MeOH (5.5 mL) was degassed with N_2. A solution of DACL2 (913 mg, 2.2 mmol, 1 eq) in a mixture of dichloromethane (5.5 mL) and methanol (5.5 mL) was degassed with N_2. The second solution was added to the first one at room temperature under N_2 and stirred for 24 h. After full completion (checked by TLC), brine was added to the solution and it was extracted with CH_2Cl_2. The organic phase was dried with anhydrous $MgSO_4$. Removal of the volatiles in vacuo yielded pure DACL3 (646 mg, 1,9 mmol, 86 % yield) as a white foam.

^{1}H NMR (400 MHz, CDCl$_3$) δ (ppm): 7.84 (dd, J = 7.1, 1.3 Hz, 1H), 7.73 (dd, J = 7.1, 1.2 Hz, 1H), 7.40 (dd, J = 7.0, 1.3 Hz, 1H), 7.35 – 7.20 (m, 5H), 4.81 (t, J = 5.7 Hz, 1H), 3.33 (q, J = 4.9 Hz, 2H), 3.30 – 3.27 (m, 2H), 3.17 (s, 1H), 3.15 – 3.03 (m, 2H).

1.1.4 Step 4: DACL 4 synthesis

(13-(2-hydroxyethyl)-9-((4-hydroxyphenyl)ethynyl)-10,11-dihydro-9H-9,10-[3,4]epipyrroloanthracene-12,14(13H,15H)-dione), noted DACL4, was synthesized by a Sonogashira reaction of DACL 3 with 4-iodophenol.
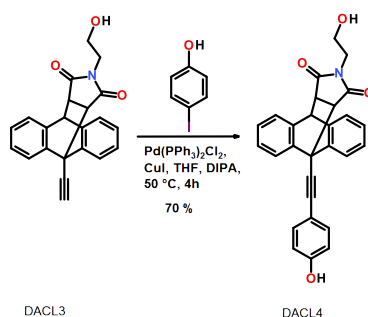
DACL3 (578 mg, 1.7 mmol, 1 eq), 4-iodophenol (423 mg, 1.9 mmol, 1.1 eq), Pd(PPh$_3$)$_2$Cl$_2$ (62 mg, 0.09 mmol, 0.05eq), and copper(I) iodide (18 mg, 0.09 mmol, 0.05 eq) were dissolved in dry THF (3.6 mL) and degassed with N_2. To this solution was added dry

diisopropylamine (3.6 mL) whereupon the solution turned black. The medium was stirred at room temperature under N_2 for 24 h. Afterwards, the solution was cooled down, diluted with THF, and filtered to remove the insoluble particles. Subsequent removal of the solvent in vacuo and purification by column chromatography (silica, cyclohexane: EtOAc = 1 : 1 gradient to pure EtOAc) yielded DACL4 (510 mg, 1.2 mmol, 70 % yield) as an off-white solid.

^{1}H NMR (400 MHz, DMSO-d_6) δ (ppm): 10.02 (s, 1H), 7.78 (dd, J = 7.1, 1.3 Hz, 1H), 7.63 - 7.55 (m, 3H), 7.53 (dd, J = 6.9, 1.6 Hz, 1H), 7.32 – 7.17 (m, 5H), 6.92 – 6.87 (m, 2H), 4.84 (s, J = 3.1 Hz, 1H), 4.65 (s, 1H), 3.35 (dd, J = 8.4, 3.2 Hz, 1H), 3.31 (d, J = 8.4 Hz, 1H), 3.03 (t, J = 7.5 Hz, 2H), 2.66 – 2.52 (m, 2H).

1.1.5 Step 5: DACL synthesis

4-((13-(2-(acryloyloxy)ethyl)-12,14-dioxo-9,10-[3,4]epipyrroloanthracen-9(10H)-yl)ethynyl)phenyl acrylate, noted DACL, was obtained by an esterification reaction of DACL4 and acryloyl chloride.

DACL4   DACL
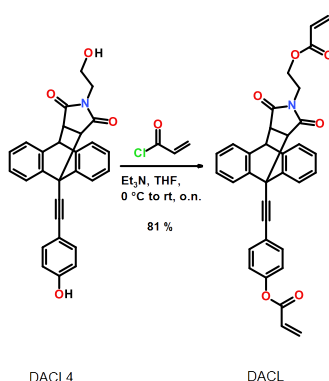
Acryloyl chloride (0.75 mL, 9.2 mmol, 20 eq) was poured in a Schlenk tube (or a 50 ml two neck flask) under N_2. THF (1 mL) was added to the solution. The solution was cooled by an ice bath. DACL4 (200 mg, 0.5 mmol, 1 eq) was dissolved in THF (3 mL) under N_2. To this solution was added triethylamine (1.27 mL, 9.2 mmol, 20 eq). This solution was introduced dropwise into the Schlenk tube whereupon the HCl salt precipitated. The medium was stirred overnight at room temperature. A saturated solution of aqueous $NaHCO_3$ was added slowly and the whole extracted with CH_2Cl_2. The organic layer was washed twice with a saturated solution of aqueous $NaHCO_3$ and a saturated aqueous

solution of NH_4Cl and subsequently dried over anhydrous $MgSO_4$. Evaporation in vacuo of the solvent gave DACL (201 mg, 0,4 mmol, 81 % yield) as an off-white foam.

^{1}H NMR (400 MHz, CDCl$_3$) δ (ppm): 7.86 (dd, J = 7.3, 1.4 Hz, 1H), 7.83 – 7.79 (m, 2H), 7.68 (dd, J = 6.8, 1.9 Hz, 1H), 7.41 (dd, J = 7.1, 1.2 Hz, 1H), 7.32 – 7.13 (m, 8H), 6.65 (dd, J = 17.3, 1.2 Hz, 1H), 6.42 – 6.31 (m, 2H), 6.09 – 5.98 (m, 2H), 5.84 (dd, J = 10.5, 1.4 Hz, 1H), 4.86 – 4.77 (s, 1H), 3.60 (dt, J = 5.9, 5.5 Hz, 1H), 3.52 (dt, J = 13.9, 4.1 Hz, 1H), 3.44 (td, J = 5.5, 2.2 Hz, 2H), 3.31 (d, J = 1.7 Hz, 2H).
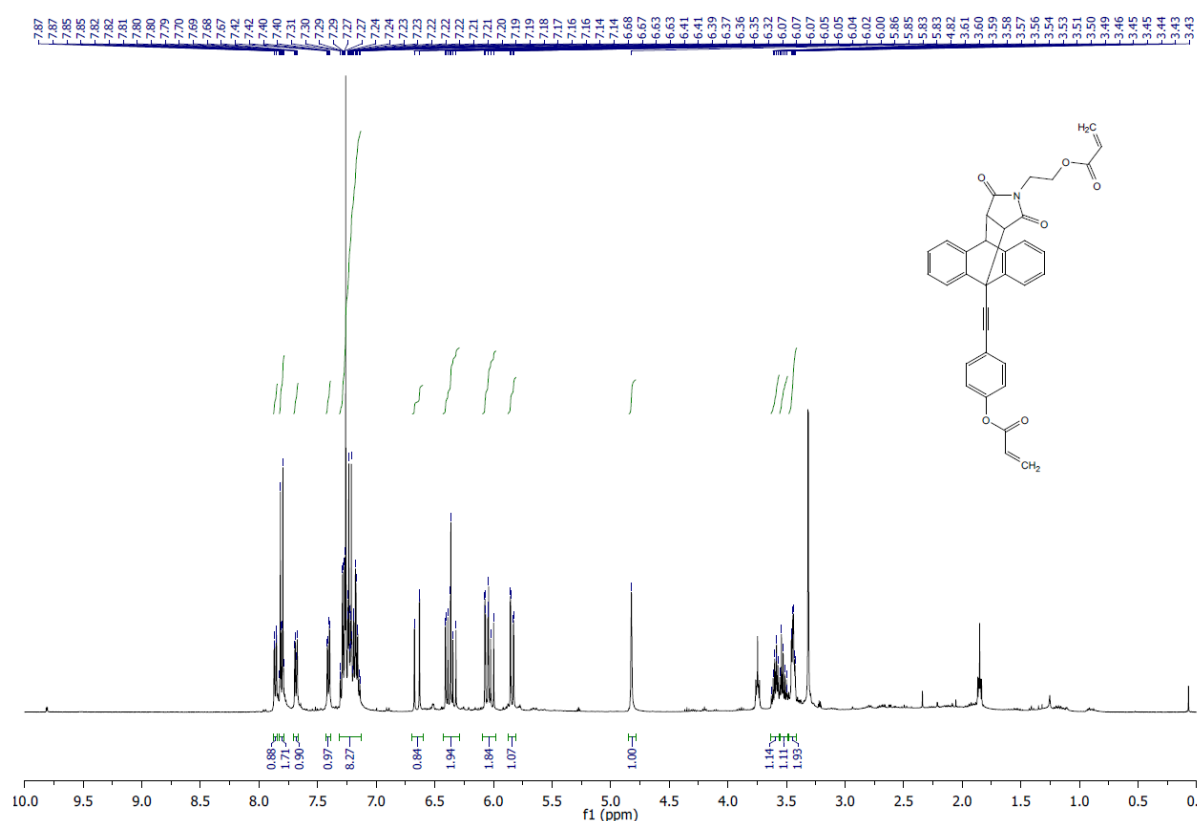
Figure 2: ^{1}H NMR spectrum of the mechanophore cross-linker (DACL)

The mechanophore crosslinker DACL was not stable because of the two acrylate functions which can homopolymerize spontaneously even in the fridge. However, DACL4, with two hydroxy moieties was stable. It was stored in the freezer for months without degradation.

The synthesis, from commercially available components up to DACL4, was done in two weeks and a half, with a total yield of 16 % (about 1g can be obtain from 4 g of 9-bromoanthracene). The last step, to give the cross-linker, was done just before single network synthesis.

1.2   Calibration molecule

1.2.1   Synthesis

The 9-((4-anisyl)ethynyl)anthracene will be called the calibration molecule and is used for signal calibration because it has the same fluorescence as the broken mechanophore (strategy detailed in chapter 3). The calibration molecule was obtained in one step by a Sonogashira reaction of 4-ethylanisole with 9-bromoanthracene.
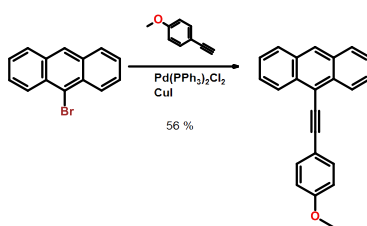
9-Bromoanthracene (505 mg, 2.0 mmol, 1 eq), 4-ethynylanisole (258 mg, 2.0 mmol, 1 eq), Pd(PPh$_3$)$_2$Cl$_2$ (68 mg, 0.1 mmol, 0.05 eq), and CuI (21 mg, 0.1 mmol, 0.06 eq) were dissolved in dry THF (5 mL) and degassed with N$_2$. To this solution was added dry diisopropylamine (5 mL) whereupon the solution turned black. The whole was stirred at 60 °C under N$_2$ overnight. Removal of the solvent in vacuo and purification by column chromatography (silica, pentane: EtOAc = 9 : 1 with 1% toluene) yielded 9-((4-anisyl)ethynyl)anthracene (328 mg, 1.1 mmol, 56 % yield) as a fluffy, yellow solid.

^{1}H NMR (400 MHz, CDCl$_3$) δ (ppm): 8.66 (ddd, *J* = 8.5, 1.8, 0.9 Hz, 2H), 8.42 (s, 1H), 8.02 (ddt, *J* = 8.4, 1.3, 0.7 Hz, 2H), 7.74 – 7.68 (m, 2H), 7.59 (ddd, *J* = 8.7, 6.6, 1.3 Hz, 2H), 7.55 - 7.49 (m, 2H), 7.01 - 6.95 (m, 2H), 3.88 (s, 3H).

The reference molecule was stored in the fridge (dark and 5 °C). The NMR of this molecule was run just after synthesis, three months later and one year and a half after synthesis. No degradation was observed.

1.2.2   Fluorescence characterization

The fluorescence of the reference molecule was characterized thanks to a collaboration with Sandrine Ithurria, LPEM, ESPCI. Photoluminescence and excitation spectra were

obtained from an Edinburgh Instrument spectrometer. The absorption spectrum was recorded between 320 nm and 450 nm for an emission at 460 nm. The emission spectrum was recorded between 420 nm and 600 nm, for an excitation at 405 nm.

The reference molecule was diluted in ethyl acetate at 6×10^{-5} mol.L^{-1}. Absorption (purple) and emission (blue) spectra are represented Figure 3. The reference molecule absorbed in UV with one maximum at 400 nm and a second maximum at 422 nm. For an excitation at 405 nm, two maxima of emission are detected 435 nm and 460 nm, one shoulder at 485 nm. This result is consistent with the spectra reported in the literature (*1*).
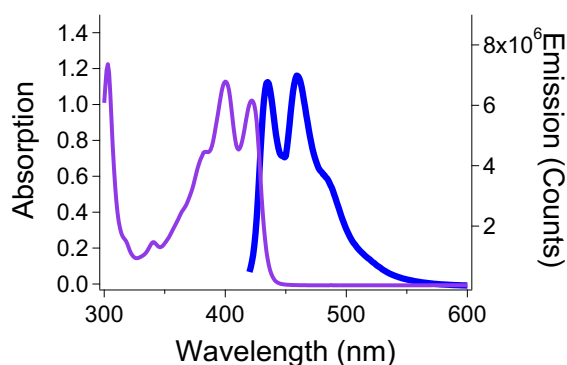
Figure 3: UV/Vis absorption and Fluorescence spectra (λexc=405 nm), 6x10^{-5} mol.L^{-1}

The absorption and emission spectra overlapped between 420 nm and 440 nm. This overlap means that a reference molecule can absorb the emission from another reference molecule. This phenomenon is called cross excitation. It also occurs for the activated mechanophore and should be kept in mind.

Settings for Laser Scanning Confocal Microscopy (LSCM) analysis were chosen based on these spectra. The wavelength of excitation was fixed at 405 nm in order to correspond to the maximum of absorption. The emission was recorded from 450 nm to 550 nm.

2 Single and multiple networks synthesis

The classical procedure will be described first; followed by the modification to render the sample mechano-fluorescent.

Reagents were purchased from commercial suppliers (VWR, Sigma Aldrich). The radical inhibitor (hydroquinone or monomethyl ether hydroquinone) was removed from acrylate species (monomers and cross-linker) by a column on basic alumina. Other reagents were used without further purification. All polymerization were carried out in a glovebox (Mbraun Unilab) under nitrogen atmosphere to avoid reactions with oxygen. Before any introduction in the glovebox, reagents are bubbled with N_2 to remove the oxygen dissolved within it. UV light was produced by a Vilbert Lourmat lamp, model VL-215.L, focused on 365 nm.

2.1 Single network synthesis

Methyl acrylate (MA) and ethyl acrylate (EA) monomers were used to compare samples with different properties. The glass transition temperature (Tg) of poly(ethyl acrylate) and poly(methyl acrylate) are -24 °C and 10 °C respectively (*2*). At ambient temperature the poly(methyl acrylate) is therefore closer to its glass transition temperature and displays marked viscoelastic properties. As the side chain is smaller, the average molecular weight between entanglements of poly(methyl acrylate) (one carbon on the side chain) is smaller than that of poly(ethyl acrylate) (two carbons on the side chain).

Samples were prepared through a free radical photo polymerization. 2-hydroxy-2-methylpropiophenone (HMP) was used as a UV initiator. Two radicals are created through the mechanism shown in Figure 4, one is active.
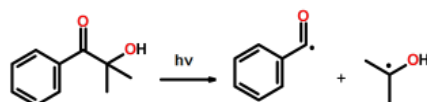

Figure 4: Schematic representation of initiator (HMP) mechanism

The standard cross-linker used was 1,4-butanediol diacrylate (BDA). Monomer, cross-linker and initiator (1.16 mol% relative to monomer) were mixed together and the

liquid solution was casted in a mold. The latter was composed of two glass plates covered with transparent PET films (with a hydrophobic surface), with a silicone spacer to control the sample thickness (0.7 mm) and two metal frames to seal the mold. Yinjun Chen showed that glass and sample interface lead to irregular fingering patterns on the surface because of heterogeneous shrinkage during polymerization (*3*). The solution he found was to cover glass plates with transparent PET films with a hydrophobic surface. The strong interaction between PET and the sample gave smooth surfaces. The mold was placed under UV for two hours. The UV power was kept low (below 10 µW/cm²) to create a slow polymerization in order to decrease the number of simultaneous growing chains and the number of termination reactions. The polymerization is summarized in the scheme of Figure 5.
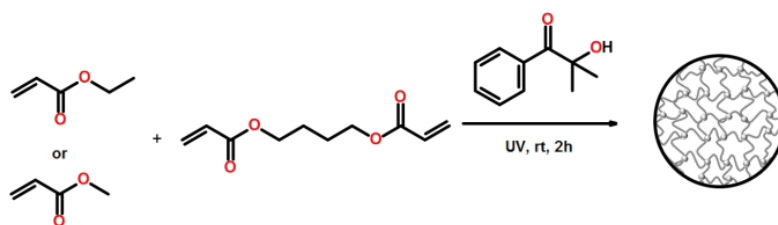
Figure 5: Schematic representation of single network synthesis

After polymerization, the sample was dried overnight under vacuum (without heating) to remove unreacted volatile monomer. The sample was weighed before and after drying. The weight loss was less than 0.2 %.

The crosslinking concentration was chosen to give materials made of ethyl and methyl acrylate with the same Young modulus. The Young's modulus E and the molecular weight between crosslinks M_x are linked by Eq 1., from the affine model of rubber elasticity (*4*). The average cross-linking concentration is linked to the average molecular weight between crosslinks by Eq 2.. The molecular weight between crosslinks was fixed at 10,000 g.mol⁻¹. It is a classical value of materials already investigated in our lab. This value is theoretical and is not representative of reality as transfer reactions occur.

$$E = \frac{3\rho RT}{M_x} \qquad\qquad \text{Eq 1.}$$

Where ρ is the network density, R the gas constant, T the temperature

$$M_{x,th} = \frac{M_{monomer}\, n_{monomer}}{2\, n_{BDA}} \qquad\qquad \text{Eq 2.}$$

Where $M_{x,th}$ is the theoretical molecular weight between crosslinks (in g/mol), $M_{monomer}$ the molecular weight of the monomer (in g/mol), $n_{monomer}$ the monomer quantity (in moles) and n_{BDA} the cross-linker quantity (in moles).

These samples were called single networks. In the manuscript, they are noted SNXX, where SN stands for Single Network and XX is either EA or MA for Ethyl or Methyl Acrylate respectively. Table 1and Table 2 summarize the compositions of SNEA and SNMA respectively. Molar percentages are relative to moles of monomer.

SNEA	Quantity (mol%)	Quantity (mmol)	Volume
Ethyl acrylate (EA)		36.7	4 mL
HMP	1.16	0.43	64.9 µL
BDA	0.50	0.18	34.6 µL

Table 1: SNEA composition

SNMA	Quantity (mol%)	Quantity (mol)	Volume
Methyl acrylate (MA)		44.4	4 mL
HMP	1.16	0.52	78.6 µL
BDA	0.43	0.19	36.1 µL

Table 2: SNMA composition

Single networks with a quantity of cross-linker divided by two were also made and are presented in chapter 4.

Single networks were used as prepared or served as filler networks in multiple networks by undergoing swelling/polymerizations steps to get multiple networks.

2.2   Multiple networks synthesis

The preparation of multiple network elastomers consisted in a sequence of free radical photo-polymerizations, following the methodology developed by Etienne Ducrot (*5*). The polymerization was performed without solvent, which was the only difference from the procedure described in ref 5. Bulk polymerization saves time, as dialysis steps are no longer necessary. During his PhD, Pierre Millereau compared synthesis with and without solvent. He concluded that the synthesis in bulk conditions created a network with a higher efficiency of crosslinking process (higher modulus)(*6*).

A piece of single network of dimension 20 mm x 40 mm was cut. The cut sample was put in a bath containing the monomer (ethyl or methyl acrylate), cross-linker (0.01 mol%) and initiator (0.01 mol%). Table 3and Table 4 summarize the composition of ethyl acrylate and methyl acrylate baths. The sample was swollen up to equilibrium for 2 h.

EA Bath	Quantity (mol%)	Quantity (mmol)	Volume
Ethyl acrylate (EA)		412.6	45 mL
HMP	0.01	0.04	6.29 µL
BDA	0.01	0.04	7.78 µL

Table 3: Bath composition for the matrix network of EA

MA Bath	Quantity (mol%)	Quantity (mmol)	Volume
Methyl acrylate (MA)		499.7	45 mL
HMP	0.01	0.05	7.62 µL
BDA	0.01	0.05	9.42 µL

Table 4: Bath composition for the matrix network of MA

The swollen sample was put between two glass slides for UV polymerization of the matrix network within the filler network (less than 10 µW/cm²). As for single networks, the sample was dried overnight under vacuum (without heating).

Following the convention of Millereau *et al.* (*7*) multiple networks can be described by the fraction ϕ_{SN} of first network within the final material (Eq 3.) and the degree of prestretching λ_0 of the filler network (Eq 4.).

$$\phi_{SN} = \frac{m_{SN}}{m_{total}} \qquad\qquad \text{Eq 3.}$$

With m_{SN} and m_{total} the weight of the filler network and of the final material repectively.

$$\lambda_0 = \frac{d_{total}}{d_{SN}} = \left(\frac{V_{total}}{V_{SN}}\right)^{1/3} = \left(\frac{m_{total}}{m_{SN}}\right)^{1/3} \qquad\qquad \text{Eq 4.}$$

With d_{total} and d_{SN} a characteristic distance such as the thickness, the length or the width of the final material and the filler network respectively. V_{SN} and V_{total} are the volume of the filler network and of the final material respectively.

To get a higher degree of prestretching of the filler network, λ_0, swelling/polymerization steps were repeated. A higher prestretching of the filler network went with a higher level of dilution of this filler network in the matrix (synthesis without solvent). If λ_0 increased, ϕ_{SN} decreased.

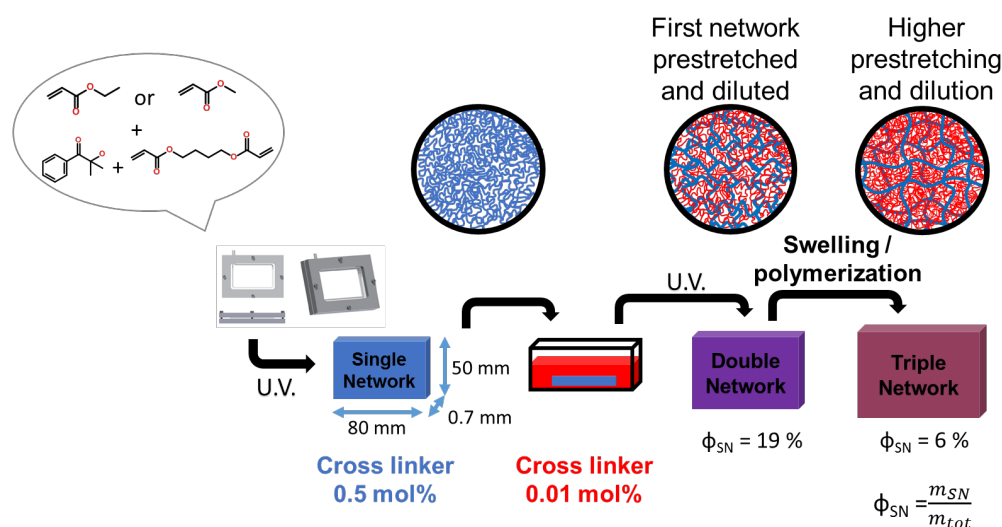Figure 6 illustrates the process for multiple network synthesis.

Figure 6; Schematic representation of multiple network synthesis

Multiple networks are noted BBCC(z)
BB: EA or MA for Ethyl Acrylate or Methyl Acrylate monomers in the filler network
CC: EA or MA for the monomer of the matrix
(z): the pre-stretching λ_0

2.3 Mechano-fluorescent network synthesis

2.3.1 Mechanophore incorporated in the filler network

In order to label the samples with mechano-fluorescent molecules, the Diels-Alder adduct mechanophore (DACL) was covalently incorporated as a cross-linker. It was used in combination with the standard crosslinker, BDA. The total amount of crosslinker was kept identical: 0.50 mol% for ethyl acrylate samples and 0.43 mol% for methyl acrylate samples. The mechanophore cross-linker was introduced at 0.02 mol%. This small quantity was enough for damage detection by fluorescence. A small amount of mechanophore made it possible to make several samples. In practice, a stock solution was made with the mechanophore diluted in the monomer. 4 mL of the stock solution were taken off to be mixed with the standard cross-linker and the initiator. The mix was injected in the mold and polymerization conditions were identical. The sample was dried under vacuum overnight.

 A solution of mechanophore in ethyl acetate was analyzed by UV-Vis absorption. No absorption was observed at 365 nm, meaning that the un-activated mechanophore does not absorb the UV light required for polymerization.

The composition of mechano-fluorescent samples is indicated in Table 5 and Table 6.

DASNEA	Quantity (mol%)	Quantity (mmol)	Volume
Ethyl acrylate (EA)		36.7	4 mL
HMP	1.16	0.43	64.9 µL
BDA	0.48	0.18	33.2 µL
DACL	0.02	0.0073	

Table 5: DASNEA composition

DASNMA	Quantity (mol%)	Quantity (mmol)	Volume
Methyl acrylate (MA)		44.4	4 mL
HMP	1.16	0.52	78.6 µL
BDA	0.41	0.18	34.4 µL
DACL	0.02	0.0073	

Table 6: DASNMA composition

Mechano-fluorescent single networks were used as prepared and are noted DASNXX, DA stands for Diels-Alder as it contains the mechanophore, SN for single network, XX is either MA or EA for methyl acrylate and ethyl acrylate respectively.

Mechano-fluorescent single networks were also used as mechano-fluorescent filler networks in multiple networks. Swelling/polymerization steps were kept unchanged. Mechanophore labeled samples looked, to the naked eye, identical as the samples without: transparent. All samples were stored in the freezer (dark and -18 °C).

Mechanofluorescent multiple networks with mechanophores in the filler network are noted DABBCC(z)

DABBCC(z): Contains Diels-Alder adduct mechanophore in the filler network, which is made of BB = EA ethyl acrylate or MA methyl acrylate
CC: EA or MA for the monomer of the matrix
(z): the level of pre-stretching of the filler network λ_0

2.3.2 Mechanophore incorporated in the matrix network

Samples with the mechanophore in the second network were also made, in this case the network was fully cross-linked with the mechanophore cross-linker at 0.01 mol%. A non mechano-fluorescent single network of ethyl acrylate (SNEA) was swollen in a bath containing ethyl acrylate (40 mL, 0.37 mol), initiator (HMP, 5.59 µL, 0.037 mmol,

0.01 mol%) and mechanophore cross-linker (19.8 mg, 0.037 mmol, 0.01 mol%). The same bath was used to swell three samples.

Mechano-fluorescent multiple networks, with mechanophore in the second network, are noted BBDACC(z)
BB: EA or MA for Ethyl Acrylate or Methyl Acrylate monomers in the filler network
DACC: Diels-Alder adduct mechanophore incorporated in the matrix made of CC = EA or MA
(z): the level of pre-stretching of the filler network λ_0

A Soxhlet apparatus was used to measure extractables but nothing was detected by ^{1}H NMR analysis.

Table 7 and Table 8 summarize materials investigated, their name and composition. Molar percentages are relative to moles of monomer.

Single network

Name	Monomer	[HMP] (%mol)	[BDA] (mol%)	[DACL] (mol%)	[Total Cross-linker] (%mol)	[DACL] (mol.m^{-3})
SNEA	EA	1.16	0.50	0	0.5	0
DASNEA	EA	1.16	0.48	0.02	0.5	2.2
SNMA	MA	1.16	0.43	0	0.43	0
DASNMA	MA	1.16	0.41	0.02	0.43	2.8
SNMA$_{0.2}$	MA	1.16	0.22	0	0.22	0
DASNMA$_{0.2}$	MA	1.16	0.20	0.02	0.22	2.8

Table 7: Single networks composition

Multiple networks

Name	Type of MN	Filler monomer	Matrix monomer	ϕ_{SN}	λ_0	[DACL] (mol/m^3)	Network containing DACL
EAEA(1.6)	DN	EA	EA	0.2	1.6	0	/
DAEAEA(1.6)	DN	EA	EA	0.2	1.6	0.5	1st
EADAEA(1.6)	DN	EA	EA	0.2	1.6	0.9	2nd
DAMAEA(1.5)	DN	MA	EA	0.3	1.5	0.9	1st
MAMA(1.6)	DN	MA	MA	0.3	1.6	0	/
DAMAMA(1.6)	DN	MA	MA	0.3	1.6	0.7	1st
EAEA(2.4)	TN	EA	EA	0.07	2.4	0	/
DAEAEA(2.3)	TN	EA	EA	0.07	2.3	0.2	1st
EADAEA(2.5)	TN	EA	EA	0.07	2.5	0.3	2nd
MAMA(2.3)	TN	MA	MA	0.08	2.3	0	/
DAMAMA(2.3)	TN	MA	MA	0.08	2.3	0.2	1st
EAEA(3.1)	QN	EA	EA	0.03	3.1	0	/
DAEAEA(3.1)	QN	EA	EA	0.03	3.1	0.08	1st
EADAEA(3.2)	QN	EA	EA	0.03	3.2	0.1	2nd

Table 8: Multiple networks composition

After their synthesis, materials properties were investigated.

3 Materials characterizations

3.1 Characterization methods

3.1.1 Small strain viscoelastic properties

Small strain linear viscoelastic properties of our materials were investigated with a Dynamic Mechanical Analysis (DMA) and a rheometer. In both methods, a sinusoidal deformation is applied in the linear region and the response of the material is analyzed (phase angle and deformation). In DMA, a small strip is loaded in uniaxial extension with a sinusoidal tensile strain, at a fixed frequency. In the rheometer with the parallel plate geometry, a sinusoidal torque is applied on a disk. The resulting stress is measured. The ratio between stress and strain is defined as a complex modulus (E* for the DMA or G* for the rheometer). This complex modulus can be decomposed into two components. The first one, in phase, is called the storage modulus (E' or G') and represents the elasticity of the material. The second one, out of phase, is called the loss modulus (E'' or G'') and represents the viscous component. The ratio of these two values, $\tan \delta$, allows a comparison of the viscous and the elastic properties of the material.

$$\tan \delta = \frac{G''}{G'} = \frac{E''}{E'}$$

Young's and shear modulus, E and G, are linked by the following equation (*4*):

$$E = 2(1 + \nu) \, G$$

With ν the Poisson's ratio.

For incompressible materials, including rubbers $\nu \approx 0.5$ and E = 3G

3.1.1.1 Dynamic Mechanical Analysis (DMA)

The DMA experiments were performed on a Q800 DMA testing machine (TA Instruments). A strip of material (5 mm x 15 mm) was cut. The thickness was defined directly by the synthesis (from 0.5 to 2 mm). The piece of sample was placed within the clamps in a tensile film configuration. A tensile preload of 0.1 N was applied to the sample in order to avoid any buckling of the sample during the experiment. The sample was

loaded with a sinusoidal strain of 0.1 % at a 1 Hz frequency. A 1 °C/min temperature ramp was imposed from -90 °C to 80 °C.

3.1.1.2 Rheometer analysis

The temperature and frequency dependence of the samples were tested with a RDAII parallel plate rheometer (Anton Paar, Physica MCR 501). The samples were cut in disk shape using an 8 mm diameter puncher. To avoid slippage from the geometry, samples were glued using Loctite 406. The limits of the linear regime were first determined for all samples, at three different temperatures. A deformation sweep was applied at 1 Hz from 0.01 % to 1 % at 20 °C and 40 °C and from 0.01 % to 0.4 % at -10 °C. Figure 7 represents the result obtained for a single network of methyl acrylate SNMA.
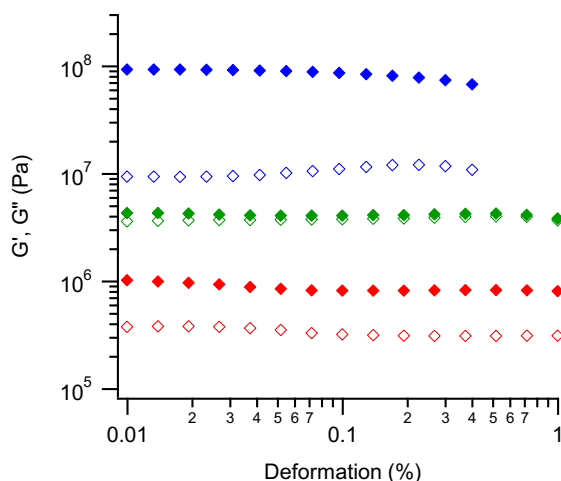
Figure 7: Evolution of G' (solid markers) and G'' (hollow markers) with deformation for SNMA at -10 °C (blue), 20 °C (green) and 40 °C (red)

A frequency sweep was then applied from 0.063 to 63 rad.s^{-1} every 1.5 °C between - 10 °C and 80 °C. The strain was fixed at 0.02 % to be in the linear regime. Using the time temperature superposition principle, data taken at different temperatures were manually shifted to construct a master curve at a reference temperature of 22 °C.

The tan δ data obtained for each temperature are first horizontally shifted one by one by a factor a_T until the best fit is achieved.

Generally in the vicinity of the glass transition the shift factors are related to the applied temperature by the Williams-Landel-Ferry (WLF) relation (*8*).

$$\log(a_T) = \frac{-C_1(T - T_{ref})}{C_2 + (T - T_{ref})}$$

Where C_1 and C_2 are constants, T_{ref} is the reference temperature (in K), T is the measurement temperature (in K).

To improve the quality of superposition of the master curve, a vertical shift of b_T was also applied taking into account the temperature and density dependence of the entropic modulus.

$$b_T = \frac{\rho T}{\rho_{ref} T_{ref}}$$

Where ρ and ρ_{ref} are the network density at T and T_{ref} respectively.

3.1.2 Uniaxial extension

Both DMA and rheology give information about small strain viscoelastic properties only. In fracture, large strain properties are also important. Uniaxial extension gives information at small strains, such as the Young's modulus; but also at larger strain, such as strain and stress at break or the existence or not of strain hardening.

Mechanical tests were performed on standard tensile Instron machines, model 5565 or 5965. A video extensometer gave a local measurement of the stretch λ, defined in Eq 5.. The extensometer monitored the distance between two white dots during the test. In case of slippage, the deformation calculated from the position of the crosshead is not the one applied to the sample while the deformation from the video extensometer is reliable. The extensometer is accurate at ± 0.11 % for the full scale up to 120 mm. The force was recorded using a 100 N load cell, accurate at ± 0.1 %.

Specimens were cut into a dogbone shape using a punch. The central part was 20 mm in length, 4 mm in width and the thickness was defined by the thickness of the plate from which the sample was punched (from 0.5 mm to 2 mm). White dots were drawn in the central part, at 1 cm apart. A picture of a typical sample is given in Figure 8.

Figure 8: Picture of a sample used for uniaxiale extension test

The sample was fixed between two pneumatic clamps. Pressure to close the clamps was adapted to each sample (from 0.7 bar to 5 bar). Tough materials need enough pressure to prevent slippage. A pressure too high on a material damages the sample and leads to a breakage at the clamp.

A temperature controlled oven imposed the temperature at 25 °C. Uniaxial tensile tests from small to large strain were performed at a constant velocity of the crosshead of 50 µm.s^{-1}. Uniaxial extension tests were also performed at other temperatures (40 °C, 60 °C and 80 °C) and crosshead speeds (5 µm.s^{-1} and 500 µm.s^{-1}), more details are given in chapters 4 and 5.

During the tensile test, force F and length L are measured. From these quantities and knowing the initial dimensions of the sample, the stretch λ and the nominal stress σ_N are calculated using the equation Eq 5. and Eq 6. respectively.

$$\lambda = \frac{L}{L_0}$$ Eq 5.

Where L_0 is the initial gauge length

$$\sigma_N = \frac{F}{w_0 \ h_0}$$ Eq 6.

Where w_0 and h_0 the intial width and thickness.

Nominal stress versus stretch curves were analyzed. Using the nominal stress and strain, the Young's modulus was calculated at a strain of less than 10 %.

3.2   Influence of the nature of the monomer on single network properties

3.2.1   Small strain viscoelastic properties

3.2.1.1 Dynamic Mechanical Analysis (DMA)

During the glass transition, additional viscoelastic dissipations occur in the material. The glass transition temperature, Tg, can be estimated by the inflexion point of the storage modulus (corresponding to the extremum of the derivative). Figure 9 represents the storage modulus and its first derivative as a function of temperature for ethyl acrylate (green) and methyl acrylate (orange) single networks. For ethyl acrylate networks, Tg is found at -18 °C and for methyl acrylate network around 18 °C. These values are in good agreement with values reported by Etienne Ducrot (*9*). The side chain of PEA is made of two carbons, one more than PMA. Because of this additional carbon on the side chain, the free volume of the polymer chain increase and chain movements are possible at lower temperature, decreasing the Tg
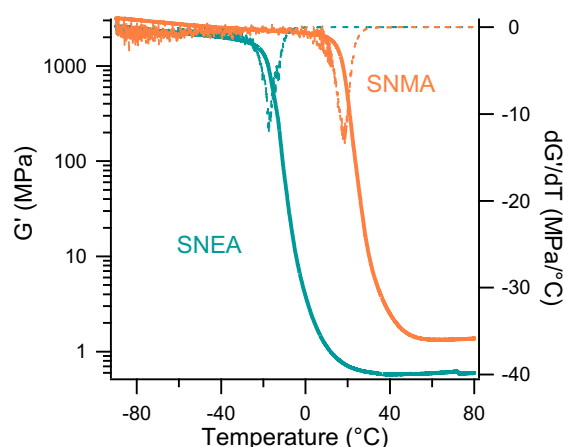
Figure 9: Evolution of the storage modulus and its first derivative with temperature, analyzed by DMA, for ethyl acrylate (in green) and methyl acrylate (in orange) single networks

3.2.1.2 Time temperature superposition

Figure 10 represents the master curve at T = 22 °C constructed for a single network of polyethyl acrylate (SNEA) in green and of polymethyl acrylate (SNMA) in orange. G'(SNMA) presents a plateau from 10^{-7} Hz to 10^{-4} Hz at 3.2×10^5 Pa and G'(SNEA) from 10^{-7} Hz to 1 Hz at 3.5×10^5 Pa. The two samples were designed to have the same theoretical average molecular weight between crosslinks and indeed G' plateau values are

similar. Our materials are assumed incompressible and E' = 3G'. Young's moduli are measured at 0.96 MPa and 1.05 MPa for SNMA and SNEA respectively.
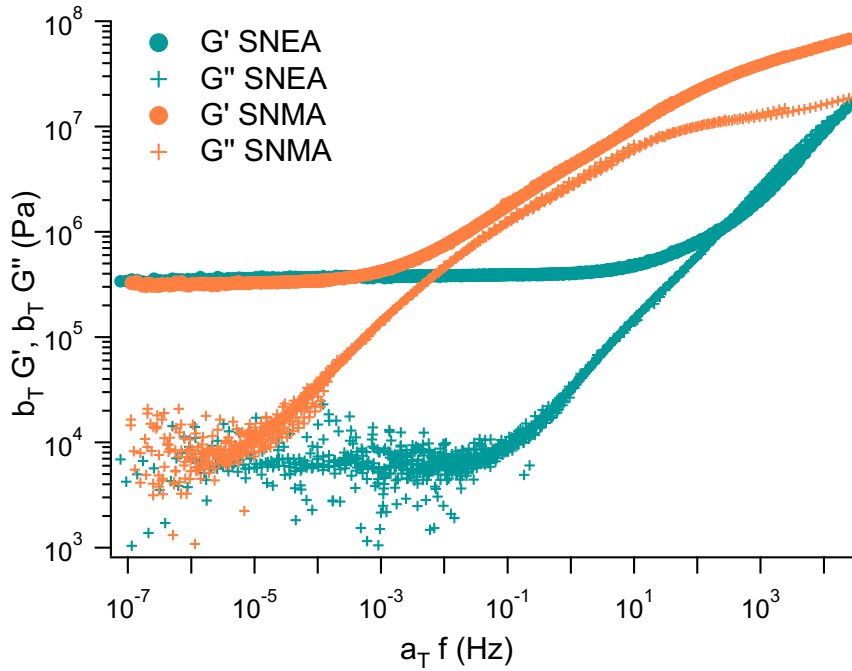
Figure 10: Master curve at 22 °C of G' and G'' for SNEA (green) and SNMA (orange) as a function of frequency

3.2.2 Uniaxial extension

The tensile curves, for single networks of polymethyl acrylate (in orange) and polyethyl acrylate (in green) are represented in Figure 11. The strain and stretch at break and the Young's moduli are reported in Table 9.

At 25 °C	$\sigma_{N,break}$ (MPa)	λ_{break}	E_{exp} (MPa)
SNEA	0.5	1.9	1.2
SNMA	2.0	4.0	1.5

Table 9: Results from uniaxial extension on SNEA and SNMA

The Young's modulus values are comparable consistent with the materials design and with the results obtained by small strain analysis.

At 25°C the polyethyl acrylate network broke at a lower extension than the polymethyl acrylate one. Since the methyl acrylate sample is closer to its Tg value additional viscoelastic dissipation from Tg can explain the enhancement of mechanical properties in the polymethyl acrylate sample.

Since the Tg of methyl acrylate is about 35 °C higher than the Tg of ethyl acrylate it is interesting to compare uniaxial extension tests at similar T – T$_g$ values. Stress strain curves, at 25 °C for polyethyl acrylate (orange) and 60 °C for polymethyl acrylate (green) are plotted in Figure 12.
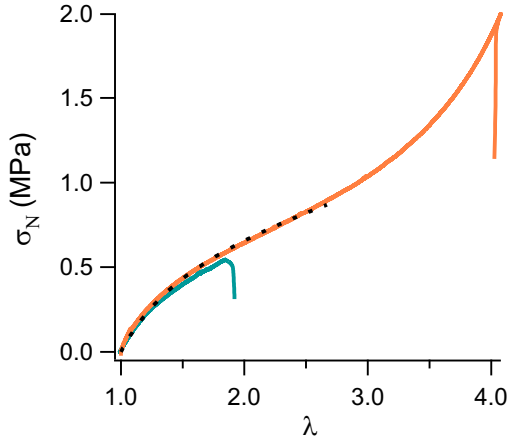
Figure 11: Nominal stress vs stretch curve at 25 °C, for SNEA (in green) and SNMA (in orange), Rubinstein-Panyukov fit in dotted line
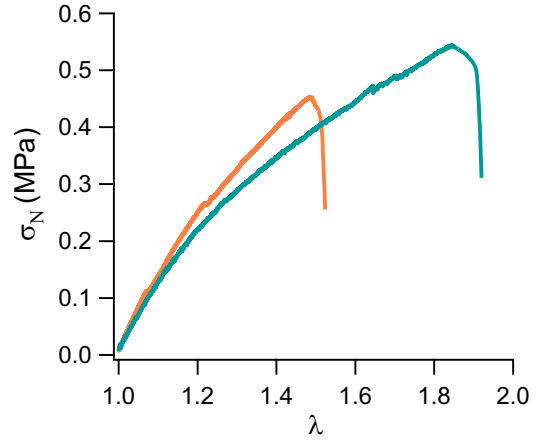
Figure 12: Nominal stress vs stretch curve for SNEA at 25 °C (in green) and SNMA at 60 °C (in orange)

At high temperature, samples broke in the clamps. The difference in the strain and stretch at break cannot give a reliable information in that case. However, the stress-strain behavior of polymethyl acrylate and polyethyl acrylate seemed more comparable.

The possible contribution of entanglements was also investigated.

Mooney and Rivlin developed a phenomenological model of elasticity to fit better the behavior of rubbers that display softening at intermediate strains. The Mooney stress is defined in Eq 7. (*4*).

$$\sigma_{Mooney} = \frac{\sigma_N}{\lambda - \frac{1}{\lambda^2}} = \left(2C_1 + \frac{2C_2}{\lambda}\right) \qquad \text{Eq 7.}$$

Where C_1 and C_2 are two adjustable parameters. In the absence of entanglements, $C_2 \sim 0$ and the Mooney stress is nearly constant. If a softening occurs in uniaxial tension, then $C_2 > 0$, in a simple unfilled rubber network, it suggests the presence of entanglements. If a hardening appears in uniaxial extension, then $C_2 < 0$, indicating the presence of pre-stretched chains.

Rubinstein and Panyukov have developed a molecularly based slip-tube model and solved a molecular model for non-linear elasticity of entangled polymer networks (*10*). The exact

solution in uniaxial extension is well approximated in the interval $0.1 < \lambda < 10$ by the analytical expression given in Eq 8.

$$\sigma_N = \frac{1}{3}\left(\lambda - \frac{1}{\lambda^2}\right)\left(E_x + \frac{E_e}{0.74\lambda + 0.61\lambda^{-0.5} - 0.35}\right) \qquad \text{Eq 8.}$$

The nominal stress vs stretch curves were fitted to this equation. Because of early breakage, the fit was only reliable for SNMA at 25 °C. The fit is represented in dotted lines on Figure 11.

The contribution of crosslinks can also be calculated, in theory, using the amount of crosslinker introduced, see Eq 9.. $E_{x,th}$ should be taken with a pinch of salt as transfer reactions occur.

$$E_{x,th} = \frac{3\rho RT}{M_{x,th}} \qquad \text{Eq 9.}$$

The theoretical contribution of crosslinks to Young's modulus $E_{x,th}$, the contribution of crosslinks E_x and entanglement E_e obtained by Rubinstein Panyukov fit, the sum of these two contributions $E_x + E_e$ and the experimental value of Young's modulus E_{exp} are all reported in the table below.

AT 25 °C	$E_{x,th}$(MPa)	E_x(MPa)	E_e(MPa)	$E_x + E_e$(MPa)	E_{exp}(MPa)
SNMA	0.9	0.7	0.7	1.4	1.5

The Rubinstein Panyukov fit gave a good estimation of the Young's modulus. The contribution of entanglement in the Young's modulus is equal to the one of crosslinks. We conclude that the effect of entanglements is not negligible in SNMA.

3.3 Multiple network properties

3.3.1 Small strain viscoelastic properties

3.3.1.1 Dynamic Mechanical Analysis (DMA)

The same monomer was used for the filler and the matrix networks. In this case, the multiple network architecture did not influence much the temperature dependence of the modulus. As represented Figure 13, the glass transition of the multiple network pre-stretched at λ_0=1.6 (dark green) is similar to that of the single network (light green). Not only the maxima are at the same temperature but also the width of the peaks are

comparable. The main difference detected is visible in Figure 14: storage and loss moduli of the multiple network, in the rubber domain, are higher than those of the single network. The modulus increases with the filler pre-stretching and entanglements. This result is consistent with previous work showing an increase of Young's modulus with λ_0 (6).
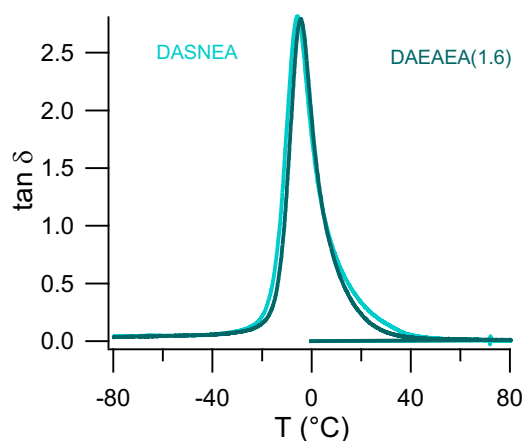
Figure 13: Evolution of tanδ with temperature, analyzed by DMA, for ethyl acrylate single (in green) and in a multiple network (in darker green)
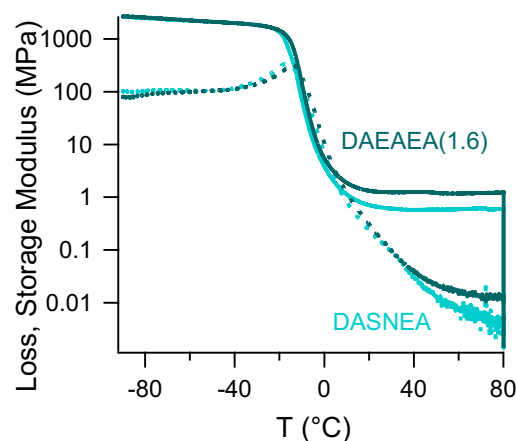
Figure 14: Evolution of loss (dotted line) an storage (solid line) moduli for EA single (in green) and multiple network (darker green)

A sample with different monomers in the filler and matrix networks is now analyzed. Figure 15 corresponds to Figure 9 with an additional curves in pink representing a multiple network with a filler network made of MA and a matrix of EA. Since the storage modulus presents only one inflection point, at -8 °C, we concluded that the two networks are mixed at a molecular level.
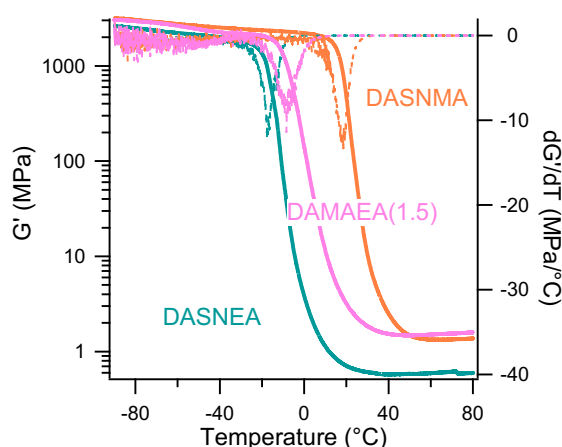
Figure 15: Evolution of storage modulus and its first derivative with temperature, analyzed by DMA, for EA (in green) and MA (in orange) single networks and a multiple network made of MA (filler) and EA (matrix) (in pink)

3.3.1.2 Time temperature superposition

As for single network, the master curves of G' and G'' were constructed from rheometer analysis. Results are plotted Figure 16 for SNMA (beige), a multiple network pre-stretched at 1.6 (MAMA(1.6) in orange) and a multiple network pre-stretched at a higher level of 2.4 (MAMA(2.4) in brown). As in the DMA analysis, the plateau value of G' in the rubber domain increases with the level of pre-stretching. For multiple networks, G' and G'' curves cross two times. G'' becomes higher than G'. An additional viscoelastic dissipation occurs close to Tg in multiple networks.
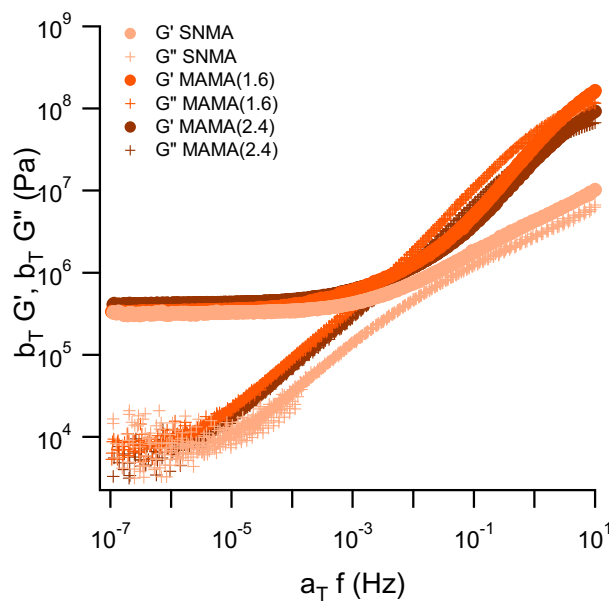
Figure 16: Master curve at 22 °C of G' and G'' for SNMA (beige) and multiple network made from it (darker curve for higher prestretching) as a function of frequency

3.3.2 Uniaxial extension

Figure 17 and Figure 18 represent the stress-strain curves of ethyl acrylate multiple network at 25 °C and methyl acrylate multiple network at 60 °C respectively. The level of pre-stretching, λ_0, is written near each curve.
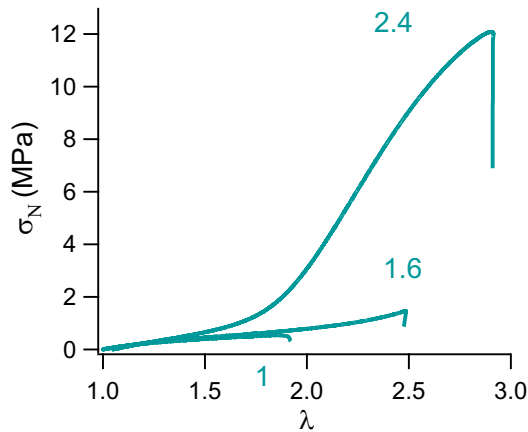
Figure 17: Stress-strain curves of multiple networks of EA at 25 °C, prestetched level noted by the curve
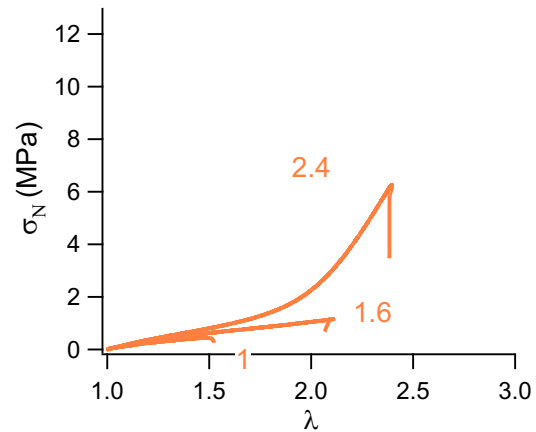
Figure 18: Stress-strain curves of multiple networks of MA at 60 °C, pre-stetched level noted by the curve

For both monomers, the behavior of multiple networks are in good agreement with Pierre Millereau's work(6):

- for $\lambda_0 = 1$, the single network is brittle
- for $\lambda_0 = 1.6$, a strain hardening phenomenon is observed, followed by a brittle fracture. The strain hardening increases the stress at break.
- for $\lambda_0 = 2.4$, the strain hardening occurs at lower λ and is followed by a slight softening. Permanent damages occurs in the bulk before breakage.

Figure 19 represents the evolution of the Young's modulus as a function of the degree of pre-stretching. For both monomers, the modulus increases with the filler pre-stretching. This result confirms the earlier small strain analysis.
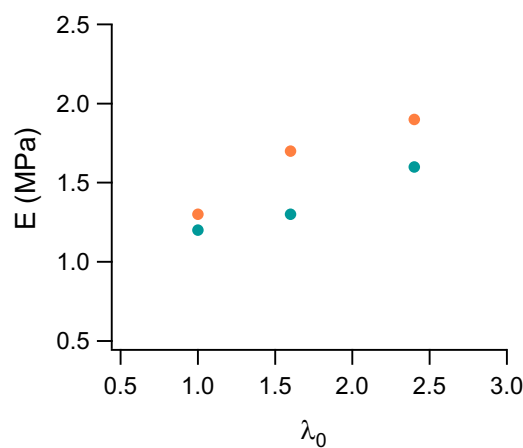
Figure 19: Evolution of Young's modulus with the degree of prestretching of the filler network for MA at 60 °C (in orange) and EA at 25 °C (in green) multiple network

Comparing the influence of the nature of the monomer, one can notice an earlier strain hardening in the polyethyl acrylate sample as shown in Figure 17 and Figure 18. As

discussed by P. Millereau (*6*) and E. Ducrot (*9*), the strain hardening is caused by the limit of extensibility of the polymer strands of the pre-stretched network. Materials were designed to have the same average molecular weight between crosslinks. The ethyl acrylate repeat unit has two carbons on the side chain and has a higher molar mass than the methyl acrylate one. The number of repeat units between crosslinks is smaller in the polyethyl acrylate sample. This is consistent with a strain hardening reached at lower stretch.

3.4   Influence of the mechanophore incorporation on mechanical properties

Mechano-fluorescent samples were tested and compared to reference samples (non mechano-fluorescent). The objective is here to investigate the influence of the mechanophore incorporation on the mechanical properties.

3.4.1   Small strain viscoelastic properties

Figure 20 represents the evolution of the storage and the loss modulus (in solid and dotted lines respectively) with temperature for a reference sample SNMA in red and for a mechano-fluorescent sample DASNMA in blue. The red and blue curves almost superimpose. In the rubber domain, the superimposition is complete. Figure 21 represents the evolution of tan δ with temperature for these two same samples. The width of the tan δ peaks are similar for both samples. There is no additional heterogeneity, at a DMA detectable scale, introduced with the mechanophore cross-linker.
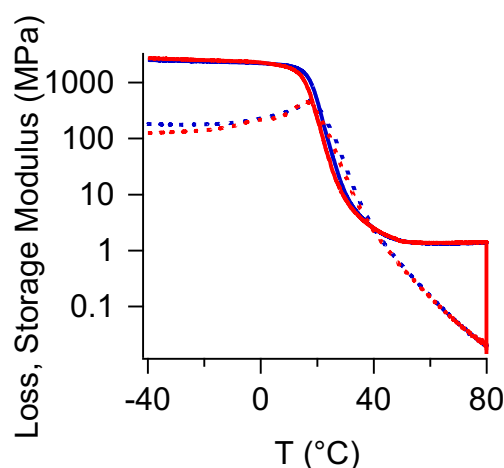
Figure 20: Storage (solid line) and loss modulus (dotted line) for a mechano-fluorescent sample (blue) and a reference sample (red)
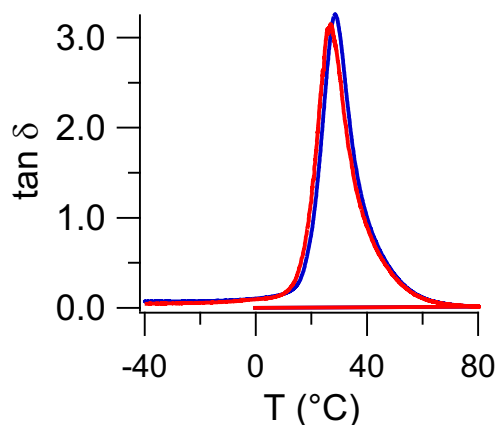
Figure 21: tan delta for a mechanofluorescent sample (blue) and a reference sample (red)

3.4.2 Uniaxial extension

Mechanical properties of mechano-fluorescent and reference samples were also tested in uniaxial extension. Figure 22 represents the stress strain curves of polyethyl acrylate single networks. The red curves correspond to two reference samples and the blue curves to two mechano-fluorescent samples. The four curves are not perfectly superimposed but are similar. Samples made by free radical polymerization are not completely reproducible. No significant differences between blue and red curve were noticed. The mechanophore introduction did not change the single network mechanical properties.

Figure 23 represents the stress strain curves of polyethyl acrylate multiple networks. The level of prestretching is written by each curve. Red curves and blue curves correspond to reference and mechano-fluorescent multiple networks respectively. The strain hardening occurs at the same level of stretch. The rupture is triggered by a flaw. Even if the mechano-fluorescent multiple network pre-stretched at 1.6 broke before the reference one, it is not the case for samples pre-stretched at 2.4. As for single network, we consider no mechanical property changes by the incorporation of mechanophore in the filler network.

It is clear from these curves that the presence of the Diels-Alder mechanophore does not change the elastic or the fracture behavior of the material, a necessary condition to be used as a label.
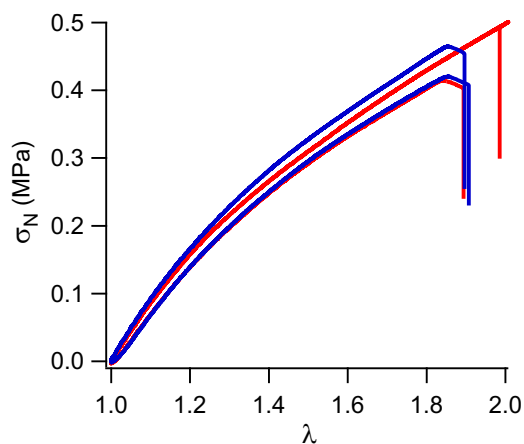
Figure 22: Stress-strain curves of single networks of EA mechanofluorescent (in blue) and non mechanofluorescent (in red) at room temperature
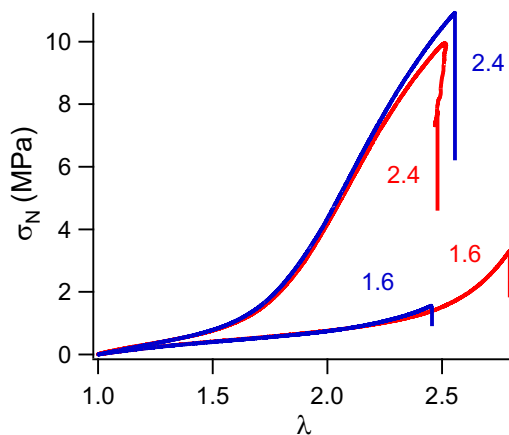
Figure 23 : Stress-strain curves of multiple networks of EA mechanofluorescent (in blue) and non mechanofluorescent (in red), prestretched levels noted by the curves

Conclusions

The mechanophore was synthesized by a 5-step reaction. Since the final product is not stable, the dihydroxy molecule, DACL4, was stored in the fridge and the last step was done just prior polymerization.

The mechanophore was chemically introduced in the single network as a cross-linker. Only 0.02 mol% of mechanophore was needed. From this mechano-fluorescent single network, multiple networks were synthesized by swelling polymerization steps. A summary of all materials investigated in this manuscript is given in the next page and at the beginning of the manuscript.

Small and large strain properties were tested by DMA, rheology and uniaxial extension. Methods and results were presented in this chapter. Multiple networks mechanical properties are consistent with prior work from Pierre Millereau (*6*). Indeed, we verified that the small strain properties were determined by the filler network. A higher level of pre-stretching of the filler network lead to a higher Young modulus. The pre-stretching of the filler network also influence the strain at which occurred the strain hardening.

Single and multiple networks were made from ethyl and methyl acrylate monomer. The polymethyl acrylate single network has a Tg close to room temperature (18 °C) and about 36 °C higher than the one of polyethyl acrylate (-18 °C). This difference in Tg leads to different mechanical properties at room temperature for these two families of materials.

The incorporation of the small amount of mechanophore cross-linker did not affect the mechanical properties. Indeed, the difference between a mechano-fluorescent sample and a reference sample is similar to the difference between two reference samples made from different polymerizations.

Materials investigated

Tables below summarize materials investigated and their mechanical properties. Molar percentages are relative to moles of monomer.

Single network

Name	Monomer	[HMP] (mol%)	[BDA] (mol%)	[DACL] (mol%)	[Total Cross-linker] (mol%)	[DACL] (mol.m^{-3})
SNEA	EA	1.16	0.50	0	0.5	0
DASNEA	EA	1.16	0.48	0.02	0.5	2.2
SNMA	MA	1.16	0.43	0	0.43	0
DASNMA	MA	1.16	0.41	0.02	0.43	2.8
SNMA$_{0.2}$	MA	1.16	0.22	0	0.22	0
DASNMA$_{0.2}$	MA	1.16	0.20	0.02	0.22	2.8

Multiple networks

Name	Type of MN	Filler monomer	Matrix monomer	ϕ_{SN}	λ_0	[DACL] (mol/m^3)	Network containing DACL
EAEA(1.6)	DN	EA	EA	0.2	1.6	0	/
DAEAEA(1.6)	DN	EA	EA	0.2	1.6	0.5	1st
EADAEA(1.6)	DN	EA	EA	0.2	1.6	0.9	2nd
DAMAEA(1.5)	DN	MA	EA	0.3	1.5	0.9	1st
MAMA(1.6)	DN	MA	MA	0.3	1.6	0	/
DAMAMA(1.6)	DN	MA	MA	0.3	1.6	0.7	1st
EAEA(2.4)	TN	EA	EA	0.07	2.4	0	/
DAEAEA(2.3)	TN	EA	EA	0.07	2.3	0.2	1st
EADAEA(2.5)	TN	EA	EA	0.07	2.5	0.3	2nd
MAMA(2.3)	TN	MA	MA	0.08	2.3	0	/
DAMAMA(2.3)	TN	MA	MA	0.08	2.3	0.2	1st
EAEA(3.1)	QN	EA	EA	0.03	3.1	0	/
DAEAEA(3.1)	QN	EA	EA	0.03	3.1	0.08	1st
EADAEA(3.2)	QN	EA	EA	0.03	3.2	0.1	2nd

Polyethyl acrylate mechanical properties at 25 °C

Name		ϕ_{SN}	λ_0	E (MPa)	σ_{break}	λ_{break}
SNEA	SN	1	1	1.2	0.5	1.9
EAEA(1.6)	DN	0.2	1.6	1.3	1.5	2.5
EAEA(2.3)	TN	0.07	2.3	1.6	12	3

Polymethyl acrylate mechanical properties at 60 °C (or 25°C when indicated)

Name		ϕ_{SN}	λ_0	E (MPa)	σ_{break} (MPa)	σ_{break} (MPa) at 25 °C	λ_{break}	λ_{break} at 25 °C
SNMA	SN	1	1	1.3	0.4	2	1.5	4
MAMA(1.6)	DN	0.2	1.6	1.7	1	8	2.1	3.5
MAMA(2.3)	TN	0.08	2.3	1.9	6	14	2.4	3.2

References

1. R. Göstl, R. P. Sijbesma, π-extended anthracenes as sensitive probes for mechanical stress. *Chem. Sci.* **7**, 370-375 (2016).
2. J. E. Mark, *Polymer data handbook*. (1999).
3. Y. Chen*, P. R. University, Ed. (2018).
4. M. Rubinstein, R. H. Colby, *Polymer Physics*. (2003).
5. E. Ducrot, Y. Chen, M. Bulters, R. P. Sijbesma, C. Creton, Toughening Elastomers with Sacrificial Bonds and Watching Them Break. *Science* **344**, 186-189 (2014).
6. P. Millereau, Large Strain and Fracture of Multiple Network Elastomers (Doctoral dissertation) UPMC (2017).
7. P. Millereau *et al.*, Mechanics of elastomeric molecular composites. *Proc Natl Acad Sci U S A*, (2018).
8. M. L. Williams, R. F. Landel, J. D. Ferry, The Temperature Dependence of Relaxation Mechanisms in Amorphous Polymers and Other Glass-forming Liquids1. *J. Am. Chem. Soc* **77**, 3701 (1955).
9. E. Ducrot, Innovative tough elastomers: Designed sacrificial bonds in multiple networks (Doctoral dissertation) UPMC (2013).
10. R. Michael, P. Sergei, Elasticity of Polymer Networks. *Macromolecules* **35**, 6670-6686 (2002).

Chapter 3

Detection and mapping of
bond scission in
multiple network elastomers
using confocal microscopy

Chapter 3: Detection and mapping of bond scission in multiple network elastomers using confocal microscopy

Introduction

Fracture of multiple networks elastomers has already been investigated by mechanochemistry in our lab. Etienne Ducrot incorporated a dioxetane mechanophore into multiple network elastomers (*1*). He proved that the toughening mechanism of multiple network elastomers relies on energy dissipation due to bond breakage of sacrificial pre-stretched chains inside the materials. Qualitatively, he showed that an increase in the degree of pre-stretching of the chains in the filler network leads to a larger dissipative volume ahead of the crack tip. As the mechanophore emits light upon breakage, dynamic information on bond scissions was obtained. However, the signal remains low and noisy. In order to obtain a good signal over noise ratio, the experiment needs to be done in a completely dark room. Despite this precaution, the signal suffers from poor spatial resolution. In fact, high magnifications cannot be achieved since the location of crack propagation is not predictable. A calibration of the dioxetane activation by heating has been done by Clough and co-workers (*2*). Nevertheless, the low signal makes it challenging to implement this calibration method to our materials for signal quantification. Moreover, the 6 step-synthesis mechanophore required specific competences and equipment for handling bromine or for the dioxetane ring formation (*3*). As the mechanophore undergoes one reaction before it is consumed, the photon emission is a one-shot event difficult to record. Due to these limitations, we chose to use the π-extended anthracene mechanophore (*4*) for its numerous advantages presented in Chapter 1 .

In the previous chapter, the synthesis of mechano-fluorescent materials and the characterization of their mechanical properties were presented. In this chapter, the method we developed to map bond scission and its added value, are demonstrated. In order to investigate the effect of the degree of pre-stretching of the filler network, all methods are applied to two specific ethyl acrylate based multiple networks with two different levels of pre-stretching of the filler network: about 1.6 for double networks and about 2.5 for triple networks.

First, crack propagation experiments are performed to provide important context to the fracture images. Then, the customized device, a laser scanning confocal macroscope which can be combined with a tensile stage controller, will be introduced. Initiation and

propagation of a crack can be explored by this new tool. Finally, the strategy to calibrate the fluorescence signal is discussed and applied to multiple network systems in order to analyze quantitatively the influence of the degree of pre-stretching of the filler network.

1 Mechanical analysis of fracture

1.1 Crack propagation test

1.1.1 Experiment

Crack propagation tests were performed on standard tensile Instron machines, model 5565 or 5965. The set up was described in Chapter 2. Samples of dimensions 5 mm x 25 mm were cut. The thickness was defined by the sample itself (from 0.5 to 2 mm). A 1 mm notch was introduced by using always a new very sharp razor blade, as shown Figure 1, to obtain as little bulk damage as possible. The actual length of the initial notch was measured from a picture of the sample with a ruler using ImageJ. Two white marks were drawn 5 mm from the notch. The sample was fixed using pneumatic clamps. During the test, an extensometer tracked and recorded the deformation between these two marks. Force and deformation were measured until failure of the sample.
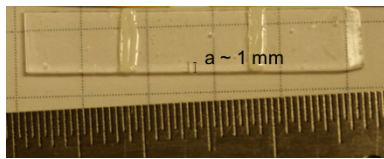
Figure 1: Picture of a sample before crack propagation test, with a the size of the initial notch and white dots for the extensometer
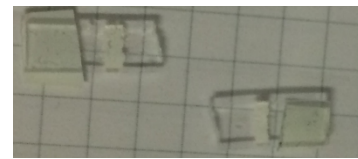
Figure 2: Picture of a sample after crack propagation test

The temperature was controlled at 25 °C by an oven connected to liquid nitrogen. The crosshead velocity was 50 μm.s^{-1}.

At the end of the crack propagation test, broken samples were collected as shown in Figure 2. Samples were then kept in the fridge (in the dark at 5 °C).

1.1.2 Fracture energy estimation

1.1.2.1 Calculation of the energy release rate and fracture energy

Greensmith proposed an empirical expression to determine the energy release rate $\mathcal{G}$ based on experiments made on a single edge notch geometry with a crack length, a, that is smaller than the sample thickness Eq 1.(*5*).

$$\mathcal{G} = 2 \times C \times W(\lambda) \times a \qquad\qquad \text{Eq 1.}$$

where C is a strain dependent empirical correction associated with the lateral contraction of the sample in extension estimated by Eq 2. and $W(\lambda)$ is the strain energy per unit volume and is typically obtained from the stress-strain curve of an un-notched sample of identical dimension.

$$C = \frac{3}{\sqrt{\lambda_c}}$$ Eq 2.

When $\lambda = \lambda_c$, the crack starts to propagate and the energy release rate $G = \Gamma$, where Γ is the fracture energy.

By combining Eq 1.and Eq 2. and applying the crack propagation criterion, the fracture energy can be estimated by Eq 3.

$$\Gamma_{exp} = \frac{6\,W(\lambda_c)a}{\sqrt{\lambda_c}}$$ Eq 3.

1.1.2.2 Results

Black curves in Figure 3 are examples of stress strain curves of notched sample of a single network made of polyethyl acrylate. The reproducibility between these two samples is poor. The notch was introduced by hand with a razorblade. Initial notches were not identical, explaining the poor reproducibility in crack initiation.
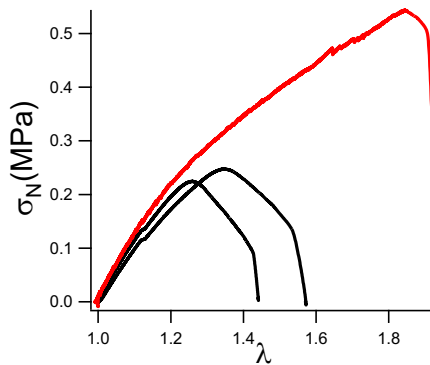
Figure 3: Stress-strain curves obtained for notched (black curves) and un-notched (red curve) sample of SNEA
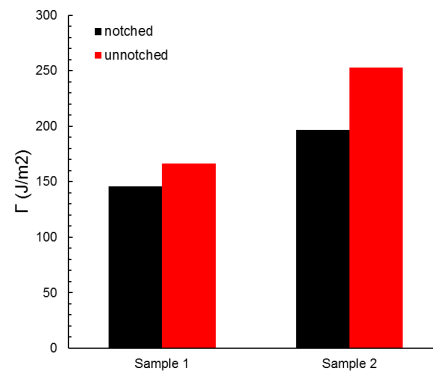
Figure 4: Fracture energy calculated using Greensmith formula with the notched (black) and un-notch (red) curves

The fracture energy is calculated using the Greensmith's formula, with the elongation at break, λ_c, taken as the maximum of the stress strain curve. $W(\lambda_c)$ is typically obtained by calculating the area under the curve up to λ_c of the stress-strain curve of an un-notched

sample. The strain stress curve of the un-notched sample is represented in red in Figure 3. Crack propagation tests were performed at different crosshead velocities and temperature conditions. The un-notched stress strain curve depends on these conditions and has to be measured for every set of conditions.

The calculation of the fracture energy estimated from the integral to λ_c under the notched or un-notched stress-strain curves are compared in Figure 4. As the reproducibility between two samples is poor, the difference between the two ways of calculation is about the same as the difference between two samples. To conserve material and optimize experimental efficiency, the fracture energies were estimated directly from the notched stress strain curve. This will lead to an under estimation of the fracture toughness for all conditions, but the relative comparisons will remain consistent.

1.2   Influence of the level of filler network pre-stretching

Crack propagation tests were performed on multiple network, made of ethyl acrylate, with different levels of pre-stretching of the filler network. Reference and mechano-fluorescent multiple networks synthesis was presented in Chapter 2 Section 2. Their name; type (double DN or triple TN network); fraction of filler network, ϕ_{SN}; level of prestretching, λ_0 and concentration of mechanophore incorporated in the filler network, [DACL], are summarized in Table 1:

6 samples tested	Type of MN	ϕ_{SN}	λ_0	[DACL] (mol.m^{-3})
EAEA(1.6)	DN	0.2	1.6	0
DAEAEA(1.6)	DN	0.2	1.6	0.5
DAEAEA(1.6)	DN	0.2	1.6	0.5
EAEA(2.4)	TN	0.07	2.4	0
DAEAEA(2.4)	TN	0.07	2.4	0.16
DAEAEA(2.6)	TN	0.06	2.6	0.13

Table 1: Multiple network elastomers tested on crack propagation test

The stress strain curves obtained during the crack propagation test on these six samples are shown in Figure 5.

As expected mechanical properties changed with the pre-stretching of the filler network. The stress at break is much higher for the more pre-stretched multiple network. However, the elongation at break is similar. The fracture energy Γ was calculated using the Greensmith's formula (Eq 3.) The fracture energy was plotted as a function of the pre-stretching, as shown Figure 6. The fracture energy is an increasing function of λ_0. This result is in good qualitative and quantitative agreement with the work done by Pierre Millereau (*6*).
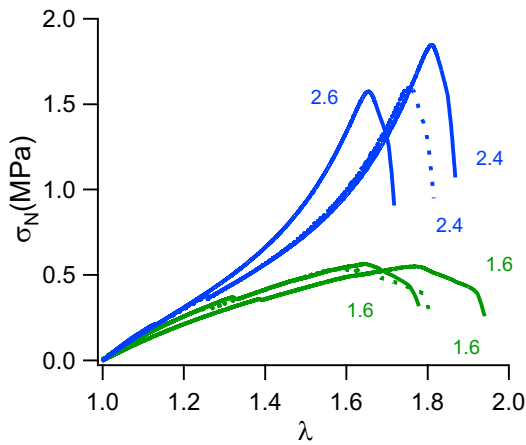
Figure 5: Strain stress curves of crack propagation test on double network (green) and triple network (blue). λ_0 is written by each curve. Dotted lines referred to non-mechanofluorescent samples.
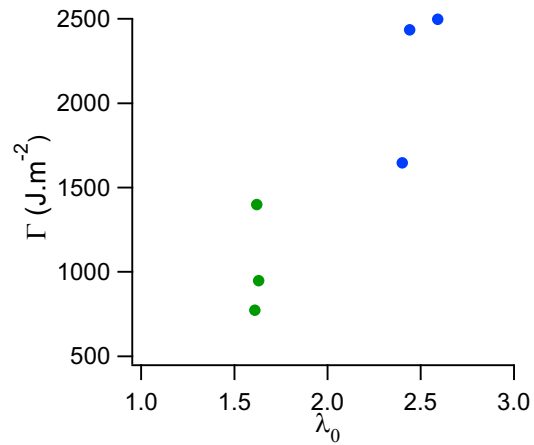
Figure 6: Evolution of the fracture energy with the level of prestretching of the filler network.

The maximum of the stress strain curves was identified as the crack initiation. The following decrease of the nominal stress with increasing elongation corresponds to the propagation of the crack. As the loading rate was constant, the end of the curve illustrated the time of breakage. In order to compare this time of crack propagation through the sample, the maximal stress was normalized by the maximum value for each sample. The time was set to zero for the maximal nominal stress. The rescaled curves are represented in Figure 7. The propagation time was clearly longer for double network than for triple network. This result is in good agreement with P. Millereau analysis (*6*): for $\lambda_0 < 2$ the time to propagate is longer than for $2 < \lambda_0 < 3$. He also found that for $\lambda_0 > 3$ the time to propagate increases again, but this case is not studied here.
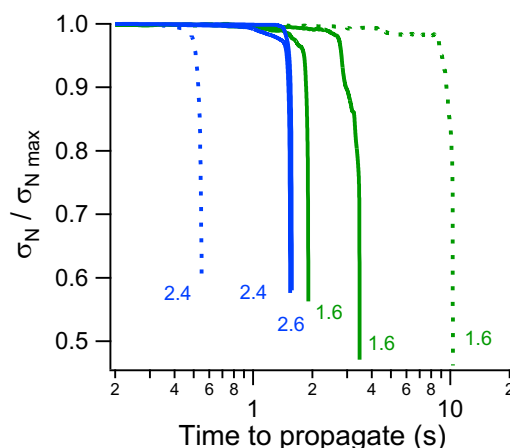
Figure 7: Time for the crack to propagate in double (green) and triple (blue) network. Dotted lines referred to non mechano-fluorescent samples, λ_0 is written by each curve.

In the less pre-stretched multiple networks, the crack initiation occurred at lower stress values and crack propagation was slower than for the more pre-stretched one. A more pre-stretched filler network delayed the initiation but once it was initiated, it led to a fast propagation.

1.3   Direct observations of crack growth

1.3.1   Method

Before any fluorescence observations were made, and in order to have an idea on how the crack propagated, crack propagation tests of materials without mechano-fluorescent molecules were filmed using a camera and different objectives.

First, the best method to notch the sample was investigated. Strips of 5 mm width were cut using a puncher. They were divided into 20 mm to 25 mm long samples. Cutting mechano-fluorescent samples with a blade leads to damage and irreversible fluorescence activation. The notch should be introduced with care in order to limit the amount of initial damage. Different methods were tested. The best option was to notch the sample, at room temperature, with a new razor blade, making sure that the cut was as uniform through the thickness as possible. Once the razor blade touched the sample, it was scratched even if it was not visible with the naked eye. A ~1 mm notch was introduced in one movement.

The notched sample was clamped on a Deben Microtest tensile stage controller (model 200N tensile tester). A single edge fracture test was performed at 0.1 mm/min crosshead

velocity. Videos were recorded during the test using two cameras (VLG-20M Baumer). One camera was recording the side view of the test where the crack propagation was visible. The other camera was focused inside the notch, to record what happens in the open crack. A drawing identifying the side view and the open crack view is given Figure 8a. Side view videos were recorded with a 110 mm VS-TCH05-110 objective from Vital Vision. Inside crack videos were also recorded with two objectives: a 110 mm, x0.5, VS-TCH05-110 from Vital Vision and a 110 mm, x3, VS-TCH3-100 from Vital Vision. Examples of picture taken from the side and open crack views are shown Figure 8b and Figure 8c respectively.
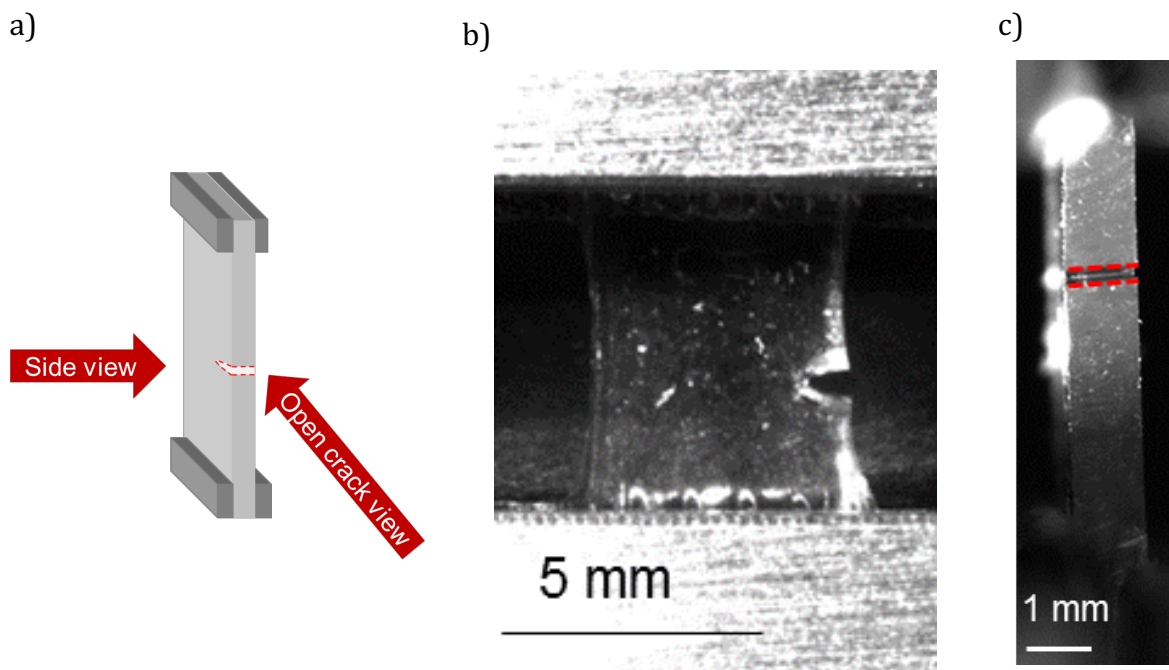
Figure 8: Schematic representation of the side and the open crack views (a) and example of the side (b) and open crack (c) views

1.3.2 Influence of the degree of pre-stretching of the filler network

Images and videos were recorded from the side and inside the crack during crack propagation tests. In addition to the two multiple networks: double EAEA(1.6) and triple EAEA(2.3), pictures of a single network, SNEA, are also shown to compare with a non-toughened material.

For the single network, the propagation was 'smooth'. The crack front is clearly visible as a nearly straight line in Figure 9a and in Figure 9b. However in multiple networks, the

crack propagated with bifurcations, as shown in Figure 9d,g and Figure 9e,h at higher magnification. Many micro-cracks were initiated at the same time and a fibril-like structure was formed, stretched up to a point where fibrils break and the crack front propagates. These structures are not strictly independent fibrils because the structures were not surrounded by air; the filaments were still connected to the crack tip. In our study, we refer to these fibril-like structures as crack bifurcations. These crack bifurcations cost energy, contributing to the material fracture toughness.

On Figure 9d and Figure 9e, from EAEA(1.6), no clear crack front was distinguishable. Numerous bifurcations lead to a three dimensional diffuse crack front. On Figure 9g and Figure 9h, from EAEA(2.4), despite crack bifurcations, a crack front was still distinguishable.

Figure 9c, Figure 9f, Figure 9i were taken from the side during crack propagation. The crack front appeared more diffuse for EAEA(1.6), while it was not the case for the multiple network with the highest level of pre-stretching, EAEA(2.4).

For both multiple networks, large and heterogeneous fibrillar deformation occurred before crack propagation and based on previous work, bond scission in the filler network also occurs (*1*). However, from these direct observations, it seems that the mechanisms of crack propagation are different.

By breaking bonds of the filler network, a damaged multiple network is created in front of the crack tip. The crack has to propagate through this damaged material and its properties will influence the way the crack can propagate. The degree of pre-stretching of the filler network and its dilution, influence the way it damages at the crack tip and of course the mechanical properties of the damaged material.

Another important observation is that material failure is clearly a 3D phenomenon and cannot be reduced to a 2D side view problem with a well defined crack plane.

From these crack propagation tests and crack propagation observations, the objective was to extract information on bond scissions. The method designed to achieve this goal is presented in the next section.
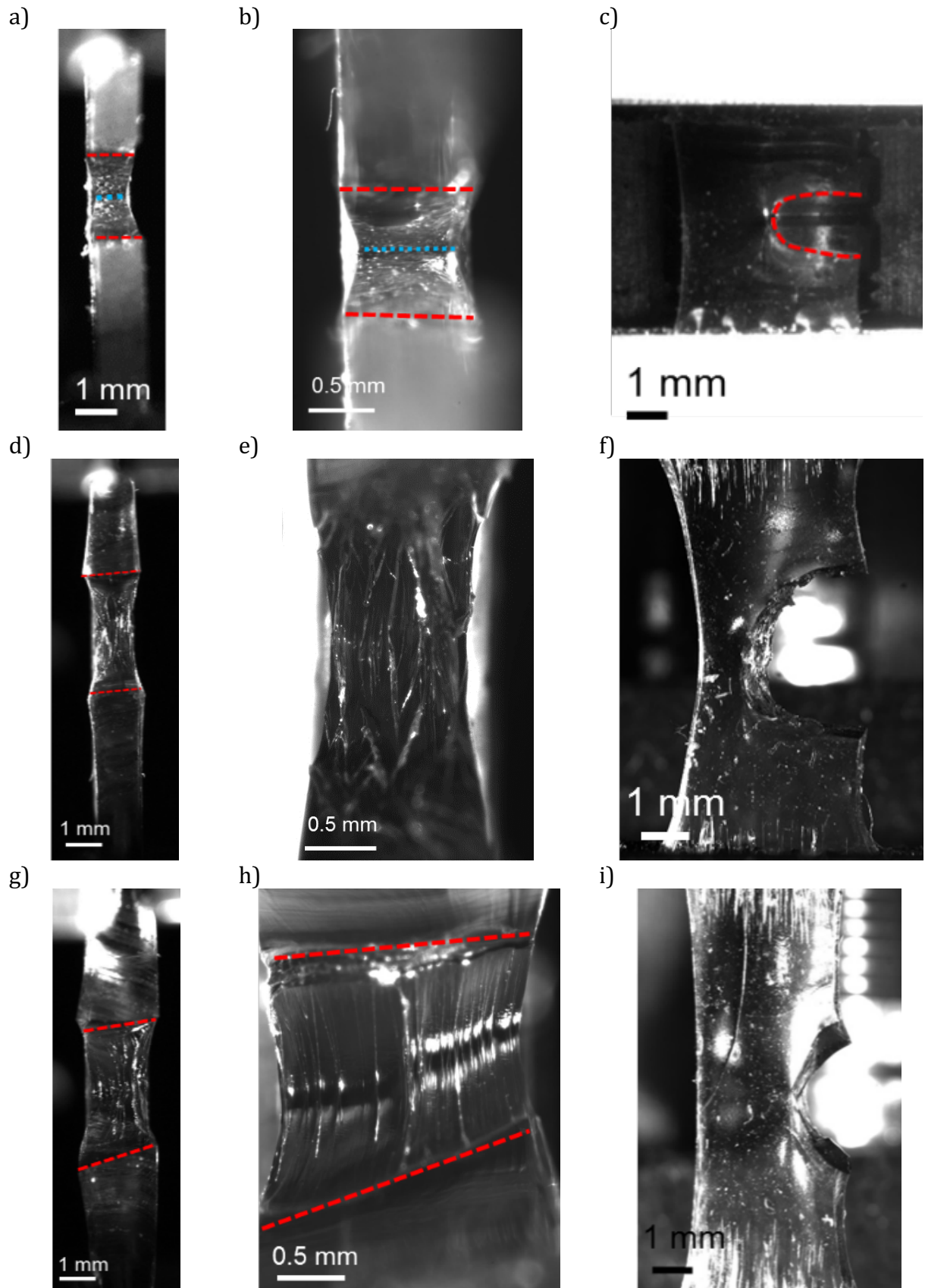
Figure 9: Images of crack propagation test for a single network SNEA a,b(inside crack view), c (side view) and for two EA multiple networks with different level of prestretching. λ_0=1.6 (d, e, inside crack view) and f (side view) and λ_0=2.3 (g, h (inside crack view) and i(side view). The red dashed lines show the crack edges and the blue dotted lines represent the crack front.

2 A new method for damage analysis

2.1 A strategy based on fluorescence activation

As presented in Chapter 1 and shown in Figure 10, the mechanically driven retro Diels-Alder reaction releases a fluorescent moiety. The strategy here was to use the fluorescence activation as a probe for chain scission. When the mechano-fluorescent multiple network is sufficiently stretched, damage occurs; the polymer chains break, leading to (an assumed) proportional breakage in mechanophores and subsequent fluorescence, as shown in Figure 11.
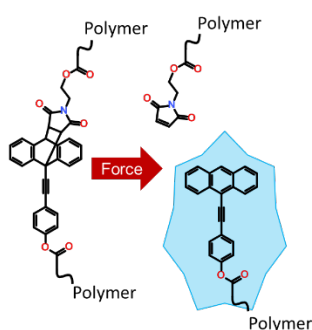
Figure 10: Schematic representation of mechanophore activation by retro Deals-Alder reaction
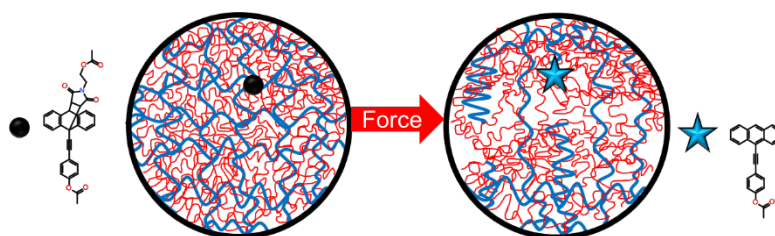
Figure 11: Schematic representation of mechanophore activation in a multiple network. The blue and red networks represent the filler and matrix networks respectively.

2.2 Laser Scanning Confocal Microscope (LSCM)

2.2.1 LSCM generalities

The Laser Scanning Confocal Microscope (LSCM) is a fluorescence microscope that allows an image to be extracted from a single focal plane (*7*). The principle of use is represented in Figure 12. A laser beam is focused through an objective lens and directed to the focal plane (in purple on the drawing), exciting any fluorochrome molecule in the path of the light. Excited fluorochrome reemits light by fluorescence at another wavelength, represented in blue (the fluorescence principle was presented in Chapter 1). The key specificity of the confocal microscope is a pinhole placed in front of the detector that eliminates out-of-focus light, resulting in a picture of the light coming from the focal plane only.

To optimize the visualization, three parameters can be adjusted: the laser intensity, the detector gain and the pinhole size. The power intensity of the laser can vary from 0 to 100 %. As the laser intensity increases, more fluorophores are excited, which generally results in a brighter image. However, a high laser intensity can cause unwanted photobleaching (phenomenon explained in Chapter 1). The detector gain amplifies the light signal, which also helps in brightening the image at a cost of a higher noise level. The pinhole diameter determines the confocality of the image; a smaller pinhole leads to a thinner focal plane and better axial resolution. To obtain high quality images, the laser intensity should be as high as possible without damaging the sample and photobleaching the fluorophores and the detector gain should be high enough without introducing too much noise. The pinhole diameter was kept at its minimum value, 20 μm for the LSCM used.
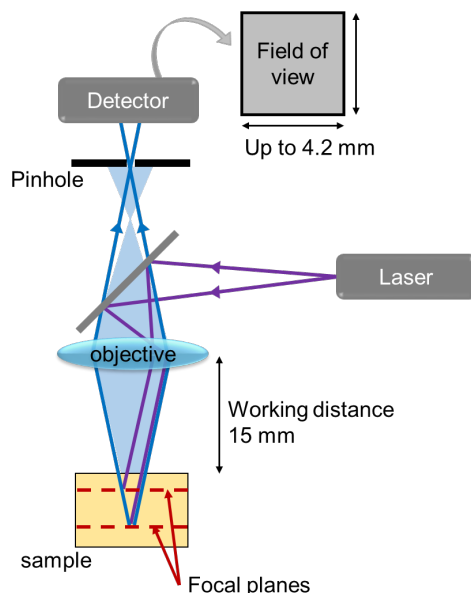
Figure 12: Schematic representation of LSCM working principle

With the LSCM, 2D pictures inside transparent materials can be recorded, which are referred to as single optical sections. Fluorescence was recorded at an image size of 512x512 with each pixel containing 12-bit digital units (intensity from 0 to 4096 a.u.). The pixel size depends on the magnification used. Note that optical sections have an associated thickness. Pixels of these images are called voxel (contraction of volume and pixel). This detail will be discussed in subsequent sections.

An advantage of the LSCM is the possibility to reconstruct three-dimensional images by stacking optical sections along the optical or z axis. To obtain reliable 3D images, adjacent optical sections are overlapped by one-third of the thickness of the optical section.

2.2.2 Customized set up

All LSCM pictures were taken with a Nikon AZ-100/C2+ confocal macroscope customized to our purpose. The objective used was an AZ Plan Fluor 5x, with a focal length of 15 mm. The objective was not inverted and can zoom from 1x to 8x. Using a Laser Scanning Confocal Macroscope instead of a Laser Scanning Confocal Microscope had three important consequences.

1. The field of view is larger than for classical LSCM. With a maximum of 4.2 mm x 4.2 mm, an overall visualization of the crack is possible.
2. The long working distance leaves room to incorporate a tensile test device into the stage.
3. The size of each voxel is larger than for a conventional LSCM limiting spatial resolution.

Four excitation wavelengths were available: 405 nm, 488 nm, 561 nm, 640 nm. For the fluorescent molecule used, a maximum of absorption was detected at 400 nm (details and spectra in Chapter 2). Thus, the 405 nm laser was used and the emission signal was recorded from 450 nm to 550 nm.

Thanks to a collaboration with the *Institut Pierre-Gilles de Gennes (IPGG),* we also had access to a classical Leica Laser Scanning Confocal Microscope SP8. Magnifications 10x, 20x, 40x and 63x were available. One major difference between the two LSCM is that the Leica LSCMicroscope has inverted objectives and the Nikon LSCMacroscope has not inverted ones. Also, to reach high resolution, the Leica LSCMicroscope 40x and 63x objectives are oil objectives (10x and 20x are dry). The working distance depends on the objective and is reduced in the Leica LSCMicroscope: 11 mm at 10x, 620 μm at 20x, 240 μm at 40x and 140μm at 63x. For these reasons, the Leica LSCMicroscope cannot be combined with the tensile test device. It was useful to confirm 'post mortem' qualitative analysis obtained from Nikon LSCMacroscope (describe in a later section).

All the study and quantitative analysis were performed with the Nikon LSCMacroscope only.

2.2.3 Fluorescence visualization

2D pictures were saved as uncompressed tiff files. Fluorescence was recorded in 12-bit digital units. Images were opened with ImageJ as a grayscale image and an example is given Figure 13a. A lookup table was used to better visualize intensity contrast. Figure 13b corresponds to the same image but re-colored using the 'fire lookup table'. Another way to highlight intensity contrast was to use surface intensity plot. X and Y axis were unchanged. Intensity level was plotted along the Z axis. The surface intensity plot of the same picture is given Figure 13c.
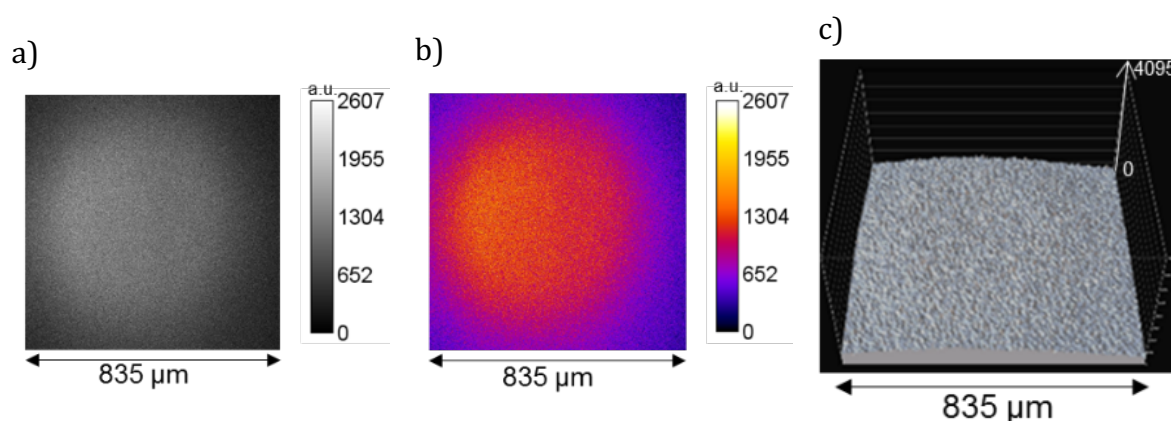
Figure 13: Fluorescence visualization: a grayscale image (a), with a lookup table (b), as a surface intensity plot (c)

In the manuscript, 2D images will be presented as re-colored images and surface intensity plots.

2.2.4 Limitations
2.2.4.1 Vignetting

Vignetting is a classic phenomenon in optics, inherent to each lens design. It corresponds to a radial and gradual darkening toward the corners, also called shading. Three types of vignetting exist: natural, optical and mechanical. Natural vignetting is caused by light reaching different locations on the camera sensor at different angles. Optical vignetting is

linked to intrinsic lens design. Mechanical vignetting is caused by objects physically blocking light in front of the lens. In photography, vignetting is used to put emphasis on the subject, in the middle of the picture. However, it is undesirable for quantitative analysis. A lens shows the most vignetting at its widest aperture. The maximum aperture of zoom lenses changes with the zoom. The widest aperture corresponds to the widest zoom setting. For the LSCM and objective used, the vignetting was particularly important at 1x (mechanical, optical and natural vignetting). Figure 14 is a re-colored image of a calibration sample taken at a magnification of 1x. Calibration samples are labelled as 1st and 2nd generations and will be described later in this chapter. A large field of view is used with moderate vignetting (only natural and optical), which corresponds to a magnification of 5x. Figure 15 represents a re-colored image of the same calibration sample taken at magnification 5x.
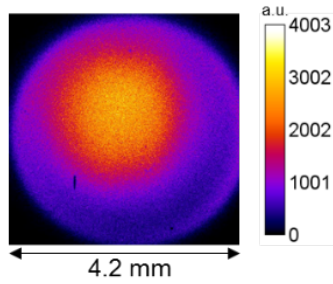
Figure 14: Re-colored image of a calibrating sample at 1x magnification
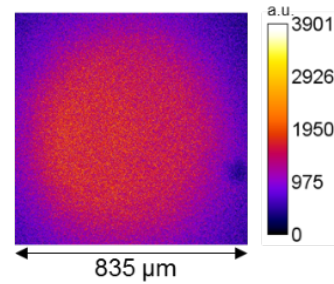
Figure 15: Re-colored image of a calibrating sample at 5x magnification

Josh Yeh, a post-doc involved in the ERC project, developed a procedure to correct vignetting. If an image has a hypothetically constant illumination, then the intensity should be the same at all pixel positions. If the illumination is not constant across the field of view due to vignetting, then a non-flat field is obtained. This shading was measured and corrected using the method developed by Young and Model (*8, 9*). From their method, the corrected intensity I_{corr} is given by Eq 4.

$$I_{corr} = \frac{I_{original} - gain_{noise}}{I_{flat\ field} - gain_{noise}}$$

Eq 4.

Where $I_{original}$ is the original intensity from the raw picture to be analyzed, $I_{flat\ field}$ is the flat field intensity from a picture of a homogenous sample and $gain_{noise}$ is the electric noise from the detector gain.

For a low detector gain the noise is negligible ($gain_{noise} \sim 0$) and corrected intensity is simplified to Eq 5.

$$I_{corr} \approx \frac{I_{original}}{I_{flat\ field}} \qquad\qquad \text{Eq 5.}$$

A picture of a sample with a homogenous fluorescence (2nd generation calibration sample, described in a following section) was recorded in order to measure shading as shown in Figure 16. The recorded image of the homogeneous sample was surface fitted, as represented Figure 17. From Eq 5., images are then divided by the surface fit to get the corrected images.

An overcorrection was noticed on the picture corners. For quantitative analysis, only the reliable and central part of the picture was kept. In order to discard corners, iso-intensity curves were plotted on the calibration picture, Figure 18 obtained from Figure 16. An intensity threshold was defined above which information in the center of the picture seemed reliable (for example, 0.4 in red on the Figure 18). Information below that threshold was removed in order to discard overcorrected corners.
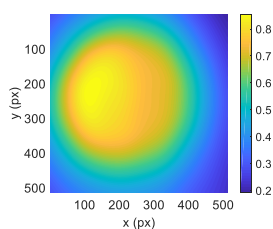
Figure 16: Re-colored image of a calibrating sample to measure shading
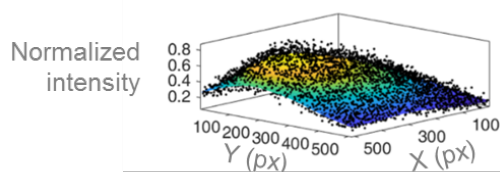
Figure 17: 2D surface fitting the shading
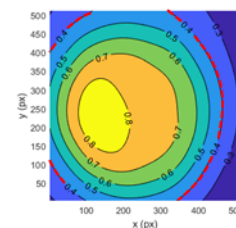
Figure 18: Iso-intensity curves on a re-colored image of a calibrating sample

I have also noticed that the pinhole position influences the flat field correction. During my PhD, the pinhole position was not exactly identical for all sets of measures. Calibration samples need to be imaged for every new set of experiments.

2.2.4.2 Distortion

Another classical phenomenon in optics is distortion. Straight lines do not appear straight on the image. An Argo-LM reference slide was bought from Argolight. This quality control tool consists of a special glass substrate in which different fluorescent patterns are embedded. The patterns are accurately positioned and stable. A field of patterns, depicted in Figure 19a was used to correct the x-y distortion. It consists in a matrix of 49 x 49 markers, separated by 50 µm, on a 2500 x 2500 µm area. A single optical section

of the marker pattern was collected. A MATLAB function developed by Josh Yeh identified the markers, as represented Figure 19b, and corrected the distortion when the markers were not equidistant, as shown Figure 19c. Each pixel was then displaced to its corrected location. A data binning process was applied in order to get back an equidistant grid of 512 x 512 pixels. The data binning consisted in calculating mean values in a small square region, called a bin. The bin corresponded to a 'new' pixel. The dimension on the bin was fixed at 2 µm x 2 µm. The bin size was set to be slightly larger than the original pixel size (1.63 µm), to prevent artifacts from appearing in the post-binned image.
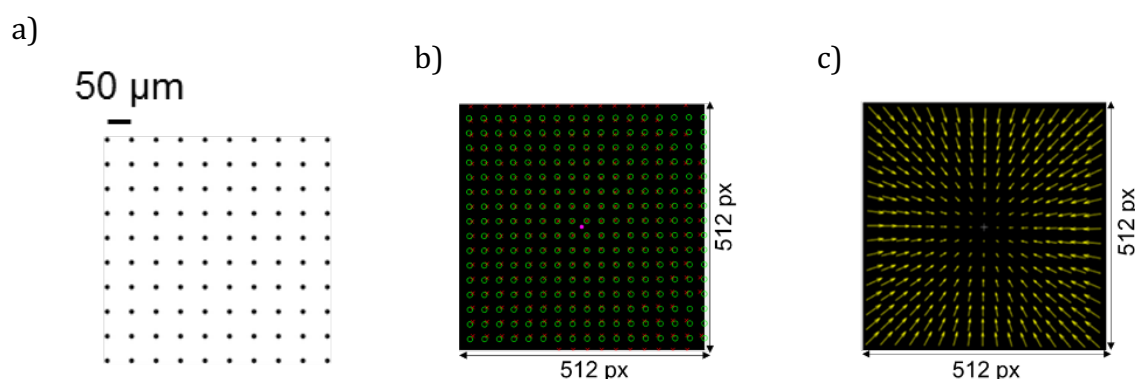
Figure 19: a) 2D marker array in the Argo-LM reference sample b) Marker detection c) X-Y distortion

2.2.4.3 Spatial resolution

In LSCM, the z-resolution is lower than the lateral resolution. The image z-resolution is approximately set by the step size. The x- and y-resolutions are approximately set by the pixel size.

The Nikon AZ-100/C2+ confocal macroscope has a magnification from 1x to 8x, the maximal pixel size is 8.15 µm and the minimal pixel size is 1.02 µm. 512 x 512 px images are recorded, corresponding to 522 µm x 522 µm to 4.2 mm x 4.2 mm images.

Magnifications at 5x resulted in limited optical aberration. At that magnification, the optical sectioning was 12.04 µm and the voxel size was 1.63 µm x 1.63 µm x 12.04 µm. After distortion correction and data binning, the voxel size was 2 µm x 2 µm x 12.04 µm.

This method gives a signficantly higher resolution than the previous method used for chemiluminescence detection by Etienne Ducrot (*1*) and Pierre Millereau (*10*) in our laboratory.

2.2.4.4 Absorption through thickness

The point spread function (PSF) is the intensity distribution collected on the image plane for a small point source. The PSF intensity profile decreases with the penetration depth (*11*). A fluorescent sample (2nd generation calibration sample) was imaged at different penetration depths. Figure 20a to d represent the re-colored 2D-images from a penetration depth of 50 to 200 µm (50 µm step). For each image, the mean fluorescent intensity was calculated and plotted as a function of the materials depth, Figure 21. An intensity decrease can be observed. For quantitative analysis the penetration depth was an important parameter. 2D-images were always recorded at 100 µm penetration depth. Calibration curves (presented in a following section) were plotted and used only for that penetration depth.
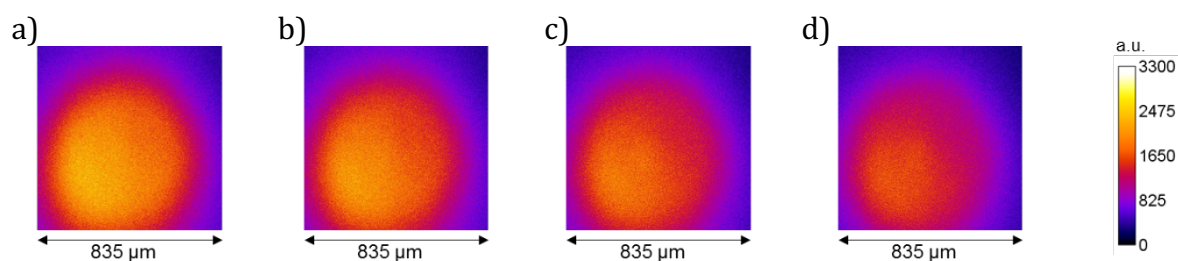
Figure 20: Re-colored 2D-image of a fluorescent sample at 50 µm (a), 100 µm (b), 150 µm (c) and 200 µm (d) penetration depth
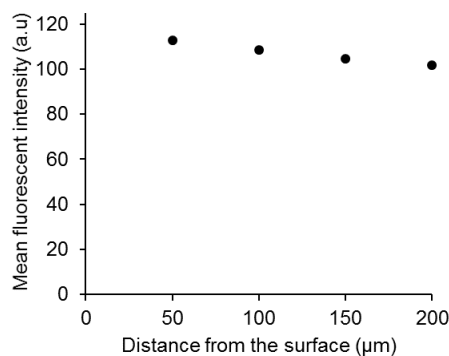
Figure 21: Fluorescent signal decrease with depth

2.2.4.5 Refractive index mismatching

Another limitation in optics is the refractive index mismatch between the sample and medium crossed by the light before reaching the sample. At the interface, light is diffracted. In a perfect lens without aberration, the PSF of a point is a sphere. In practice, axial and lateral aberrations spread the sphere into a broad and asymmetric PSF. Axial (horizontal) refractive index mismatch leads to a progressively broadening of the PSF along the optical axis, as represented Figure 22 (*11*). The grey rectangle represents the sample with a higher refractive index than the surrounding air. Purple lines represent light rays. In the case of a lateral (vertical) refractive index mismatch, only half of the illuminating cone is affected, as represented Figure 23 (*12*). Light refracted is not focused and leads to a PSF distortion. These effects increase with the depth.

The refractive indexes of poly ethyl acrylate and poly methyl acrylate are 1.464 and 1.479 respectively (13). As we were investigating fracture, the edge of the sample (the fracture surface) was a crucial area to analyze.
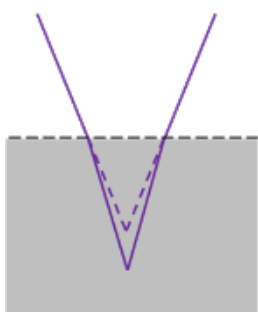
Figure 22: Schematic representation of axial aberration caused by light going in a material with higher refractive index
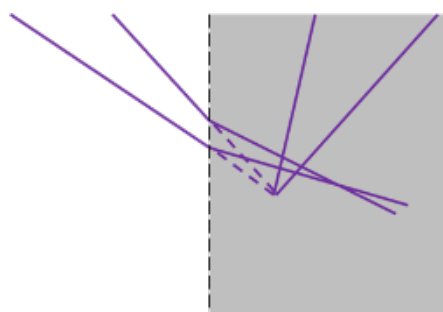
Figure 23: Schematic representation of lateral aberration caused by light going in a material with higher refractive index

Figure 24 is a re-colored 3D-image of a fluorescent sample (calibration sample 1st generation). As we imaged deeper in the material, the edge was not clear-cut. Figure 25 is another visualization of the same reconstruction showing a top view in the center (XY) and side cuts, (YZ) on the left and (XZ) on the bottom. On the (YZ) slice, the diffusive edge is visible. On the (XZ) slice, the decrease in intensity with penetration is visible.
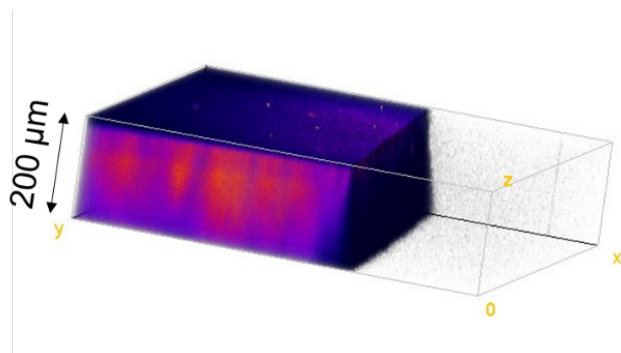
Figure 24: Re-colored 3D-image of a calibration sample with PSF distorsion visible
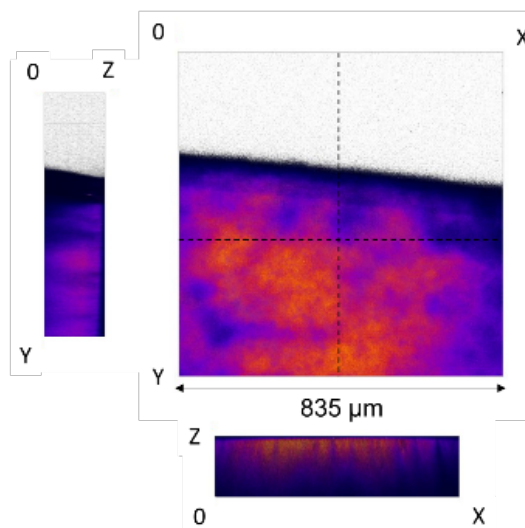
Figure 25: Top view and side views of a re-colored 3D-image of a calibration sample

In order to overcome this limitation, samples were immersed in glycerol. The refractive index of glycerol is 1.4722, which is close to that of polyacrylate samples. Figure 26 represents re-colored 2D-images of a broken mechano-fluorescent sample. Figure 26a and Figure 26b are imaged in air, at 100 µm and 200 µm respectively. A deeper penetration depth results in a more severe distortion in the PSF. Figure 26c and Figure 26d correspond to the same material but immersed in glycerol. The interface between glycerol and the sample is sharper, even at 200 µm depth.

a)

b)

c)

d)
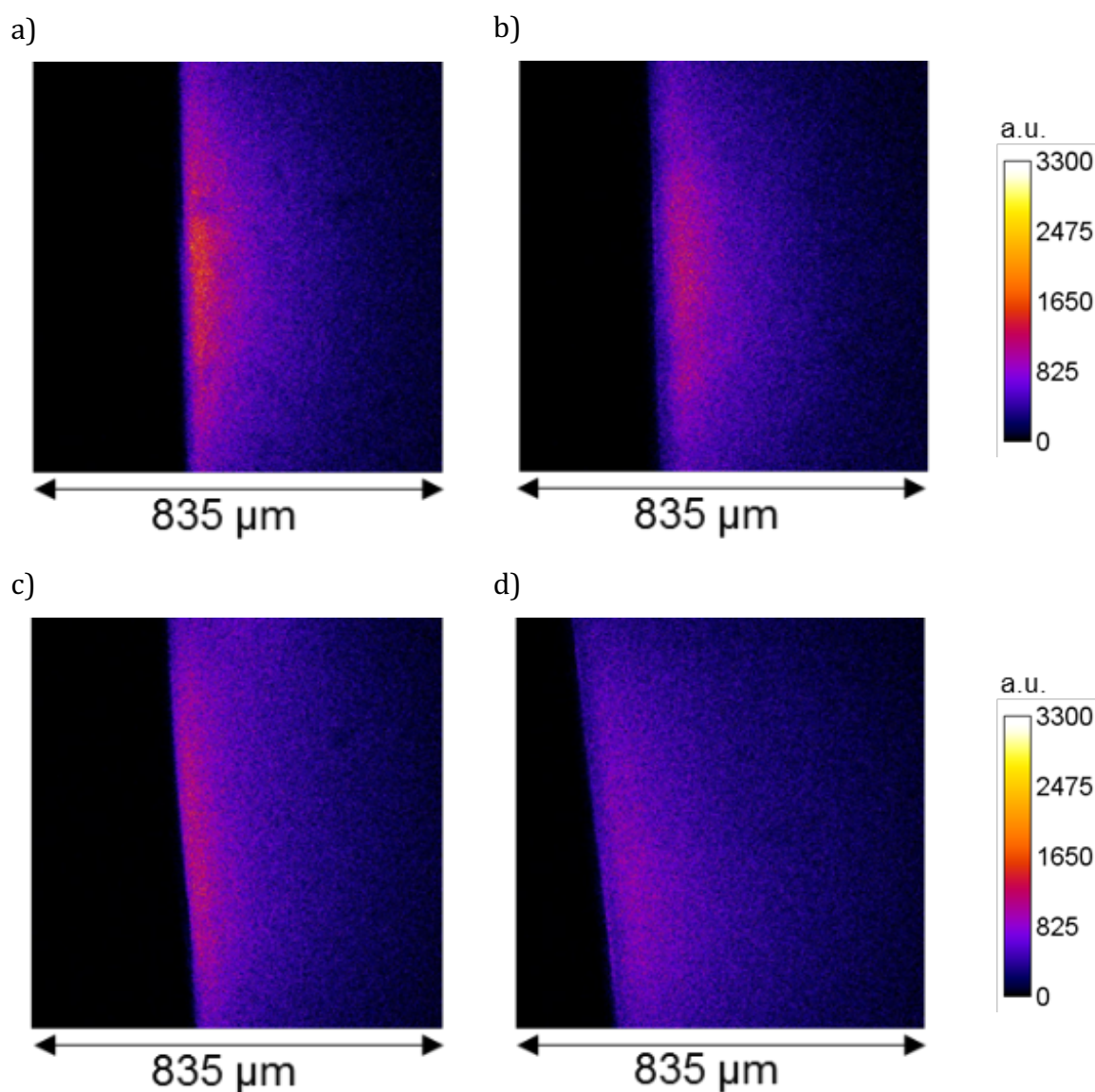
Figure 26: re-colored 2D-images of a broken mechano-fluorescent sample in air at 100 μm (a) and 200 μm (b)
depth and in glycerol at 100 μm (c) and 200 μm (d) depth

For quantitative analysis, samples were immersed in glycerol and imaged at 100 μm depth to limit PSF distortion and PSF intensity profile reduction.

2.2.4.6 Photobleaching

As presented in Chapter 1, the π-extended anthracene is resistant to photobleaching. However, a molecule is never completely photobleaching resistant. At 60 % laser intensity, photobleaching was observed. Photobleaching was detected when a darker square appeared while going from a magnification of 5x to 1x for example. 60 % of laser was more than needed for imaging. To estimate photobleaching in a more realistic

condition, a sample was continuously scanned at 20 % laser at 1x magnification. Images were recorded every 20 min for 1h30. We calculated a loss of 20% of fluorescence intensity in 90 min. In practice, the time of scan was of the order of few seconds for a 2D image and 1 to 3 minutes for 3D reconstructions. At a laser intensity of 20 % and below, photobleaching was negligible within typical acquisition time scales.

3 Observations of crack initiation and propagation

3.1 3D LSCM observations before crack propagation

In order to investigate molecular damage, the experiment of crack propagation observation (describe in section 1.3) was performed with mechano-fluorescent samples. The same Deben Microtest tensile stage controller was placed into the LSCM stage. Samples of the same dimensions, 5 mm x 25 mm, were cut. The thickness was measured for each sample and typically varied between ∼ 0.5 mm for single networks to ∼ 2 mm for triple networks. A 1 mm notch was introduced by a new razorblade. A single edge notch fracture test was performed at a crosshead speed of 0.1 mm/min (corresponding to an initial strain rate of about 3×10^{-4} s^{-1}). During the test, the controller was stopped in order to image samples at different levels of extension. The scan took a few seconds per optical section. In the case of a three-dimensional imaging, scanning the images can take 1 to 3 minutes, depending on the number of sections taken (total thickness along the z axis). It was not possible to record images while the tensile stage was moving due to the slow image acquisition.

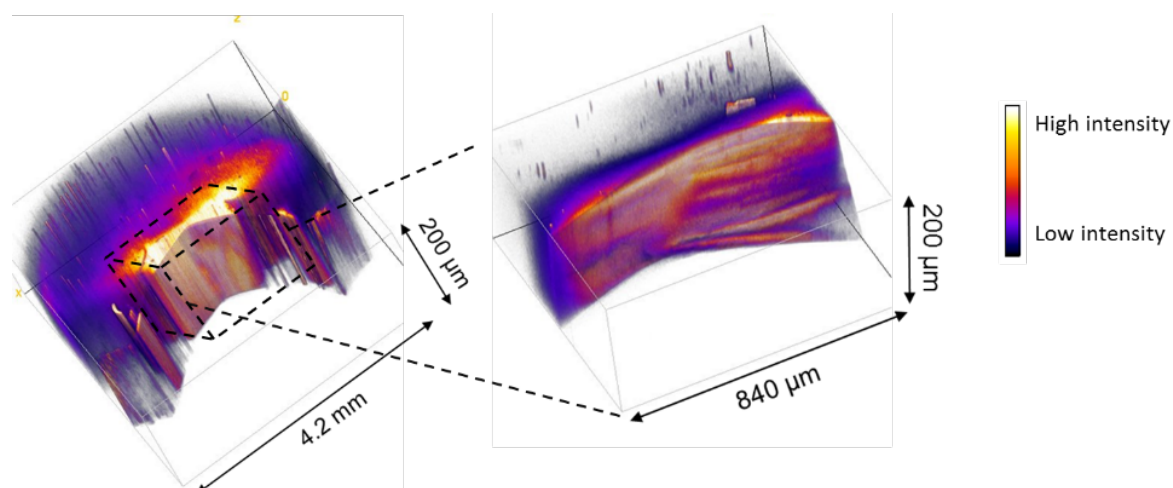Figure 27 represents a 3D image of an open crack in a triple network, EAEA(2.4).

Figure 27: 3D reconstruction from LSCM observation of a crack in a multiple network at different magnification (1x on the left and 5x on the right). Re-colored fluorescence intensity represents bond scission

The color scale (re-colored) represents the fluorescence intensity, which correlates to the damage level. As aforementioned, vignetting occurs at this magnification. The circular shape of the overall signal should not be taken into account. However, it was clear that damage occured over a longer distance along the direction normal to the crack plane than

along the crack propagation direction. The image at higher magnification show crack bifurcations, indicating a high level of damage.

Comparing 3D images of a crack at different opening stages (before propagation) was difficult for various reasons:

1. The geometry changes significantly in three dimensions with the extension due to the Poisson effect. When the crack is opening, regions near the crack tip go out of the field of view, preventing fair comparisons between images.
2. The complex 3D (crack bifurcations) geometry cannot be easily simplified to 2D. Keeping the 3D analysis leads to too much data to process and requires sophisticated and complex analytical tools that have not been developed.

To overcome some of these limitations, images were taken with the notched sample in the closed and un-deformed configuration.

3.2 Cyclic loading observations of initiation

3.2.1 Methodology

Cyclic loading experiments were performed on notched samples with an increased extension after every cycle, up to crack propagation. An example of the extension *vs.* time curve of a cyclic test is given in Figure 28. The reference position was taken as the initial closed position, noted 1 in Figure 28. While clamping the sample, it buckled. To get back to a flat position, an initial extension was applied, explaining why the reference position was at 2 mm extension.

After every cycle, a single optical section at the reference position was recorded (among others, 3 and 5 in Figure 28). The zone of interest is represented in Figure 29, including sample edges and initial notch (in dotted lines). Going back to the reference position before taking an image was a strategy to compare images at a nearly identical sample geometry. In principle, regardless of the maximal extension experienced by the material during the loading stage, at the reference (closed crack) position:

- the geometry is the same (only the fluorescence activation is different)
- the thickness of the sample is the same (no more effect of Poisson ratio)

- one plane at a fixed depth can be imaged

The cyclic loading is also a way to visualize the damage occurring in the sample before the crack propagates. It gives information on the initiation process.
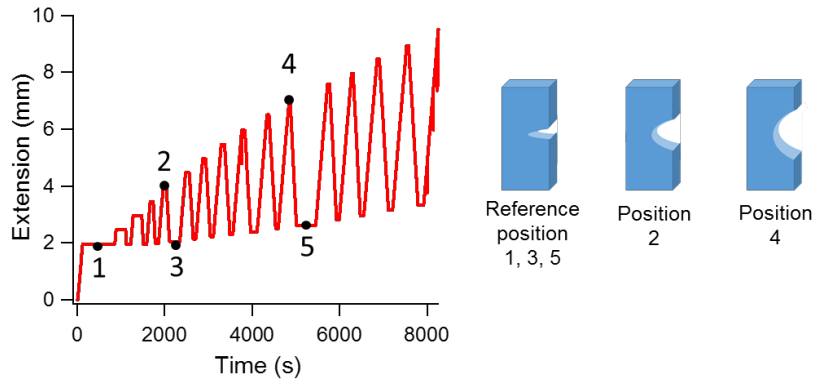

Figure 28: Cyclic test on notched sample and corresponding schematic representation of the sample. For cycles 1 to 4, an extension criteria was chosen to get back to the reference position (initial clamp position). From 5th cycle, a force criteria was chosen (F=0N); as returning to the initial clamp displacement led to sample buckling because of slippage in the clamps.
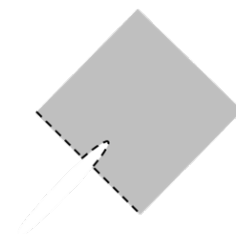
Figure 29: schematic representation of the single optical section of the notch sample in the reference position

3.2.2 Influence of the level of filler network pre-stretching

Cyclic loading tests were performed on mechano-fluorescent multiple networks with mechanophores either incorporated in the first (filler) network or in the second (part of the matrix) network. For each type of material, one sample with the mechanophore in the filler network was tested in order to investigate the influence of the level of pre-stretching on the filler network damage. Then, multiple networks with the same level of filler network pre-stretching, but with the mechanophore incorporated in the second network, were tested in order to investigate the damage induced by cycling loading of a notched sample in the matrix network.

Table 2 summarizes the materials tested. The mechanophore concentration corresponds to the molar concentration of mechanophore per cubic meter of the final material. Concentration of mechanophore (introduced either in the filler or the second network) in different materials were comparable.

Name	DAEAEA (1.6)	EADAEA (1.6)	DAEAEA (2.4)	EADAEA (2.5)	DAEAEA (3.1)	EADAEA (3.2)
Multiple network type	DN	DN	TN	TN	QN	QN
Network containing mechanophores	Filler	2nd	Filler	2nd	Filler	2nd
Mechanophore concentration (mol/m^3)	0.5	0.9	0.2	0.3	0.08	0.1
λ_0	1.6	1.6	2.4	2.5	3.1	3.2
ϕ_{SN}	0.2	0.2	0.07	0.07	0.03	0.03

Table 2: Mechano-fluorescent multiple networks tested in cyclic loading combined with LSCM analysis

The LSCM imaging near the tip of the crack was done at two different magnifications (1x and 5x).

First, surface intensity plots are given for pictures recorded at 1x magnification. A single optical section was recorded before starting the cycling loading and after a few cycles but before macroscopic crack propagation occurred. The laser intensity and gain value were adapted to the sample to obtain images with good signal over noise ratio. During the cyclic test, the laser and acquisition settings were kept identical.

Then, surface intensity plot of single optical sections recorded at higher magnification, 5x, are presented. Two pictures are given both in the closed position: one before starting the test and one after crack propagation. In all cases single optical sections were recorded at 100 μm depth. When the mechanophore was in the filler network, the laser intensity was fixed at 5 % and the gain value at 5x. When the mechanophore was in the second network, these settings were not sufficient for imaging, as the signal was too weak. The gain was increased to 15.

3.2.2.1 Double networks

Figure 30 represents a typical stress-strain curve obtained from the Deben mini tensile tester for the cyclic loading experiments performed on a double network with a level of filler network pre-stretching of $\lambda_0 = 1.6$.
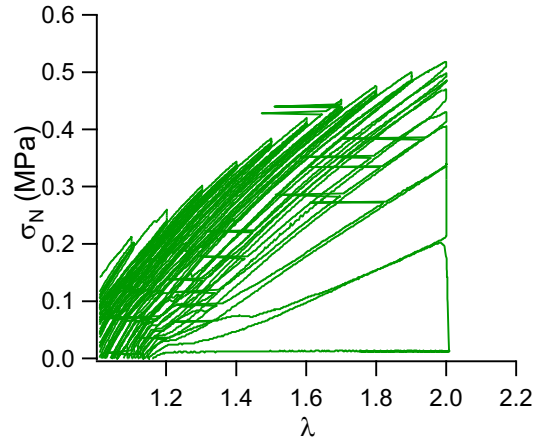
Figure 30: Stress strain curve of cyclic loading experiment performed on notched DAEAEA(1.6)

Figure 31a represents a surface intensity plot of DAEAEA(1.6) before starting the test. Some fluorescence activation (Z axis) was detected at the edge of the sample and near the notch, as indicated in the dotted lines. This activation was caused by the procedure of cutting the sample and making the notch. One can notice that the punch (used to cut edges) introduced more damage than the razorblade (used to notch the sample). Just before propagation (at λ=1.9), fluorescence activation was detected only at the crack tip (Figure 31b). The damage was localized around the crack tip.
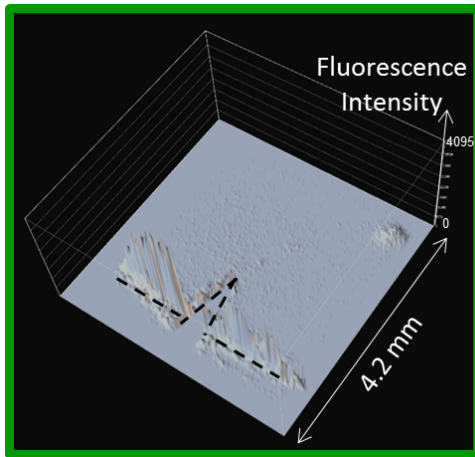
a) b)
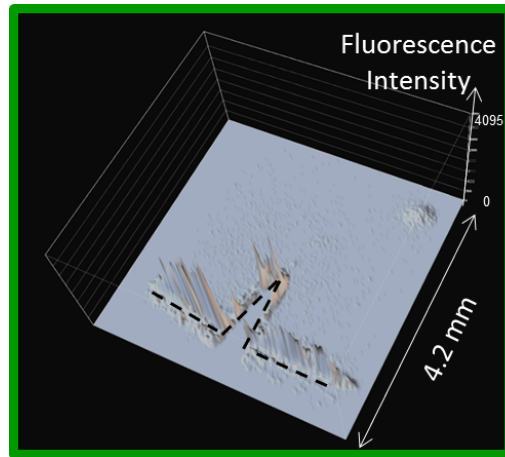
Figure 31: Surface intensity plots of single optical sections (1x, 4.2 mm x 4.2 mm, Laser 20 Gain 50 non linear) of DAEAEA(1.6) in the initial position (a) and after cyclic loading, just before crack propagation, λ=1.9 (b)

Observations at higher magnification (5x) were then performed. Figure 32a represents the initial notch and Figure 32b the propagated crack (propagation from the back to the front of the image). Before starting the test, the fluorescence activation in the filler network was only detected at the crack tip (indicated by yellow dotted line in Figure 32a). After propagation, fluorescence was localized, close to the newly created surfaces,

showing that the filler network only broke in a localized area close to the crack tip (initial notch and propagation are indicated by yellow dotted lines in Figure 32b), in agreement with the previous results obtained at lower magnification.
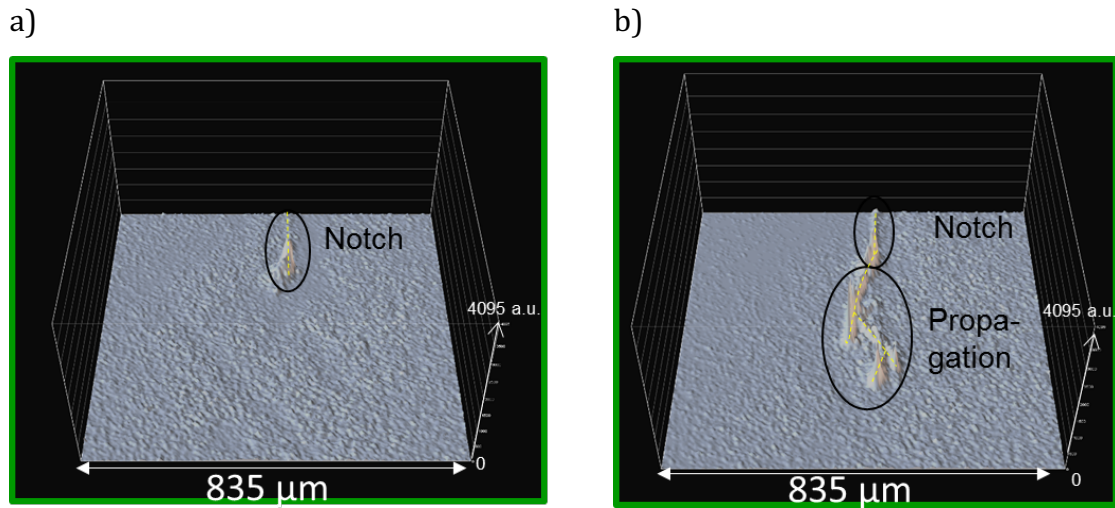
a)

b)

Figure 32: Surface intensity plots of single optical sections (5x, 835 µm x 835 µm, Laser 5 Gain 5) of DAEAEA(1.6)(mechanophore in filler network) in the initial position (a) and after cyclic loading, after macroscopic crack propagation (b) Yellow dotted lines indicate crack edge.

The same experiment was performed on a double network ($\lambda_0 = 1.6$) containing the mechanophore in the second network. When the mechanophore was introduced in the matrix, the activation level was too low to be detected (similar to the noise level), Figure 33. The notch was distinguishable at the surface and was placed at the back of the field of view. Once the stage position was selected, XY were fixed and images were recorded at 100 µm depth. Even if the notch and its propagation are not visible on Figure 33, the dotted circles indicate the area where they should localized. Either bond scission in the second network is localized over a thickness smaller than 1.63 µm (pixel size) or the polymer strands that break do not contain a mechanophore.
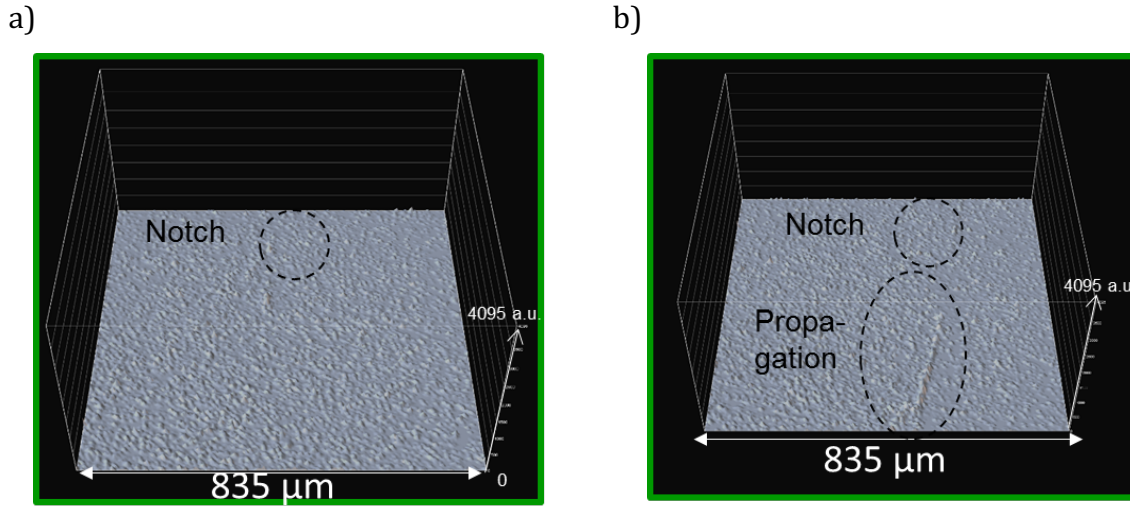
a)   b)

Figure 33: Surface intensity plots of single optical sections (5x, 835 µm x 835 µm, Laser 5 Gain 15) of EADAEA(1.6)(mechanophore in the 2nd network) in the initial position (a) and after macroscopic crack propagation (b)

3.2.2.2 Triple network

A triple network, a multiple network with a higher level a filler network pre-stretching of $\lambda_0 = 2.4$, was cyclically loaded. Typical stress-strain curves of cycle loading experiments performed on a triple network DAEAEA(2.4) and a double network DAEAEA(1.6) are represented in blue and in green respectively on Figure 34.
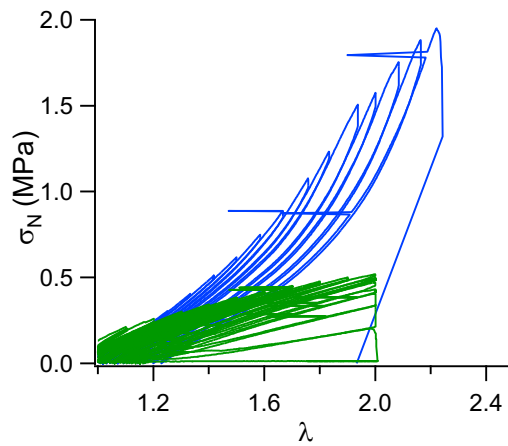
Figure 34: Stress strain curve of cyclic loading experiment performed on notched DAEAEA(1.6) in green and DAEAEA(2.4) in blue

As already observed for crack propagation tests, the multiple network with the higher level of filler pre-stretching has a higher stress at break.

Figure 35a is a surface intensity plot of DAEAEA(2.4), containing the mechanophore in the first network, before starting the test. As for the double network, some fluorescence activation (Z axis) was detected at the edge of the sample and near the notch, as indicated

by the dotted lines. After a few cycles at low extension (up to $\lambda \sim 1.5$), no additional fluorescence activation was detected. For larger extensions, additional fluorescence activation starts to be detected. Figure 35b is a surface intensity plot of the same material at the reference position (closed back) after having experienced high extension, just before crack propagation, at $\lambda = 2$. In a large zone around the crack tip, a diffuse fluorescence activation was visible. Vignetting occurred at a magnification of 1x and the circular shape of the activated zone is an artefact. Molecular damage was clearly detected in a large area around the crack tip before crack propagation in DAEAEA(2.4).

a)   b)
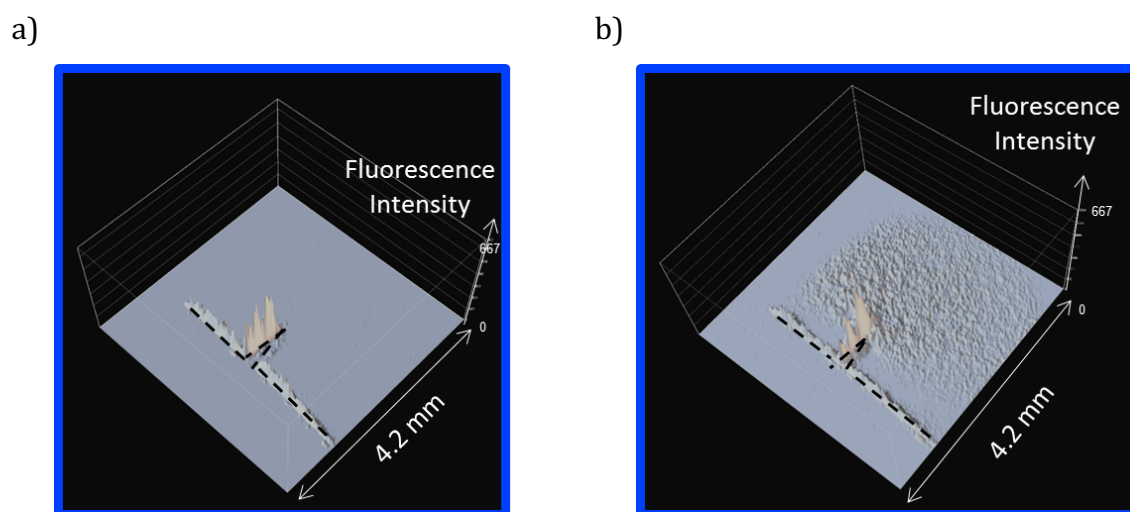
Figure 35: Surface intensity plots of single optical sections (1x, 4.2 mm x 4.2 mm, Laser 2 Gain 5)) of DAEAEA(2.4) in the initial position (a) and after cyclic loading, just before crack propagation, λ = 2 (b)

Observation were done at a higher magnification in Figure 36. A relatively delocalized fluorescence activation after propagation was detected in a larger area than in the previous case (Figure 36b compared with Figure 32b). The filler network was damaged over a broad zone.
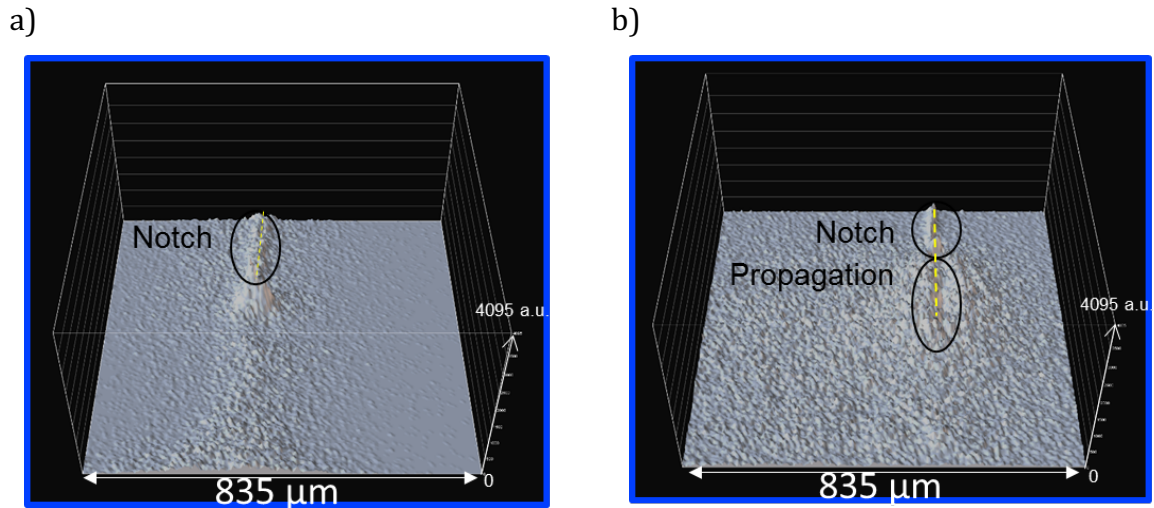
a)

b)

Figure 36: Surface intensity plots of single optical sections (5, 835 µm x 835 µm, Laser 5, Gain 5) of DAEAEA(2.4)(mechanophore in filler network) in the initial position (a) and after cyclic loading, after macroscopic crack propagation (b) Yellow dotted lines indicate crack edge.

When the mechanophore was incorporated in the 2nd network, Figure 37, the crack edge was distinguishable but again the fluorescence level was low. Dotted circles indicate the area where the notch was localized in Figure 37. The crack edges were distinguishable after crack propagation and are indicated by the yellow dotted lines on Figure 37b. The damage of the 2nd network was again low and localized (below 1.63 µm).
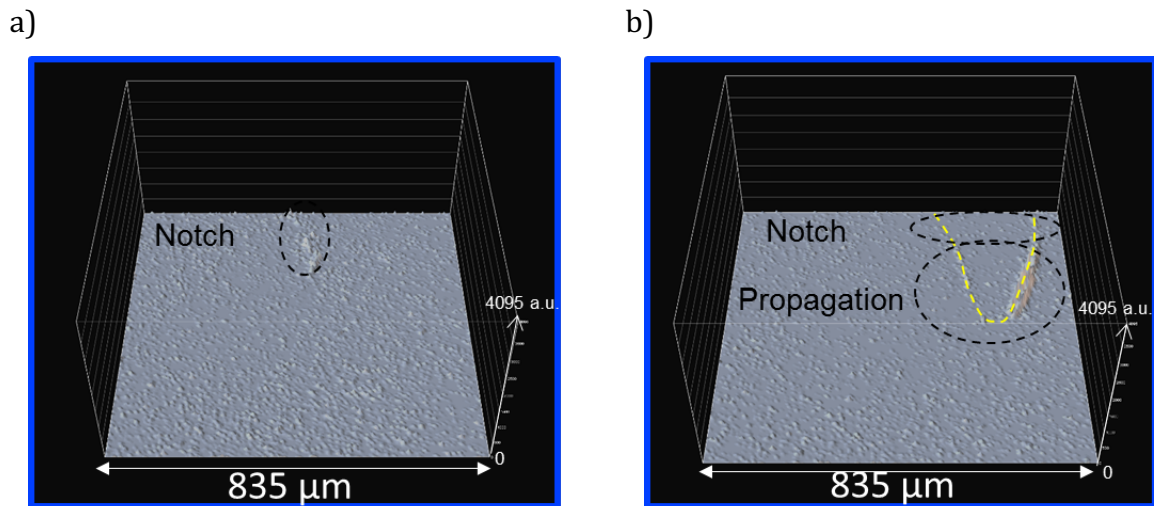
a)

b)

Figure 37: Surface intensity plots of single optical sections (5x, 835 µm x 835 µm, Laser 5 Gain 15) of EADAEA(2.5)(mechanophore in the 2nd network) in the initial position (a) and after cyclic loading, after macroscopic crack propagation (b) Yellow dotted lines indicate crack edge. The crack is slightly opened as the reference position was defined slightly opened to better visualize edges.

For both levels of prestretching λ_0=1.6 or λ_0=2.4, sacrificial bonds breakages were detected around the crack tip, before crack propagation and the sample made from a filler network that was more pre-stretched exhibited a larger damage zone.

3.2.2.3 Quadruple network

A third set of materials with an even higher level of pre-stretching of the filler network, a quadruple network at $\lambda_0 = 3.1$, was investigated to check if the damage of the matrix was still very low and barely detectable. The stress-strain curve is represented in red in Figure 38, corresponding to Figure 34 with one additional curve. For this quadruple network, DAEAEA(3.1), the stress at break was higher than in the two other multiple networks, DAEAEA(1.6) and DAEAEA(2.3). The strain hardening occurred at lower stretch, as expected since the filler network is more pre-stretched.
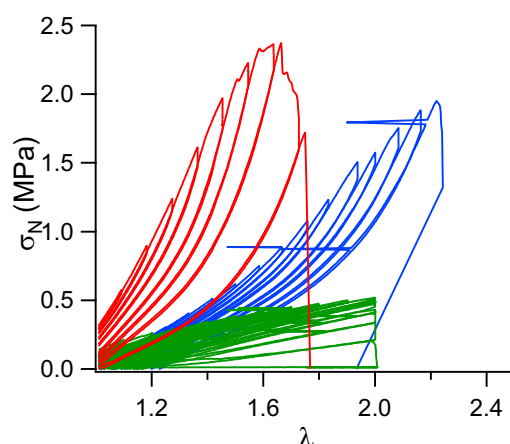

Figure 38: Stress-strain curve of cyclic loading experiment performed on notch DAEAEA(1.6) in green, DAEAEA(2.3) in blue and DAEAEA(3.1) in red

When the mechanophore was in the filler network, Figure 39, the fluorescence activation with crack propagation was detected over a large area. The filler network was damaged in a broad zone before and during propagation.
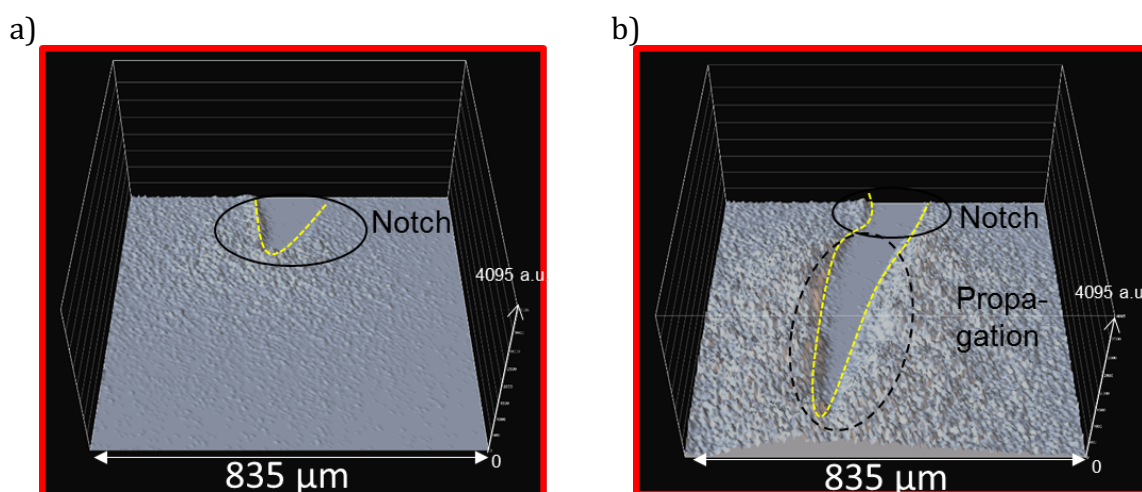

Figure 39: Surface intensity plots of single optical sections (5x, 835 µm x 835 µm, Laser 5 Gain 5) of DAEAEA(3.1)(mechanophore in filler network) in the initial position (a) and after cyclic loading, after crack propagation over hundreds of microns (b) Yellow dotted lines indicate crack edge. The crack is slightly opened as the reference position was defined slightly opened to better visualize edges.

When the mechanophore was incorporated in the second network (Figure 40) the crack edge was distinguishable. Dotted circles indicate where the notch was localized. Yellow dotted lines indicate the edge of the sample. After crack propagation, the fluorescence level was similar to the noise level. The damage of the second network was low and localized.
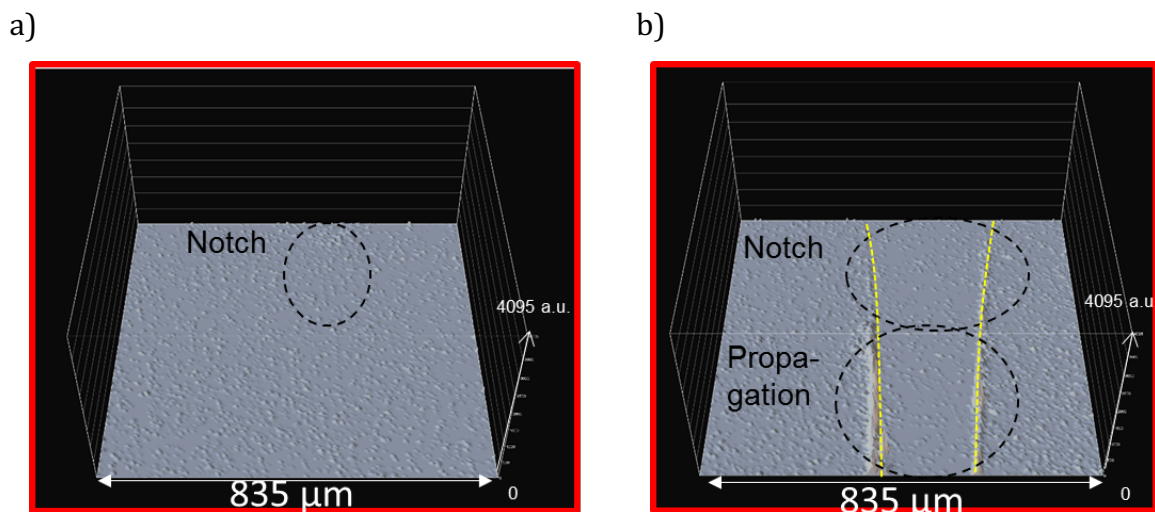
a)   b)

Figure 40: Surface intensity plots of single optical sections (5x, 835 µm x 835 µm, Laser 5 Gain 15) of EADAEA(3.2)(mechanophore in the 2nd network) in the initial position (a) and after cyclic loading, after macroscopic crack propagation (b). The crack is slightly opened as the reference position was defined slightly opened to better visualize edges.

In multiple networks, the filler network acts as a sacrificial network. For a higher level of pre-stretching of the filler network, the damaged zone becomes larger and more diffuse. The activation of the fluorescence in the matrix network was too low to be properly analyzed by the method we developed. However, this barely detectable signal is an important result: damage of the matrix was low and localized at a distance below 1.63 µm from the crack surface.

During his PhD, Yinjun Chen mapped stress in multiple network elastomers (*14*). He introduced spiropyran, a stress sensor mechanophore (color change and fluorescence activation, presented in Chapter 1), in the second network of a quadruple network ($\lambda_0 = 3.0$). He observed no color change in front of the crack tip prior to or after propagation but he observed a fluorescence activation in front of the crack tip before propagation. These results suggest that the second network is loaded when the filler network breaks but that its failure is localized.

3.2.3 Limitations

In practice, when going back to the closed configuration after applying a large extension, the crack tip did not return to the exact same position. For the first cycles, an extension criteria was chosen for the reference position. For cycles with a higher level of extension ($\lambda = 1.5$ for double networks), a force criteria was chosen (F=0N); as returning to the initial clamp displacement led to sample buckling. This change of criteria is visible in Figure 28, where the reference position is taken at an increasing value of extension. This can be attributed to sample relaxation and damage at large deformations and clamp slippage. In addition, it was not easy to identify the onset of crack propagation. Propagation over few microns at the crack tip led to the creation of new surfaces and to fluorescence activation, which can be difficult to distinguish from accumulating damage ahead of the crack tip before propagation.

Since the quantitative high resolution study of initiation proved to be challenging, we investigated damage after crack propagation. The crack was now propagated over the entire sample and the two fracture surfaces were analyzed. Quantitative analysis of these 'post-mortem' sample is presented in the next section.

4   Post mortem quantitative analysis

4.1   Toward quantification : Calibration

4.1.1   Assumptions

To get quantitative information, the calibration of the fluorescence signal is of the utmost importance.

In order to calibrate the signal, two important assumptions were made:

1. The mechanophore cross-linker was homogenously and randomly incorporated within the material
2. The fraction of mechanophore activation is the same as the fraction of chain scission.

For the first point, we did not find a way to verify the statistical incorporation. The second point will be discussed in more detail.

The mechanophore breakage corresponds to a retro Diels-Alder reaction. The retro Diels-Alder reaction does not have the same activation energy than a carbon-carbon homolytic bond dissociation (also called homolysis). It would be an oversimplified picture to think about chain scission as only homolysis with the activation energy associated. Chain scission mechanisms are more complicated and the activation energy change with the force applied, as described is Chapter 1. The environment and the orientation of chain play a crucial role in the amount of energy needed to break a chain.

Figure 41 is a typical force-elongation curve of a single polymer chain (*15*). When uniaxial extension is applied, the chain is first uncoiled, which corresponds to Gaussian entropic elasticity at a low level of force to elongate the chain (few pN). Then, the force increases very non-linearly to high values, since the limit of extensibility approaches and the Langevin stretching regime kicks in (hundreds of pN). Finally, the bonds themselves are stretched before bond scission (3-4 nN for a C-C bond).

The retro Diels-Alder probably occurs at a lower force level than a C-C homolysis but the elongation will be close. The mechanophore reports for a chain that reaches its limit of extensibility. In fact, the retro Diels-Alder reaction will occur in a chain, containing the mechanophore, close to its limit of extensibility. If no mechanophore was present in that

chain it may have broken slightly later but the extensibility at break would be comparable. As the probability of chain rupture is high when the chain is close to the limit of extensibility, we are assuming that the mechanophore activation reports for the limiting extensibility of a chain and therefore reports for chain scission. The fraction of chain scission should correspond to the fraction of chains getting closer to its limit of extensibility and for that reason should be reported by the fraction of mechanophore activation.
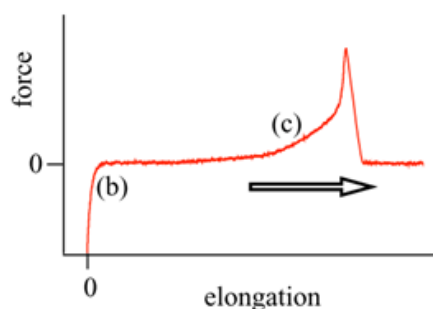
Figure 41: Force elongation curve of a single polymer chain (15)

The mechanophore was incorporated as a cross-linker and was not introduced in the middle of a chain. Chain rupture and crosslinks point rupture may seem different but what is important, when a sample is loaded, is the loading path along the chain. Because anything along the loading path can break, no matter if it is a cross-linker or the backbone bonds along the chain. Figure 42 is a drawing of a network, the loading path is represented by the dashed red lines (Figure 42b).
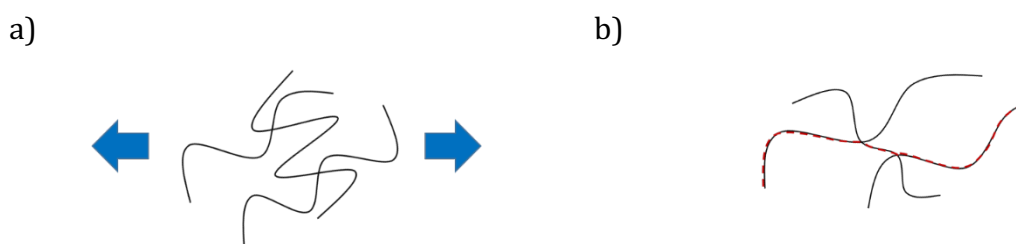
a)   b)

Figure 42: Schematic representation of a loaded network (a) and the loading path in dashed red line when a network is under extension (b)

With these two considerations in mind, we believe that the fluorescence activation, triggered by the retro Diels-Alder reaction fulfills assumption 2 and therefore is a good probe for chain scissions.

4.1.2 Strategy

The calibration molecule, shown in Figure 43, was used to calibrate the fluorescence signal from the π-extended anthracene, released by the retro Diels-Alder reaction. The calibration molecule was designed to have the same fluorescence behavior (*4*). A methyl group was used in place of the polymer chain. Synthesis of the calibration molecule was reported in Chapter 2.
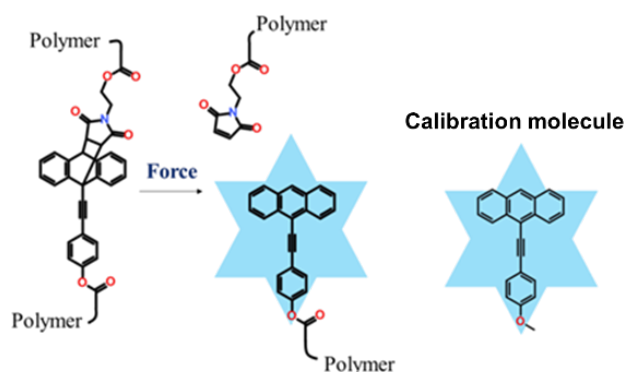

Figure 43: Schematic representation of mechanophore activation and chemical structure of the reference molecule

4.1.2.1 Calibration samples of first generation

A first strategy was to mix the calibration molecule with the ethyl acrylate monomer, the cross-linker and the initiator for a UV polymerization (same conditions as single networks synthesis). The reference molecule absorbed UV and the polymerization was slow. After 2 hours, the mixture was still liquid. After 6 hours, solid samples were obtained. The final samples were not transparent due to light scattering, indicating inhomogeneity, as shown in Figure 44. The slow polymerization was responsible for sample inhomogeneity.

Figure 44: Picture of an inhomogenous stripe of 1st generation of calibration sample

4.1.2.2 Calibration samples of second generation

To avoid inhomogeneity caused by slow polymerization and maintain the same chemical environment surrounding the fluorophore, the calibration molecule was mixed directly with linear poly(ethylacrylate) chains (Mw ~ 95,000 g.mol^{-1} in toluene from Sigma

Aldrich). The solvent was evaporated under a hood for one day and under vacuum overnight. Homogenous calibration samples were obtained. Since the calibration molecule had the same fluorescence as the activated mechanophore, the activated mechanophore concentration can be estimated based on the concentration of the calibration molecule. By varying the concentration of the calibration molecule in poly(ethyl acrylate), a calibration curve of fluorescence intensity vs activated mechanophore concentration (mol/m^3) was constructed.

4.1.3 Construction of the calibration curve

Calibration samples were imaged on the LSCM in order to get the calibration curve correlating the fluorescent intensity and the activated mechanophore concentration. A minimum of three pictures were recorded at different XY positions, always at 100 µm depth. Images were corrected (pre-processing is detailed later in this chapter) and the averaged fluorescent intensity per bin (the 'new' pixel after distortion correction) was calculated for each concentration. Figure 45 is an example of the evolution of the intensity per bin with the concentration of calibration molecule. The associated re-colored pictures of sample at different concentrations are also given. A calibration curve was obtained by a linear fit.
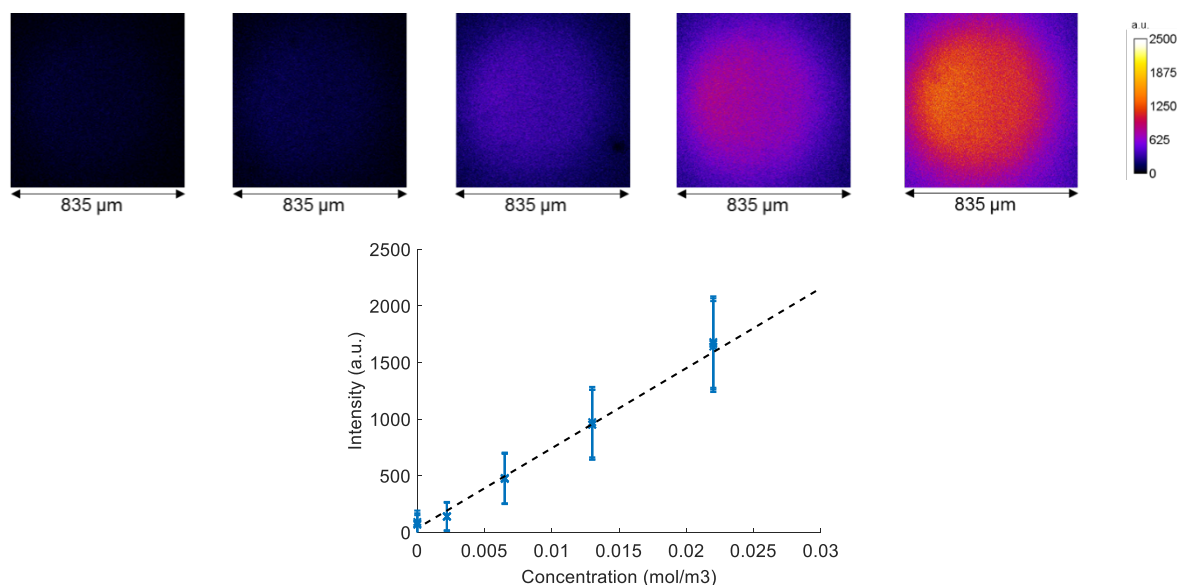

Figure 45: Example of a calibration curve and recolored pictures of the calibration samples associated (laser 7 and gain 3, image size 835 µm x 835 µm)

A new calibration curve should be plotted every time a setting is changed: either the wavelengths (excitation, emission), laser power, detector gain or the depth in the material. Note that the intensity of the laser can decrease because of pinhole misalignment. One calibration sample should be tested before every set of experiment. If the intensity does not fall on the calibration curve, a new one should be plotted.

From this calibration curve, the intensity per bin (the 'new' pixel after distortion correction) can be converted in a concentration of activated mechanophore in moles per cubic meter within that bin.

This calibration curve was also useful to estimate the noise. The noise in each bin was taken as the intensity per bin for the sample without any calibration molecule.

The sensitivity of the method was estimated from this noise value and the detection limit is estimated at about $10^{-4}\ mol/m^3$.

From a fluorescence point of view, an environment of polyethyl acrylate is comparable with an environment of polymethyl acrylate. Figure 46 represents the evolution of the fluorescence intensity with concentration of the calibration molecule in polyethyl or polymethyl acrylate. The difference is within the experimental error. Calibration curve from poly ethyl acrylate was used for poly ethyl acrylate and for poly methyl acrylate samples.
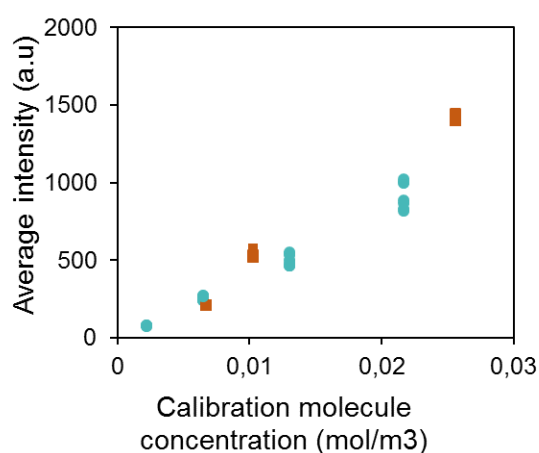

Figure 46: Evolution of the average intensity with the calibration molecule in PEA (in blue circle) and in PMA (in brown square).

4.2   Systematic analysis

The analysis work flow is described in Figure 47. First, a crack propagation test was performed on a notched sample (see Section 1). Then, the broken sample was imaged with the LSCM. Images were pre-processed and corrected (flat field and distortion) using MATLAB scripts developed by Josh Yeh. The last three steps are presented in the next sections.

Figure 47: Systematic analysis process

4.2.1   LSCM image collection

After propagating the crack, the sample was analyzed by LSCM, as shown in Figure 48. The area were the crack propagated is the zone of interest. Figure 49a represents a re-colored 3D reconstruction of the zone of interest, where the crack propagated in a multiple network. The sample is on the right-hand side of the colored activation line. Color at the edge corresponds to fluorescence activation, representing damage. When stable propagation occurred, the signal was relatively homogenous through the thickness. In that case, the 3D phenomenon can be simplified to a 2D analysis. Figure 49b represents a re-colored single optical section extracted from the 3D reconstruction. This 2D picture seemed representative of the damage.

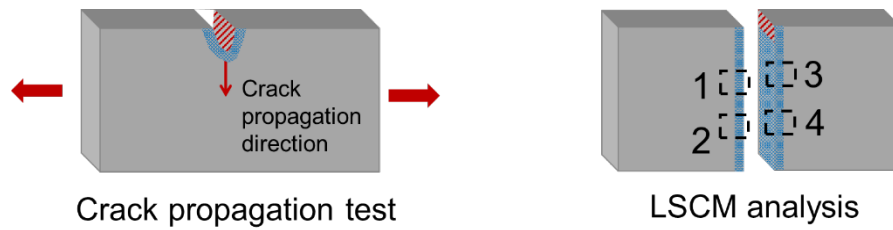The case of large crack bifurcations will be discussed later in Chapter 5.

Figure 48: Schematic representation of the test, The blue area represents the region of fluorescence activation. The zone of interests are represented by the black squares on the right drawing. Four pictures are recorded per samples.
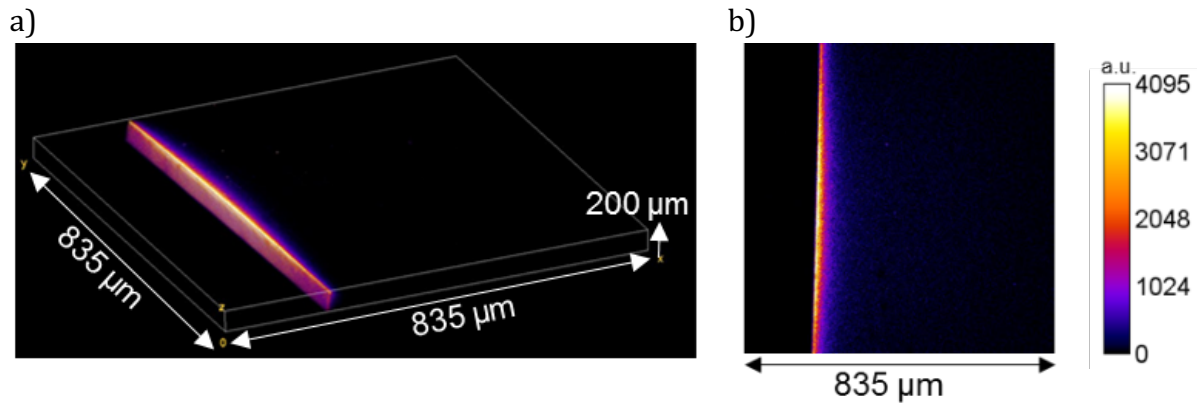

Figure 49: re-colored 3D reconstruction of a sample after crack propagation (a); extraction of a plane at 100 µm depth (image size 835 µm x 835 µm) (b)

For the systematic analysis, single optical sections were recorded in the area where the crack propagated. The pictures were taken perpendicular to the crack surface. Samples were immersed in glycerol to avoid reflective index mismatch. The top of the sample was identified as the plane of maximal intensity. The focal plane was then displaced at 100 µm depth from the top of the sample (signal decreases with depth as discussed earlier in this Chapter). The sample was broken in two pieces during the crack propagation test. Two images along the crack edge were recorded for each side (four pictures per sample as shown in Figure 48). Magnifications at 5x resulted in limited optical aberrations. Laser and gain were adapted for each set of experiments.

4.2.2 Image pre-processing

An example of a surface intensity plot of a raw image of the crack edge after crack propagation is represented in Figure 50a. These experimental images were pre-processed using MATLAB functions. The pre-processing consisted in a flatfield and distortion correction.

145

The flatfield was obtained with a calibration sample (2nd generation) with the highest concentration of calibration molecule possible without any saturated pixels (2.2×10^{-2} mol/m³). The flatfield correction was applied and overcorrected corners were removed (details in Section 2.2). The distortion measured from the Argolight slide was used to remove xy distortions in the image (details in Section 2.2).

The noise was estimated from a polyethyl acrylate sample without any mechanophore or calibration molecule inside. With a high gain (> 20), even if the material is not fluorescent, the sample surface was distinguishable. The focal plane was displaced at 100 µm depth from the detected surface. Laser and gain were adjusted to the setting used for the analysis. A single optical section was recorded. Three to five pictures were saved at different XY positions (always at 100 µm depth).

Figure 50b represents the same image as Figure 50a after the correction and ready for quantitative analysis. The color scale corresponds to the intensity signal in arbitrary units. The scale goes from 0 to 4096 a.u. as the fluorescence was recorded in 12-bit digital units ($2^{12} = 4096$). Surface intensity plots are shown to better visualize trends and pre-processed images are given to give an idea of the actual corrected image over which the quantification was carried out.
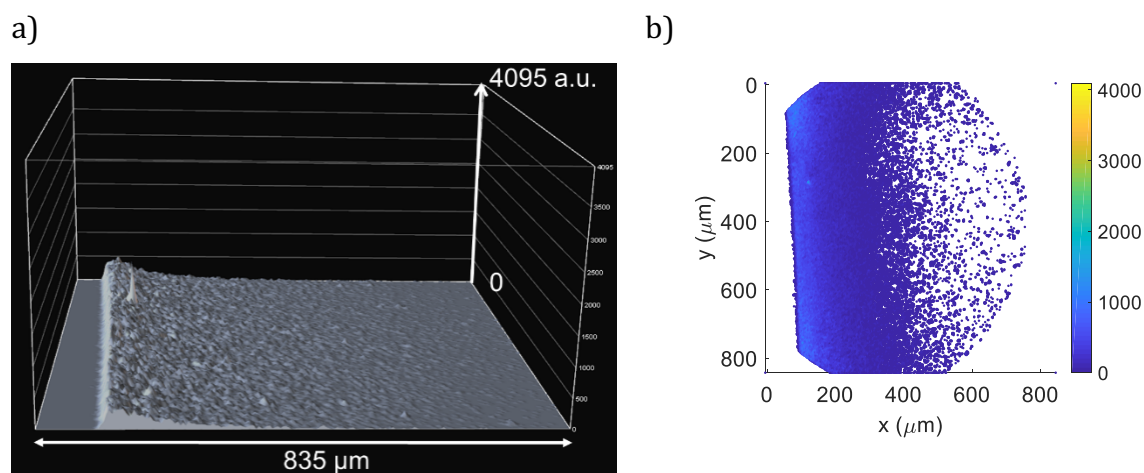
a)

b)

Figure 50: Images of a multiple network crack edge, surface intensity plot from the raw image, image size 835 µm x 835 µm (a) and re-colored image after the pre-processing step (b)

4.2.3 Quantification of the size of the damage zone and extent of damage

The objective of this calculation is to estimate the concentration of broken chains from the pre-processed image. The methodology is illustrated by the example of Figure 51.

A straight line was used to fit the crack edge on the pre-processed image, as shown in Figure 52.

An equivalent 150 bin (the 'new' pixel after distortion correction) (along the crack edge) by 250 bin (300-by-500 µm) region normal to the crack edge was drawn, as represented in Figure 53. This area was used to perform intensity statistics as a function of the distance from the crack edge. This area is composed of 150 lines of 1 bin width by 250 bin long, as visible in Figure 54 (zoom of Figure 53). In fact, we consider a matrix of 150 bin by 250 bin. As discussed earlier (see section 2.2.1), bins are actually voxels since the single optical section has a thickness (12.04 µm).

The average intensity, over the 150 lines, as a function of the distance from the crack edge was plotted and is given in Figure 55. A cutoff was defined at the noise level (from a sample without mechanophore or calibration molecule). This cutoff point corresponds to the distance from the crack where no more signal above noise was detected. This distance was considered as a characteristic length, L_{damage}, over which damage was detected. L_{damage} is estimated at 200 µm in Figure 55.

For better understanding, the intensity profile, given in Figure 55, should be seen as a bar chart, given in Figure 56, with each bar corresponding to the averaged intensity (averaged over the 150 lines) of one voxel. The following calculation is done voxel by voxel, only on voxels with intensity higher than noise.
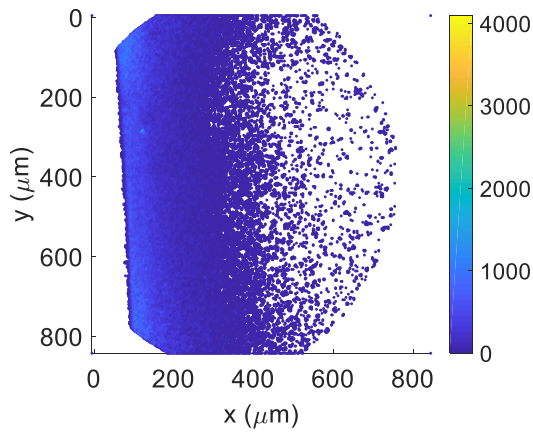
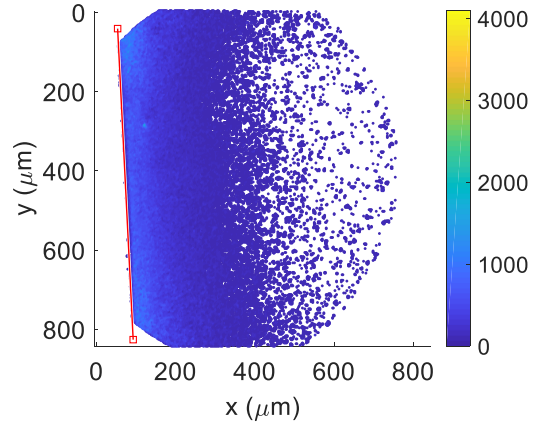*Figure 51: Pre processed image for quantitative analysis*

Figure 52: Detection of the crack edge (red straight line) in the corrected image of the crack edge
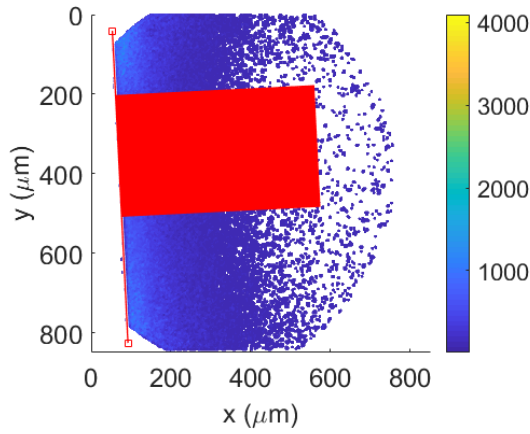

Figure 53: Determination of the area where intensity statistic were performed (red rectangle)
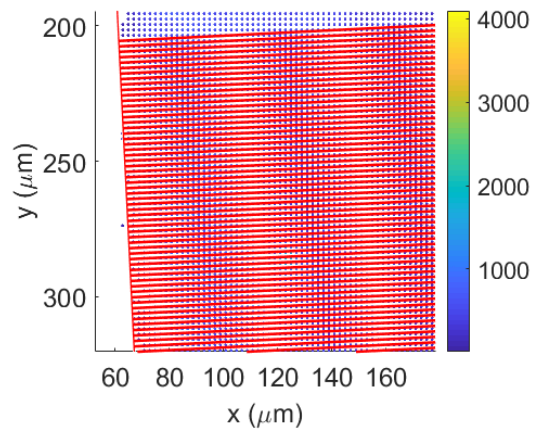

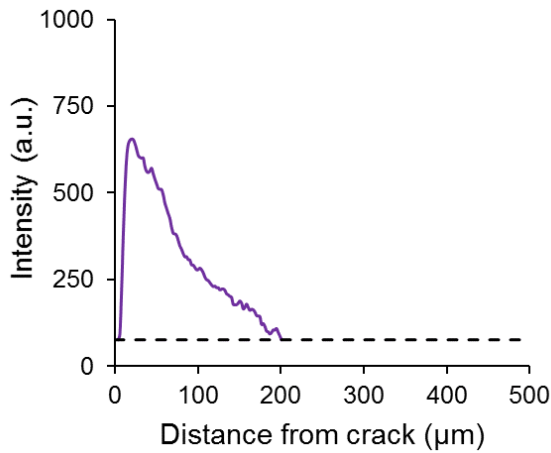*Figure 54: Intensity statistic performed line by line (red lines)*

Figure 55: Evolution of the average intensity with the distance from the crack edge
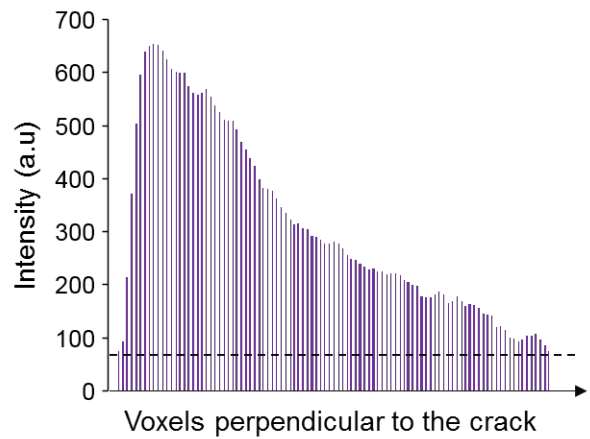

Figure 56: Bar chart of the averaged intensity per bin with the distance from the crack edge. Each bar corresponds to a voxel. Only voxel with averaged intensity above noise are considered

148

The MATLAB data analysis is illustrated by a simplified drawing, given in Figure 57. In the drawing only 8 voxel (2x4) are considered instead of the 37500 (150x250).

We consider the intensity, $i_{n,n}$, of each voxel. L_{damage} is represented in Figure 57. Above this length, the fluorescence signal is below noise. On the drawing, L_{damage} corresponds to a 3 px length. The average intensity, I_n, over the 2 lines, is calculated (corresponding to Figure 55 and Figure 56 for the real image).

For each voxel, the averaged intensity, I_n, is converted in a concentration of activated mechanophore, C_n (in mol/m³), within this voxel, using a calibration curve (see section 4.1.3 and the example of calibration curve in Figure 45). Knowing the volume of a voxel, these concentrations were converted in a number, n_n, of activated mechanophore in each voxel. The sum of all the quantities gives the total number, $n_{act.DACL}$, of activated mechanophores per unit of crack length over a distance from the crack = L_{damage}.
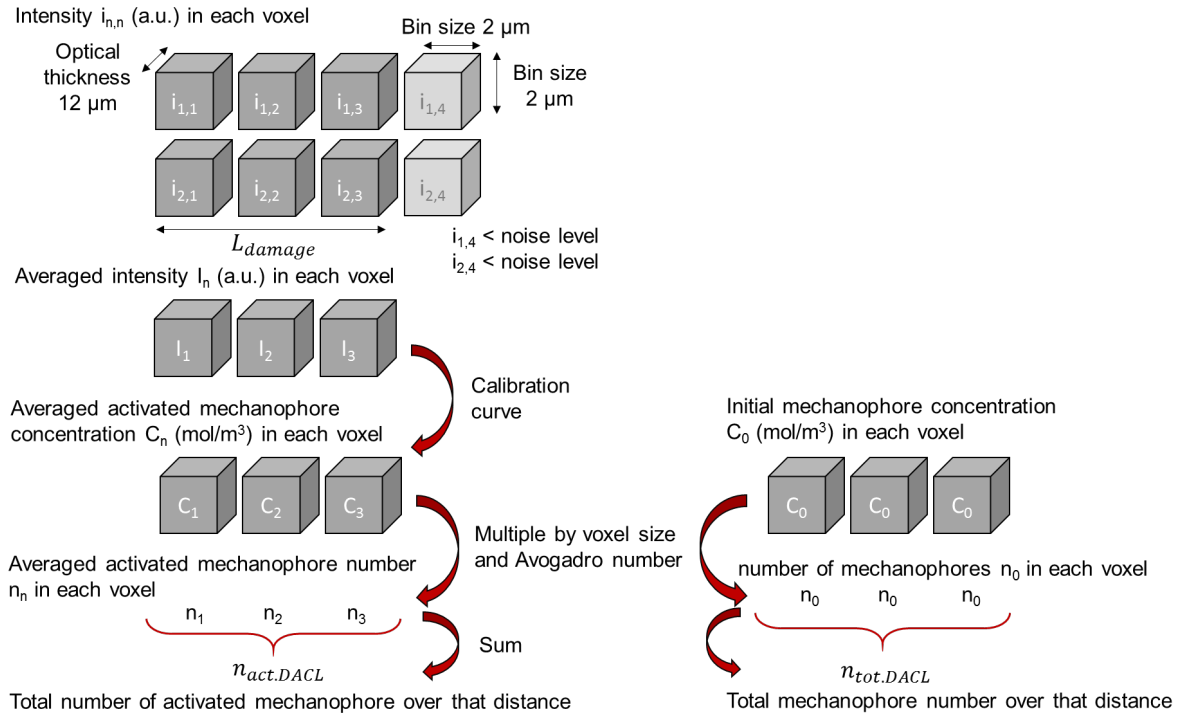

Figure 57: Schematic representation of MATHLAB data analysis

The fraction of activated mechanophores, $\phi_{act.DACL}$, can be estimated up to that length by normalizing $n_{act.DACL}$ by the quantity of mechanophore initially introduced in the same volume (of 3 voxels), $n_{tot.DACL}$ (Eq 6.):

$$\phi_{act.DACL} = \frac{n_{act.DACL}}{n_{tot.DACL}}$$

Eq 6.

149

$\phi_{act.DACL}$ represents the average fraction of mechanophore activation up to the distance L_{damage}. This average fraction of activated mechanophore was assumed to be the same as the fraction of broken chains (an assumption discussed earlier in the Chapter).

In the case of a single network, the average number of elastic strands per cubic meter (between crosslinks) v_x, can be estimated by Eq 7., from the affine network model (*16*).

$$v_x = \frac{E}{3\,k_B T},$$
Eq 7.

where E is the Young's modulus, k_B is the Boltzmann constant and T is the temperature.

In the case of a multiple network, the filler network is diluted by a factor ϕ_{SN}. The average number of elastic strands per cubic meter is then defined by Eq 8.

$$v_x = \phi_{SN}\,\frac{E_{SN}}{3\,k_B T},$$
Eq 8.

where E_{SN} is the Young's modulus of the filler network alone (the single network before swelling and polymerization).

To calculate the areal density of broken chains in the filler network, Σ_{exp}, the fraction of activated mechanophore $\phi_{act.DACL}$ (corresponding to the average fraction of chain breakage up to the distance L_{damage}) was multiplied by the chain number density v_x and the length L_{damage}.

$$\Sigma_{exp} = \phi_{act.DACL}\,v_x\,L_{damage}$$
Eq 9.

To have a point of comparison, the areal chain density, Σ, can be estimated. We consider a single network randomly cross-linked with a cross-linker with a functionality of four. The areal chain density can be estimated by Eq 10. (*10*):

$$\Sigma = \frac{v_x \langle R_0{}^2 \rangle^{1/2}}{2},$$
Eq 10.

where $\langle R_0{}^2 \rangle^{1/2}$ is the average distance between cross-links.

From Gaussian statistics, the areal density can be calculated Eq 11.:

$$\Sigma = \frac{l_{cc} E\,\sqrt{C_\infty N_x}}{6\,k_b T},$$
Eq 11.

where l_{cc} is the length of a C-C bond, C_∞, is the polymer characteristic ratio, N_x, is the number of carbon bonds between cross-links.

Finally, Σ can be estimated by Eq 12.:

$$\Sigma = l_{cc} \left(\frac{E \, \rho \, N_a \, C_\infty}{6 \, M_0 \, k \, T} \right)^{1/2}$$ Eq 12.

where ρ is the material density, N_a is the Avogadro constant and M_0 is the monomer molecular weight.

In the case of multiple networks, the areal density of chain is diluted in the matrix and is given by:

$$\Sigma = \phi_{SN}{}^{2/3} \, \Sigma_{SN}$$ Eq 13.

with Σ_{SN} as the areal density of the single network.

We define $\bar{\Sigma}$ as the normalization of the experimental number of broken chains per square meter, Σ_{exp}, by a monolayer, Eq 14.:

$$\bar{\Sigma} = \frac{\Sigma_{exp}}{\Sigma}$$ Eq 14.

It is interesting to note that to get the intrinsic fracture energy, according to Lake-Thomas theory, the number of broken chains is equal to the areal chain density. In the case of single network elastomer, the normalization $\bar{\Sigma}$, can be seen as a normalization by the Lake-Thomas prediction.

4.2.4 Image dispersity over one sample

The image analysis was applied to every image. Four images were recorded per broken sample (two on each side), as represented Figure 48 and Figure 58 (except when bifurcations occurred). Figure 58 represents the surface intensity plots of the four raw images obtained from one sample after crack propagation.

In order to give an idea of the dispersity, Figure 59 represents the intensity profile obtained from the four images of Figure 58. The distance over which damage is detected evolves from about 130 μm to about 240 μm. From these intensity profiles, the areal density of broken chains in the filler network, Σ_{exp}, were calculated and plotted in Figure 60. The dispersity is important. In the following and in next Chapters, results are averaged

over the four images and error bar indicate the standard deviation to give an idea of the dispersity.
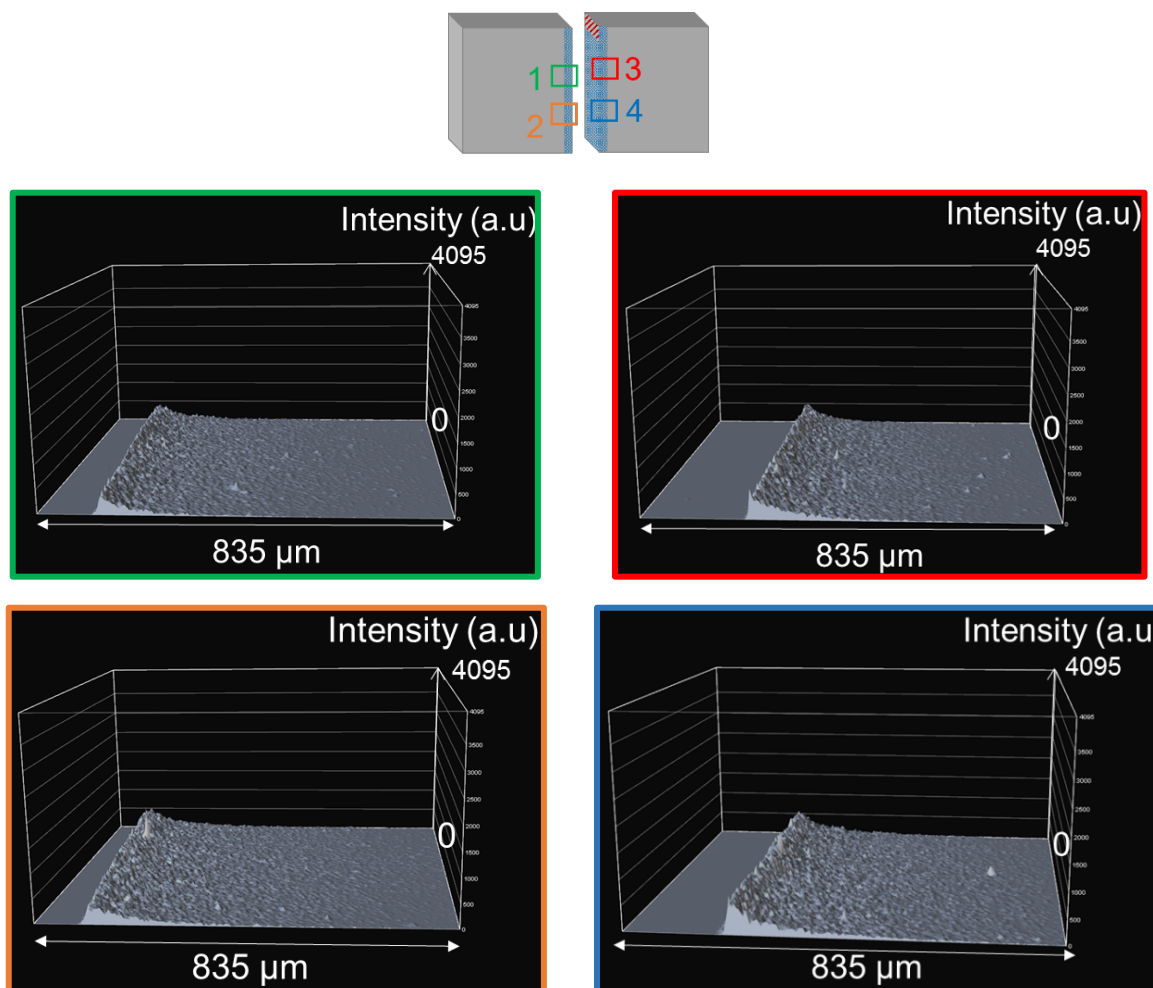

Figure 58: Surface intensity plots from four raw pictures of one broken sample. Image size 835 μm x 835 μm.
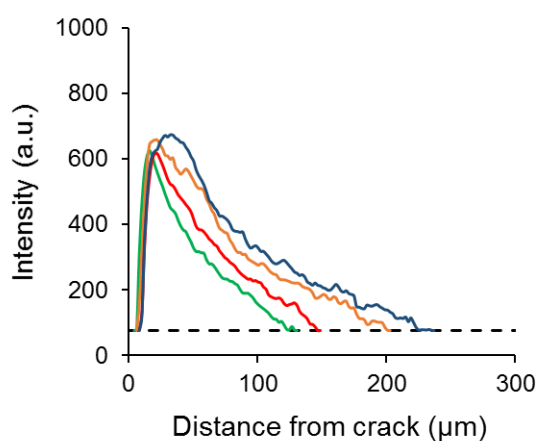

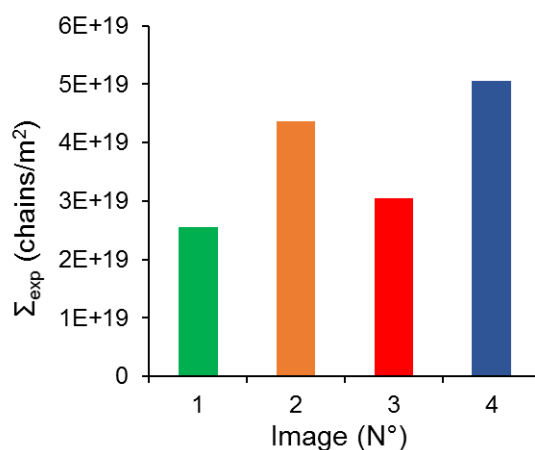Figure 59: Intensity profiles of from four pictures of one broken sample

Figure 60: Areal density of broken chains calculated from four images of one sample.

It is interesting to note that the fluorescence signal is higher in images n°2 and n°4, which are far from the notch. This increase was attributed to crack acceleration and will be discussed in more details in next Chapter.

4.3 Influence of the level of pre-stretching of the filler network

The LSCM systematic analysis was then applied to the multiple networks with the two different levels of filler pre-stretching: two samples of double network, two DAEAEA(1.6), and one sample of triple network, DAEAEA(2.4). Examples of corrected images of crack edges used for the quantitative analysis are given in Figure 61.
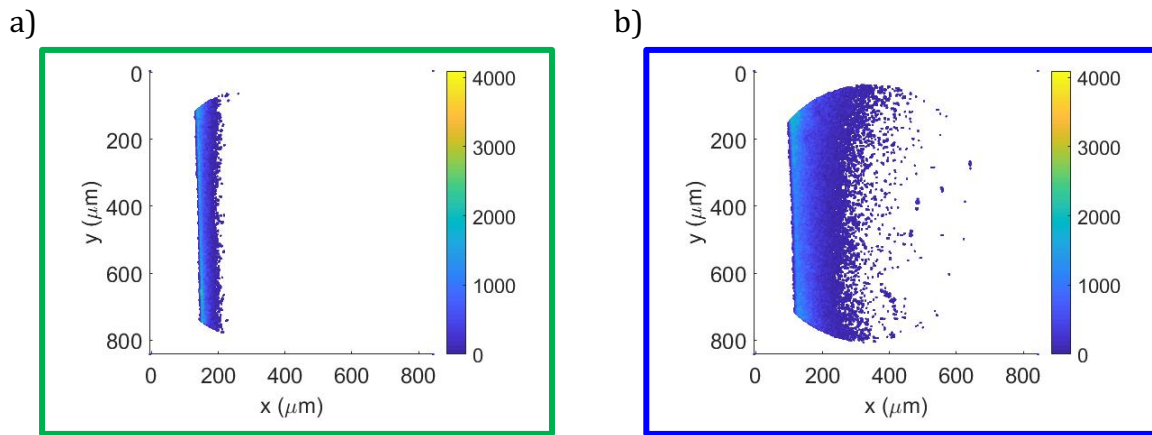
a)   b)

Figure 61: Pre-processed images for quantitative analysis of DAEAEA(1.6) (a) and DAEAEA(2.4) (b) crack edges

For DAEAEA(1.6), the multiple network with the less pre-stretched filler (Figure 61a), the fluorescence activation was detected over a smaller area than in DAEAEA(2.4) (Figure 61b). The characteristic length over which fluorescence activation was detected corresponds to the distance from the crack plane over which molecular damage occurred above the noise level. The damage lengths, L_{damage}, are reported in Table 3. From double to triple networks of poly ethyl acrylate the damage length increased from about 40 µm to about 180 µm.

Type of network	Sample name	λ_0	ϕ_{SN}	L_{damage} (µm)
DN	DAEAEA(1.6)	1.6	0.2	42 ± 16
TN	DAEAEA(2.4)	2.4	0.07	178 ± 42

Table 3: Detected damage length for multiple network elastomers

Based on the methodology exposed previously, the number of broken chains per square meter were calculated. Table 4 shows the areal density of the filler, Σ, the experimental value of areal density of broken chains of the filler network, Σ_{exp}, and the normalization, $\bar{\Sigma}$, of the Σ_{exp} by Σ.

Type of network	Sample name	λ_0	Σ (chains.m^{-2})	Σ_{exp} (chains.m^{-2})	Normalized $\bar{\Sigma}$
DN	DAEAEA(1.6)	1.6	1×10^{17}	$(9 \pm 3) \times 10^{18}$	84 ± 33
TN	DAEAEA(2.4)	2.4	5×10^{16}	$(4 \pm 1) \times 10^{19}$	788 ± 210

Table 4: Numbers of broken chains in the filler network of multiple network elastomers

For double networks, Σ_{exp} was about 80 times higher than a monolayer. While for triple networks, Σ_{exp} was 800 times higher. In both cases, it was clear evidence that when a multiple network was broken, the filler network broke over a much larger volume near the crack plane than a monolayer of strands at the crack propagation plane.

From these results, we concluded that an increase of about 50% of pre-stretching of the filler network (from double to triple networks) led to an increase of the filler damage of about one order of magnitude. This was the first time we were able to quantify this increase in damage with the level of the filler pre-stretching.

Conclusions

In this chapter, our new methodology relying on fluorescence activation to map molecular damage was presented. Mechano-fluorescent samples were analyzed by a customized Laser Scanning Confocal Macroscope (LSCM). A tensile test device was introduced into the LSCM stage to perform crack propagation tests, punctuated by fluorescence observations. Open cracks were visualized and 3D-damage mappings of open cracks were obtained. Higher level of damage was detected perpendicular to the crack propagation direction.

Direct and fluorescence observations of open cracks revealed the presence of crack bifurcations, corresponding to large and heterogeneous fibrillar deformation. The fibrillar-like structures are highly damaged. The fracture propagation is a three dimensional phenomenon.

Fracture occurred in two steps: initiation and propagation. The propagation can be fast and is challenging to analyze, in real time and in 3D. Our strategy was to investigate first crack initiation by cyclic loading and then crack propagation by 'post mortem' observations.

First, initiation was investigated to evaluate the level of damage before macroscopic crack propagation. Cyclic loading experiments on notched samples were selected as the best strategy to observe the material in the same position but with different levels of fluorescence activation. Indeed, at every cycle, an increasing extension level was reached and one plane of every closed (reference) position were compared. Mechano-fluorescent multiple networks, containing the mechanophore either in the first (and filler) network or in the second (and part of the matrix) network, were cyclically loaded up to crack propagation. Three levels of pre-stretching of the filler network were compared $\lambda_0 = 1.6$, $\lambda_0 = 2.3$ and $\lambda_0 = 3.1$. From the damage mapping, we conclude that:

- A larger and more diffuse damage zone of the filler network was detected for filler networks at a higher level of pre-stretching.
- At every tested level of pre-stretching of the filler network, the damage of the matrix was barely detectable. Even after crack propagation, the damage was localized close to the newly created surfaces. We conclude that the damage in the

2nd network of multiple network, with a level of pre-stretching up to 3.1, was low and localized at the crack edge (<1.6 μm).

Quantification of these observations was challenging for several reasons, such as the difficulty to dissociate micron-scale crack propagation to accumulating damage ahead of the crack tip.

The best strategy was the following: to run systematic and quantitative analysis of a crack propagation test followed by fluorescence observations 'post mortem' and image analysis. As the fluorescence is stable, information on the level of damage that occurred during crack propagation can be obtained after propagation.

Calibration samples were prepared by mixing a calibration molecule in linear polymer chains with identical chemical structure as the networks. A calibration curve enabled us to get the concentration of activated mechanophore from the fluorescence signal intensity.

Using this calibration method, double and triple networks were compared. In these multiple networks, we confirmed that the damage zone is clearly larger for more pre-stretched filler networks. The length over which damage occurs was detected from about 40 μm to about 180 μm, for a level of pre-stretching of 1.6 and about 2.5 respectively. The number of broken chains was also estimated. For the more pre-stretched filler network, the areal density of filler chains scission was about one order of magnitude larger than for the less pre-stretched one. These results were consistent with earlier studies but with a much better spatial resolution, sensitivity and quantification (1). Thanks to a calibration of the fluorescence signal, this was the first time we were able to get quantitative results.

References

1.   E. Ducrot, Y. Chen, M. Bulters, R. P. Sijbesma, C. Creton, Toughening Elastomers with Sacrificial Bonds and Watching Them Break. *Science* **344**, 186-189 (2014).
2.   J. M. Clough, C. Creton, S. L. Craig, R. P. Sijbesma, Covalent Bond Scission in the Mullins Effect of a Filled Elastomer: Real-Time Visualization with Mechanoluminescence. *Advanced Functional Materials*, (2016).
3.   E. W. Meijer, R. Groningen, Ed. (1982).

4.   R. Göstl, R. P. Sijbesma, π-extended anthracenes as sensitive probes for mechanical stress. *Chem. Sci.* **7**, 370-375 (2016).

5.   H. W. Greensmith, Rupture of rubber. X. The change in stored energy on making a small cut in a test piece held in simple extension. *Journal of Applied Polymer Science* **7**, 993-1002 (1963).

6.   P. Millereau, *Large Strain and Fracture of Multiple Network Elastomers* (Doctoral dissertation) UPMC (2017).

7.   S. W. Paddock, Principles And Practices Of Laser Scanning Confocal Microscopy. *Molecular Biotechnology* **16**, 127 (2000).

8.   I. T. Young, Shading Correction: Compensation for Illumination and Sensor Inhomogeneities. *Current Protocols in Cytometry* **14**, 2.11.11–12.11.12 (2003).

9.   M. Model, Intensity calibration and flat-field correction for fluorescence microscopes. *Curr Protoc Cytom* **68**, 10 14 11-10 (2014).

10.   P. Millereau *et al.*, Mechanics of elastomeric molecular composites. *Proc Natl Acad Sci U S A*, (2018).

11.   A. Diaspro, F. Federici, M. Robello, Influence of refractive-index mismatch in high-resolution three-dimensional confocal microscopy. *Applied Optics* **41**, 685-690 (2002).

12.   E. P. Jonasova, A. Bjorkoy, B. T. Stokke, Recovering fluorophore concentration profiles from confocal images near lateral refractive index step changes. *J Biomed Opt* **21**, 126014 (2016).

13.   J. E. Mark, *Polymer data handbook.* (1999).

14.   Y. Chen, *Quantitative mapping of stress in soft materials by mechanochemistry 5Doctoral dissertation* PSL (2018).

15.   F. Oesterhelt, M. Rief, H. E. Gaub, Single molecule force spectroscopy by AFM indicates helical structure of poly(ethylene-glycol) in water. *New Journal of Physics* **1**, 6.1-6.11 (1999).

16.   M. Rubinstein, R. H. Colby, *Polymer Physics.* (2003).

Chapter 4

Bond scission
in single network elastomers

Introduction

In the previous chapter, we characterized the molecular damage in multiple network elastomers with different levels of pre-stretching of the filler network. Because of the existence of the sacrificial bond breakage mechanism, we expected damage to occur in a certain volume near the plane of the crack.

However, in conventional single network elastomers, the amount of chain scission during macroscopic fracture is still an open question. The hypothesis about molecular damage is that in order to break a sample in two pieces, at least a molecular plane of chains needs to be broken (*1*). The methodology, presented in Chapter 3 Section 4 of damage analysis by mechano-fluorescence using a LSCM, can also be applied to single network elastomers in order to characterize the extent and localization of bond scission.

The first objective of this Chapter is therefore to quantify and map the amount of bond scission occurring near the crack plane during the propagation of a crack in a single network elastomer. This result can be compared to a monolayer, corresponding to the Lake and Thomas model predicting of the intrinsic fracture energy of an elastomer (presented in Chapter 1 Section 1). The conditions in which this model is relevant and the assumptions on which it relies will be specifically addressed in light of new experimental evidence.

Then, the influence of stretch rate and temperature on molecular damage during crack propagation will be investigated. In fact, soft materials generally appear tougher when they are loaded at high stretch rates or close to their glass transition temperature. Several examples of measurements of Γ for typical soft materials show that the fracture energy generally increases very significantly with crack propagation velocity (*2*).

This increase in fracture energy with rate is generally attributed to viscoelasticity only. This rate (and temperature) dependence is generally taken into account in the second contribution, $f(v,T)$, of the definition of the adhesion energy Γ proposed by Gent and Schultz and given Eq 1. (presented in Chapter 1 Section 1) (*3*).

$$\Gamma = \Gamma_0\big(1 + f(v,T)\big) \qquad \text{Eq 1.}$$

Adhesion and fracture are not exactly the same but imply the same dependence of rate. For adhesion the value of Γ_0 is the thermodynamic work of adhesion that can in principle be obtained from the knowledge of surface and interfacial tensions. In the case of bulk fracture, Eq 1. is also used (*4*) but Γ_0 is here the threshold fracture energy at vanishingly low crack velocity (constant value). $f(v,T)$ is a function representing viscoelastic energy dissipation in front of the crack tip (time and temperature dependent).

Although Γ_0 must include chain scission, until now, there was no information on the extent and localization of chain scission and its dependence (if any) on crack velocity or on temperature. The second objective of this chapter is therefore to investigate the coupling between molecular damage and viscoelasticity in single network elastomers.

1 Detecting molecular damage in Single Networks

1.1 Materials

In order to be able to vary the viscoelastic properties of the material easily within a narrow range of temperatures, in this Chapter, we mainly used single networks of polymethyl acrylate. The synthesis of the reference and of the mechano-fluorescent single networks was described in Chapter 2 Section 2. The composition of the reference, SNMA, and mechano-fluorescent, DASNMA, is indicated in Table 1. Molar percentages are relative to moles of monomer. 2-hydroxy-2-methylpropiophenone, HMP, is the initiator. DACL corresponds to the mechanophore cross-linker and 1,4-butanediol diacrylate, BDA, to the standard cross-linker. The mechanophore concentration, DACL, is given first in molar percent then in quantity per cubic meter of the final material (mol/m³). The Young's modulus at 25 °C, E, and glass transition temperature, Tg, were experimentally determined by uniaxial extension and DMA respectively (details in Chapter 2 Section 3).

Name	Monomer	HMP (mol%)	BDA (mol%)	DACL (mol%)	DACL (mol.m^{-3})	E (MPa)	Tg (°C)
SNMA	MA	1.16	0.43	0	0	1.5	18
DASNMA	MA	1.16	0.41	0.02	2.8	1.5	18

Table 1: Composition and properties of materials investigated in Section 1 to 3.

1.2 Crack propagation test

First, the stress-strain curve in uniaxial extension of un-notched single networks of polymethyl acrylate, SNMA, was plotted in Figure 1.

Then, crack propagation tests were performed on two notched samples (from two separate polymerizations) of SNMA and three notched samples (from three separate polymerizations) of DASNMA at 25 °C and at a crosshead velocity of 50 µm.s^{-1} (corresponding to a stretch rate of $\dot{\lambda} = 3 \times 10^{-3} \ s^{-1}$). Figure 2 represents an example of the stress-strain curve obtained on a notched sample DASNMA. The fracture energies, Γ_{exp}, were calculated using the Greensmith's approximation (Chapter 3, Eq. 3). Γ_{exp},

ranged from about 1700 to 3000 J.m^{-2}. As discussed in Chapter 2, the presence of the mechanophore does not change the elastic or the fracture behavior of the material. The poor reproducibility between crack propagation tests is due to the fact that notches are handmade and not fully identical (discussed in Chapter 3 Section 1).
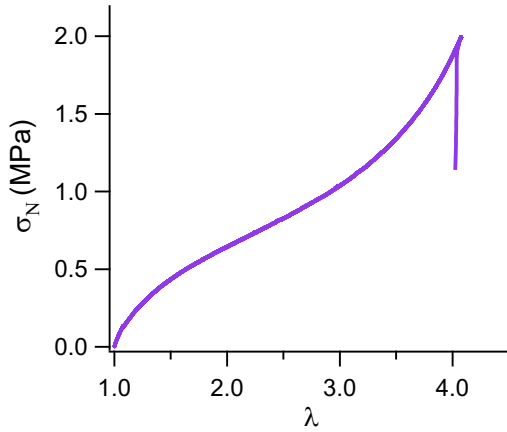

Figure 1: Stress-strain curve of uniaxial extension performed on SNMA at 25 °C and $\dot{\lambda} = 3 \times 10^{-3}\ s^{-1}$
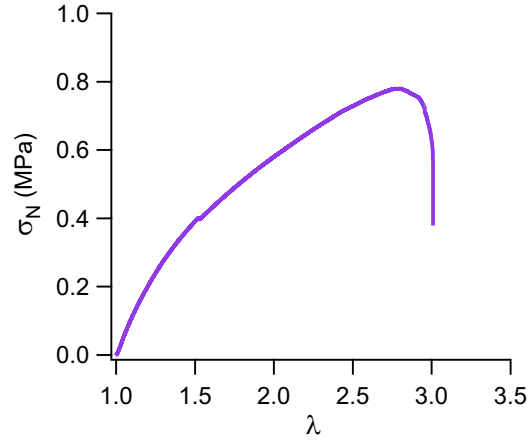

Figure 2: Stress-strain curve of crack propagation test performed on notched DASNMA at 25 °C and $\dot{\lambda} = 3 \times\ 10^{-3}\ s^{-1}$

1.3   Post-mortem quantitative LSCM damage analysis in standard conditions

Broken samples, from crack propagation tests (example in Figure 2) were analyzed by LSCM 'post-mortem'. For each crack propagation test, four single optical sections (two on each side) were recorded at a magnification 5x and at 100 μm depth from the surface.

Figure 3 represents an example of surface intensity plot of a raw image (from Nikon software) of the crack edge. Figure 4 corresponds to the same recorded single optical section but pre-processed and re-colored (using MATLAB software). Figure 4 was used for quantitative analysis. Intensity statistics was performed over an area of 150 px (along the crack edge) by 250 px (300-by-500 μm) as a function of the distance from the crack edge (details in Chapter 3 Section 4). An example of the evolution of the averaged fluorescence intensity with the distance normal to the crack edge is represented in Figure 5 (considering the same single optical section).

The fluorescence, reporting for damage, was visible at the micron scale even for single network elastomers.
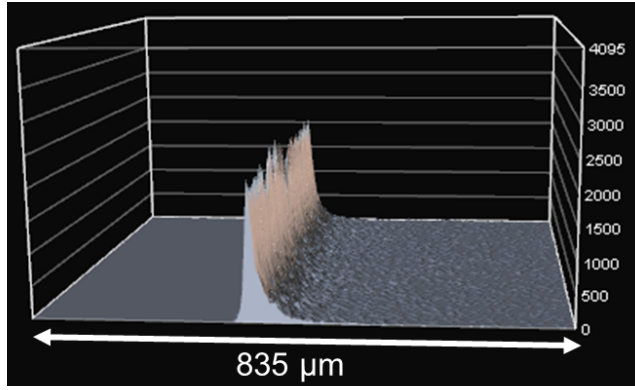
Figure 3: Surface intensity plot after crack propagation at 25 °C and $\dot{\lambda} = 3 \times 10^{-3} \, s^{-1}$ in DASNMA (Laser 10 Gain 3). 835µmx835µm.
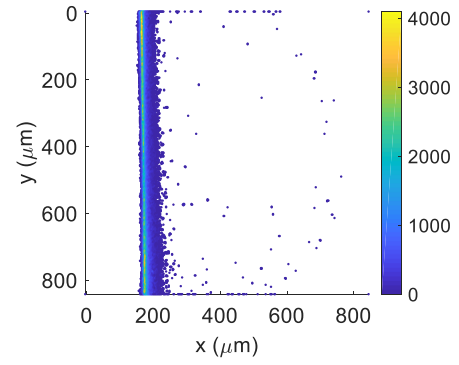

Figure 4: Pre-processed and re-colored image after crack propagation 25 °C and $\dot{\lambda}=3 \times 10^{-3} \, s^{-1}$ in DASNMA (Laser 10 Gain 3)
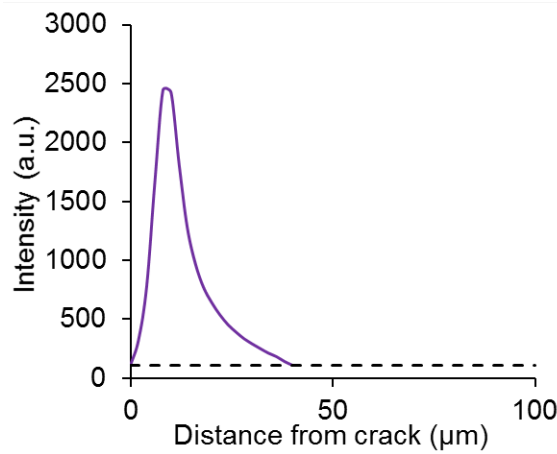

Figure 5: Example of intensity profile after crack propagation in DASNMA at $\dot{\lambda} = 3 \times 10^{-3} \, s^{-1}$ and at 25 °C. The cut-off (dotted line) is at noise level

The quantitative analysis of the fluorescent signal after fracture, described in Chapter 3 Section 4 for multiple networks, is also suitable for single networks. The intensity detected above the noise level was converted into concentration of activated mechanophores using a calibration curve. The quantity of activated mechanophore was normalized by the initial concentration of mechanophore to get a fraction of activation. By considering that this fraction of activation is representative of the fraction of chains broken, we first obtain the density of bonds broken per unit volume for each pixel and after an integration over a characteristic distance, the number, Σ_{exp}, of broken chains, per square meter (more details in Chapter 3, Section 4).

For each image, the areal density, Σ_{exp}, of broken chains was estimated. The length, L_{damage}, over which damage was detected was also calculated. Figure 6a and Figure 6b show the reproducibility of the measurements for standard conditions. In those conditions, the damage was detected over about 60 µm from the fracture plane. It is worth

noting that this length is much higher than the mesh size (hundreds of angstroms). Even in single network elastomers (polymethyl acrylate at 25 °C and $\dot{\lambda} = 3 \times 10^{-3} s^{-1}$), the damage occurs in a volume.
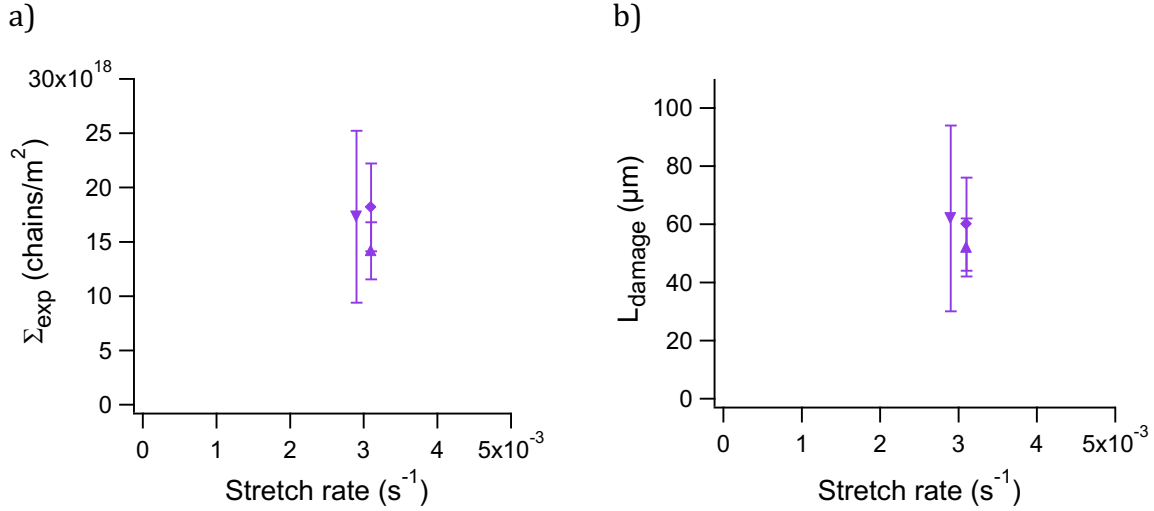
a)

b)

Figure 6: Reproducibility of the areal density of broken chains, Σ_{exp} (a) and the length, L_{damage}, over which damage was detected (b). Average value calculated over 4 pictures, error bar correspond to the standard deviation. Different symbols correspond to samples from separate polymerizations.

Σ_{exp} can be normalized by the areal chain density Σ_{SN}, to give $\bar{\Sigma}$, (details in Chapter 3, section 4). Average values of this normalized number of broken chains are represented as a function of the macroscopically measured fracture energy, Γ_{exp}, Figure 7.
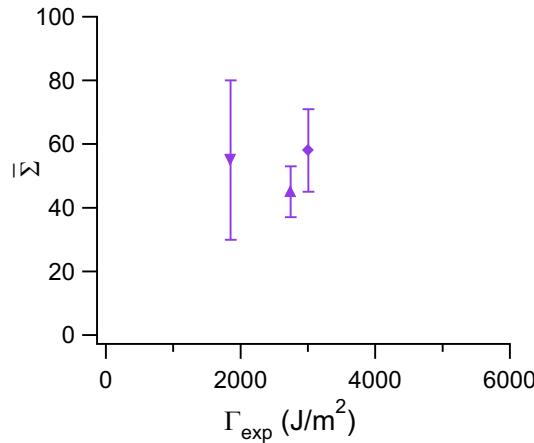

Figure 7: Evolution of the normalized number, $\bar{\Sigma}$, of broken chains with the fracture energy for crack propagation test on DASNMA at 25 °C and $\dot{\lambda} = 3 \times 10^{-3} s^{-1}$. Average value calculated over 4 pictures, error bar correspond to the standard deviation. Different symbols correspond to samples from separate polymerizations.

The number of broken chains per unit area of crack, in those test conditions (25°C and $\dot{\lambda} = 3 \times 10^{-3} s^{-1}$) estimated by our method, is about 50 times a monolayer, corresponding to the number used in Lake-Thomas model (Lake Thomas theory

presented in Chapter 1 Section 1). Not only the chains crossing the crack plane are broken but fracture must occur over a volume as obvious also from Figure 5.

From the number, Σ_{exp}, of broken chains, a value of energy dissipated from bond scission, Γ_{damage}, can be estimated. In order to do so, an assumption on the energy dissipated per chain is needed. Inspired from Lake-Thomas theory, we assumed that the total bond energy of each bond of the stretched chain is irreversibly lost. The Lake-Thomas theory predicts the intrinsic fracture toughness, Γ_0, given Eq 2.

$$\Gamma_0 = N_x U_b \Sigma \qquad \text{Eq 2.}$$

Where N_x is the number of carbon-carbon bonds between cross-links (about 140 carbon-carbon bonds, estimated from Eq 3.), U_b is the bond energy (350 kJ.mol^{-1} for a carbon-carbon bond) and Σ is the areal density of chain crossing the plane of the crack, corresponding to the number of broken chains in Lake-Thomas prediction ($\Sigma \sim 3 \times 10^{17}$ chains).

N_x was estimated from the affine model of rubber elasticity (5), Eq 3.

$$N_x = \frac{2}{M_{monomer}} \left(\frac{3 \rho R T}{E} \right) \qquad \text{Eq 3.}$$

Where $M_{monomer}$ is the molecular weight of the monomer (in g/mol) and E the Young's modulus.

Adapted from Eq 2., the breakage component of the fracture energy, Γ_{damage}, was estimated by Eq 4.

$$\Gamma_{damage} = N_x U_b \Sigma_{exp} \qquad \text{Eq 4.}$$

Γ_{damage} was plotted as a function of Γ_{exp}, as shown in Figure 8a. Γ_{damage} cannot be lower than Γ_0, as it is the energy needed to break a monolayer. Γ_{damage} cannot be higher than Γ_{exp} the macroscopically measured fracture energy, since Γ_{exp} takes into account all the energy dissipation mechanisms, such as the viscoelastic dissipation, in addition to damage. Γ_{damage} is included in Γ_{exp} and represents only the contribution from chain scission.

Γ_{damage} calculated using the Lake-Thomas assumption is in a good range but seems high. Indeed, the crack propagated in single networks of polymethyl acrylate at 25 °C, close to

the glass transition temperature and viscoelasticity is expected to have an important contribution to the energy dissipation.

As discussed in Chapter 1 Section 1.5, S. L. Craig and co-workers suggested an adjustment to the energy parameter of the Lake-Thomas theory (6). From the force-elongation curve of a single polymer chain at the fracture point, they refine the estimation of the energy, U, dissipated per broken chain to about 64 kJ/mol that is five times lower than the carbon-carbon bond dissociation energy. This difference is mainly due to the fact that the chain does not need to extended all its chemical bonds to break.

We calculated the breakage component of the fracture energy, $\Gamma_{damage}\ adjusted$, based on this more realistic energy estimation, Eq 5.

$$\Gamma_{damage}\text{adjusted} \ = \ N_x U \ \Sigma_{exp}$$ Eq 5.

$\Gamma_{damage}\ adjusted$ was plotted as a function of Γ_{exp}, as shown in Figure 8b.

The results, obtained using U instead of U_b, seem more realistic. $\Gamma_{damage}\ adjusted$ is higher than Γ_0 and clearly lower than Γ_{exp}.
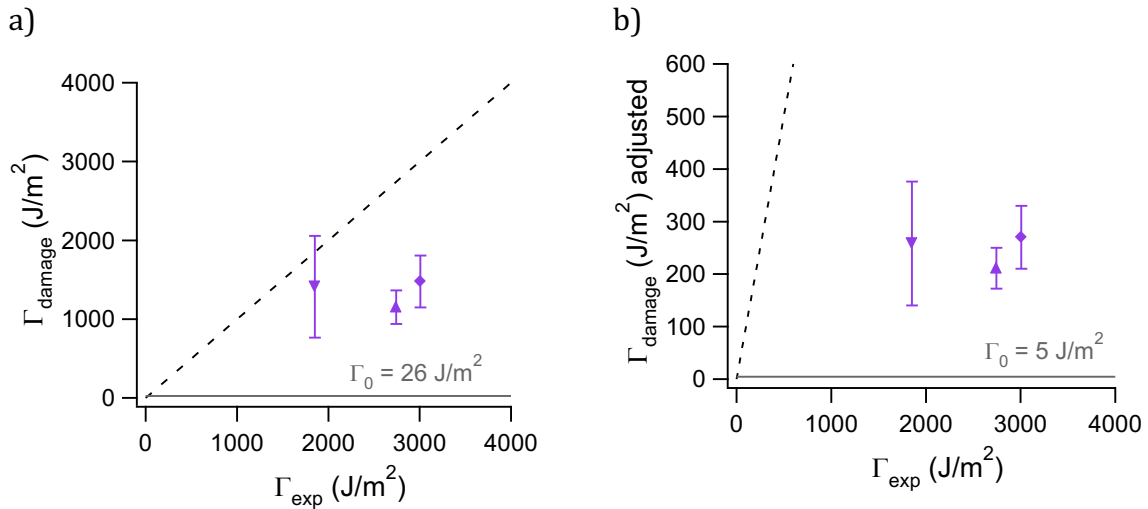

Figure 8: *Evolution of Γ_{damage} (using U_b=350 kJ/mol) (a) and Γ_{damage} adjusted (using U=64 kJ/mol) (b) with Γ_{exp} for crack propagation test on DASNMA at 25 °C and $\dot{\lambda} = 3 \times 10^{-3}\ s^{-1}$. Average value calculated over 4 pictures, error bar correspond to the standard deviation. Different symbols correspond to samples from separate polymerizations. Dotted line corresponds to $\Gamma_{damage} = \Gamma_{exp}$ curve. Γ_0 is the intrinsic fracture toughness.*

This result suggests that the Lake and Thomas theory may give a good scaling prediction for the fracture energy thanks to a compensation of an overestimate and an underestimate. In fact, the energy dissipated per chain is estimated by its maximum value (the addition of every C-C bond energy) and the number of broken chain is estimated by

its minimum value (a molecular plane). In a more realistic point of view, the intrinsic fracture energy has to be lower than the classical Lake-Thomas prediction.

We should note however, that at 25°C the fracture of a polymethyl acrylate network is far from the threshold conditions relevant to the Lake and Thomas model.

One can note that the error bars for the L_{damage} are important. An increase of the damage length scale with increasing distance from the initial notch (along the crack surface) is frequently observed. In Figure 9, the length scale of the damage closer to the notch is smaller than the length further away from the notch. The crack propagated from the bottom to the top of the picture. This increase in damage length can be due to an acceleration of the crack. In fact, in the geometry used (1 mm notch on a 5 mm width sample), the energy release rate increases with crack length so that crack will accelerate once it starts to move. Experiment at different speeds were done to elucidate if the speed has an influence on the damage. The results are presented in the next section.
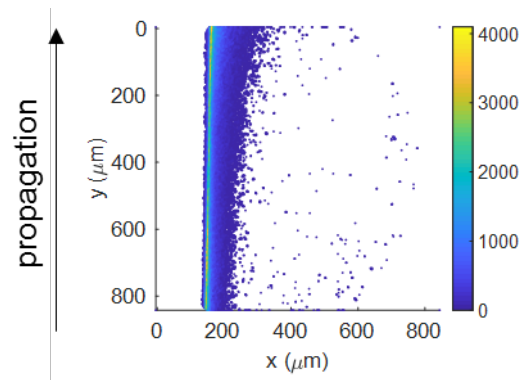

Figure 9: Pre-processed and re-colored image of a DASNMA where crack propagated from the bottom to the top of the image, taken far away from the notch (Laser 10 Gain 3)

2 Influence of stretch rate on bond scission in the fracture of single networks

2.1 Crack propagation tests at different stretch rates

Crack propagation tests were performed, on notched polymethyl acrylate networks, at 25 °C at three different crosshead velocities: 5 µm/s, 50 µm/s and 500 µm/s corresponding to stretch rates of $\dot{\lambda} = 3 \times 10^{-4}\ s^{-1}$, $\dot{\lambda} = 3 \times 10^{-3} s^{-1}$ and $\dot{\lambda} = 3 \times 10^{-2}\ s^{-1}$ respectively. An example of stress-strain curves at each stretch rate is given in Figure 10. One reference sample (SNMA) and three mechano-fluorescent samples (DASNMA) were tested.

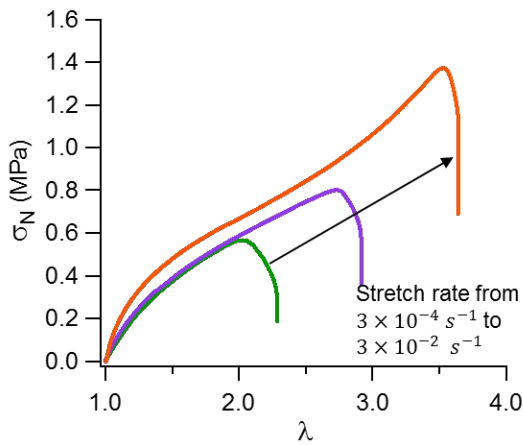As expected, at higher stretch rate, the stress and strain at break were enhanced.

Figure 10: Example of stress-strain curve of crack propagation test on notched DASNMA at 25 °C and at $\dot{\lambda} = 3 \times 10^{-4}\ s^{-1}$ (in green), $\dot{\lambda} = 3 \times 10^{-3}\ s^{-1}$ (in purple) and $\dot{\lambda} = 3 \times 10^{-2}\ s^{-1}$ (in orange). Three DASNMA and one SNMA were tested.
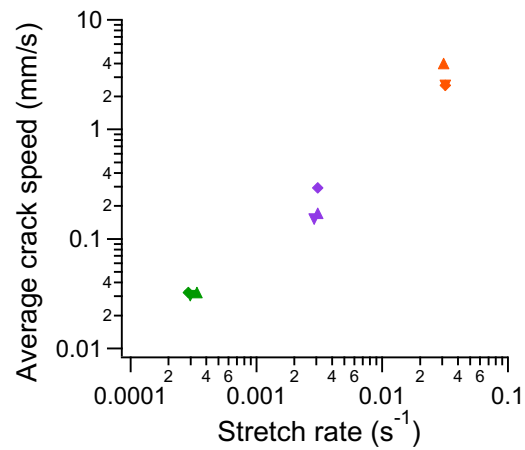
Figure 11: Evolution of the average crack speed, v_{crack}, as a function of stretch rate. Different symbols correspond to samples from separate polymerization.

First, the correlation between stretch rate and crack speed was verified. The stretch rate was estimated by the initial slope of the deformation *vs.* time curve. The mean crack velocity, v_{crack}, was estimated by dividing the propagation length, $d_{propagation}$, by the time to failure, $t_{propagation}$, Eq 6.

$$v_{crack} = \frac{d_{propagation}}{t_{propagation}} \qquad \text{Eq 6.}$$

This speed is an average over the sample width and cannot be considered as a local speed. The averaged crack speed was plotted as a function of the stretch rate, as shown Figure

11. Stretch rate correlated well with average crack speed suggesting that the propagation of the crack is controlled by the viscoelastic dissipation in the sample.

In the following fracture energies, Γ_{exp}, were calculated from Greensmith's approximation (Chapter 3, Eq. 3) and plotted against stretch rate, Figure 12. As expected, a clear trend is visible: higher fracture energies are reached with faster pulling.
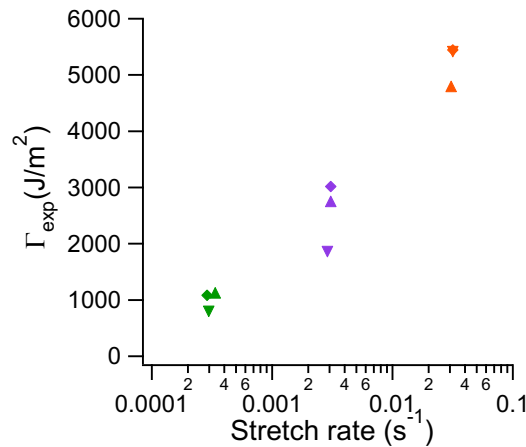

Figure 12: Evolution of the macroscopically measured fracture energy with the stretch rate. Different symbols correspond to sample from separate polymerization.

The question of the influence of the loading rate on bond scission will now be addressed.

2.2 Post-mortem quantitative LSCM analysis of bond scission

For each crack propagation test, four single optical sections (two on each side) were recorded at magnification 5x and 100 μm depth. Figure 13a,c,e represent examples of surface intensity plots of raw images at each stretch rate. Figure 13b,d,f represent corresponding pre-processed and re-colored 'post-mortem' image ready for MATLAB analysis. The fluorescence, reporting for damage, appeared to increase with the crack propagation speed.

Following the procedure described in Chapter 3 Section 4, the averaged evolutions of the fluorescence intensity as a function of distance from the crack plane were plotted, as shown in Figure 14. The maximum intensities are similar for all three stretch rates. The distance over which the damage is detected however evolved.
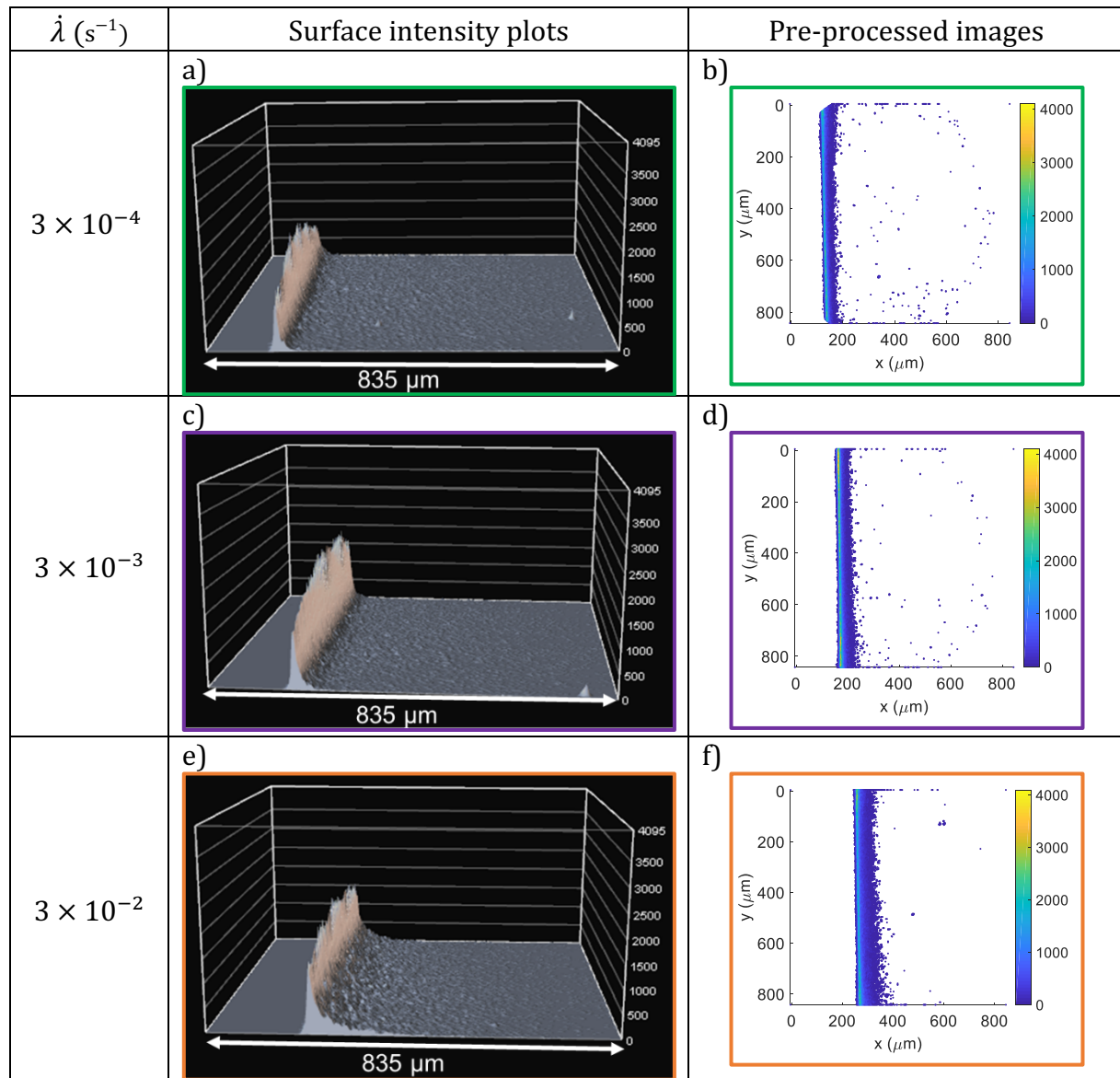
171

$\dot{\lambda}$ (s^{-1})	Surface intensity plots	Pre-processed images
3×10^{-4}	a)	b)
3×10^{-3}	c)	d)
3×10^{-2}	e)	f)

Figure 13: Surface intensity plots and pre-processed (re-colored) pictures after crack propagation in DASNMA at 25 °C and $\dot{\lambda}$ = 3×10^{-4} s^{-1} (a and b), 3×10^{-3} s^{-1} (c and d) and 3×10^{-2} s^{-1} (e and f) (Laser 10 Gain 3)
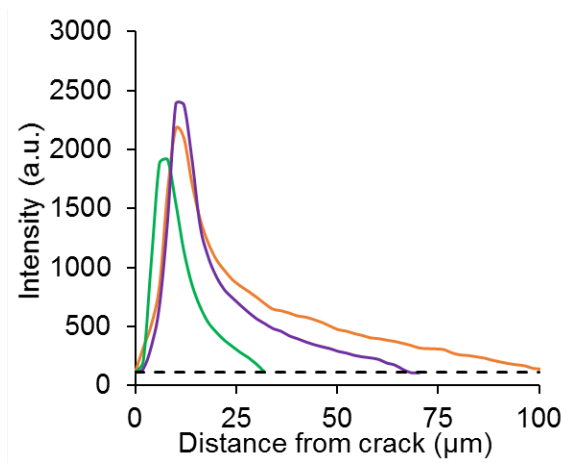
Figure 14: Evolution of the intensity with the distance to the crack edge in DASNMA broken at 25 °C and at $\dot{\lambda}$= 3×10^{-4} s^{-1} (green), $\dot{\lambda}$ = 3×10^{-3} s^{-1} (purple) and $\dot{\lambda}$ = 3×10^{-2} s^{-1} (orange). The cut-off is at noise level.

To compare the different stretch rates quantitatively, the number, Σ_{exp}, of broken chains per square meter was calculated and plotted as a function of stretch rate, as shown in Figure 15. The evolution of the macroscopically measured fracture energy, Γ_{exp}, with the stretch rate is also reported on Figure 15. Despite the uncertainty, an increase of Σ_{exp} with stretch rate is visible. Γ_{exp} is however multiplied by 5 between the lowest and the highest loading rate, while Σ_{exp} is only multiplied by 2. Γ_{exp} increases therefore faster than Σ_{exp}.

Σ_{exp} can be normalized by the areal chain density Σ_{SN}, to give $\bar{\Sigma}$, (details in Chapter 3, Section 4). Figure 16 represents the evolution of $\bar{\Sigma}$ with stretch rate. The areal density of broken chains increases with stretch rate from 30 to 60 times a monolayer.
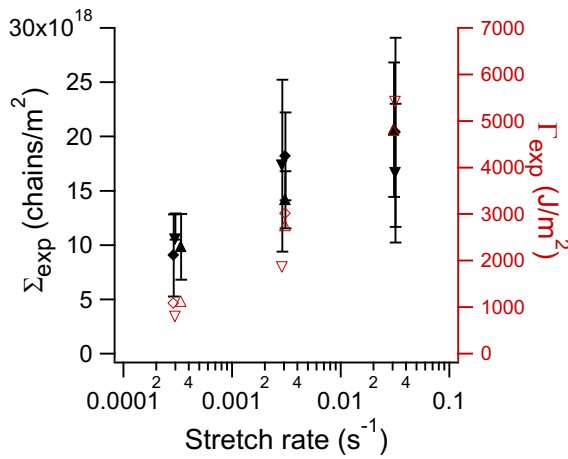

Figure 15: Evolution of the number, Σ_{exp}, of broken chain (in black) and of the fracture energy, Γ_{exp}, (in red) as a function of the stretch rate in DASNMA. Average value calculated over 4 pictures, error bar correspond to the standard deviation. Different symbols correspond to samples from separate polymerizations.
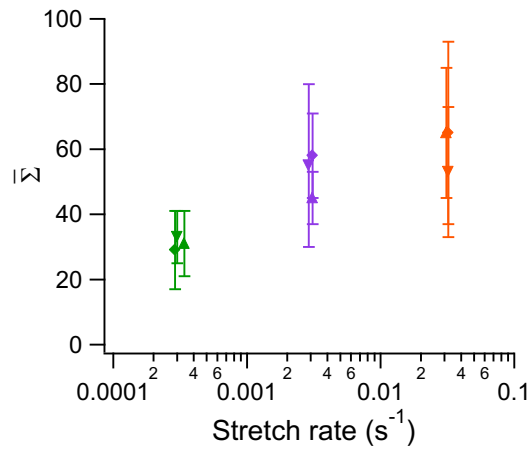
Figure 16: Evolution of the normalized number, $\bar{\Sigma}$, of broken chain as a function of the stretch rate in DASNMA. Average value calculated over 4 pictures, error bar correspond to the standard deviation. Different symbols correspond to samples from separate polymerizations.

The length, L_{damage}, over which the damage was detected was also calculated and plotted as a function of the stretch rate, as shown in Figure 17. Even if the error bars are not negligible, the length over which damage is detected increases with loading rate, from ~30 μm at $\dot{\lambda} = 3 \times 10^{-4} s^{-1}$ to ~60 μm at $\dot{\lambda} = 3 \times 10^{-2} s^{-1}$.

Figure 17: Evolution of the length, L_{damage}, over which damage is detected as a function of the stretch rate after crack propagation in DASNMA. Average value calculated over 4 pictures, error bar correspond to the standard deviation. Different symbols correspond to samples from separate polymerizations.
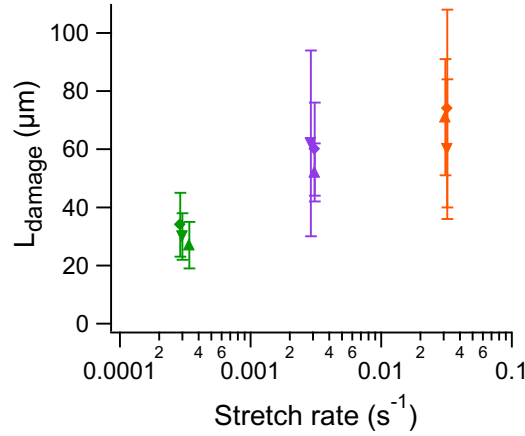
The quantitative analysis shows that the size of the damage zone and the areal density of broken bonds both increase with loading rate and with crack speed. The increase of fracture energy Γ with loading rate is not only due to viscoelastic dissipation but also to increased chains breakage and both processes are coupled.

To better visualize the contribution of chains breakage to the increase in fracture toughness, the breakage component of the fracture energy, Γ_{damage}, was estimated from Σ_{exp} (Eq 4. U_b = 350 kJ/mol) and plotted as a function of the macroscopically measured fracture energy, Γ_{exp} (Chapter 3, Eq. 3), as shown in Figure 18a. At low loading rate, Γ_{exp} is very close to Γ_{damage}. For one sample Γ_{damage} is higher than Γ_{exp} which confirm that U_b overestimate the energy dissipated by polymer strand.

Craig and co-worker adjustment (6) to the Lake-Thomas theory was applied to calculate Γ_{damage} *adjusted* (Eq 5. U = 64 kJ/mol). Γ_{damage} *adjusted* was plotted as a function of Γ_{exp}, as shown Figure 18b. This result is more consistent since all values of Γ_{damage} *adjusted* are significantly lower than Γ_{exp}.
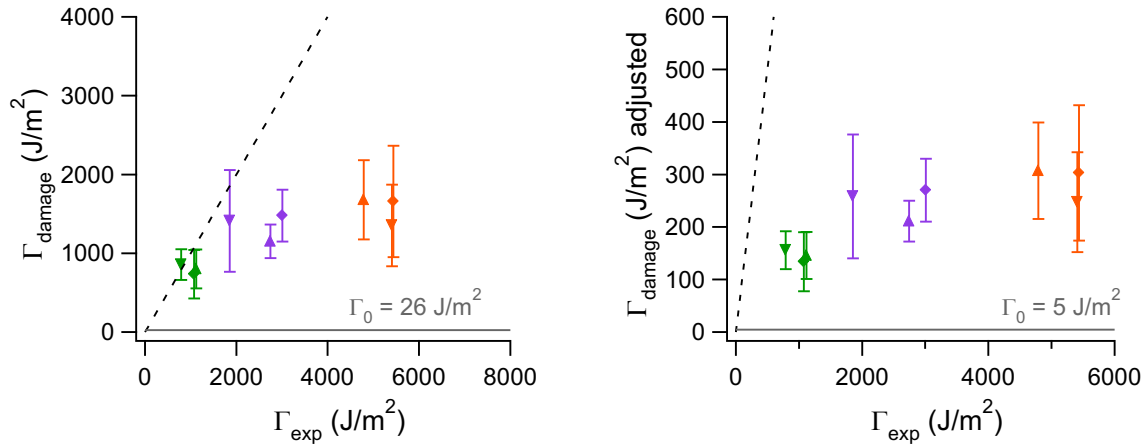
Figure 18 : Evolution of Γ_{damage} (using U_b=350 kJ/mol) (a) and Γ_{damage} adjusted (using U=64 kJ/mol) (b) with Γ_{exp} for crack propagation test on DASNMA at 25 °C and different loading rates $\dot{\lambda} = 3 \times 10^{-4} \, s^{-1}$ (in green), $3 \times 10^{-3} \, s^{-1}$ (in purple) and $3 \times 10^{-2} \, s^{-1}$ (in orange). Average value calculated over 4 pictures, error bar correspond to the standard deviation. Different symbols correspond to samples from separate polymerizations. Dotted line corresponds to $\Gamma_{damage} = \Gamma_{exp}$ curve.

With increasing loading rate, Γ_{exp} increases faster than Γ_{damage}. Indeed, at low loading rate, viscoelastic dissipation is reduced and the chains breakage contribution is relatively speaking more important. With increasing loading rate, viscoelastic dissipation increases and its contribution increases.

This trend is highlighted in Figure 19, where the ratio $\frac{\Gamma_{damage}}{\Gamma_{exp}}$ is plotted as a function of stretch rate. The overestimate using the classical Lake-Thomas assumption (in pink) is clearly visible as the ratio gets higher than the unity. As it seems more relevant, in the following sections, Γ_{damage}adjusted will be calculated directly (using 64 kJ/mol) and Γ_{damage} (using 350 kJ/mol) will not be presented.

Using the adjusted estimation of the energy dissipated by polymer strand (in blue), the contribution of chain breakage to the macroscopically measured fracture energy goes from 15 % at $\dot{\lambda} = 3 \times 10^{-4} \, s^{-1}$ to 10 % at $\dot{\lambda} = 3 \times 10^{-3} \, s^{-1}$ to 6 % at $\dot{\lambda} = 3 \times 10^{-4} \, s^{-1}$.

To conclude, with increasing stretch rate, both viscoelastic dissipation and dissipation by chain breakage increase in a coupled way. However, in these conditions (SNMA at 25 °C), the increase of the dissipation by chain breakage is not the dominant parameter compared to all other dissipative mechanisms involved.
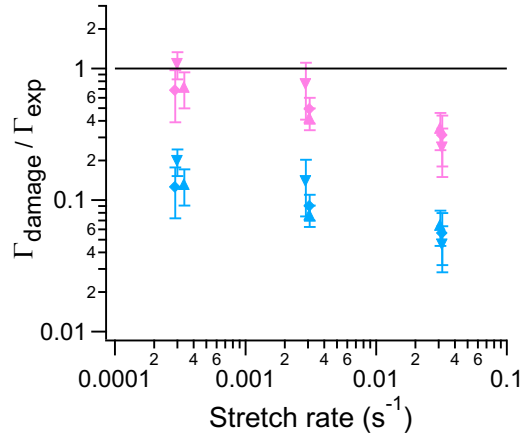
Figure 19: Evolution of $\Gamma_{damage}/\Gamma_{exp}$ with the loading rate for crack propagation test on DASNMA at 25 °C. Γ_{damage} calculated using Ub=350 kJ/mol (in pink) and using U=64 kJ/mol (in blue)

From Figure 10, it is also clearly visible that the elongation at break increases with stretch rate. $\bar{\Sigma}$ was plotted as a function of the elongation at break, Figure 20. $\bar{\Sigma}$ increases with λ_{break}. At higher stretch rate, the material withstands higher macroscopic deformations before the crack propagates and hence more bond scission occurs during the propagation itself.
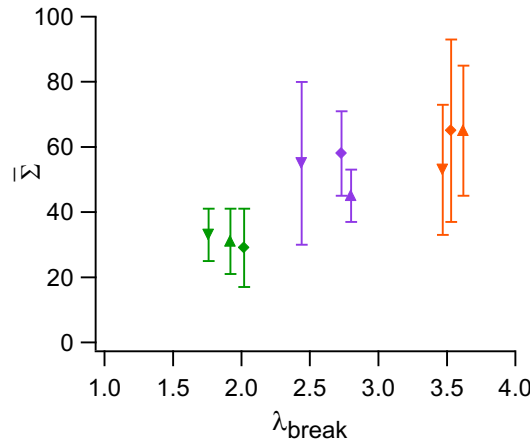

Figure 20: Evolution of the normalized number, $\bar{\Sigma}$, of broken chains with the elongation at break for crack propagation test on DASNMA at 25 °C and 3×10^{-4} s^{-1} (green), 3×10^{-3} s^{-1} (purple) and 3×10^{-2} s^{-1}. Average value calculated over 4 pictures, error bar correspond to the standard deviation. Different symbols correspond to samples from separate polymerizations.

All the crack propagation tests presented in this Chapter, up to that point, were performed at 25 °C on polymethyl acrylate. The experiment was done at a temperature close to the glass transition temperature (18 °C). Any simple network becomes tougher as the testing temperature approaches its glass transition and molecular friction is active (*2*). Viscoelastic dissipation was therefore enhanced at the tested temperature. The evolution of damage with increasing temperature is then the obvious next question to ask.

3 Influence of the temperature on bond scission in the fracture of single networks

3.1 Crack propagation tests at temperatures well above the Tg

The crosshead velocity of the crack propagation test was fixed at 50 μm/s (stretch rate of $\dot{\lambda} = 3 \times 10^{-3}\ s^{-1}$). Different temperatures were imposed, during the test, by a heating oven also connected to liquid nitrogen to regulate the temperature: 25 °C, 40 °C, 60 °C and 80 °C. Examples of stress-strain curves of crack propagation tests at each temperature are given in Figure 21. When increasing the temperature, the viscoelastic dissipation in the material decreases which for classical elastomers generally results in decreasing stress and strain at break (*4, 7*) (discussed in Chapter 1 Section 1).

The fracture energies were calculated here using the Greensmith's approximation from the singe-edge notch tests (Chapter 3, Eq. 3) and are plotted as a function of the temperature in Figure 22.

The intrinsic fracture energy predicted from the Lake-Thomas model, Γ_0, was calculated by Eq 5. (U = 64 kJ/mol) and represented by the grey line in Figure 22.
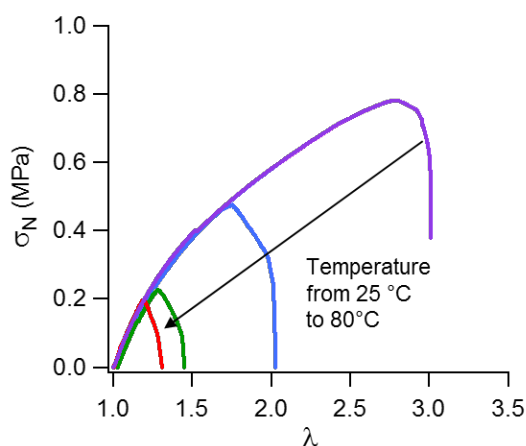
Figure 21: Example of stress strains curve of crack propagation test on notched DASNMA at $\dot{\lambda} = 3 \times 10^{-3}\ s^{-1}$ and at 25 °C (in purple), 40 °C (in blue), 60 °C (in green) and 80 °C (in red). One DASNMA and one SNMA were tested.
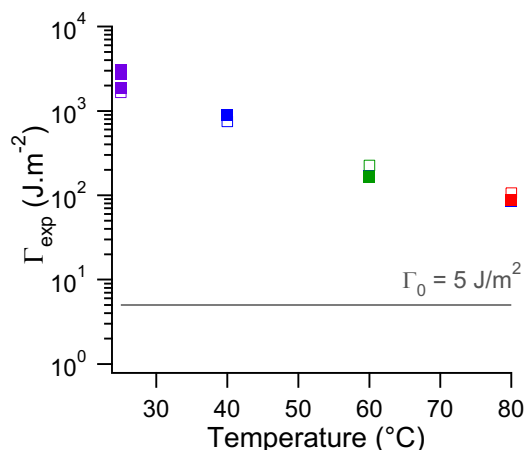
Figure 22: Evolution with the temperature of the fracture energy after crack propagation test in DASNMA, at $3 \times 10^{-3}\ s^{-1}$. Grey line indicates Lack Thomas adjusted prediction of Γ_0 (U=64 kJ/mol).

By increasing the temperature, the fracture energy decreases sharply and approaches Γ_0 but even at 80 °C (Tg + 62°C) the measured Γ_{exp} remains significantly higher than Γ_0. This decrease of Γ_{exp} with temperature is expected and can be understood qualitatively by the

differences in viscoelastic dissipation. Indeed, when the temperature approaches Tg, the dissipation factor tan δ in linear viscoelasticity increases and the viscous friction is enhanced. The evolution of the dissipation factor, obtained from dynamic mechanical analysis at 1% deformation, 1 Hz and 1°C/min temperature ramp (details in Chapter 2 Section 3), is plotted as a function of the temperature in Figure 23. It is obvious that in particular between 25 °C and 40 °C and then 40 °C and 60°C there are large drops in viscoelastic dissipation.
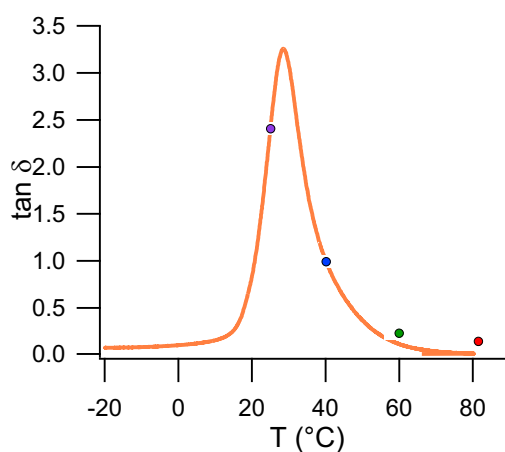
Figure 23: Evolution of tanδ with the temperature, analyzed by DMA, for DASNMA.

3.2   Post-mortem quantitative LSCM damage analysis

Damage was analyzed 'post-mortem' at room temperature in order to elucidate if the increase in toughness close to Tg, was only due to viscoelastic dissipation or if the chain scission mechanism was also affected by the temperature.

For each crack propagation test, four single optical sections (two on each side) were recorded at magnification 5x and 100 µm depth. Figure 24 a,c,e,g are examples of surface intensity plots (from Nikon software) at each temperature. Figure 24 b,d,f,h are same images but pre-processed and re-colored for the quantitative analysis. The fluorescence signal appeared brighter for the sample broken at 25 °C and decreased progressively with increasing temperature.

	Surface intensity plots	Pre-processed images
25 °C	a)	b)
40 °C	c)	d)
60 °C	e)	f)
80 °C	g)	h)

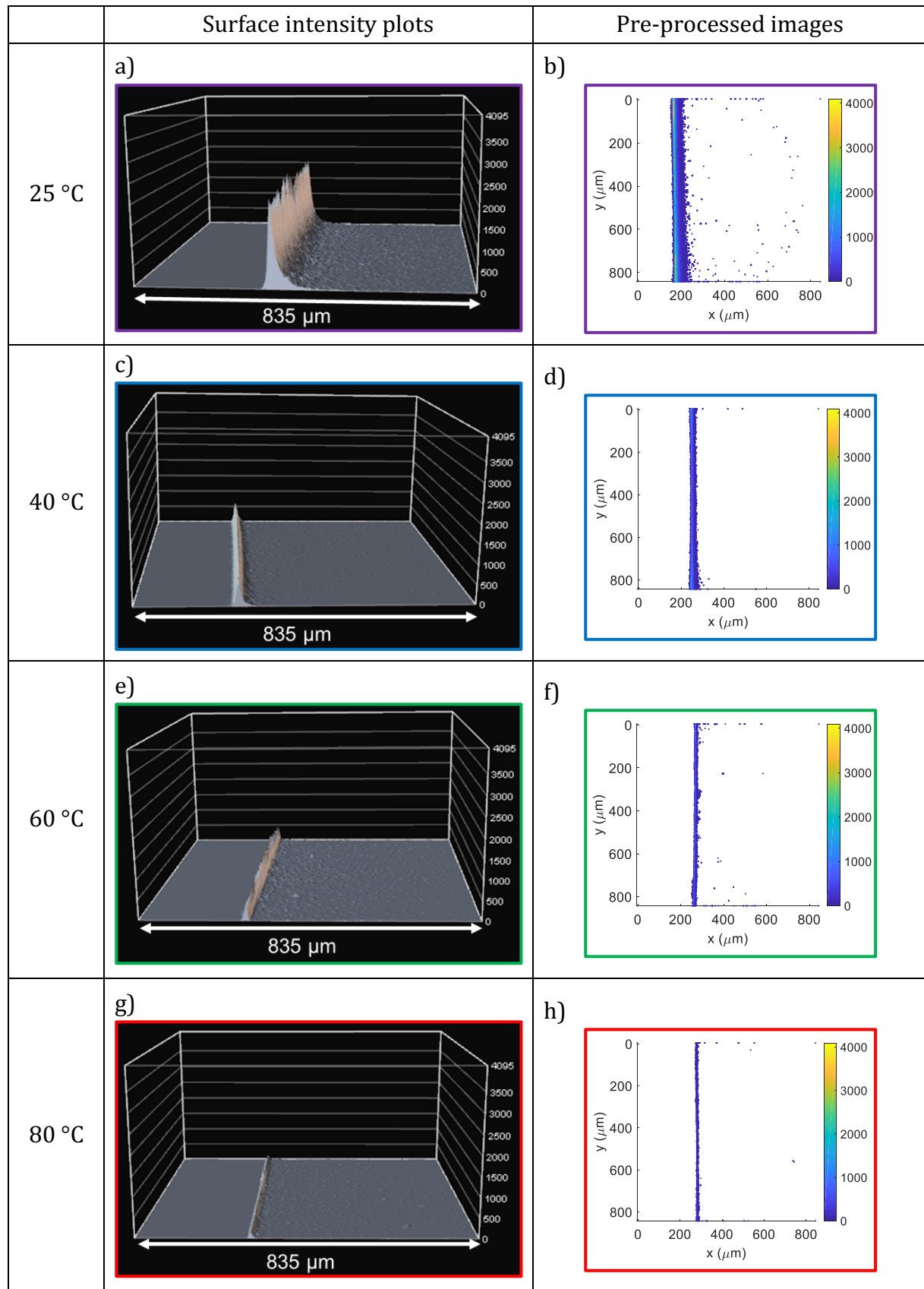*Figure 24: Surface intensity plots and pre-processed (re-colored) pictures after crack propagation in DASNMA at $3 \times 10^{-3} \ s^{-1}$ and 25 °C (a and b), 40 °C (c and d), 60 °C (e and f) and 80 °C (g and h) (Laser 10 Gain 3).*

Figure 25 represents the averaged intensity profiles, obtained from the method described in Chapter 3 section 4, from image analysis of Figure 24 b,d,f,h. The higher the temperature, the lower the maximal intensity and the smaller the distance over which damage was detected.
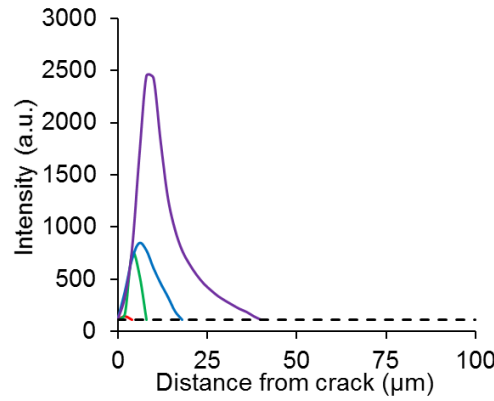

Figure 25: Evolution of the intensity with distance to the crack edge in DASNMA broken at 3×10^{-3} s^{-1} and at 25 °C (purple), 40 °C (blue), 60 °C (green) and 80 °C (purple). The cut-off is at noise level.

The areal density, Σ_{exp}, of broken chains was calculated and plotted as a function of the temperature, Figure 26. The macroscopically measured fracture energy, Γ_{exp}, calculated using Greensmith's approximation (Chapter 3, Eq. 3) was also plotted in Figure 26. Both, the macroscopic fracture energy and the number of broken chain decrease sharply with increasing temperature. Γ_{exp} is divided by 30 from 25 °C to 80 °C, and Σ_{exp} is divided by 10. Γ_{exp} decreases faster with increasing temperature than Σ_{exp}.
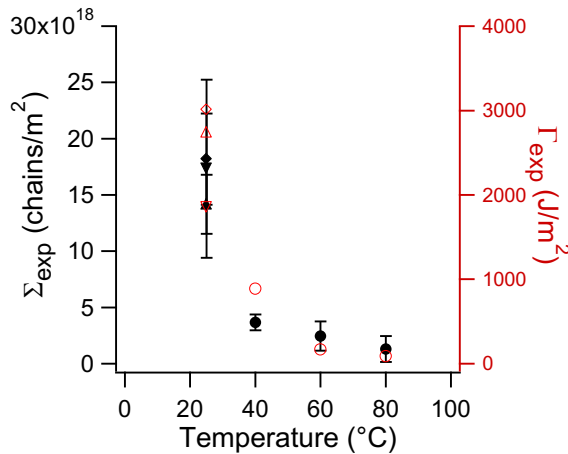
Figure 26: Evolution of the number, Σ_{exp}, of broken chain (in black) and of the fracture energy, Γ_{exp}, (in red) as a function of the temperature in DASNMA. Average value calculated over 4 images, error bar correspond to the standard deviation. Different symbols correspond to samples from separate polymerizations.
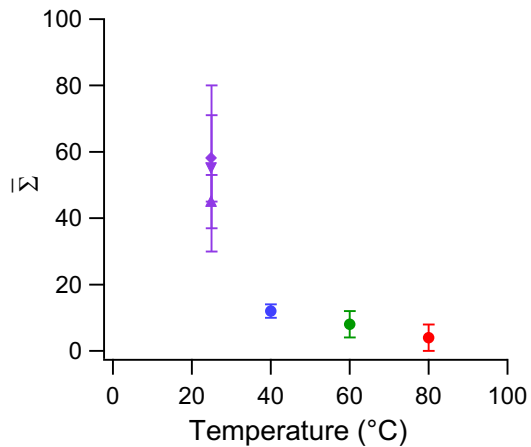
Figure 27: Evolution of the normalized number, $\bar{\Sigma}$, of broken chains with temperature on DASNMA at 3×10^{-3} s^{-1}. Average value calculated over 4 pictures, error bar correspond to the standard deviation. Different symbols correspond to samples from separate polymerizations.

Σ_{exp} was normalized by the areal chain density Σ_{SN}, to give $\bar{\Sigma}$, (details in Chapter 3, Section 4) and plotted as a function of the temperature in Figure 27. The areal density of broken chains is about 60 times higher than a monolayer at 25 °C and decreases down to 4 times a monolayer at 80 °C. As the temperature increases above Tg, the number of broken bonds decreases to become closer to the Lake-Thomas prediction of intrinsic fracture energy.

The length over which the damage was detected, L_{damage}, was also calculated and plotted as a function of the temperature in Figure 28. The damage length decreases with increasing temperature. At 60 °C and 80 °C, the limit of the method were almost reached since the fluorescence was detected over about only three pixels of 2 μm each. However, these values are still much higher than the mesh size.
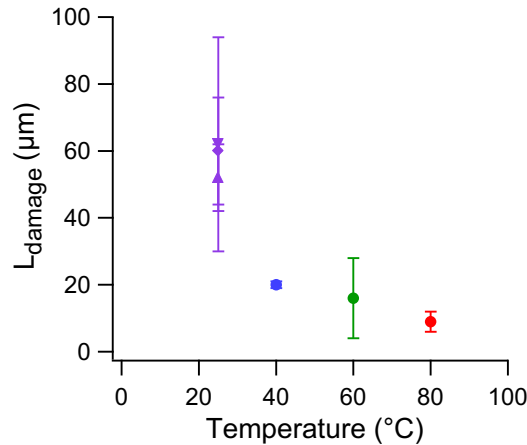
Figure 28: Evolution of the length over which damage is detected, L_{damage}, as a function of the temperature after crack propagation in DASNMA. Average value calculated over 4 images, error bar correspond to the standard deviation. Different symbols correspond to samples from separate polymerizations

Higher resolution observations can be made with a classical Laser Scanning Confocal Microscope using an objective of higher magnification. Thanks to a collaboration with the *Institut Pierre-Gilles de Gennes*, observations at higher magnification were possible. However, the quantification analysis was not adapted and no quantitative results are available (discussed in Chapter 3).

To better visualize the contribution of chains breakage to the increase in fracture toughness, the bond scission component of the fracture energy, Γ_{damage}, was estimated from Σ_{exp} (Eq 5. with U = 64 kJ/mol) and plotted as a function of the macroscopically measured fracture energy, Γ_{exp}.(Chapter 3, Eq. 3), as shown in Figure 29.

Figure 29: Evolution of Γ_{damage} (using U=64 kJ/mol) with Γ_{exp} for crack propagation test on DASNMA at $\dot{\lambda} = 3 \times 10^{-3} \ s^{-1}$ and at 25 °C (purple), 40 °C (blue), 60 °C (green) and 80 °C (red). Average value calculated over 4 pictures, error bar cor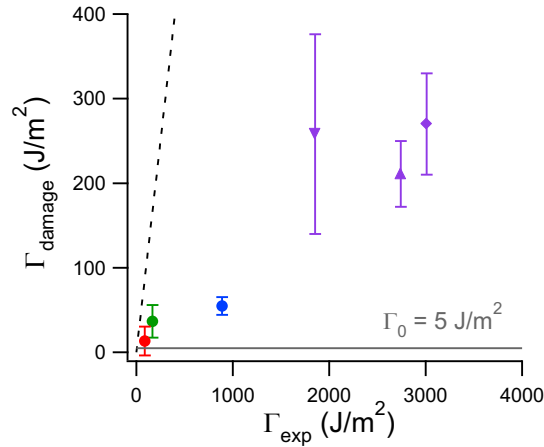respond to the standard deviation. Different symbols correspond to samples from separate polymerizations. Dotted line corresponds to $\Gamma_{damage} = \Gamma_{exp}$ curve.

It seems that at high temperature, Γ_{exp} gets closer to Γ_{damage}, and that Γ_{exp} increases faster than Γ_{damage} as the temperature is lowered closer to Tg.

To better visualize the trend, the ratio $\dfrac{\Gamma_{damage}}{\Gamma_{exp}}$ estimated with the adjusted assumption was calculated and plotted as a function of temperature, as shown Figure 30.

The trend is not as clear as for the loading rate. However, an increase of the bond breakage contribution still appears as it goes from ~10 % at 25 °C to ~20 % at 80 °C.

The importance of the synergy between all dissipative mechanisms is highlighted. Indeed, at high temperature, the viscoelastic dissipation is reduced, the macroscopically measured fracture energy is reduced but the molecular damage is also reduced. Each contribution slightly evolves, as the chain scission contribution increases with increasing temperature. However, the evolution of Γ_{exp}, is multiplied by 30 between 80 °C and 25 °C, and cannot be explained by a change in viscoelasticity only.
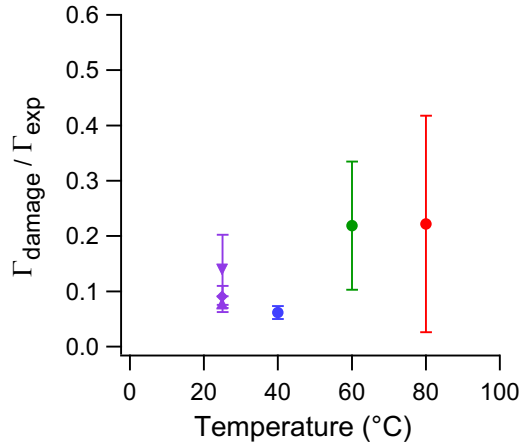
Figure 30: Evolution of $\Gamma_{damage}/\Gamma_{exp}$ with the temperature for crack propagation test on DASNMA at $\dot{\lambda} = 3 \times 10^{-3}\ s^{-1}$. Γ_{damage} calculated using U=64 kJ/mol

From Figure 21, an increase of the stress at break with temperature when getting closer to Tg is visible. $\bar{\Sigma}$ was plotted as a function of the elongation at break in Figure 31. The normalized areal density of chain scission increases monotonically with the elongation at break.
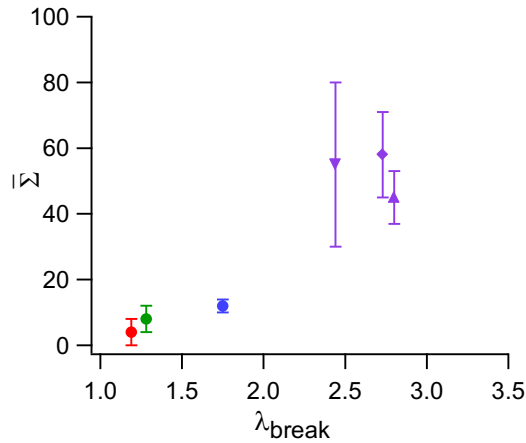
Figure 31 : Evolution of the normalized number, $\bar{\Sigma}$, of broken chains with the elongation at break for crack propagation test on DASNMA at $3 \times 10^{-3}\ s^{-1}$ and 25 °C (purple), 40 °C (blue), 60 °C (green) and 80 °C (red). Average value calculated over 4 pictures, error bar correspond to the standard deviation. Different symbols correspond to samples from separate polymerizations.

The quantitative analysis shows that the size of the damage zone and the areal density of broken bonds both increase with decreasing temperature. The increase of fracture energy Γ as temperature becomes closer to the glass transition temperature is not only due to viscoelastic dissipation but also to the chains breakage increase and both processes are coupled.

In fact, at a temperature close to the glass transition, chain friction is enhanced. These frictions lead to viscoelastic dissipation during deformation. We can think of two effects due to chain friction:

1) The neighboring chains cannot relax and reorganize, causing generally higher stresses along the backbone chains (and an increased probability of scission at the same extension)

2) The load transfer from one broken bond to the next is less efficient and can be dissipated by friction. In other words as one highly extended chain breaks, the energy dissipated while it returns to the equilibrated random coil, is absorbed by the local friction. This process will delay the localization of bond breakage which initiate macroscopic fracture.

In other words the increased bond scission is not toughening the material per se (although it dissipates energy), but is a side effect of the existence of viscous friction at the monomer level.

As the temperature increases the chains can relax and the probability of scission decreases for a given stretch. However, the load transfer from one strand to the next is much more efficient in the absence of friction and favors localized bond scission and eventually crack propagation.

In the terms of Pierre Millereau, viscoelasticity favors random bond scission and early damage while elasticity delays random bond scission (the chains relax) but as soon as bonds start to break the correlated bond scission appears and localized fracture propagates.

4 Influence of the cross-linking density

4.1 Materials

After the stretch rate and the temperature, the influence of the crosslink density was investigated. Two single polymethyl acrylate networks with different levels of crosslinking density were compared to investigate its effect on damage during fracture. This work was done in collaboration with Victoria Waltz, another PhD student from our lab involved in the ERC project.

The total quantity of cross-linker introduced in the network was divided by two: from 0.43 mol% for SNMA to 0.22 mol% for $SNMA_{0.2}$. The materials composition are detailed in Table 2. Molar percentages are relative to moles of monomer. 2-hydroxy-2-methylpropiophenone, HMP, is the initiator. DACL corresponds to the mechanophore cross-linker and 1,4-butanediol diacrylate, BDA, to the standard cross-linker. The mechanophore concentration, DACL, is given first in molar percent then in quantity per cubic meter of the final material (mol/m^3).

Name	Monomer	HMP (mol%)	BDA (mol%)	DACL (mol%)	DACL (mol.m^{-3})
SNMA	MA	1.16	0.43	0	0
DASNMA	MA	1.16	0.41	0.02	2.8
$SNMA_{0.2}$	MA	1.16	0.22	0	0
$DASNMA_{0.2}$	MA	1.16	0.20	0.02	2.8

Table 2: Composition of materials investigated to compare the influence of the cross-linking density

4.2 Mechanical tests

The stress-strain curves of un-notched samples in uniaxial extension are given in Figure 32. With a higher level of cross-linker, the strain hardening occurs at lower extension. This result is consistent since the average chain length between cross-links decreases with increasing cross-linker concentration.
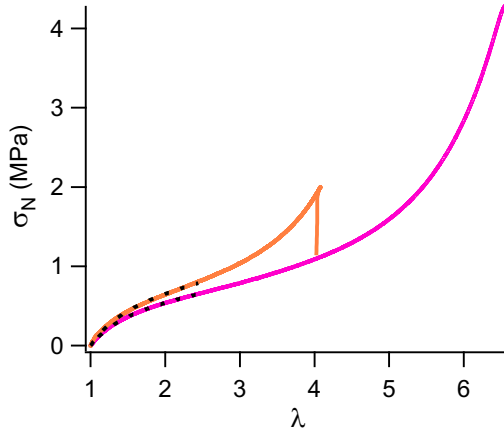
Figure 32: Stress-strain curve in uniaxial extension performed on SNMA (orange) and SNMA₀.₂ (pink) at 25 °C and $\dot{\lambda} = 3 \times 10^{-3} \ s^{-1}$. Rubinstein-Panyukov fit in dotted line.
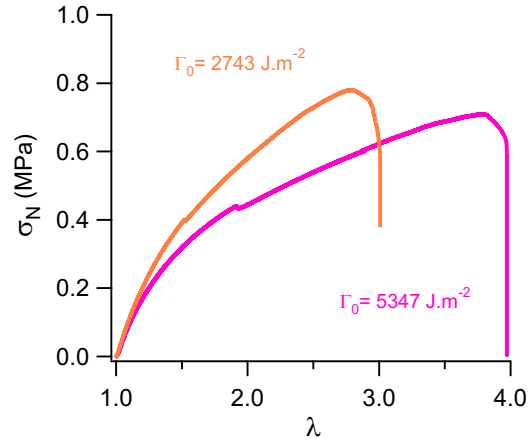
Figure 33: Stress-strain curve of crack propagation test on notched SNMA (orange) and SNMA₀.₂ (pink) at 25 °C and $\dot{\lambda} = 3 \times 10^{-3} \ s^{-1}$.

The initial part of the uniaxial extension curves were fitted with the Rubinstein and Panyukov model (presented in Chapter 2, Section 3) (*8*) in order to extract the contribution of crosslinks E_x and entanglement E_e. The fit is represented by dotted lines on Figure 32. The results are given in Table 3. The number, N_x, of carbon-carbon bonds between crosslinks was also estimated, from E and from E_x, Eq 7. adapted from Eq 3.

$$N_x \ = \ \frac{2}{M_{monomer}} \left(\frac{3\rho RT}{E_x} \right)$$
Eq 7.

	Total Cross-linker (mol%)	E (MPa)	N_x (unit) from E	E_x (MPa)	N_x (unit) from E_x	E_e (MPa)
SNMA	0.43	1.5	140	0.7	300	0.7
SNMA₀.₂	0.22	1.2	175	0.5	421	0.7

Table 3: Cross-linker concentration and moduli of considered materials

As expected, the contribution of entanglements, E_e, is the same. The cross-links contribution, E_x , is predicted to scale with N_x^{-1}, from the affine model of rubber elasticity (*5*). Dividing the cross-linker concentration by two, should multiply by two the average number of repeat units between crosslinks and to divide by two E_x. However, the ratio between cross-links contribution is not exactly two. We hypothesize that the free radical polymerization of SNMA₀.₂ was less homogenous.

Then, crack propagation tests were performed on both samples at 25 °C and $\dot{\lambda} = \ 3 \times 10^{-3} s^{-1}$. An example of stress-strain curves obtained for each sample is given in Figure 33. The macroscopically measured fracture energy Γ_{exp} is written by each curve

(calculated by Greensmith's approximation, Chapter 3, Eq. 3). From Lake Thomas theory the fracture energy should scale with $N_x^{1/2}$. Experimentally, the ratio between the Γ was not exactly $\sqrt{2}$ but the evolution went in the right direction.

4.3 Post-mortem quantitative LSCM damage analysis

Four single optical sections were recorded for each broken sample (two on each side) at magnification 5x and 100 µm depth. Figure 34 a and c are examples of surface intensity plots from raw images (Nikon software) after crack propagation in DASNMA and DASNMA$_{0.2}$ respectively. These images were then pre-processed using MATLAB, examples of images used for the quantitative analysis are presented in Figure 34 b and d.

	Surface intensity plots	Pre-processed images
SNMA	a)	b)
SNMA$_{0.2}$	c)	d)

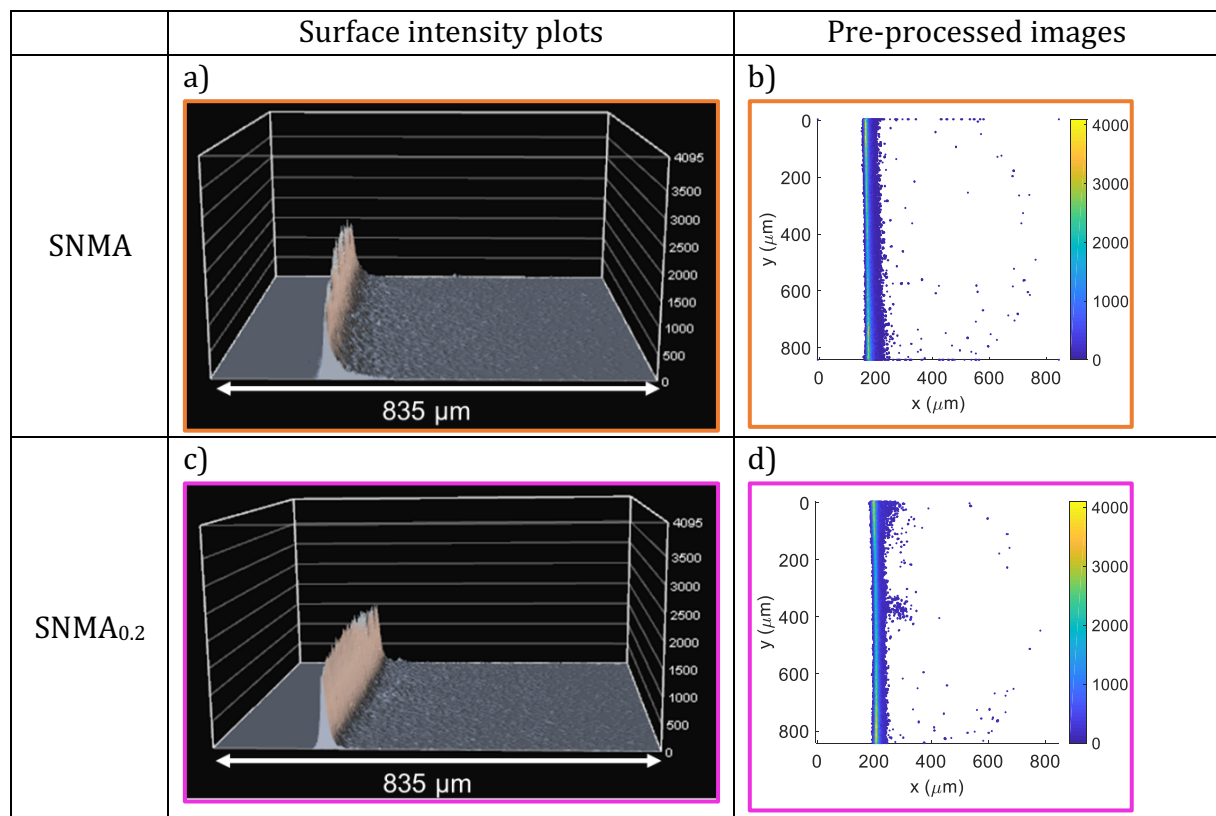*Figure 34: Examples of surface intensity plots (a and c) and pre-processed re-colored images (b and d) of DASNMA (a and b) and DASNMA$_{0.2}$ (c and d) after crack propagation at 3x10^{-3} s^{-1} and 25 °C. Laser 10 Gain 3.*

Surface intensity plots seem similar for both samples. Intensity profiles are obtained after performing intensity statistics as a function of the distance from the crack edge, Figure 35.
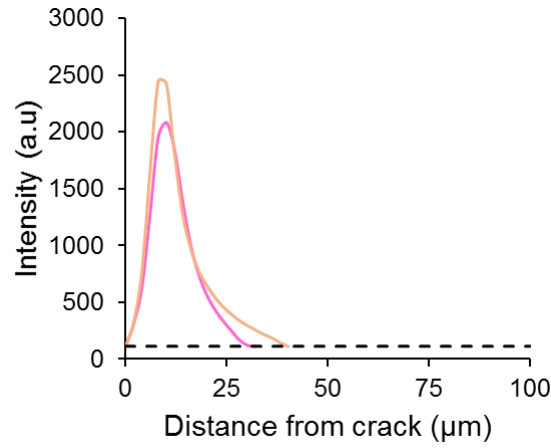
Figure 35: Evolution of the intensity with distance to the crack edge after crack propagation in DASNMA (orange) and DASNMA$_{0.2}$ at $\dot{\lambda} = 3x10^{-3}$ s^{-1} and at 25 °C. The cut-off is at noise level

Intensity profiles obtained for the two levels of cross-linking densities are comparable.

After LSCM analysis, the areal density, Σ_{exp}, of broken chains was calculated. Figure 36 represents the average value of Σ_{exp} calculated for four pictures as a function of the cross-linker concentration. The error bars represent the standard deviation. No significant difference was noticed. It seems that, at the microns length scale, there is no evolution of the number of broken chains from 0.2 to 0.4 mol% of cross-linker in polymethyl acrylate (at 25°C and $\dot{\lambda} = 3 \times 10^{-3}$ s^{-1}).
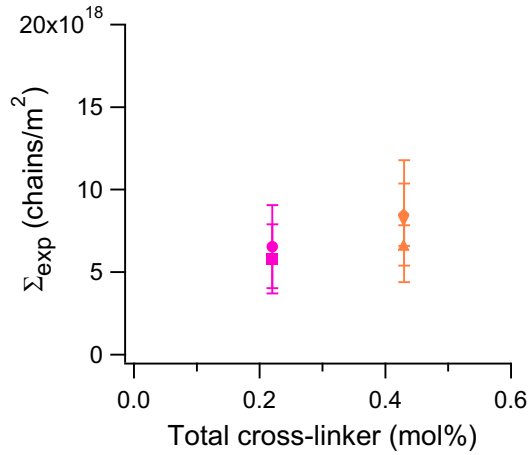
Figure 36: Evolution of the areal density of broken chains with the cross-linker concentration after crack propagation in DASNMA (orange) and DASNMA$_{0.2}$ (pink) at 25 °C and $\dot{\lambda}$ =3x10^{-3} s^{-1}. Average value calculated over 4 pictures, error bar correspond to the standard deviation. Different symbols correspond to samples from separate polymerizations.
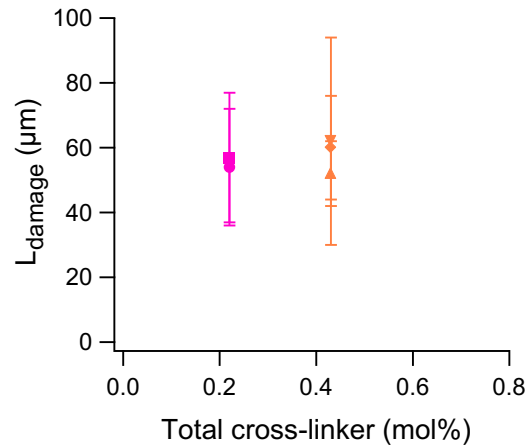
Figure 37: Evolution of the length over which damage is detected, L_{damage}, with the cross-linker concentration after crack propagation in DASNMA (orange) and DASNMA$_{0.2}$ (pink) at 25 °C and $\dot{\lambda}$ =3x10^{-3} s^{-1}. Average value calculated over 4 images, error bar correspond to the standard deviation. Different symbols correspond to samples from separate polymerizations

188

The length over which damage was detected was plotted as a function of the total cross-linker concentration, as shown in Figure 37. Despite the difference in the chain strand length, the length over which damage was detected was similar.

The amount of bond scission is similar but the length between cross-links is not. This trend is expected from Lake Thomas model: the same amount of bond scission leads to a higher dissipated energy for the less cross-linked material. To verify if the result can be rationalized by a Lake and Thomas argument, the breakage component of the fracture energy, Γ_{damage}, was estimated from Σ_{exp} (Eq 5., using U = 64 kJ/mol), as shown in Figure 38a. Γ_{damage} is slightly higher for the less cross-linked network but error bars are not negligible.

Table 4 is given to summarize results obtained for these two type of materials.

	Σ_{exp} $(chains.m^{-2})$	Σ $(chains.m^{-2})$	$\bar{\Sigma}$	Γ_{damage} $(J.m^{-2})$	Γ_{exp} $(J.m^{-2})$
SNMA	$(8 \pm 3) \times 10^{18}$	2.2×10^{17}	36 ± 12	246 ± 84	2535 ± 494
SNMA$_{0.2}$	$(6 \pm 2) \times 10^{18}$	1.8×10^{17}	34 ± 13	276 ± 105	4987 ± 361

Table 4: Molecular damage comparison in single networks at two cross-linking density

The relative contribution to the fracture energy, $\Gamma_{damage}/\Gamma_{exp}$, was calculated and plotted as a function of the total cross-linker concentration, as shown Figure 38b.
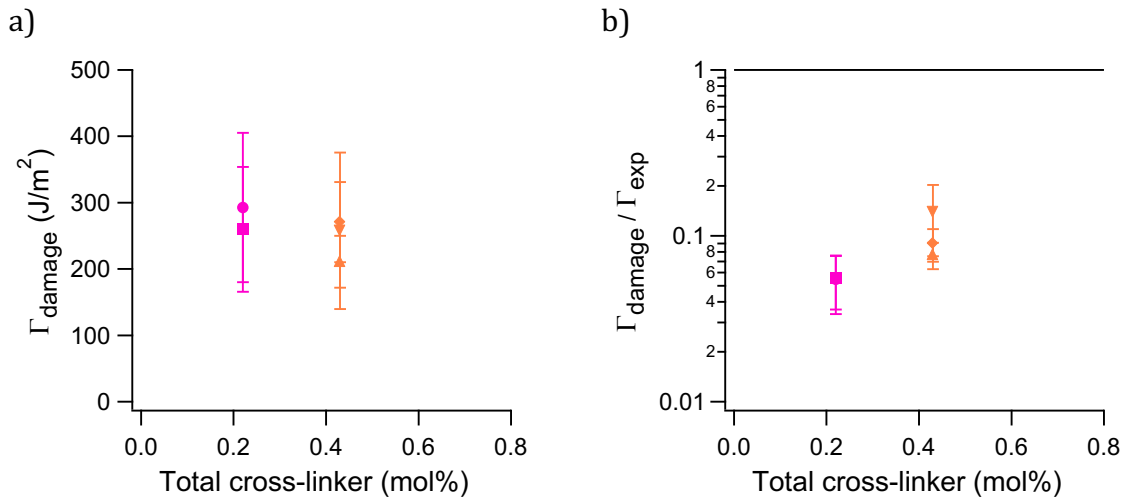
Figure 38: Evolution of Γ_{damage} (a) and $\Gamma_{damage}/\Gamma_{exp}$(b) for crack propagation test on DASNMA (orange) and DASNMA$_{0.2}$ (pink) at 25 °C and $\dot{\lambda}$ =3x10^{-3} s^{-1}. Γ_{damage} calculated using Craig's assumption (U=64 kJ/mol). Average value calculated over 4 pictures, error bar correspond to the standard deviation. Different symbols correspond to samples from separate polymerizations.

The relative contribution of chain breakage is lower in the less cross-linked network and cannot therefore explain the increase in fracture toughness at lower cross-linking density. The increase in Γ_{exp} is attributed to other dissipative mechanism such as viscoelastic contribution. This increase in viscoelastic dissipation at lower cross-linker concentration can be explained by the increase of networks defects, such as dangling chains. A more detailed analysis is needed to confirm this hypothesis.

One limit of this comparison is the variation in the ratio of mechanophore cross-linker over total cross-linker. In the more cross-linked network, about 5 % of cross-linker is the mechanophore cross-linker while it represents 9% of total cross-linker in the less cross-linked network. As we assumed that the mechanophore is representative of the chain breakage (assumption discussed in Chapter 3 Section 4), we believe this change in ratio is not responsible for the observed trend.

It is interesting to note that, in this section calculations were done using the cross-links contribution E_x of Young modulus. Using E_x instead of E, influences Σ_{exp} (Eq 8., adapted from Chapter 3, section 4) but does not change Γ_{damage} (Eq 9. from Eq 4.)

$$\Sigma_{exp} = \phi_{act.DACL}\, v_x\, L_{damage} = \phi_{act.DACL} \frac{E_x}{3\, k_B T} L_{damage} \qquad \text{Eq 8.}$$

Where $\phi_{act.DACL}$ is the fraction of activated mechanophores, $\phi_{act.DACL}$; v_x is the average number of elastic strands, between crosslinks, per cubic meter and L_{damage} the length over which damage was detected.

$$\Gamma_{damage} = N_x U_b \Sigma_{exp} = \frac{2}{M_{monomer}} \left(\frac{3\rho RT}{E_x}\right) U_b \phi_{act.DACL} \frac{E_x}{3\, k_B T} L_{damage} \qquad \text{Eq 9.}$$

Where N_x is the number of C-C bonds between cross-links and U_b is the bond energy.

5 Different monomers at temperature well above the Tg

5.1 Materials

Networks made from two different monomers will be compared at nearly the same value of T- Tg where T is the test temperature and. Crack propagation tests were performed at 50 μm/s ($\dot{\lambda} = 3 \times 10^{-3} s^{-1}$) and 60 °C on polymethyl acrylate network (Tg = 18 °C; T – Tg = 42 °C) and at 25 °C on polyethyl acrylate network (Tg = -18 °C, T – Tg = 43 °C). Materials composition are given Table 5. Molar percentages are relative to moles of monomer. 2-hydroxy-2-methylpropiophenone, HMP, is the initiator. DACL corresponds to the mechanophore cross-linker and 1,4-butanediol diacrylate, BDA, to the standard cross-linker. Samples were designed to have the same molecular weight between cross-links as discussed in Chapter 2 Section 2.

Filler	Monomer	HMP (mol%)	DACL (mol%)	BDA (mol%)	Total CL (mol%)
DASNMA	MA	1.16	0.02	0.48	0.5
DASNEA	EA	1.16	0.02	0.41	0.43

Table 5: Composition of materials investigated to compare the influence of monomer nature

Glass transition temperature and Young's moduli, from DMA and uniaxial extension respectively are indicated in Table 6 (details in Chapter 2 Section 3).

Name	Monomer	Tg (°C)	E at 25 °C (MPa)	[DACL] (mol.m^{-3})
DASNMA	MA	18	1.5	2.8
DASNEA	EA	-18	1.2	2.2

Table 6: Properties of materials used to compare different monomers at the same difference from Tg

5.2 Mechanical tests

Figure 39 represents examples of stress-strain curves of the crack propagation tests. The fracture energies, Γ_{exp}, were calculated and are noted near each curve. Fracture energy values are similar, slightly higher for DASNEA at 25 °C.
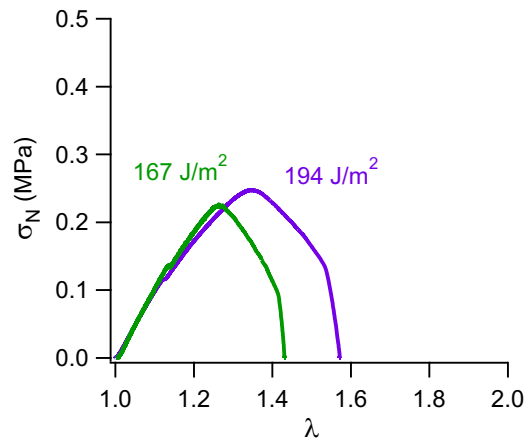
Figure 39: Stress-strain curve of crack propagation test on DASNEA at 25 °C (in purple) and DASNMA at 60 °C (in green) at $\dot{\lambda} = 3 \times 10^{-3} \ s^{-1}$.

5.3   Post-mortem quantitative LSCM damage analysis

For each crack propagation test, four single optical sections (two on each side) were recorded at magnification 5x and 100 µm depth. Figure 40 a and c are examples of surface intensity plots obtained from raw images. Figure 40 b and d are examples of pre-processed and re-colored LSCM images ready for quantitative analysis.
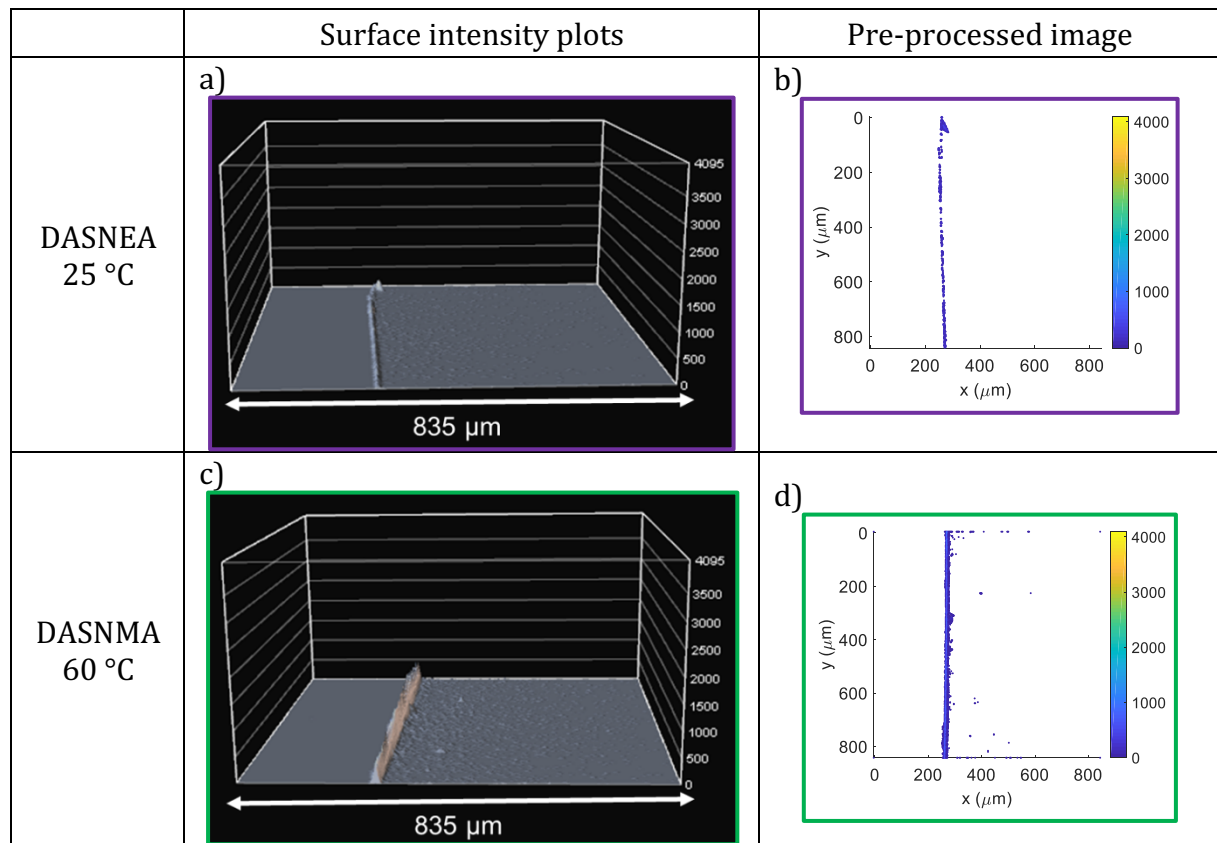
	Surface intensity plots	Pre-processed image
DASNEA 25 °C	a)	b)
DASNMA 60 °C	c)	d)

Figure 40: Surface intensity plots and pre-processed (re-colored) pictures after crack propagation at $3 \times 10^{-3} \ s^{-1}$ in DASNEA at 25 °C (a and b) and in DASNMA at 60 °C (c and d) (Laser 10 Gain 3).

The signal was too close to noise level to be quantified for DASNEA sample. The fluorescent intensity was dramatically decreased from DASNMA (60 °C) to DASNEA (25 °C).

The difference between poly methyl acrylate and poly ethyl acrylate networks cannot be limited to their difference in Tg. Analyzing these two materials at about 40 °C from their Tg revealed a different level of damage. While the damage is barely detected for poly ethyl acrylate network, it is clearly visible for methyl acrylate. The damage in poly ethyl acrylate seems to be more localized than in poly methyl acrylate. The origin of this difference is not obvious. If one rules out the process of statistical incorporation of the Diels-Alder mechanophore in the network, the other possible difference is the entanglement structure, although very reliable data has not been published yet to the best of our knowledge. At this stage, further systematic studies are needed.

Conclusions

Crack propagation test on single network of polymethyl acrylate elastomers was performed at $50\,\mu m/s$ ($\dot{\lambda} = 3 \times 10^{-3} s^{-1}$) and $25\,°C$, followed by 'post mortem' observations and quantitative image analysis.

The chain scission was proven to occur over a volume, from few microns to few tens of microns. This length scale is much larger than was previously thought, i.e. the mesh size (hundreds of angstrom). Therefore, we proved that at ambient conditions, the fracture of poly methyl acrylate was not limited to a molecular plane.

From crack propagation tests carried out on single networks of poly methyl acrylate at different conditions, we observed that the number of chain scissions increases with increasing loading rate and decreasing temperature (getting closer to Tg). While, these parameters are commonly believed to influence only viscoelastic phenomena, we proved that more damage occurred at a temperature close to the glass transition temperature and at higher speed. Actually, viscoelastic mechanisms, such as monomer friction, dissipate energy and must reduce the load transfer from one stretched chain to the next. The stress is delocalized and higher macroscopic extension can be achieved. Bulk chains friction can also facilitate chain scission away from the crack tip.

As introduced in Chapter 1 the chain scission can be seen as a probabilistic event with a probability of chain rupture, $P_{rupture}$. This probability increases with the force applied to the chain (*9-11*). In turn to load the bonds the chain needs to be close to fully stretched and Figure 41 is a schematic representation of a crack tip to illustrate this discussion.

At low macroscopic extension, in a material with low viscoelastic dissipation (situation 1 on the drawing), the stress is more concentrated at the crack tip where the chains are highly stretched and present a high probability of rupture leading to an early material failure. This high concentration stems from the easy force transfer from a broken bond to a neighboring intact one.

At the same low macroscopic stretch, in a material with high viscoelastic dissipation (situation 2 on the drawing), the stress is more delocalized by energy dissipation and chain overloading at the very crack tip is prevented. In other words, higher viscoelastic

dissipation decreases the probability of rupture at the very crack tip (due to dissipation in the load transfer process) but enlarges the volume where the probability is more moderate (due to friction during loading). The crack will not propagate at that strain level and higher level of macroscopic extension (situation 3 on the drawing) can be reached.

In the viscoelastic case, the region of high deformation and high stress extends over a much larger volume. The region where extended chains have a high probability of rupture is broad and hence the probability of bond scission (related to chain stretch) increases. More damage occurs before crack propagation.
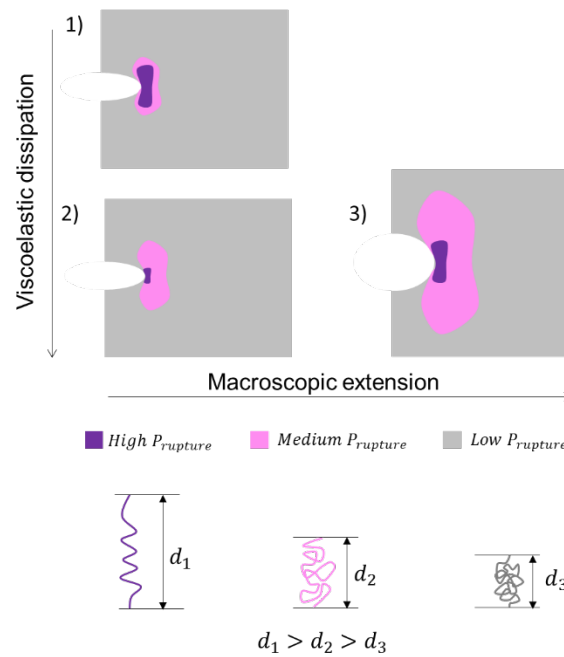
Figure 41: Schematic representation of the evolution of the probability of chain rupture at a crack tip at low extension 1) and 2) and high extension 3)

This simplified picture illustrates why at higher stretch rate and low temperature, when viscoelastic dissipation is enhanced, the damage detected is higher and over a larger area.

A major result, highlighted by this study, is that chain breakage depends on temperature and stretch rate and cannot be considered as a constant. Decoupling the fracture energy in two contributions: the threshold value below which no fracture occurs Γ_0 and energy dissipation in front of the crack tip Γ_D is still possible (Eq 10.). However, Γ_0 corresponds to an unrealistic lower limit that should not be confused with the contribution due to chain scission. This latter contribution is included in the second dissipative term, which is time and temperature dependent.

$$\Gamma = \Gamma_0 + \Gamma_D \qquad\qquad \text{Eq 10.}$$

References

1. G. J. Lake, A. G. Thomas, The Strength of Highly Elastic Materials. *Proceedings of the Royal Society of London. Series A, Mathematical and Physical Sciences* **300**, 108-119 (1967).
2. C. Creton, 50th Anniversary Perspective: Networks and Gels: Soft but Dynamic and Tough. *Macromolecules* **50**, 8297-8316 (2017).
3. A. N. Gent, J. Schultz, Effect of Wetting Liquids on the Strength of Adhesion of Viscoelastic Material. *The Journal of Adhesion* **3**, 281-294 (1972).
4. A. N. Gent, Adhesion and Strength of Viscoelastic Solids. Is There a Relationship between Adhesion and Bulk Properties? *Langmuir* **12**, 4492-4496 (1996).
5. M. Rubinstein, R. H. Colby, *Polymer Physics*. (2003).
6. S. Wang, S. Panyukov, M. Rubinstein, S. L. Craig, Quantitative Adjustment to the Molecular Energy Parameter in the Lake–Thomas Theory of Polymer Fracture Energy. *Macromolecules* **52**, 2772-2777 (2019).
7. B. N. J. Persson, O. Albohr, G. Heinrich, H. Ueba, Crack propagation in rubber-like materials. *Journal of Physics: Condensed Matter* **17**, R1071-R1142 (2005).
8. R. Michael, P. Sergei, Elasticity of Polymer Networks. *Macromolecules* **35**, 6670-6686 (2002).
9. K. R. Evan Evans, Dynamic Strength of Molecular Adhesion Bonds. *Biophysical Journal* **72**, 1541-1555 (1997).
10. E. Evans, Looking inside molecular bonds at biological interfaces with dynamic force spectroscopy. *Biophysical Chemistry* **82**, 83-97 (1999).
11. R. N. Merkel, P.; Leung, A.; Ritchie, K.; Evans, E., Energy landscapes of receptor-ligand bonds explored with dynamic force spectroscopy. *Nature* **397**, 50-53 (1999).

Chapter 5

Bond scission in the filler of multiple network elastomers

Introduction

In the previous Chapter, crack propagation tests were performed on single networks at different crosshead velocities and at different temperatures in order to investigate the influence of these parameters on damage. In single network elastomer, the fracture toughness is dependent of viscoelastic dissipation. This dependence was proven to be coupled with damage.

The multiple network strategy is appreciated because fracture energy is expected to be less rate and temperature dependent than other reinforcement mechanisms. Indeed, the dissipative mechanism, based on sacrificial covalent bonds breakage, is not directly based on viscoelasticity. Gong's group highlighted the low dependence of fracture energy on tearing velocity in double network hydrogels (*1*).

Pierre Millereau was the first to investigate the effect of the viscoelastic dissipation occurring at the crack tip in multiple network elastomers made of polyethyl acrylate (*2*). He performed crack propagation tests at different temperatures on multiple networks with different level of pre-stretching of the filler network. He concluded that some viscoelastic dissipation still occurs in multiple network of polyethyl acrylate at room temperature, as the fracture energy decreased with increasing temperature. However, the comparison between the evolution of the fracture energy of multiple networks and the simple network (or a reference styrene butadiene rubber) showed that the effect of the viscoelasticity is much smaller in multiple networks. He concluded that the multiple networks have drastically decreased their viscoelastic dissipation occurring at the crack tip in comparison to simple network.

Pierre Millereau did not run experiments on mechano-luminescent multiple networks. He was able to conclude only on the mechanical properties. Thanks to the method we developed and presented in Chapter 3 Section 4, it is now possible to analyze damage after crack propagation at different stretch rate or temperature.

The objective of this Chapter is to investigate the rate and temperature dependence of fracture in multiple network elastomers from both fracture toughness and molecular damage points of view. Crack propagation tests were performed at different temperatures and different crosshead velocities, followed by quantitative damage analysis.

In this study, only the breakage of the sacrificial (1st or filler) network chains was analyzed. The synthesis of the reference and mechano-fluorescent multiple networks was presented in Chapter 2 section 2.

The composition of mechano-fluorescent and reference first networks, used as filler networks, are indicated in Table 1. Molar percentages are relative to moles of monomer. 2-hydroxy-2-methylpropiophenone, HMP, is the initiator. DACL corresponds to the mechanophore cross-linker and 1,4-butanediol diacrylate, BDA, to the standard cross-linker. The mechano-fluorescent filler network is cross-linked by the two cross-linkers (Total CL in the Table 1).

Filler	HMP (mol%)	DACL (mol%)	BDA (mol%)	Total CL (mol%)
DASNMA	1.16	0.02	0.48	0.5
SNMA	1.16	0	0.5	0.5
DASNEA	1.16	0.02	0.41	0.43
SNEA	1.16	0	0.43	0.43

Table 1: Filler networks composition

The composition of the second and third networks are given in Table 2. No mechanophore was introduced in the matrix networks. Mechano-fluorescent and reference filler networks underwent one to two swelling polymerization steps in order to obtain mechano-fluorescent and reference double and triple networks.

Matrix	HMP (mol%)	DACL (mol%)	BDA (mol%)	Total CL (mol%)
MA	0.01	0	0.01	0.01
EA	0.01	0	0.01	0.01

Table 2: Matrix network composition

Table 3 summarizes composition and properties of multiple network elastomers tested in this Chapter. The mechanophore concentration, [DACL], is given in quantity per cubic meter of the final material (mol/m^3). The Young's modulus at 25 °C, E, and glass transition temperature, Tg, were experimentally determined by uniaxial extension and DMA respectively.

Name	Type of MN	Filler monomer	Matrix monomer	ϕ_{SN}	λ_0	[DACL] (mol/m^3)	E (MPa)	Tg (°C)
DAMAMA(1.6)	DN	MA	MA	0.3	1.6	0.7	1.8	18
MAMA(1.6)	DN	MA	MA	0.3	1.6	0	1.8	18
DAMAEA(1.5)	DN	MA	EA	0.3	1.5	0.9	1.2*	-8
MAEA(1.5)	DN	MA	EA	0.3	1.5	0	1.2*	-8
DAEAEA(1.6)	DN	EA	EA	0.2	1.6	0.5	1.4	-18
EAEA(1.6)	DN	EA	EA	0.2	1.6	0	1.4	-18
DAMAMA(2.3)	TN	MA	MA	0.08	2.3	0.2	2.2	18
MAMA(2.3)	TN	MA	MA	0.08	2.3	0	2.2	18
DAEAEA(2.3)	TN	EA	EA	0.07	2.3	0.2	1.6	-18
EAEA(2.3)	TN	EA	EA	0.07	2.3	0	1.6	-18

*Table 3: Multiple network elastomers investigated in this chapter. * are (under)estimated from notched curves. Grey values were not tested, from previous work (3) and from Chapter 2, multiple networks have the same Tg as the single network if the matrix and the filler are made from the same monomer.*

In a first section, crack bifurcations will be discussed. Then, the influence of the stretch rate at ambient temperature will be investigated, followed by the influence of temperature.

1   Crack bifurcations

Direct observations of crack propagations in multiple networks was reported in Chapter 3. Crack bifurcations, broad or localized, were noticed during crack propagation in multiple network elastomers. These crack bifurcations were also visible during 'post-mortem' LCSM analysis. In the 3D-reconstruction, shown in Figure 1.a, a fracture surface showing a crack bifurcation is visible. First, as illustrated on the crack path drawing Figure 1b, the crack propagated straight from A to B. Then, at the point B, a first crack bifurcation to the left side occurred, up to the point C. From the point C, two cracks were initiated and propagated up to points D and E. Finally, the D path stopped and the crack further propagated through E path.
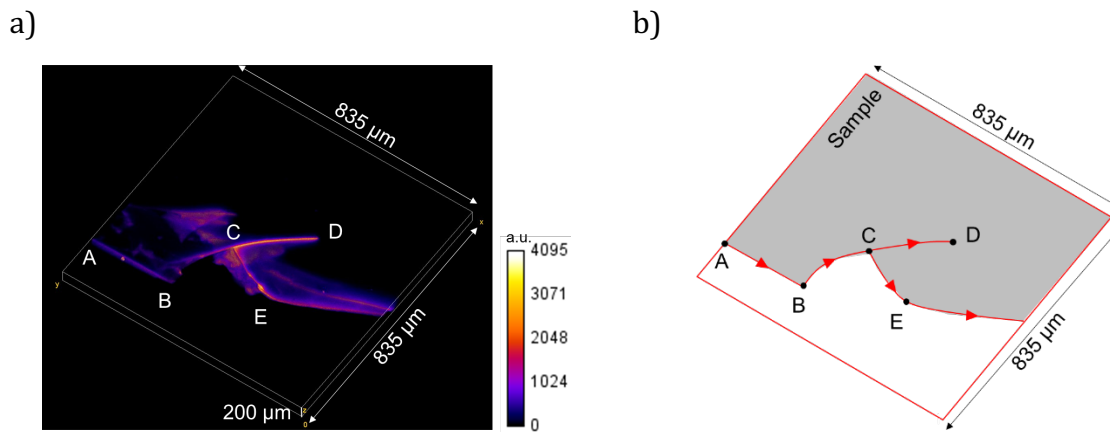
a)   b)

Figure 1: Re-colored 3D reconstruction (a) and associated drawing of the crack path (b) of a crack bifurcation in DAEAEA(1.6)

From 'post mortem' observations of crack edges after propagation at different conditions, three regimes were defined and summarized in Table 4.

A first stable regime corresponds to a crack propagation without crack bifurcations. In this case, the systematic analysis developed and presented in Chapter 3 was perfectly adapted.

The opposite case corresponds to a propagation with many crack bifurcations. The average distance between bifurcations was lower than 200 µm. The LSCM systematic analysis was not possible because the damage was too heterogeneous.
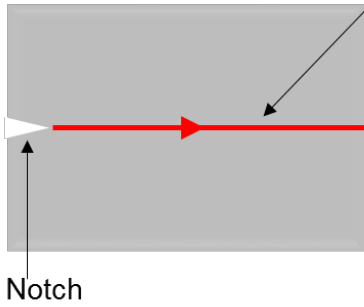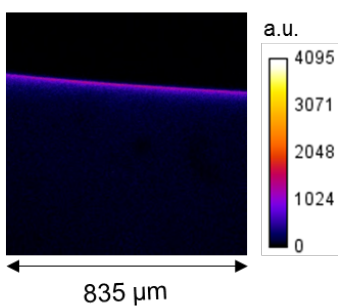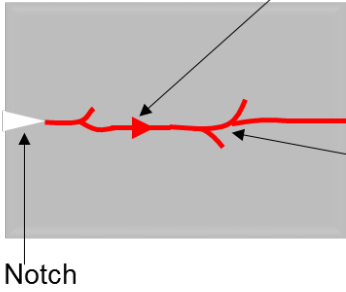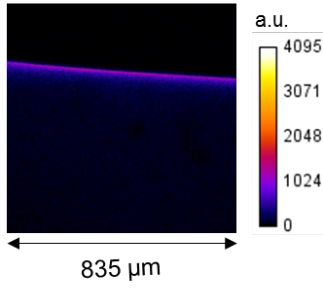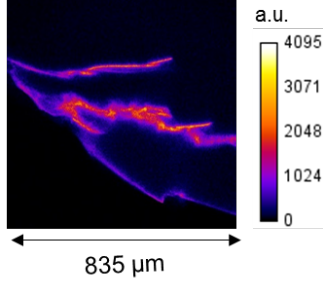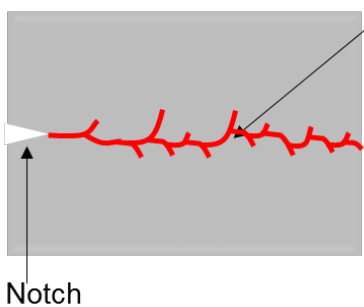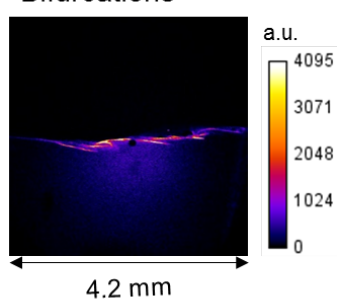
Regime		Schematic representation of the crack path	Examples of recolored 2D picture	Possible analysis
Stable propagation		Notch	Straight propagation	Yes
Intermediate		Notch	Straight propagation / Bifurcation	Yes
Many bifurcations		Notch	Bifurcations	No

Table 4: Three propagation regimes observed after crack propagation in multiple network elastomers

An intermediate propagation profile was observed. It consists of a succession of regions of crack bifurcations and of regions of straight propagations, similar to a stick and slip phenomenon. The systematic LSCM analysis was performed over the area where the crack propagated straight. However, this stick and slip like propagation means that the crack speed varied from low values at crack bifurcation points and high values during straight

propagation. We previously showed that the extent of damage by bond scission depends on crack speed, suggesting that the damage is heterogeneous. This heterogeneity was taken into account by averaging values over four images per sample. The comparison of averaged values for propagation in different conditions seems reliable.

The limitation between each regime was defined by the systematic quantitative method described in Chapter 3 Section 4.2 (200 µm straight length along the crack is needed) and should not be regarded as a sharp border. Table 5 and Table 6 summarize the propagation conditions and the possibility of LSCM analysis for the different samples at different stretch rate and temperatures.

Stretch rate (s^{-1})	3×10^{-2}	3×10^{-3}	3×10^{-4}
DASNMA	🟩	🟩	🟩
DAMAMA(1.6)	🟩	🟧	🟧
DAMAEA(1.5)	🟩	🟩	🟧
DAMAMA(2.3)	🟧	🟧	🟧

Table 5: Crack propagation regime for different samples and stretch rates. Green corresponds to stable propagation and orange to a succession of crack bifurcations and straight propagations.

Temperature (°C)	25	40	60	80
DASNMA	🟩	🟧	🟧	🟩
DASNEA	🟩	🟧	🟧	🟧
DAMAMA(1.6)	🟧			
DAEAEA(1.6)	🟧	🟧	🟥	🟥
DAMAMA(2.3)	🟧			🟩
DAEAEA(2.3)	🟧	🟧	🟧	🟧

Table 6: Crack propagation regime for different samples and temperatures. Green corresponds to stable propagation, orange to a succession of crack bifurcations and straight propagations and red to too many bifurcations for analysis.

Figure 2 is an example of a stitching of about 20 images along the crack surface after crack propagation from left side to the right side of the image, in DAEAEA(1.6) at room temperature and 1 mm/min ($\dot{\lambda} = 3 \times 10^{-4} \ s^{-1}$). From this reconstruction, the fluorescence signal heterogeneity along the sample is visible. Higher fluorescence signal is visible at bifurcation and at the very end of the sample (at the right).

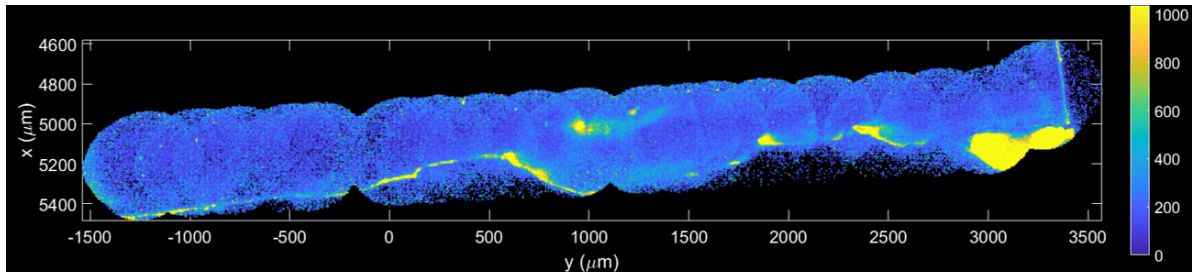*Figure 2: Stitching of several corrected images of a DAEAEA(1.6) after crack propagation at room temperature (from left side to right side)*

The systematic LSCM analysis was not possible on DAEAEA(1.6) at 60 °C and 80 °C. The influence of temperature on that sample will not be investigated. Otherwise, the systematic fluorescence analysis was performed and results are presented in the following sections.

2 Influence of stretch rate on bond scission in the fracture of multiple network elastomers

2.1 Double networks based on poly methyl acrylate

Crack propagation tests were performed on double networks based on poly methyl acrylate pre-stretched at $\lambda_0 = 1.6$ (two reference samples, MAMA(1.6), and two mechano-fluorescent samples of DAMAMA(1.6)) at 25°C and different crosshead velocities: 5, 50 and 500 µm/s ($\dot{\lambda} = 3 \times 10^{-4} \, s^{-1}$, $3 \times 10^{-3} \, s^{-1}$ and $3 \times 10^{-2} \, s^{-1}$ respectively). Examples of stress strain curves of crack propagation are given in Figure 3. The fracture energies, Γ_{exp}, were calculated using the Greensmith's approximation (Chapter 3, Eq. 3) and are plotted as a function of the stretch rate, Figure 4.
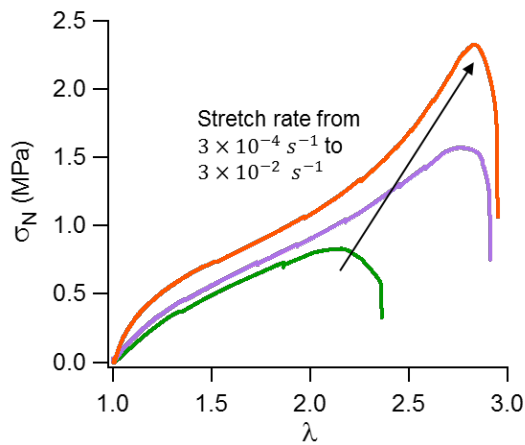
Figure 3: Examples of stress-strain curves of crack propagation test on notched DAMAMA(1.6) samples at 25 °C and $\dot{\lambda} = 3 \times 10^{-4} \, s^{-1}$(in green), $3 \times 10^{-3} \, s^{-1}$ (in purple) and $3 \times 10^{-2} \, s^{-1}$ (in orange). Four replicates were tested (two MAMA(1.6) and two DAMAMA(1.6)).
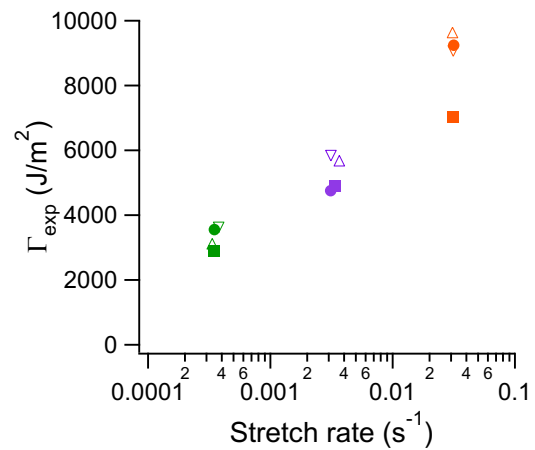
Figure 4: Evolution of the fracture energy with the stretch rate. Different symbols correspond to different samples and hollow symbols to non mechano-fluorescent samples

In double networks based on methyl acrylate ($\lambda_0 = 1.6$), at 25 °C, the fracture energy increases with stretch rate. The test was conducted at a temperature close to the Tg and viscoelastic phenomena are enhanced. One can expect the speed dependence to be due only to viscoelastic dissipation in the polymethyl acrylate matrix. The LSCM analysis was performed to analyze the influence of stretch rate on damage of the filler network.

For each crack propagation test, four pictures (two on each side) were recorded at magnification 5x and 100 µm depth. Figure 5 represents example of surface intensity plot

from raw pictures (Nikon software) and corresponding pre-processed and re-colored pictures ready for quantitative analysis (using MATLAB), after crack propagation at each stretch rate.

$\dot{\lambda}$ (s^{-1})	Surface intensity plots	Pre-processed pictures
3×10^{-4}		
3×10^{-3}		
3×10^{-2}		

Figure 5: Surface intensity plots and pre-processed (re-colored) pictures after crack propagation in DAMAMA(1.6) (Laser 7 Gain 3) at 25 °C and $\dot{\lambda} = 3 \times 10^{-4} \ s^{-1}$ (a and b), $3 \times 10^{-3} \ s^{-1}$ (c and d) and $3 \times 10^{-2} \ s^{-1}$ (e and f).

Fluorescence signal increases with the stretch rate, as visible on the surface intensity plots.

The quantitative analysis, detailed in Chapter 3 section 4, was performed. The evolution of fluorescence intensity, averaged over 150 px along the crack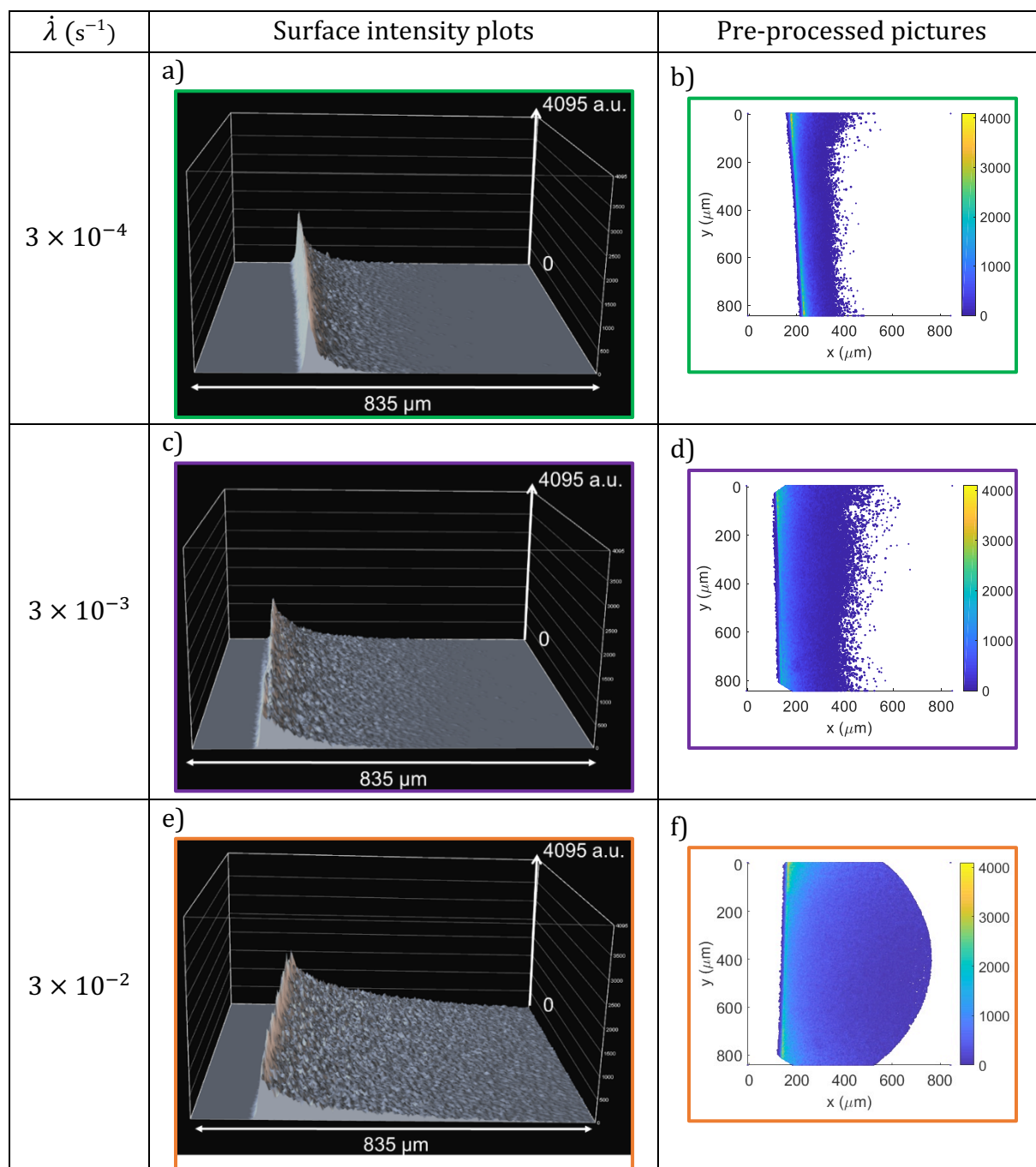 edge, with the distance normal to the crack edge is represented in Figure 6. Fluorescence was detected over a larger distance from the crack after propagation at higher stretch rate.
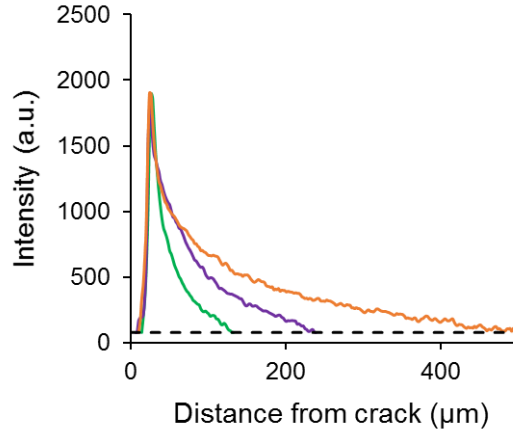
Figure 6: Example of intensity profiles after crack propagation in DAMAMA(1.6) at 25°C and at $\dot{\lambda} = 3 \times 10^{-4} s^{-1}$(green), $\dot{\lambda} = 3 \times 10^{-3} s^{-1}$ (purple) and $\dot{\lambda} = 3 \times 10^{-2} s^{-1}$ (orange). The cut-off (dotted line) is at the noise level.

The fluorescence intensity was converted into concentration of activated mechanophore using a calibration curve. The quantity of activated mechanophore was normalized by the initial concentration of mechanophore to get a fraction of activation. By considering this fraction of activation representative of the fraction of chains breaking, we obtain the areal density, Σ_{exp}, of broken chains, of the filler network per area of fracture surface(more details in Chapter 3, section 4).

Σ_{exp} is plotted as a function of the stretch rate in Figure 7. The evolution of the fracture energy with stretch rate is also reported on Figure 7. Both fracture energy and the number of broken chains from the filler network increase with the stretch rate.

The length, L_{damage}, over which bond scission was detected is plotted as a function of stretch rate in Figure 8. Damage was detected over hundreds of microns. This broad damage of the filler network is consistent with the reinforcement mechanism based on chain scissions of the sacrificial network. It is also clear that L_{damage} increases with the stretch rate.

Figure 7: Evolution of the number, Σ_{exp}, of broken chain of the filler network (in black) and of the fracture energy, Γ_{exp}, (in red) as a function of the stretch rate in DAMAMA(1.6)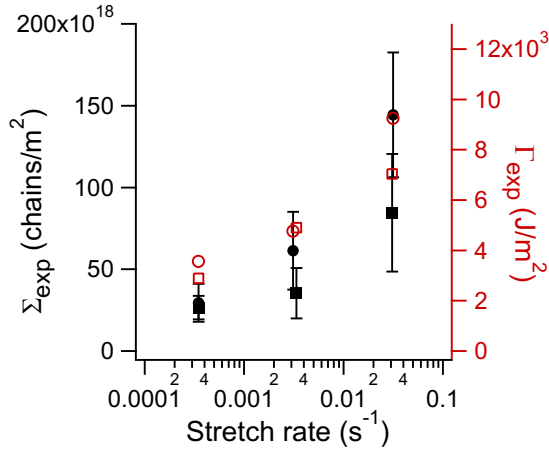. Average value calculated over 4 pictures, error bar correspond to the standard deviation. Different symbols correspond to samples from different polymerizations.
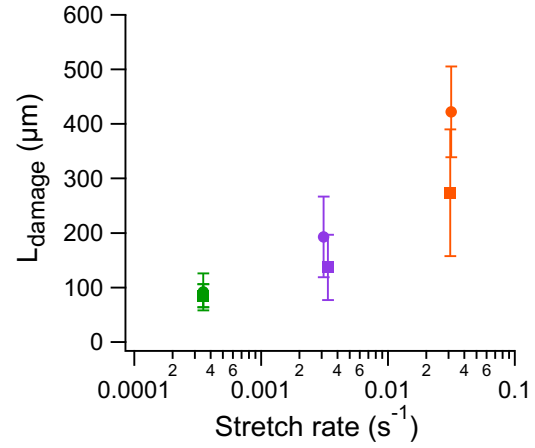
Figure 8: Evolution of the length over which damage is detected, L_{damage}, as a function of the stretch rate after crack propagation in DAMAMA(1.6). Average value calculated over 4 pictures, error bar correspond to the standard deviation. Different symbols correspond to samples from different polymerizations.

In summary, at higher stretch rates the strands of the filler network break more frequently and over a larger volume around the crack surface

Σ_{exp} can be normalized by the areal chain density of the filler network Σ_{SN}, crossing the plane of the interface to give $\bar{\Sigma}$. Mean values of this normalized number of broken chains are represented as a function of the fracture energy, in Figure 9.

The areal density of broken chains is a few hundred times the value of a single monolayer (over a thickness of the order of the mesh size) of the filler network. This very large amount of detected bond scission is consistent with the toughening mechanism based on sacrificial bonds in the filler network, discussed in Chapter 3.
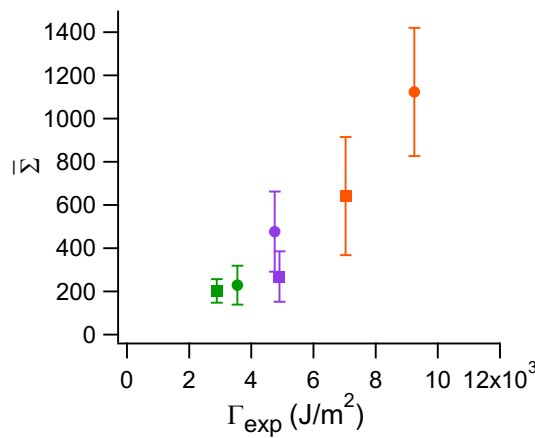
Figure 9: Evolution of the normalized number, $\bar{\Sigma}$, of broken chains in the filler network with the fracture energy for crack propagation tests on DAMAMA(1.6) at 25 °C and different stretch rate: $3 \times 10^{-4}\ s^{-1}$ (in green), $3 \times 10^{-3}\ s^{-1}$ (in purple) and $3 \times 10^{-2}\ s^{-1}$ (in orange). Average values calculated over 4 pictures for each sample, error bars correspond to the standard deviation. Different symbols correspond to samples stemming from different polymerizations.

The areal density of broken chains and the damage length both increase with the measured macroscopic value of the fracture energy that integrates all dissipative mechanisms. The question of its relative contribution will now be addressed.

From the areal density Σ_{exp}, of broken chains of filler network, an energy dissipated, Γ_{damage}, was calculated. The strategy used is similar to that of Chapter 4 on single networks but extended to multiple networks.

Inspired from the Lake-Thomas analysis, we assumed that the total bond energy of each carbon-carbon bond of the stretched chain is irreversibly lost. The filler breakage component of the fracture energy, Γ_{damage}, can then be estimated by Eq 1.

$$\Gamma_{damage} = N_x U_b \Sigma_{exp} \qquad\qquad\qquad \text{Eq 1.}$$

Where N_x is the number of C-C bonds between cross-links in the filler network (about 140 C-C bonds) and U_b is the bond energy (350 kJ.mol^{-1} for a C-C bond).

N_x was estimated from the affine model of rubber elasticity (4), considering the single network used as a filler, Eq 2.

$$N_x = \frac{2}{M_{monomer}} \left(\frac{3\rho RT}{E_{SN}} \right) \qquad\qquad\qquad \text{Eq 2.}$$

Where $M_{monomer}$ is the molecular weight of the monomer (in g/mol) and E_{SN} the Young's modulus of the single network before the swelling and polymerization steps to get the multiple network. In this estimation of N_x, the filler and the matrix networks are considered independent, meaning that transfer reactions are neglected.

Γ_{damage} was calculated and plotted as a function of the macroscopically measured fracture energy Γ_{exp}, as shown in Figure 10a. For high stretch rate, Γ_{damage} is higher than Γ_{exp}, which is inconsistent since Γ_{damage} has to be included in Γ_{exp}. Indeed, Γ_{damage} takes only into account the filler network breakage. Γ_{exp} corresponds to the overall material failure, including the matrix breakage component, bulk viscoelasticity, and other dissipative mechanism. As discussed in Chapter 4 for simple networks, the overestimate of Γ_{damage} can only be explained by the overestimate of energy dissipated per broken chain (U_b=350 kJ/mol).

As discussed in Chapter 1 Section 1.4, S. L. Craig and co-workers suggested an adjustment to the energy parameter of the Lake-Thomas theory (5). From the force-elongation curve

of a single polymer chain, they refine the estimation of the energy, U, dissipated per broken chain. U is estimated at about 64 kJ/mol for typical hydrocarbon polymers that is five times lower than the carbon-carbon bond dissociation energy.

We also calculated the breakage component of the fracture energy, Γ_{damage} *adjusted*, based on this more realistic energy estimation, Eq 3.

$$\Gamma_{damage}\text{adjusted} \ = \ N_x U \Sigma_{exp}$$

Eq 3.

Γ_{damage}adjusted was calculated and plotted as a function of Γ_{exp}, as shown in Figure 10b. Γ_{damage}adjusted is always below Γ_{exp}, which seems more realistic.
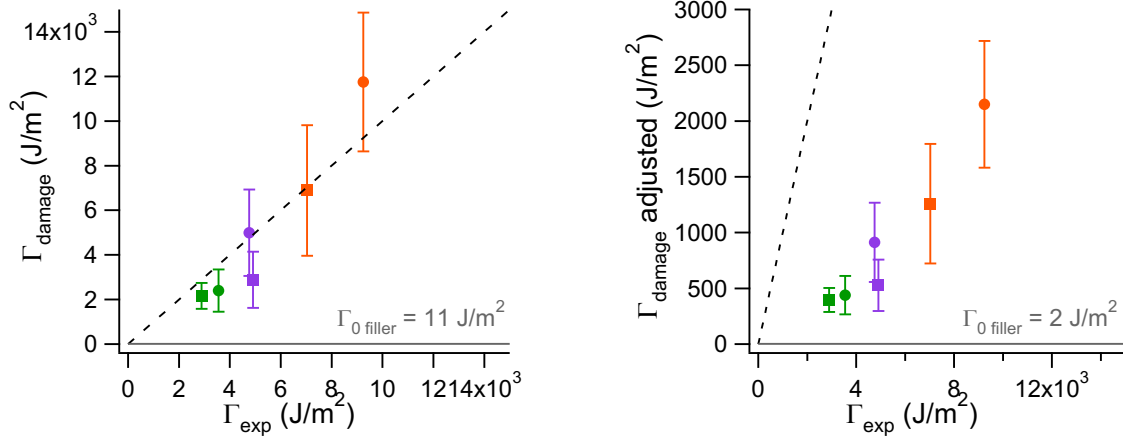
Figure 10: Evolution of Γ_{damage} (using U_b=350 kJ/mol) (a) and Γ_{damage} adjusted (using U=64 kJ/mol) (b) with Γ_{exp} for crack propagation test on DAMAMA(1.6) at 25 °C and different stretch rate: $3 \times 10^{-4} \ s^{-1}$ (in green), $3 \times 10^{-3} \ s^{-1}$ (in purple) and $3 \times 10^{-2} \ s^{-1}$ (in orange). Mean values calculated over 4 pictures, error bars correspond to the standard deviation. Different symbols correspond to samples from different polymerizations. Dotted line corresponds to $\Gamma_{damage} = \Gamma_{exp}$ curve.

As stretch rates increase Γ_{damage} increases clearly. To better visualize its contribution to the macroscopically measured fracture energy, the ratio $\frac{\Gamma_{damage}}{\Gamma_{exp}}$ was calculated and plotted as a function of the stretch rate, as shown Figure 11.

The overestimate using the classical Lake-Thomas assumption is clearly visible as the ratio gets higher than the unity. Since it seems more relevant, in the following sections, Γ_{damage}adjusted will be calculated directly (using 64 kJ/mol) and Γ_{damage} (using 350 kJ/mol) will not be calculated.
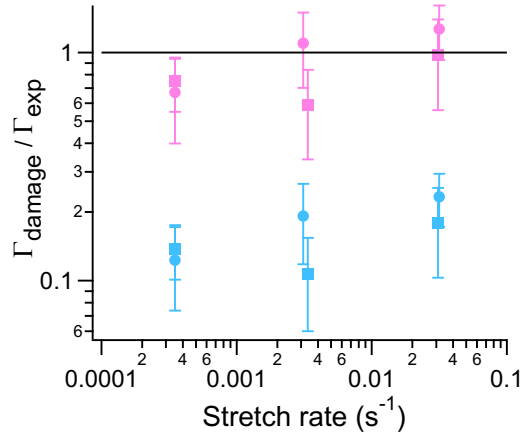
Figure 11: Evolution of $\Gamma_{damage}/\Gamma_{exp}$ with the loading rate for crack propagation test on DAMAMA(1.6) at 25 °C. Γ_{damage} calculated using Ub=350 kJ/mol (in pink) and using U=64 kJ/mol (in blue)

In double networks of poly methyl acrylate, the contribution of scission of sacrificial bonds to the total energy dissipation does not decrease. The contribution seems constant or slightly increases with stretch rate, from about 13 % at $\dot{\lambda} = 3 \times 10^{-4} \; s^{-1}$ to about 21 % at $\dot{\lambda} = 3 \times 10^{-2} \; s^{-1}$.

At higher stretch rates, more filler network chains are broken near the crack, ending up in a higher energy dissipation. The number of chains that break and the overall dissipation in the matrix both increase in a coupled way. In turn the presence of viscoelasticity enhances the sacrificial bond breakage phenomenon by preventing the filler network chains to relax stresses.

The strain at break, λ_{break}, also increases with increasing stretch rate. Σ_{exp} was plotted as a function of λ_{break}, as shown on Figure 12. Interestingly, while the number of broken chains of the filler network increases with the elongation at break, it does so non-linearly.

The increase in fracture toughness and in filler damage has two possible origins:

1. Because the probability of breaking a bond is rate dependent, higher elongations before crack propagation are experienced at higher stretch rates, so that more damage in the filler network can be caused by the higher extension withstood by the material before failure.
2. The stretch rate can have an intrinsic effect on damage, independent of the level of strain because of viscous friction at the monomer level.
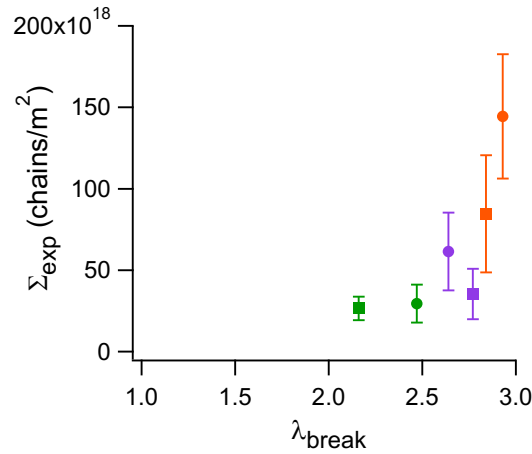
Figure 12: Evolution of the number, Σ_{exp}, of broken chain of the filler network with strain at break in DAMAMA(1.6) at 25 °C and different stretch rate: $3 \times 10^{-4}\ s^{-1}$(in green), $3 \times 10^{-3}\ s^{-1}$ (in purple) and $3 \times 10^{-2}\ s^{-1}$ (in orange). Average value calculated over 4 pictures, error bar correspond to the standard deviation. Different symbols correspond to samples from different polymerizations.

Both hypotheses are linked to the degree of viscoelastic dissipation from the matrix. At temperatures close to the glass transition temperature of the elastomer (Tg), friction between monomers is very high in the matrix and dissipates a lot of energy. Due to time-temperature superposition, molecular friction becomes also more important with increasing stretch rate. Molecular friction in the matrix increases the stress borne by chains (from the matrix but also from the filler) and facilitates filler chains ruptures, at the same level of macroscopic elongation. Higher molecular friction in the matrix will also dissipate energy and delay crack propagation. Finally, the material breaks at higher extension and at higher strain and stress at break.

It is interesting to note that, the energy, $N_x U$, dissipated per broken polymer strand of the filler network was estimated in absence of the matrix. In fact, U was estimated first by the U_b=350 kJ/mol (from classical Lake-Thomas assumption) and then refined by Craig's estimation (U=64 kJ/mol). However, this adjusted value of U was obtained from the force-elongation curve of a single polymer chain. The viscoelastic matrix surrounding the filler strand may influence this force-elongation curve and the actual energy dissipated as the bond fails.

2.2 Influence of the nature of the matrix

In the previous experiments, performed at 25 °C, the multiple networks made from poly methyl acrylate were close to their Tg, resulting in an enhancement of viscoelastic

dissipation in the matrix. This latter double network elastomer, DAMAMA(1.6), will now be compared with a double network, at an equivalent level of pre-stretching of the methyl acrylate filler network, but with a matrix made of poly ethyl acrylate, DAMAEA(1.5). Tg evolves from 18 °C to -8 °C, while going from DAMAMA(1.6) to DAMAEA(1.5). Figure 13 corresponds to Figure 3 with additional stress-strain curves corresponding to crack propagation tests at 25 °C and at 5 μm/s ($\dot{\lambda} = 3 \times 10^{-4} \ s^{-1}$), 50 μm/s ($\dot{\lambda} = 3 \times 10^{-3} \ s^{-1}$) and 500 μm/s ($\dot{\lambda} = 3 \times 10^{-2} \ s^{-1}$) on DAMAEA(1.5).
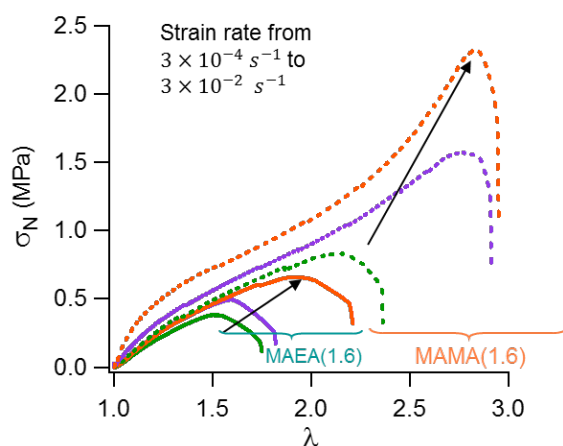
Figure 13: Stress-strain curves of crack propagation tests on notched DAMAMA(1.6) (dotted lines) and DAMAEA(1.5) (solid lines) at 25 °C and $\dot{\lambda} = 3 \times 10^{-4} \ s^{-1}$(in green), $3 \times 10^{-3} \ s^{-1}$ (in purple) and $3 \times 10^{-2} \ s^{-1}$ (in orange). One DAMAEA(1.5) and one MAEA(1.5) were tested.
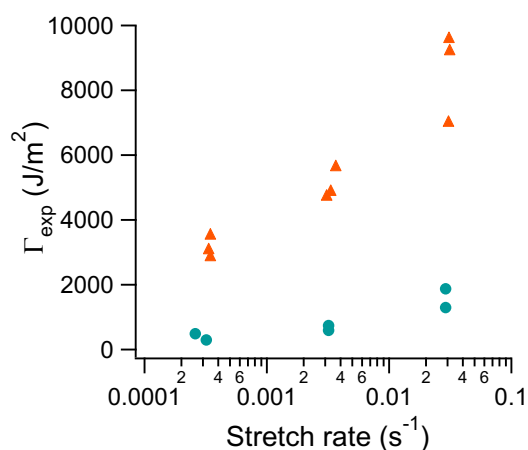
Figure 14: Evolution of the fracture energy with the stretch rate for DAMAMA(1.6) and MAMA(1.6) (orange triangles) and DAMAEA(1.5) and MAEA(1.5) (green circles)

Fracture energies were calculated using the Greensmith's formula (Chapter 3, Eq. 3) and plotted against the stretch rate in Figure 14. Fracture toughness values of DAMAEA(1.5) are clearly lower than for DAMAMA(1.6) emphasizing the effect of molecular friction on the fracture process as often reported.

For each crack propagation test, four pictures (two on each side) were recorded at magnification 5x and 100 μm depth. Figure 15 represents examples of surface intensity plots of raw pictures and pre-processed and re-colored associated pictures, after crack propagation in DAMAEA(1.5) at each stretch rate.

The fluorescent signal is much lower in DAMAEA(1.5) than in DAMAMA(1.6), as shown in Figure 5.

$\dot{\lambda}$ (s^{-1})	Surface intensity plots	Pre-processed pictures
3×10^{-4}		
3×10^{-3}		
3×10^{-2}		
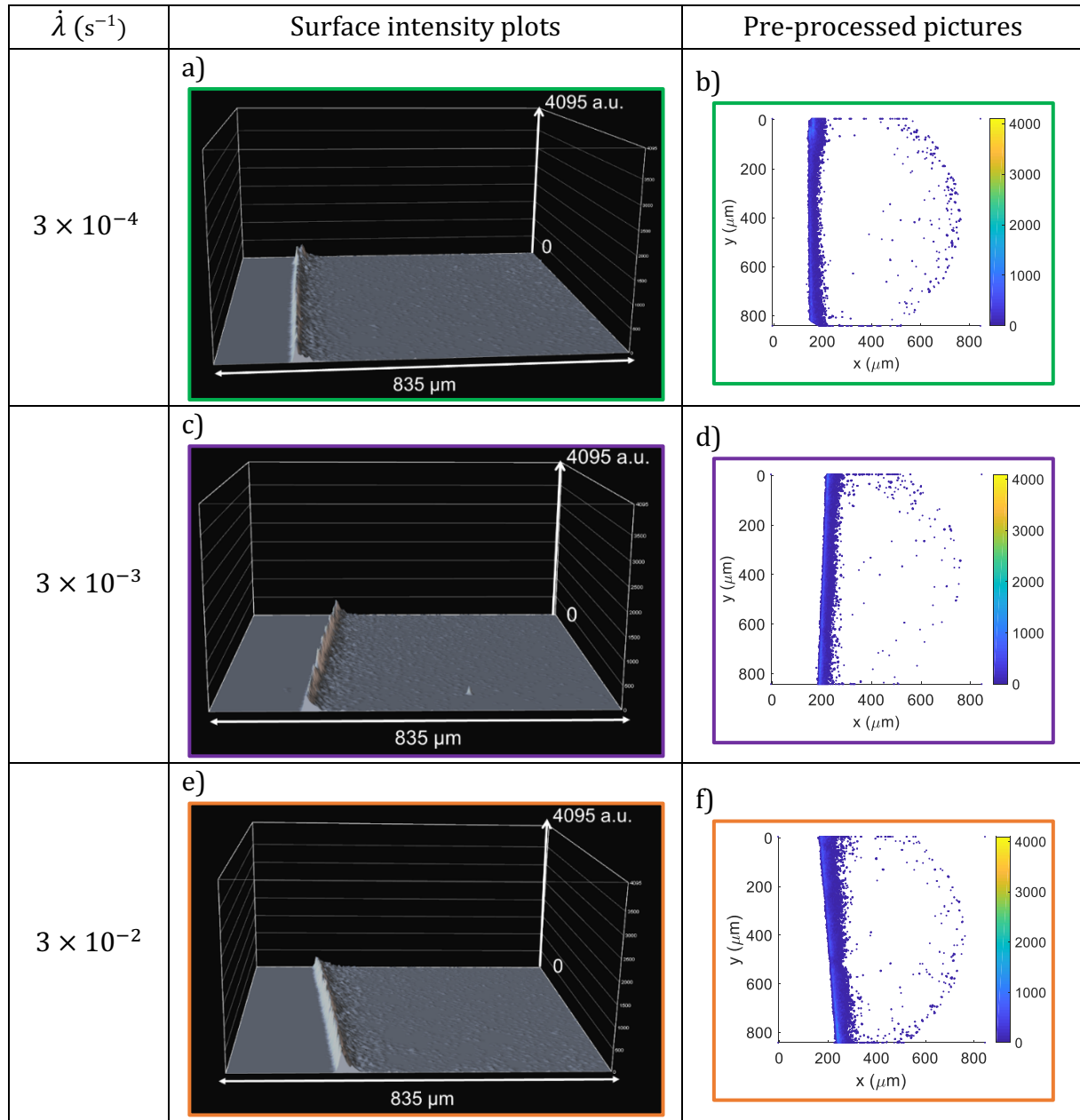
Figure 15: Surface intensity plots and pre-processed (re-colored) pictures after crack propagation in DAMAEA(1.5) (Laser 7 Gain 3) at 25 °C and $\dot{\lambda} = 3 \times 10^{-4}$ s^{-1} (a and b), $\dot{\lambda} = 3 \times 10^{-3}$ s^{-1} (c and d) and $\dot{\lambda} = 3 \times 10^{-2}$ s^{-1} (e and f).

The corresponding evolution of the fluorescence intensity with distance normal to the crack plane is represented in Figure 16. The signal is low and no clear trend is visible for the different stretch rates.

The quantitative analysis of the fluorescent signal described in Chapter 3 was performed. The number, Σ_{exp}, of broken chains, of the filler network, per square meter, was calculated and is plotted as a function of stretch rate in Figure 17 alongside the evolution of the fracture energy with stretch rate. There is no clear evolution of the number of broken chains in the filler network with stretch rate.
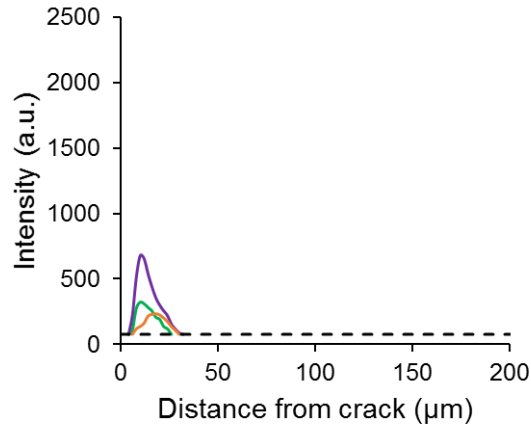
Figure 16: Intensity profile after crack propagation in DAMAEA(1.5) at 25°C and at $\dot{\lambda} = 3 \times 10^{-4} \ s^{-1}$(green), $\dot{\lambda} = 3 \times 10^{-3} \ s^{-1}$ (purple) and $\dot{\lambda} = 3 \times 10^{-2} \ s^{-1}$ (orange).

For the sake of comparison, the evolution of Σ_{exp} with stretch rate was plotted for both DAMAMA(1.6) and DAMAEA(1.5) on the same graph, Figure 18. A log scale was used to better visualize both sets of data. Indeed, the number of broken chains per square meter is one order of magnitude higher in DAMAMA(1.6) than in DAMAEA(1.5).

DAMAEA(1.5) appears to show a constant damage when the damage in the DAMAMA(1.6) increases with stretch rate.
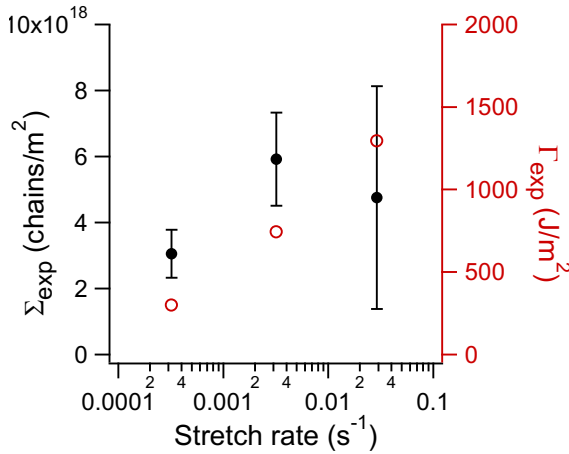
Figure 17: Evolution of the number, Σ_{exp}, of broken chain of the filler network (in black) and of the fracture energy, Γ_{exp}, (in red) as a function of the stretch rate.
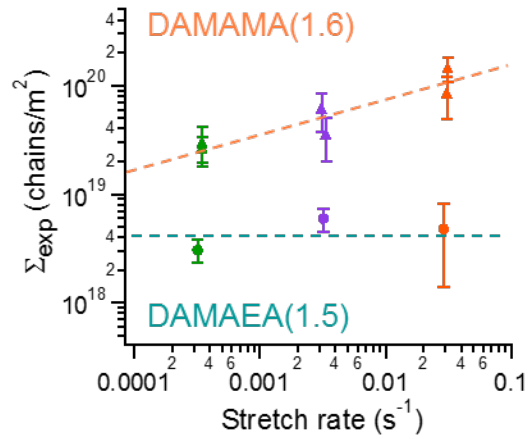
Figure 18: Evolution of the number, Σ_{exp}, of broken chain of the filler network with the stretch rate for crack propagation test on DAMAEA(1.5) (circles) and DAMAMA(1.6) (triangles) at 25 °C and at different stretch rate: $3 \times 10^{-4} \ s^{-1}$(in green), $3 \times 10^{-3} \ s^{-1}$ (in purple) and $3 \times 10^{-2} \ s^{-1}$ (in orange). . Dotted line are guide for the eye.

The length, L_{damage}, over which damage was detected is plotted as a function of the stretch rate in Figure 19. A log scale was used to visualize both DAMAEA(1.5) and DAMAMA(1.6). The damage is detected over tens of microns in DAMAEA(1.5) while it is detected over hundreds of microns in DAMAMA(1.6). It is also clear that the influence of

the stretch rate on the detected damage length is much reduced in DAMAEA(1.5) compared with DAMAMA(1.6).
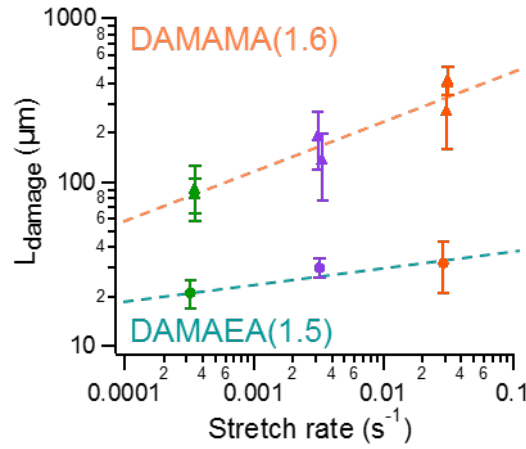
Figure 19: Evolution of the length, L_{damage}, over which damage is detected as a function of the stretch rate for crack propagation test on DAMAEA(1.5) (circles) and DAMAMA(1.6) (triangles) at 25 °C and at different stretch rate: $3 \times 10^{-4}\ s^{-1}$(in green), $3 \times 10^{-3}\ s^{-1}$ (in purple) and $3 \times 10^{-2}\ s^{-1}$ (in orange). . Dotted line are guide for the eye.

At 25 °C, by changing the matrix from poly methyl acrylate to poly ethyl acrylate, the damage in the filler network is reduced and much more localized. In addition, the damage appeared less rate dependent.

The component of the fracture energy due to bond scission in the filler network, Γ_{damage}, was calculated with Eq 3. (U=64 kJ/mol), and is plotted as a function of Γ_{exp}, in Figure 20. Γ_{exp} increases much faster than Γ_{damage}. Knowing that Γ_{exp} also takes into account the damage of the matrix and other dissipation mechanisms, a faster increase in Γ_{exp} compared to Γ_{damage} means that these other sources of energy dissipation, such as viscoelasticity, control the overall energy dissipation mechanisms but do not influence the damage in the filler network.

To compare the relative contribution of the energy dissipation by bond scission in DAMAMA(1.6) and DAMAEA(1.5), the ratio $\frac{\Gamma_{damage}}{\Gamma_{exp}}$ was plotted as a function of stretch rate for both double networks, as shown in Figure 21.

At lower stretch rate, the relative contributions of the filler bond breakage on the macroscopic measured fracture energy, $\frac{\Gamma_{damage}}{\Gamma_{exp}}$, are similar for both double networks, about 13 % for DAMAMA(1.6) and 15 % for DAMAEA(1.5). These comparable values can be explained by the similar structure of the filler network. Indeed, in both double networks, the filler network is a single networks of polymethyl acrylate, DASNMA. At low

stretch rate, viscoelasticity is reduced, and the bond breakage is determined by the filler network structure.

When the stretch rate increases however, viscoelastic dissipation is enhanced differently in both materials and the difference in coupling between the molecular damage and the viscoelasticity becomes visible. As described in the previous Section, in double networks fully made of polymethyl acrylate DAMAMA(1.6), the contribution of the scission of sacrificial bonds to the total energy dissipation slightly increases with stretch rate (from 13 % to 20 %). Interestingly, in double networks with a matrix made of polyethyl acrylate DAMAEA(1.5), the contribution of scission of sacrificial bonds to the total energy dissipation decreases with stretch rate (from 15 % to 5 %). In DAMAEA(1.5) the contribution of other dissipative mechanisms, such as viscoelasticity, increases with the stretch rate, which is the opposite effect than what is observed in DAMAMA(1.6). This result can be surprising at first: the fracture of a double network with a less viscoelastic matrix is more dominated by viscoelasticity. However, this result can be understood, by discussing the coupling between the two contributions.
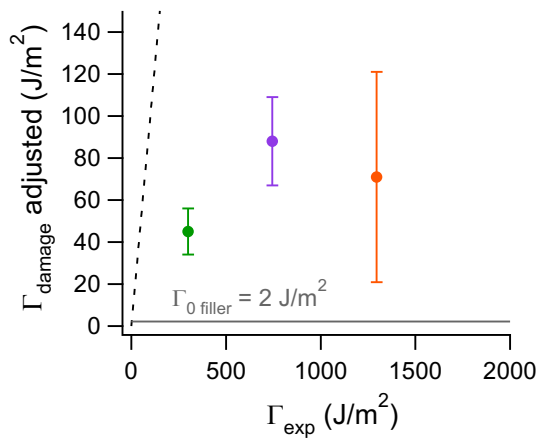
Figure 20: Evolution of Γ_{damage} adjusted (using U=64 kJ/mol) with Γ_{exp} for crack propagation test on DAMAEA(1.5) at different stretch rate: $3 \times 10^{-4}\ s^{-1}$ (in green), $3 \times 10^{-3}\ s^{-1}$ (in purple) and $3 \times 10^{-2}\ s^{-1}$ (in orange). Average value calculated over 4 pictures, error bar correspond to the standard deviation. Dotted line corresponds to $\Gamma_{damage} = \Gamma_{exp}$ curve.
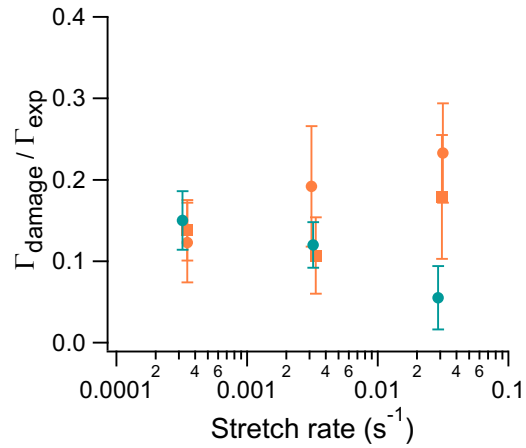
Figure 21: Evolution of $\Gamma_{damage}/\Gamma_{exp}$ with the loading rate for crack propagation test on DAMAMA(1.6) at 25 °C (in orange) and DAMAEA(1.5) (in green). Γ_{damage} calculated using Ub=64 kJ/mol

In DAMAMA(1.6) the sacrificial bond breakage of the filler network is closely coupled to the molecular friction. In that case, the filler damage is enhanced by the increase in friction and controls the fracture toughness. In DAMAEA(1.5) viscoelastic dissipation is reduced, and the probability of breaking a bond of the filler network is not enhanced by the matrix since the friction is too low. But increasing the stretch rate may actually still

have consequences on bulk viscoelastic dissipation. Another option to rationalize the results is the role played by the deformation and fracture of the matrix network once the filler network is broken(*6*). Such a process is bound to be rate dependent but is a high stretch rate/high strain dissipative process which may be distinctly different from the linear viscoelastic properties of the matrix material typically used for bulk dissipation.

This result can also be rationalized by a discussion in terms of strain at break, started in the previous section. Figure 22 represents the number of broken chains of the filler network as a function of the strain at which the crack starts to propagate. The filler structure is the same in both double networks. In DAMAMA(1.6), the filler network experienced a much higher elongation before rupture ($\lambda_{break} > 2$). Since the damage clearly increases with strain (*2, 7*) the chain scissions measured post-mortem are one order of magnitude higher in DAMAMA(1.6) than in DAMAEA(1.5).
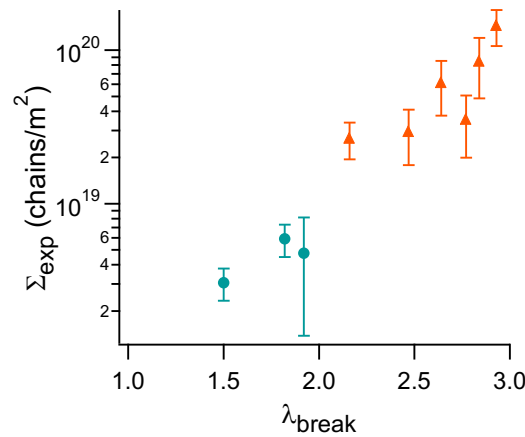
Figure 22: Evolution of the number, Σ_{exp}, of broken chain of the filler network with strain at crack propagation in DAMAMA(1.6) (orange triangles) and DAMAEA(1.5) (green circles).

The main difference comes from the nature of the matrix.

- In DAMAMA(1.6) the polymethyl acrylate matrix dissipates locally the energy transferred from the filler breakage so that as strain increases, the critical strain where the chains break goes from random bond scission in the material to correlated bond scission and crack nucleation is delayed and the crack propagation is delayed too(*6*). Thanks to this delay in crack propagation, the material does not break macroscopically and reaches a regime where large scale filler damage occurs and dominates the fracture behavior.

- In the poly ethyl acrylate matrix of DAMAEA(1.5), less viscoelastic dissipation occurs locally and the energy transferred from the filler to the matrix is less

dissipated and more transferred to the neighboring filler loaded strand. However, because of the lower energy dissipation, the double network breaks before reaching the regime where chain scission govern the fracture behavior. In that case, the fracture is not dictated by filler chain scission and viscoelasticity and matrix chain scission also play relative important roles.

The level of pre-stretching of the filler network is not exactly the same $\lambda_0 = 1.6$ in DAMAMA(1.6) against $\lambda_0 = 1.5$ in DAMAEA(1.5). The double network with the matrix made of ethyl acrylate is slightly less swollen. Therefore, in principle the lower level of pre-stretching of the filler network may also explain the decrease in fracture toughness. This decrease in the swelling ratio can be attributed to a difference in monomers miscibility. However, the difference between these two values may not be critical. P. Millereau investigated the influence of the level of pre-stretching of the filler network on mechanical properties (*2, 6*). Double networks at these two values of pre-stretching exhibit similar trends with strain hardening, as can be deducted from Figure 23.
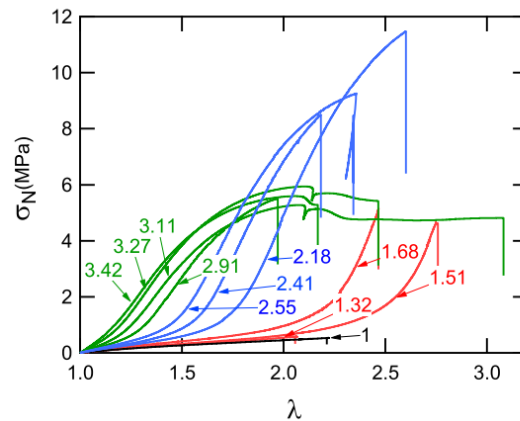
Figure 23: Stress-strain curves of different multiple network made of polyethyl acrylate, λ_0 value of is written by each curve, from Millereau et al. (6)

2.3 Comparison of different levels of pre-stretching of the filler network

After changing the nature of the matrix network, the influence of the level of pre-stretching of the filler network will now be discussed. Filler and matrix networks are made from polymethyl acrylate.

The same systematic analysis was repeated on triple networks fully made from poly methyl acrylate with a level of pre-stretching of the filler network of $\lambda_0 = 2.3$, DAMAMA(2.3). Stress-strain curves of crack propagation tests are plotted in Figure 24. Stresses at break increase with the stretch rate. The fracture energies were calculated, using the Greensmith's approximation (Chapter 3, Eq. 3), and plotted as a function of the stretch rate for single (SN) double (DN) and triple networks (TN), Figure 25.
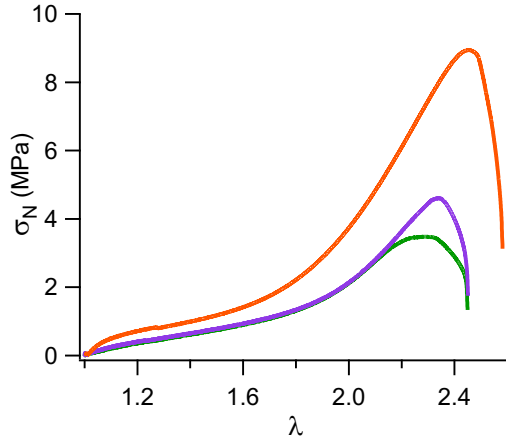
Figure 24: *Example of stress-strain curves of crack propagation test on notched DAMAMA(2.3) at $\dot{\lambda} = 3 \times 10^{-4} \ s^{-1}$(in green), $3 \times 10^{-3} \ s^{-1}$ (in purple) and $3 \times 10^{-2} \ s^{-1}$ (in orange). One DAMAMA(2.3) and one MAMA(2.3) were tested.*
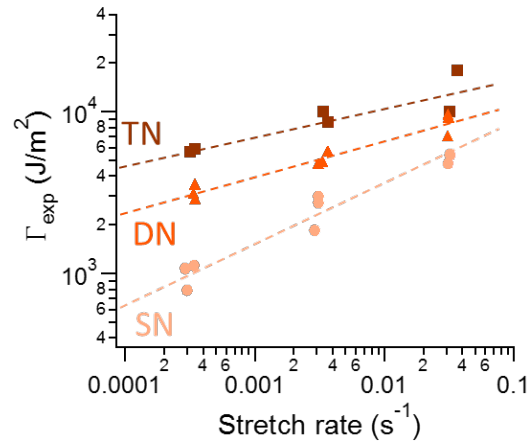
Figure 25: *Evolution of the fracture energy with the stretch rate for DASNMA (circles), DAMAMA(1.6) (triangles) and DAMAMA(2.3) (squares). Dotted lines are guide for the eye: single (SN), double (DN) and triple (TN) networks.*

At a fixed value of stretch rate, a higher level of pre-stretching of the filler network leads to higher fracture toughness as previously reported (*2, 3, 6, 7*). For each level of filler pre-stretching, the fracture energy increased with the crosshead velocity. However, comparing single, double and triple networks, this rate dependence decreases with an increasing level of pre-stretching of the filler network. But even for the triple networks, DAMAMA(2.3), the fracture energy increases with crosshead velocity. In fact, the multiple network is made of poly methyl acrylate and the crack propagation temperature is close to Tg. The viscoelastic dissipation from the matrix is important and plays a crucial role, as discussed in previous sections.

In order to record information on the damage associated, four single optical sections (two on each side) were recorded at magnification 5x and 100 μm depth. Figure 26 represents example of surface intensity plots of raw pictures and pre-processed, re-colored, pictures after crack propagation in DAMAMA(2.3) at $\dot{\lambda} = 3 \times 10^{-4} \ s^{-1}$ (a and b), $\dot{\lambda} = 3 \times 10^{-3} \ s^{-1}$ (c and d) and $\dot{\lambda} = 3 \times 10^{-2} \ s^{-1}$ (e and f). The level of damage increases at $\dot{\lambda} = 3 \times 10^{-2} \ s^{-1}$compared to $\dot{\lambda} = 3 \times 10^{-4} \ s^{-1}$ and $\dot{\lambda} = 3 \times 10^{-3} \ s^{-1}$.

$\dot{\lambda}\ (s^{-1})$	Surface intensity plots	Pre-processed images
3×10^{-4}	a)	b)
3×10^{-3}	c)	d)
3×10^{-2}	e)	f)
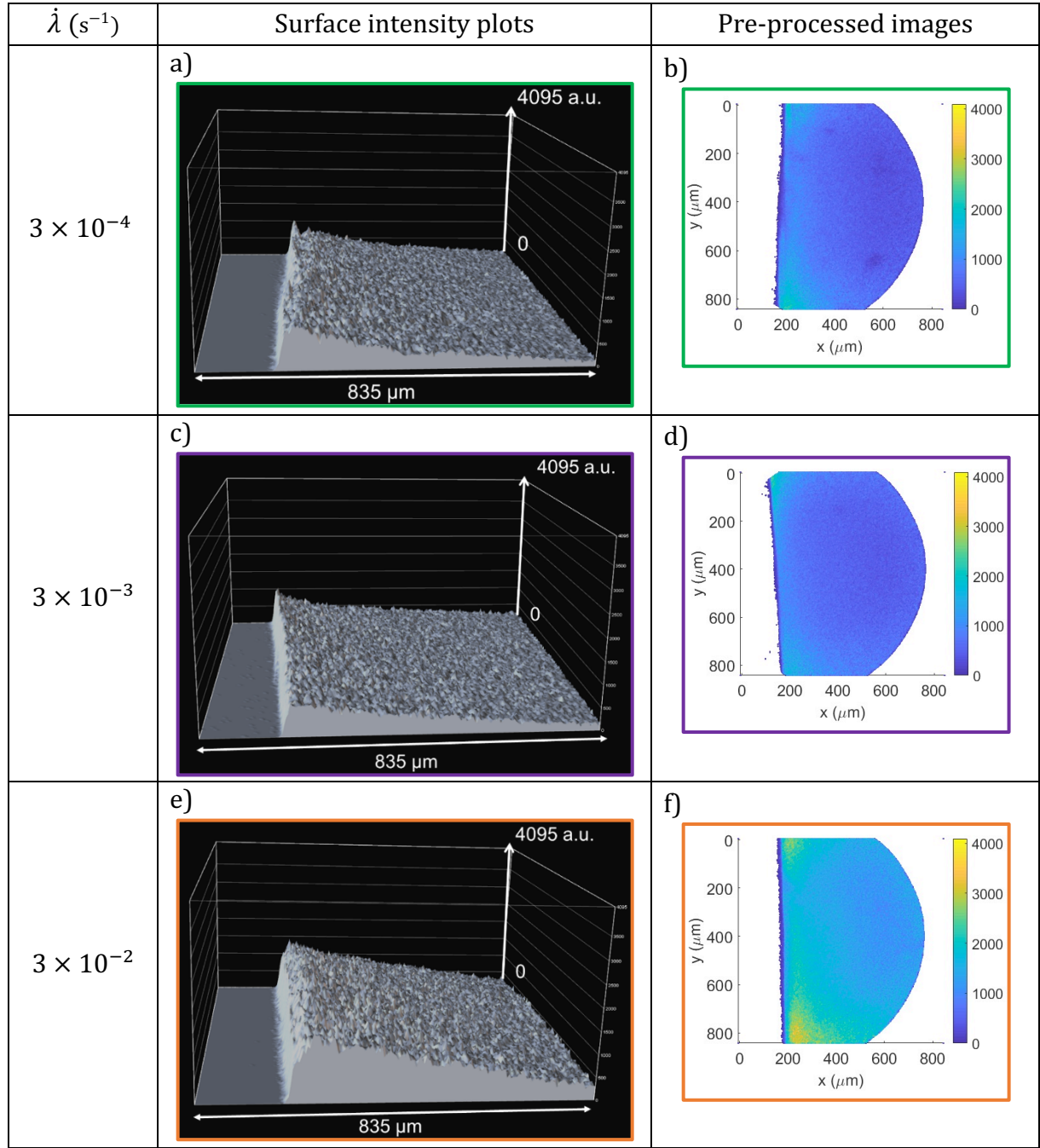
Figure 26: Surface intensity plots and pre-processed (re-colored) pictures after crack propagation in DAMAMA(2.3) (Laser 7 Gain 3) at 25 °C and $\dot{\lambda} = 3 \times 10^{-4}\ s^{-1}$ (a and b), $\dot{\lambda} = 3 \times 10^{-3}\ s^{-1}$ (c and d) and $\dot{\lambda} = 3 \times 10^{-2}\ s^{-1}$ (e and f).

The evolution of fluorescence intensity with distance normal to the crack plane for each crosshead velocity is represented Figure 27 . For all three stretch rates, a fluorescent signal higher than the noise level is visible at 500 μm. As presented in Chapter 3, for quantification, the signal is integrated up to the noise level. The distance of integration is our definition of L_{damage} and the integrated signal is converted into a concentration of activated mechanophores and then in a number of broken chains. However, in the case of

DAMAMA(2.3), the signal was still higher than the noise level at the end of the volume where intensity measurements were carried out ($L_{damage} > 500 \ \mu m$).
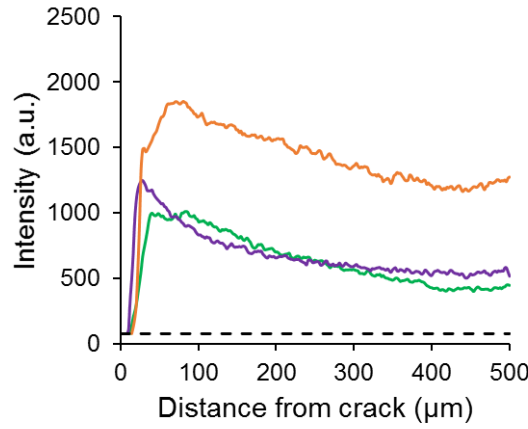
Figure 27: Intensity profiles after crack propagation in DAMAMA(2.3) at 25°C and at $\dot{\lambda} = 3 \times 10^{-4} \ s^{-1}$(in green), $3 \times 10^{-3} \ s^{-1}$ (in purple) and $3 \times 10^{-2} \ s^{-1}$ (in orange)..

L_{damage} was estimated at about 2.2 mm by a manual stitching of several pictures taken away from the crack surface. Indeed, the total decay was estimated by the superimposition of the several intensity profiles reported on the same graph as shown in Figure 28.
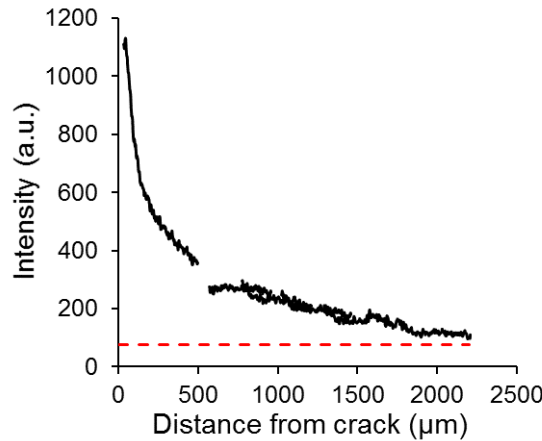
Figure 28: Intensity decay with the distance from the crack edge in DAMAMA(2.3) at 25 °C and $\dot{\lambda} = 3 \times 10^{-3} \ s^{-1}$. Dotted line corresponds to the noise level.

The stitching method was not developed and implemented for all pictures. When the noise threshold was not reached, the signal was integrated up to 500 μm. For these images, the areal density of chains scissions is underestimated and will be used only to get trends. These data points are notified by black edges.

The evolution of Σ_{exp} with stretch rate was plotted for single (SN), double (DN) and triple networks (TN) in Figure 29a. At a fixed value of stretch rate, a higher level of

223

pre-stretching of the filler network leads to a higher number of broken chains. In triple networks, the filler network is diluted ($\phi_{SN} = 6\%$). To get a fair comparison of single, double and triple networks, the number of broken chains was normalized by the areal chain density of a monolayer of the filler network (thickness taken as the mesh size) to get $\bar{\Sigma}$ (details on normalization in Chapter 3). $\bar{\Sigma}$ is plotted as a function of the stretch rate in Figure 29b. In single networks of poly methyl acrylate, the damage is about ten times a monolayer, at 25°C. The level of chain scission detected is about hundred and thousand times a filler network monolayer in double and triple networks of poly methyl acrylate respectively.
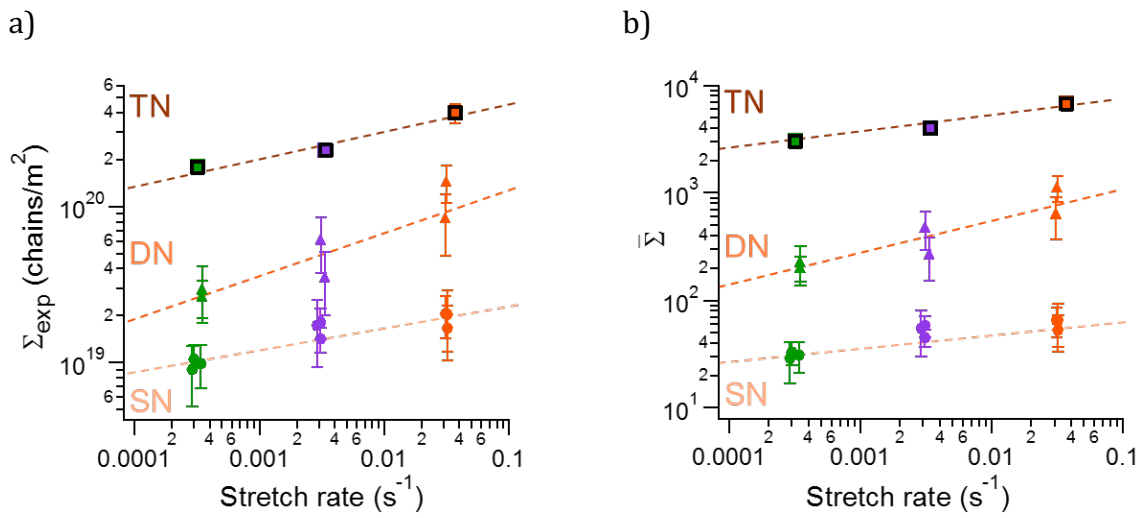
Figure 29: Evolution of the number, Σ_{exp} (a) and normalized number $\bar{\Sigma}$ (b) of broken chain of the filler network with the stretch rate for crack propagation test on DASNMA(circles) DAMAMA(1.6) (triangles) and DAMAMA(2.3) (squares, off-limit) at different stretch rate: $3 \times 10^{-4}\ s^{-1}$(in green), $3 \times 10^{-3}\ s^{-1}$ (in purple) and $3 \times 10^{-2}\ s^{-1}$ (in orange). Values for TN are underestimated, identified by black edges (off-limit)

A slight rate dependence is still visible at 25 °C in poly methyl acrylate triple network elastomers. When viscoelastic dissipation occurs in the matrix, damage in multiple networks depends on stretch rate. This result is true even with a filler network pre-stretched at $\lambda_0 = 2.3$.

However, this last result is to take with a pinch of salt as the signal was off-limit. For that reason no further quantitative analysis were performed, as the Σ_{exp} is underestimated.

3 Influence of the temperature on bond scission in the fracture of multiple network elastomers

3.1 At temperatures far from Tg: Triple networks of polyethyl acrylate

Crack propagation tests were performed on triple networks fully made from polyethyl acrylate, DAEAEA(2.3), at a crosshead velocity of 50 µm/s ($\dot{\lambda} = 3 \times 10^{-3}\ s^{-1}$) and at 25 °C (Tg + 43°C), 40 °C, 60 °C and 80 °C. Examples of stress-strain curves of crack propagation tests are shown in Figure 30. Figure 31 represents the evolution of the fracture energy (calculated by the Greensmith's approximation, Chapter 3, Eq 3) with temperature.
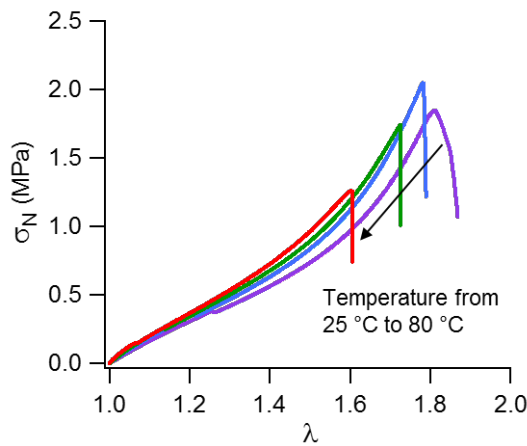
Figure 30: Examples of stress-strain curves of crack propagation tests on notched DAEAEA(2.3) at $\dot{\lambda} = 3 \times 10^{-3}\ s^{-1}$ and 25 °C (in purple), 40 °C (in blue), 60 °C (in green) and 80 °C (in red). One experiment was done on one DAEAEA(2.3) and one EAEA(2.3)
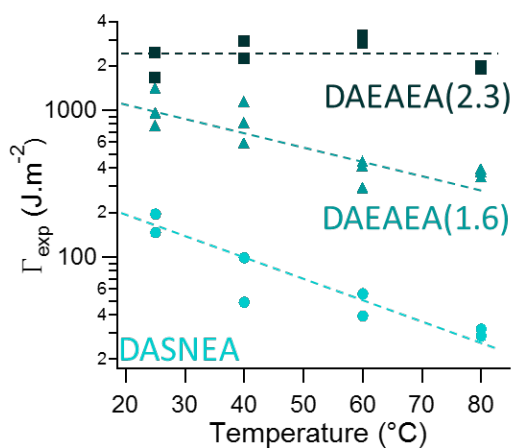
Figure 31: Evolution of the fracture energy with the temperature for DASNEA (light blue circles) DAEAEA(1.6) (green triangles) and DAEAEA(2.3) (dark green squares)

The influence of temperature on the level of damage in double networks made of poly ethyl acrylate, DAEAEA(1.6), could not be estimated due to too many crack bifurcations occurring during crack propagation (as discussed in Section 1). However, mechanical tests were performed and the fracture energies calculated are compared with triple networks of DAEAEA(2.3) in Figure 31.

As Pierre Millereau reported (2), the fracture energy decreases with increasing temperature for single network elastomer and this decrease with temperature is attenuated with an increasing level of pre-stretching of the filler network. Indeed, the fracture energy of triple networks of poly ethyl acrylate appear nearly constant with temperature.
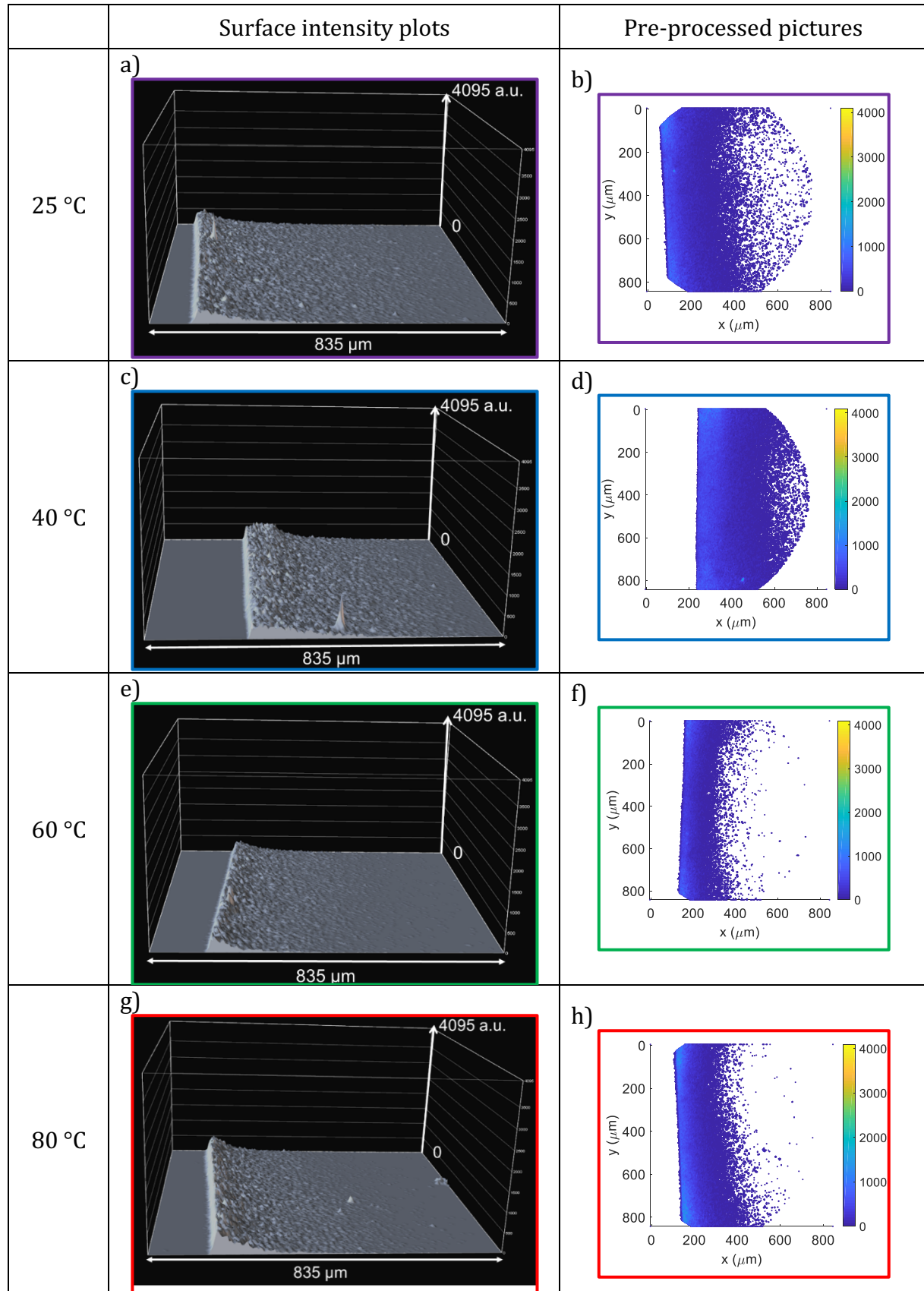
	Surface intensity plots	Pre-processed pictures
25 °C	a)	b)
40 °C	c)	d)
60 °C	e)	f)
80 °C	g)	h)

Figure 32: Surface intensity plots and pre-processed (re-colored) pictures after crack propagation in DAEAEA(2.3) (Laser 7 Gain 3) at $\dot{\lambda} = 3 \times 10^{-3} \ s^{-1}$ and 25 °C (a and b), 40 °C (c and d), 60 °C (e and f) and 80 °C (g and h).

For each crack propagation test on DAEAEA(2.3), four single optical sections (two on each side) were recorded at magnification 5x and 100 µm depth. Figure 32 represents examples of surface intensity plots of raw pictures and pre-processed (re-colored) pictures associated, after crack propagation in DAEAEA(2.3) at each temperature.

The corresponding evolution of fluorescence intensity with the distance normal to the crack edge is represented Figure 33.
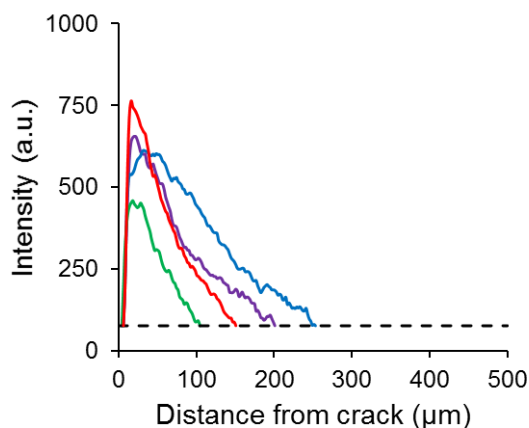
Figure 33: Intensity profiles after crack propagation in DAEAEA(2.3) at $\dot{\lambda} = 3 \times 10^{-3}\ s^{-1}$ and 25℃ (purple),40 ℃ (blue), 60 ℃ (green) and 80 ℃ (red).

From the comparison of all the images, the difference in intensity profile are almost included in the error bars.

The areal density, Σ_{exp}, of broken chains, of the filler network, was calculated and averaged over four pictures per sample. Average values of Σ_{exp} are plotted as a function of temperature in Figure 34. Despite the large error bars, the number of broken chains seems to decrease from 25 °C to 60 °C and then to increase from 60 °C to 80 °C.

The evolution of the fracture energy with the temperature is also reported on Figure 34. Fracture energy slightly increases from 25 °c to 40 °C and then decreases from 40 °C to 80 °C. In that case macroscopically measured fracture energy and the number of broken chains does not follow similar trends.
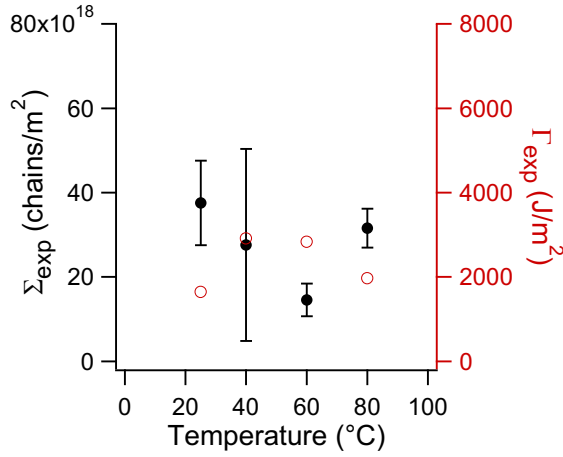
Figure 34: Evolution of the number, Σ_{exp}, of broken chain of the filler network (in black) and of the fracture energy, Γ_{exp} , (in red) as a function of the temperature after crack propagation in DAEAEA(2.3) at $\dot{\lambda} = 3 \times 10^{-3}\ s^{-1}$. Mean values calculated over 4 pictures, error bars correspond to the standard deviation
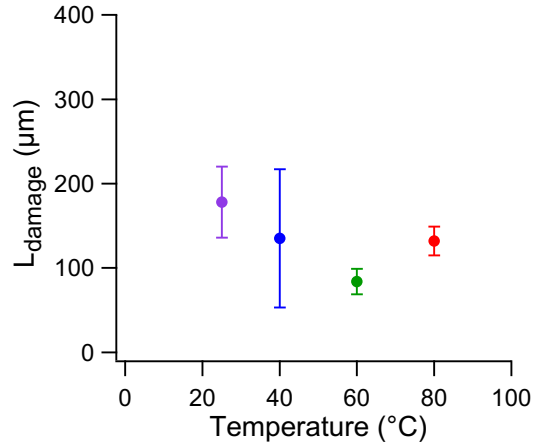
Figure 35: Evolution with temperature of the length, L_{damage}, over which damage is detected after crack propagation in DAEAEA(2.3) at $\dot{\lambda} = 3 \times 10^{-3}\ s^{-1}$. Mean values calculated over 4 pictures, error bars correspond to the standard deviation

The length, L_{damage}, over which damage was detected was also calculated, averaged over four pictures per sample, and is plotted as a function of temperature in Figure 35. Because of the reinforcement mechanism by sacrificial bond breakage, the damage is spread over hundreds of microns. As Σ_{exp}, L_{damage} decreases from 25 °C to 60 °C and then increases from 60 °C to 80 °C

Σ_{exp} was normalized by the areal chain density of the filler network Σ_{SN}, to give $\bar{\Sigma}$. Mean values of this normalized areal density of broken chains is represented as a function of the fracture energy in Figure 36. The extent of bond scission is large, about few hundred times more than a filler monolayer, and rather decreases with increasing fracture energy, but there is no clear trend as values are comparable.
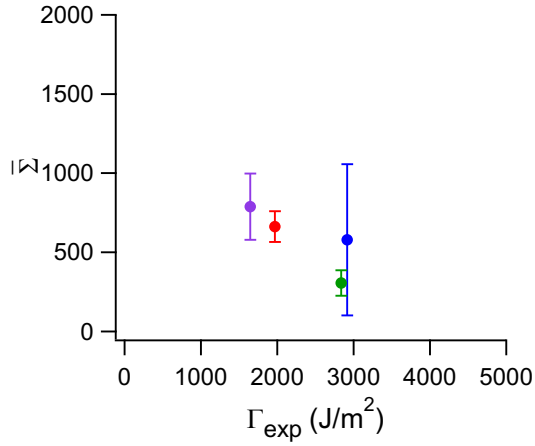
Figure 36: Evolution of the normalized number of broken chains per square meter in the filler network with the fracture energy for crack propagation test on DAEAEA(2.3) at $\dot{\lambda} = 3 \times 10^{-3}\ s^{-1}$ and different temperatures: 25 °C (in purple, 40 °C (in blue), 60 °C (in green) and 80 °C (in red). Means values calculated over 4 pictures, error bars correspond to the standard deviation.
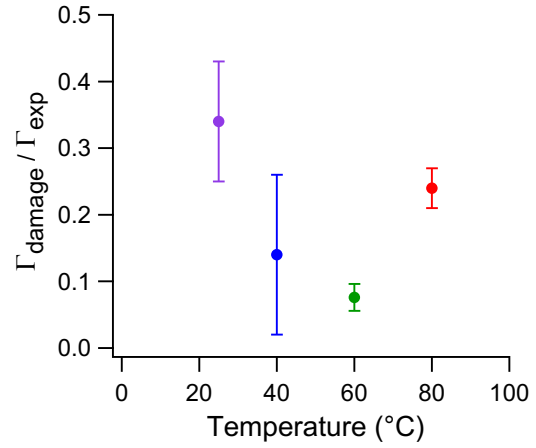
Figure 37: Evolution of $\Gamma_{damage}/\Gamma_{exp}$ with the temperature for crack propagation test on DAEAEA(2.3) at 50 μm/s. Γ_{damage} calculated using U=64 kJ/mol

The bond scission in the filler component of the fracture energy, Γ_{damage}, was calculated from Eq 3. (U=64 kJ/mol). The ratio $\frac{\Gamma_{damage}}{\Gamma_{exp}}$ was plotted as a function of the temperature, as shown in Figure 37. The contribution of the chains scission clearly goes through a minimum at 60 °C.

The contribution of filler breakage on total energy dissipation was also plotted as a function of the strain at break, as shown in Figure 38. As there is no clear trend, the elongation at break cannot explain the evolution of the contribution of energy dissipated by chain scission.
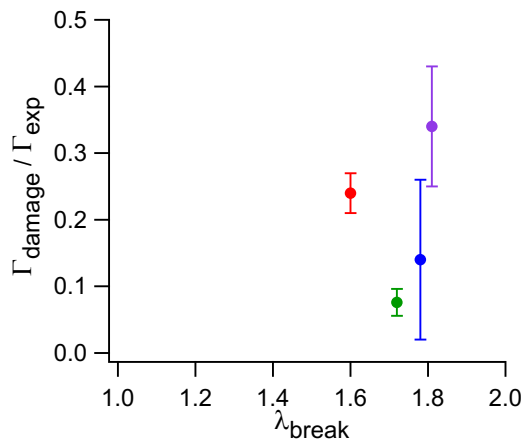
Figure 38: Evolution of $\Gamma_{damage}/\Gamma_{exp}$ with the strain at break for crack propagation test on DAEAEA(2.3) at 50 μm/s. Γ_{damage} calculated using U=64 kJ/mol

In an attempt to explain the results, the nominal stress was normalized by its maximum value (where the crack starts to propagate) and represented as a function of propagation time, Figure 39. In these experiments, where the crack velocity is not controlled, the average crack velocity, v_{crack}, can be estimated by Eq 4.

$$v_{crack} = \frac{d_{propagation}}{t_{propagation}} \qquad \text{Eq 4.}$$

Where $d_{propagation}$ is the distance of crack propagation and $t_{propagation}$ the propagation time.
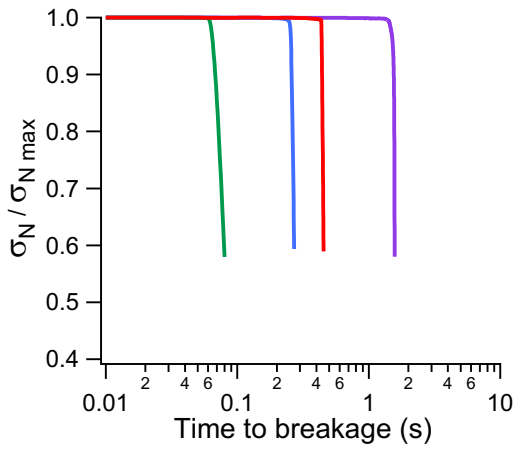
Figure 39: Normalized stress as a function of time during crack propagation in DAEAEA(2.3) at $\dot{\lambda} = 3 \times 10^{-3}\ s^{-1}$ and 25 °C (in purple), 40 °C (in blue), 60 °C (in green) and 80 °C (in red)
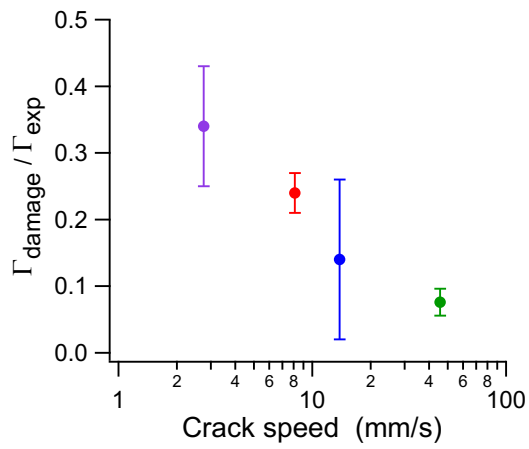
Figure 40 : Evolution of $\Gamma_{damage}/\Gamma_{exp}$ with the averaged crack velocity for crack propagation test on DAEAEA(2.3) at $\dot{\lambda} = 3 \times 10^{-3}\ s^{-1}$. Γ_{damage} calculated using U=64 kJ/mol

The contribution of filler breakage on total energy dissipation was then plotted as a function of the averaged crack speed, as shown in Figure 40. $\frac{\Gamma_{damage}}{\Gamma_{exp}}$ decreases with increasing velocity.

This result can be compared with results obtained in Section 2.2. When the matrix is made of poly ethyl acrylate, DAMAEA(1.5) or DAEAEA(2.3), the contribution of filler damage in energy dissipation decreases with increasing rate or crack velocity (to be compared with Figure 21). In DAEAEA(2.3), when the crack propagate faster, all other dissipative mechanisms, such as viscoelastic dissipation, become relatively more important compared to the contribution of chain scission. The matrix is not viscoelastic and adding friction from faster propagation will first have consequences on viscoelastic dissipation. However, the reproducibility was not tested on this set of samples and more analysis need to be done to confirm the result.

In conclusion, the triple network fully made of poly ethyl acrylate is far enough from its Tg (T - Tg > 40 °C) to be not directly temperature dependent. This result confirmed Pierre Millereau's analysis (*2*) and add quantitative information on damage. In multiple network of ethyl acrylate, at ambient temperature and above, the reinforcement mechanism based on sacrificial bond breakage is slightly temperature dependent.

The variation in molecular damage are slight and can be explained by crack velocity difference more than by the temperature dependence. The crack velocity was not controlled and depends on many parameters such as the initiation from the introduced notch.

Ethyl acrylate based multiple networks were tested far from their Tg (+43 °C and above). So that the viscoelasticity from the glass transition was negligible.

However, our previous results show that closer to the Tg, elastomers become tougher thanks to energy dissipation by molecular friction and the influence of the temperature on bond scission in multiple networks, close to the glass transition temperature, has never been studied. In the next section, results on multiple networks made of poly methyl acrylate will be presented to address this question.

3.2   At temperatures closer to the Tg

3.2.1   Double networks based on poly methyl acrylate

Crack propagation tests were performed on double networks, fully made from methyl acrylate, DAMAMA(1.6), at a crosshead velocity of 50 μm/s ($\dot{\lambda} = 3 \times 10^{-3}\ s^{-1}$) and at four different temperatures, from 25 °C (Tg + 7 °C) to 80 °C (Tg + 62 °C). Examples of stress-strain curves, of crack propagation tests, at each temperature, are given in Figure 41. The fracture energies were calculated using the Greensmith's approximation (Chapter 3, Eq 3) and are plotted as a function of the temperature in Figure 42. The evolution of the fracture energy with the temperature of single network of methyl acrylate, DASNMA, is also plotted on Figure 42.

From 60 °C (Tg + 42 °C) to 25 °C (Tg + 7 °C), the fracture toughness of single and double networks increases as the temperature gets close to Tg. The temperature dependence is

similar in single and double networks. The multiple network becomes tougher as the testing temperature approaches the glass transition temperature and molecular friction is active in the matrix.

From 60 °C (Tg + 42 °C) to 80 °C (Tg + 62 °C), the fracture energy appears to stay nearly constant or even to slightly increase.
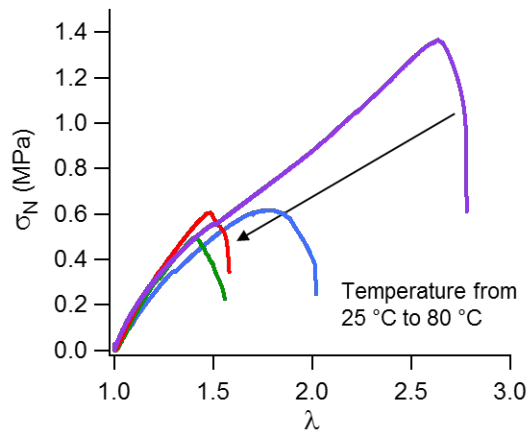
Figure 41: Examples of stress-strain curves of crack propagation tests on notched DAMAMA(1.6) at $\dot{\lambda} = 3 \times 10^{-3}\ s^{-1}$ and 25 °C (in purple), 40 °C (in blue), 60 °C (in green) and 80 °C (in red). Two samples of DAMAMA(1.6) and one of MAMA(1.6) were tested.
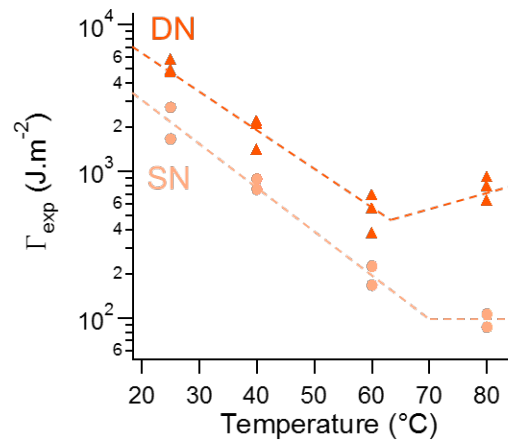
Figure 42: Evolution of the fracture energy with the temperature for DASNMA (beige circles) and DAMAMA(1.6) (orange triangles). Dotted lines are guide for the eye.

For each crack propagation test, four single optical sections (two on each side) were recorded at magnification 5x and 100 µm depth. Figure 43 represents examples of surface intensity plots of raw pictures and pre-processed, re-colored, pictures associated, after crack propagation in DAMAMA(1.6) at each temperature.

	Surface intensity plots	Pre-processed pictures
25 °C	a)	b)
40 °C	c)	d)
60 °C	e)	f)
80 °C	g)	h)
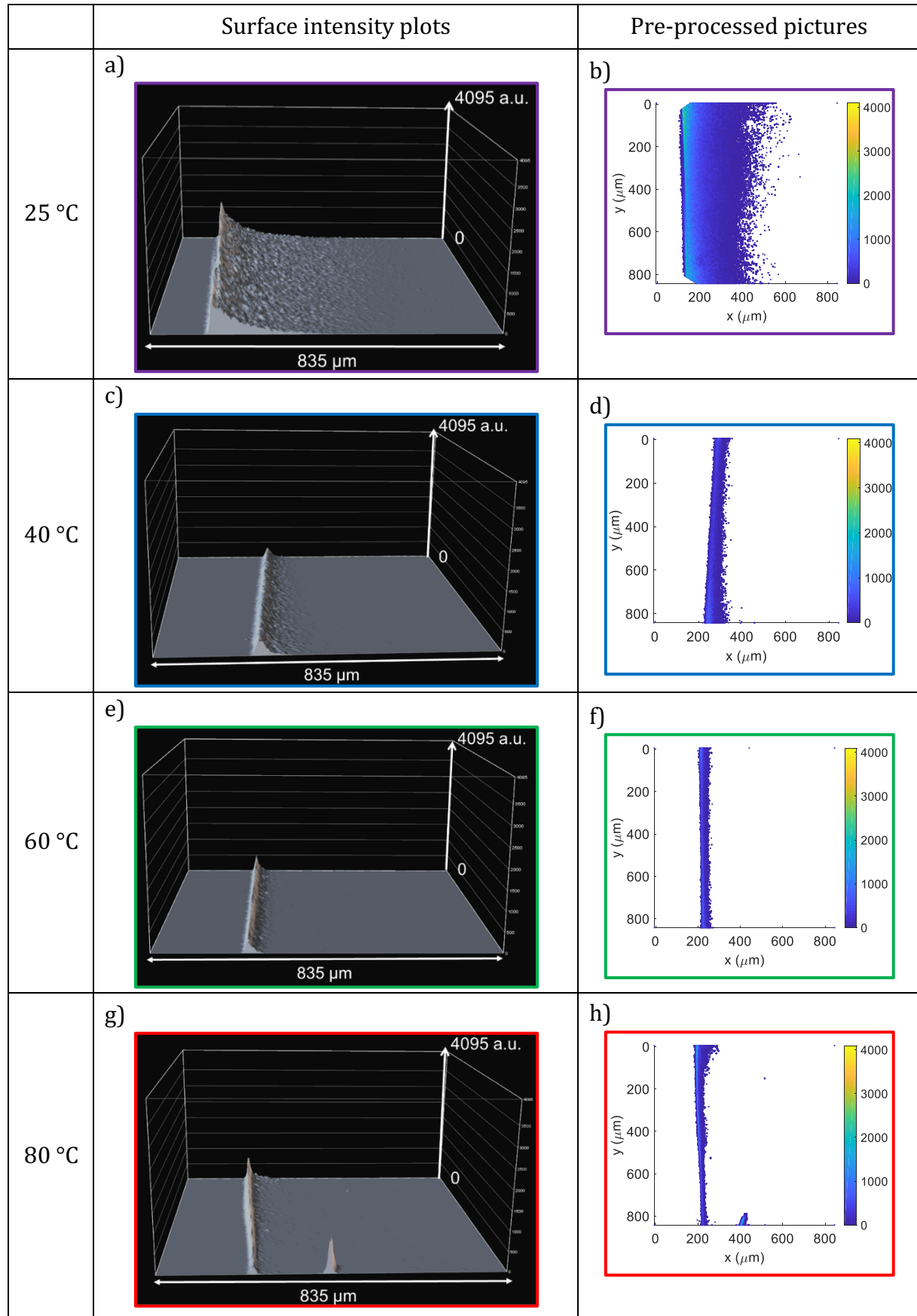
Figure 43: Surface intensity plots and pre-processed (re-colored) pictures after crack propagation in DAMAMA(1.6) (Laser 7 Gain 3) at $\dot{\lambda} = 3 \times 10^{-3}\ s^{-1}$ and 25 °C (a and b), 40 °C (c and d), 60 °C (e and f)and 80 °C (g and h).

The corresponding evolution of the averaged fluorescence intensity with distance normal to the crack plane is represented in Figure 44. A large difference was observed between 25 °C and other temperatures. The fluorescence intensity, reporting for filler damage, is much higher at 25 °C, while it is similar at 40 °C, 60 °C and 80 °C.
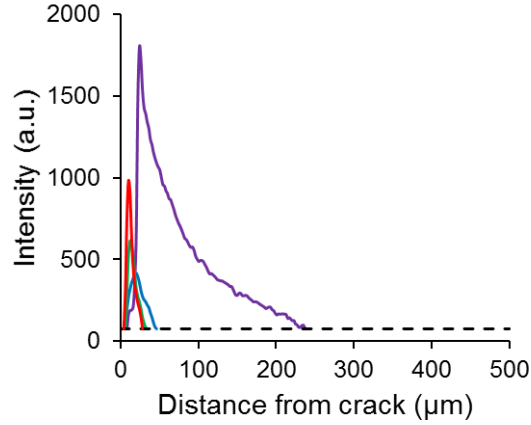
Figure 44: Intensity profile after crack propagation in DAMAMA(1.6) at $\dot{\lambda} = 3 \times 10^{-3}\ s^{-1}$ and 25°C (purple),40 °C (blue), 60 °C (green) and 80 °C (red).

To obtain more quantitative information, the areal density, Σ_{exp}, of broken chains of the filler network was calculated and is plotted as a function of the temperature in Figure 45 alongside the evolution of the fracture energy with the temperature. Both the areal density of broken chains of the filler network and the fracture energy decrease sharply between 25 and 40°C and remain relatively constant afterwards or slightly increasing at 80 °C.
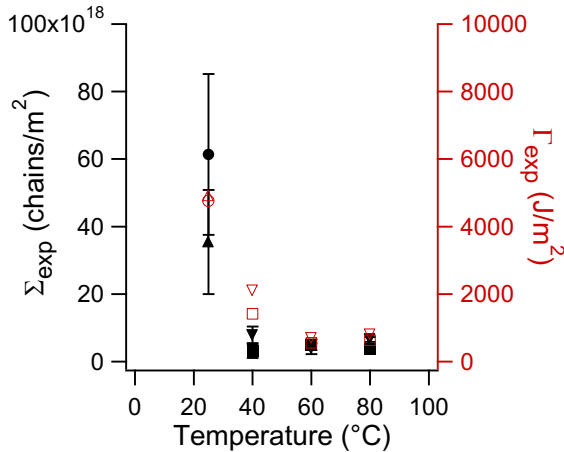
Figure 45: Evolution of the number, Σ_{exp}, of broken chain of the filler network (in black) and of the fracture energy, Γ_{exp} , (in red) as a function of the temperature after crack propagation in DAMAMA(1.6) at $\dot{\lambda} = 3 \times 10^{-3}\ s^{-1}$. Different symbols correspond to samples from different polymerizations
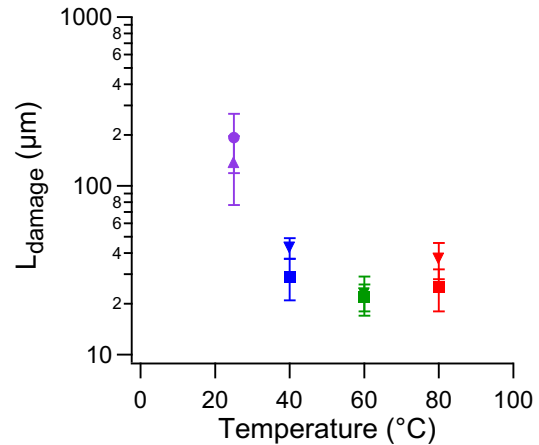
Figure 46: Evolution with temperature of the length, L_{damage}, over which damage is detected after crack propagation in DAMAMA(1.6) at $\dot{\lambda} = 3 \times 10^{-3}\ s^{-1}$. Different symbols correspond to samples from different polymerization

The length, L_{damage}, over which damage was detected was also plotted as a function of the temperature, in a log scale. L_{damage} decreases with increasing temperature, from about hundreds of microns at 25 °C to tens of microns at other temperatures.

From the areal density, Σ_{exp}, of broken chains of filler network, the energy dissipated by bond scission, Γ_{damage}, can be calculated, with Eq 3. (U=64 kJ/mol). Γ_{damage} was divided by Γ_{exp}, to get $\frac{\Gamma_{damage}}{\Gamma_{exp}}$ that was plotted as a function of the temperature, as shown in Figure 47.

Between 40 °C and 80 °C, the contribution of energy dissipation by scission of filler strands increases from about 5 % to about 10 %. When the temperature increases and gets away from Tg, the viscoelasticity is reduced. As a result, the contribution of bond scission becomes more important as other dissipative mechanisms are reduced.

However, at 25 °C (Tg + 7 °C), the contribution of bond breakage is higher than at other temperatures. This result can be explained by two reasons, previously mentioned:

1. At a temperature close to Tg, molecular friction is drastically increased. Chains friction increases the stress felt by the filler network chains. Because of this overloading, the chain breakage is facilitated and chain scissions occur in large amount and in a large volume.

2. At a temperature close to Tg, the matrix itself dissipates a lot of energy. The energy transferred from filler network to the matrix network by chain scissions is dissipated and the overall material can stretch more before failure. Figure 48 shows $\bar{\Sigma}$ as a function of the elongation at break. It illustrates that, at 25 °C, the material can indeed stretch more before the crack propagates, hence increasing the probability to break sacrificial bonds in synergy.
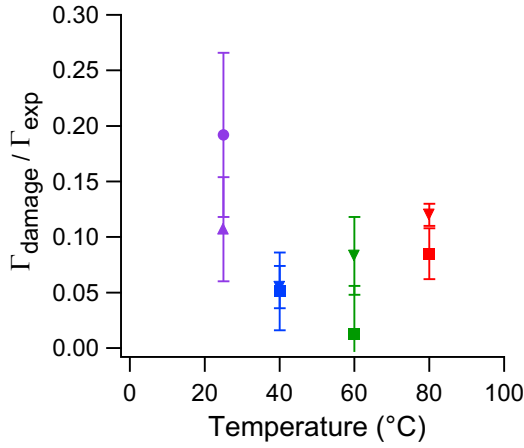
Figure 47: Evolution of $\Gamma_{damage}/\Gamma_{exp}$ with the temperature for crack propagation test on DAMAMA(1.6) at $\dot{\lambda} = 3 \times 10^{-3}\ s^{-1}$. Γ_{damage} calculated using U=64 kJ/mol Mean value calculated over 4 pictures, error bar correspond to the standard deviation. Different symbols correspond sample from different polymerizations
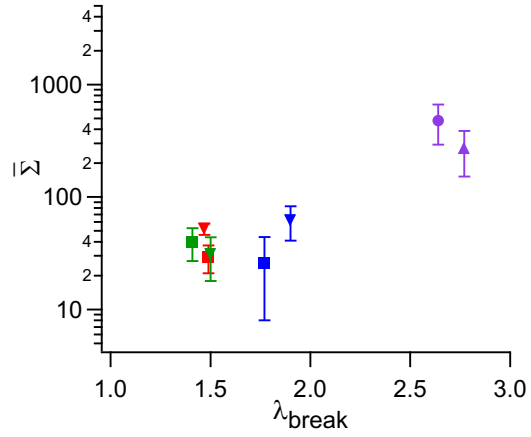
Figure 48: Evolution of the normalized number, $\bar{\Sigma}$, of broken chain of the filler network with maximal strain before crack propagation in DAMAMA(1.6) at $\dot{\lambda} = 3 \times 10^{-3}\ s^{-1}$ and different temperature: 25 °C (in purple), 40 °C (in blue), 60 °C (in green) and 80 °C (in red). Mean value calculated over 4 pictures, error bar correspond to the standard deviation. Different symbols correspond to sample from different polymerizations.

3.2.2 Triple networks based on poly methyl acrylate

A last set of materials was tested: triple networks made of poly methyl acrylate, two samples of DAMAMA(2.3) and one of MAMA(2.3). This material has a higher level of pre-stretching of the filler network, which is expected to decrease the temperature dependence of damage, but a Tg close to the test temperature, which is expected to enhance viscoelasticity and the temperature dependence.

Crack propagation tests were performed on at a crosshead velocity of 50 µm/s ($\dot{\lambda} = 3 \times 10^{-3}\ s^{-1}$) and at 25 °C, 40 °C, 60 °C and 80 °C. Example of stress-strain curves of crack propagation tests are given Figure 49.

From 25 °C to 60 °C, as in single and double networks, the stress at break decreases with increasing temperature.

Surprisingly, the stress-strain curves at 80 °C has a different shape. In fact, the stress and strain at break is much higher at 80 °C (in red) than at 60 °C (in green) and the stress drops sharply as the crack propagates. For better visualization, the nominal stress was normalized by its maximum value (where the crack starts to propagate) and represented

as a function of propagation time, Figure 50. The crack propagated much faster at 80 °C, in tens of milliseconds, than at other temperatures, in few seconds.
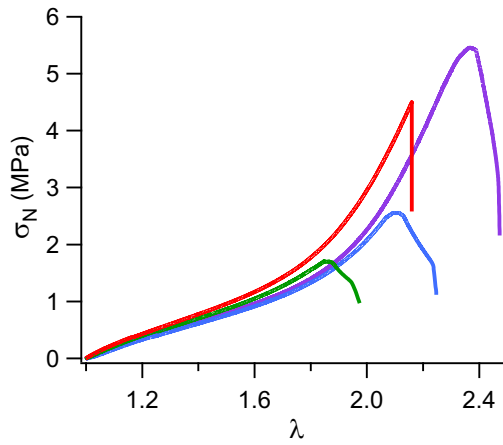
Figure 49: Example of stress-strain curves of crack propagation test on notched DAMAMA(2.3) at $\dot{\lambda} = 3 \times 10^{-3} \ s^{-1}$ and 25 °C (in purple), 40 °C (in blue), 60 °C (in green) and 80 °C (in red). Two DAMAMA(2.3) and one MAMA(2.3) were tested.
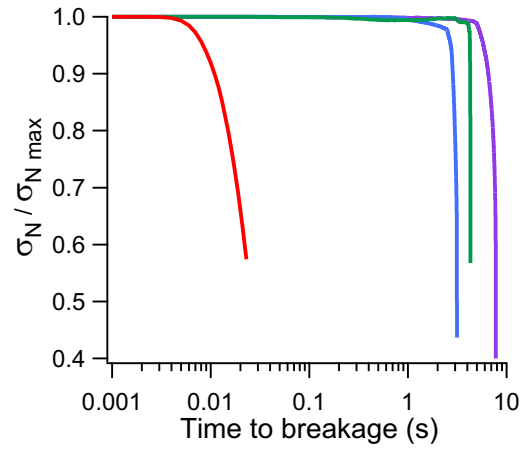
Figure 50: Normalized stress as a function of time during crack propagation in DAMAMA(2.3) at $\dot{\lambda} = 3 \times 10^{-3} \ s^{-1}$ and 25 °C (in purple), 40 °C (in blue), 60 °C (in green) and 80 °C (in red)

The fracture energies were calculated for the triple network DAMAMA(2.3) using the Greensmith's formula (Chapter 3, Eq. 3) and added to Figure 42, to give Figure 51.
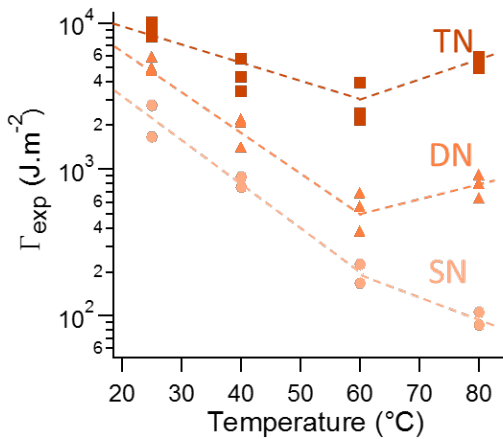
Figure 51: Evolution of the fracture energy with the temperature for DASNMA (beige circles), DAMAMA(1.6) (orange triangles) and DAMAMA(2.3) (brown squares)
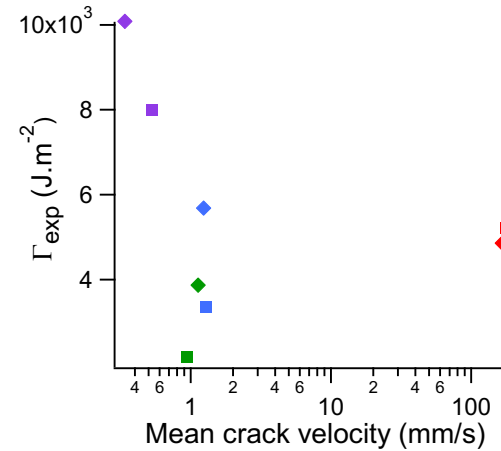
Figure 52: Evolution of the fracture energy with the mean crack velocity in DAMAMA(2.3) at 25 °C (purple), 40 °C (in blue), 60 °C (in green) and 80 °C (in red). Different symbols correspond to samples from different polymerizations.

From 25 °C to 60 °C, a decrease of fracture energy with increasing temperature is visible. However, the dependence is reduced in triple networks compared to single and double networks. As observed for poly ethyl acrylate multiple networks (Figure 31), the more pre-stretched the filler network, the less temperature dependent is the fracture energy. At 80 °C, the fracture energy increases, as noticed for the double network.

The fracture energy depends on temperature but also on crack velocity, as previously discussed. In these experiments, where the crack velocity is not controlled, the average crack velocity, v_{crack}, can be estimated by Eq 4. (discussed in Section 3.1).

The fracture energy was plotted as a function of the mean crack velocity in Figure 52 and shows clearly no sign of a controlled propagation where Γ increases with a power law of v.

When crack velocity is lower than 2 mm/s, the fracture energy decreases with increasing temperature. At 80 °C, the crack propagates much faster, more than 100 mm/s, and the fracture energy is higher than at 60 °C. At 80 °C, the fracture mechanism seems different.

The difference in crack propagation mechanism, linked with the difference in crack velocity, was confirmed by observations on crack surfaces. Scanning electron microscopy (SEM) observations were done thanks to Bruno Bresson. A Thermofisher FEI Magellan scanning electron microscope with a FEG tip was used in order to visualize metallized crack surfaces.

Figure 53 represents SEM pictures of the crack surface of triple networks, MAMA(2.3), broken at different temperatures. Figure 53a, c, e and g depict the border (indicated by dotted lines) between the introduced notch and the crack propagation. Figure 53b, d, f and h are snapshots from an area where the crack propagated.

At 25 °C (Figure 53 a and b), 40 °C (Figure 53 c and d) and 60 °C (Figure 53 e and f) 'wavy' patterns, coming from crack bifurcations, are clearly visible. However, at 80 °C (Figure 53 g and h), the crack surface was flat and no mark from crack bifurcations were observed.

The absence of crack bifurcations is consistent with the high crack velocity. Two different fracture mechanisms are identified:

1. On the one hand, at 25 °C, 40 °C and 60 °C, once nucleated, the crack propagated over a few seconds through crack bifurcations.
2. On the other hand, at 80 °C, the crack propagated, in tens of milliseconds, fast and straight.

	Initiation	Propagation
25°C	a)	b)
40°C	c)	d)
60°C	e)	f)
80°C	g)	h)
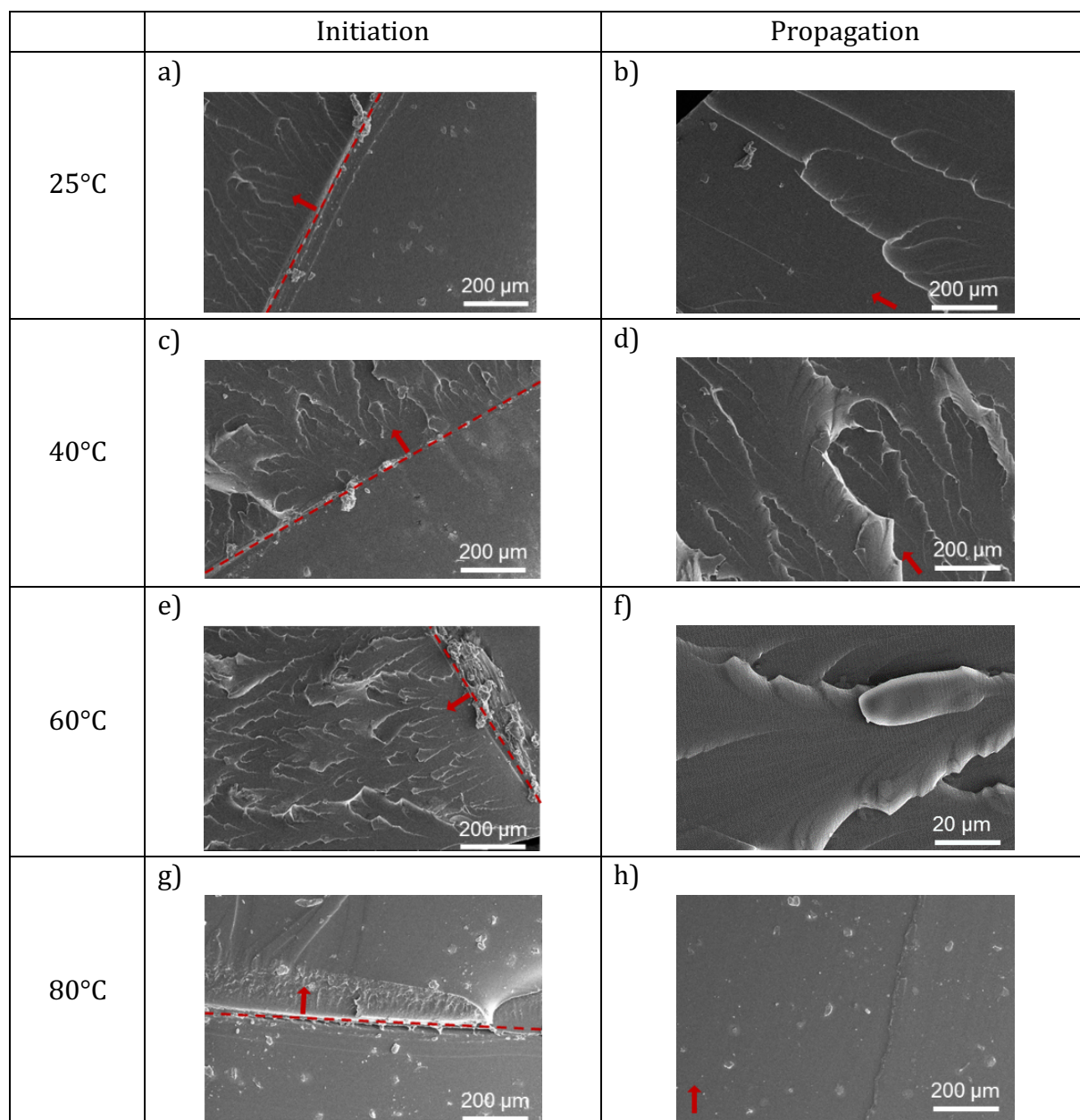
Figure 53: SEM images of crack surfaces after crack propagation in MAMA(2.3) at 25 °C (a, b), 40 °C (c, d), 60 °C (e, f) and 80 °C (g, h). The dotted lines (a, c, e, g) represent the crack nucleation from the introduced notch. Red arrows represent crack propagation direction.

The influence of the temperature and the associated fracture mechanism on damage will now be investigated.

For each crack propagation test, four single optical sections (two on each side) were recorded at magnification 5x and 100 μm depth. Figure 54 represents examples of surface intensity plots of raw pictures and associated pre-processed and re-colored pictures after crack propagation in DAMAMA(2.3) at each temperature.

	Surface intensity plots	Pre-processed pictures
25°C	a)	b)
40°C	c)	d)
60°C	e)	f)
80°C	g)	h)
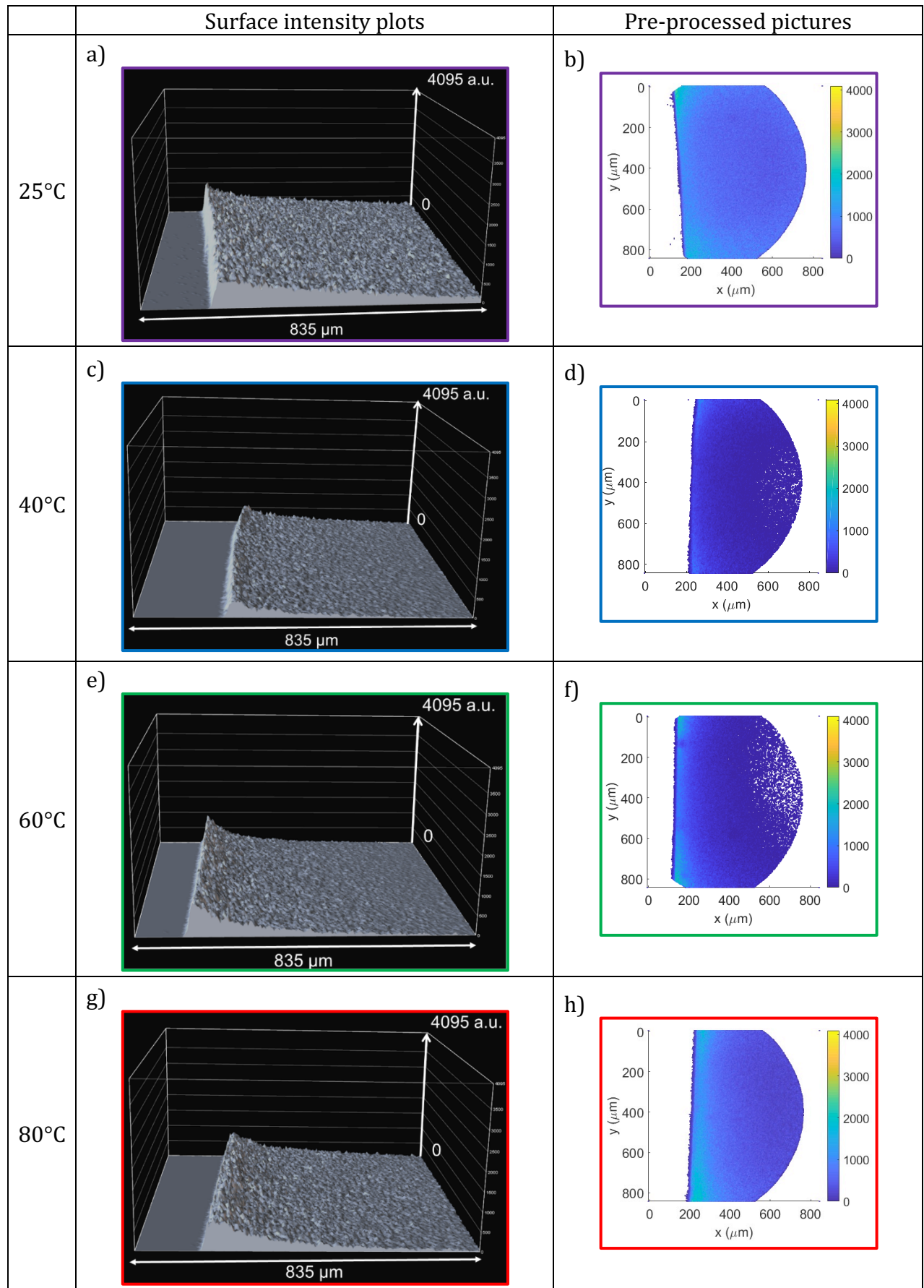
Figure 54: Surface intensity plots and pre-processed and re-colored images after crack propagation in DAMAMA(2.3) (Laser 7 Gain 3) at 25 °C (a and b), 40 °C (c and d), 60 °C (e and f) and 80 °C (g and h).

The damage seems to slightly decreases from 25 °C, to 40 °C, to 60 °C and then increases again at 80 °C.

The corresponding evolution of fluorescence intensity with the distance normal to the crack edge is represented in Figure 55. At 25 °C and 80 °C, the intensity does not reach the noise level (as discussed earlier in this Chapter, Section 2.3) at 500 µm from the crack face. The analysis underestimates the damage at 25 °C and for a few pictures at 80 °C and 40 °C (for one sample). Note also that the bond scission appears to be more localized near the crack plane at 80°C than at 25°C.
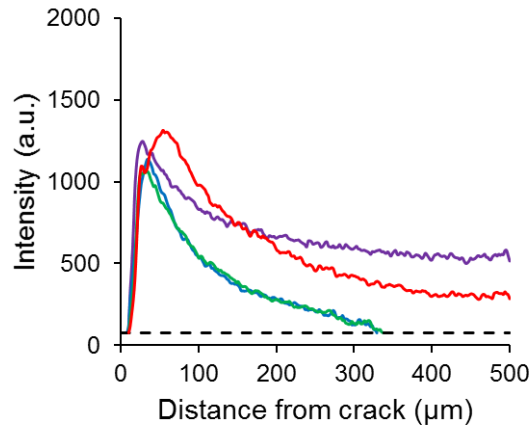
Figure 55: Intensity profiles after crack propagation in DAMAMA(2.3) at $\dot{\lambda} = 3 \times 10^{-3} \ s^{-1}$ and 25°C (purple),40 °C (blue), 60 °C (green) and 80 °C (red).

To obtain quantitative information, the areal densities, Σ_{exp}, of broken chains of the filler network were calculated, averaged over the four pictures and are plotted as a function of the temperature in Figure 56. The evolution of the fracture energy with temperature is also reported on Figure 56. Despite the underestimate of Σ_{exp} at 25 °C, 80 °C (and one sample at 40 °C), the evolution of Σ_{exp} follows well the evolution of Γ_{exp}.

The length, L_{damage}, over which damage was detected is also plotted as a function of the temperature in Figure 57. L_{damage} decreases from 25 °C to 60 °C and then increases at 80 °C.
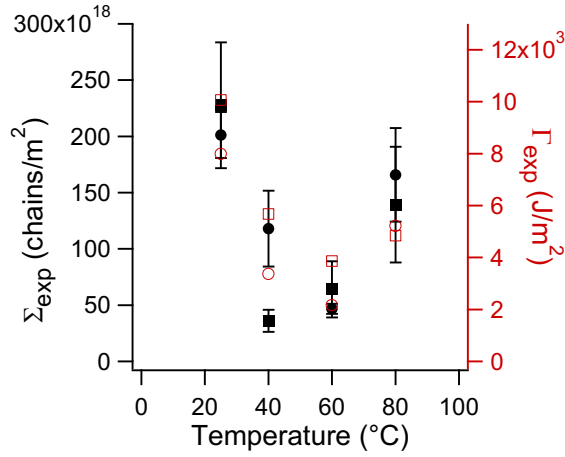
Figure 56: Evolution of the areal density, Σ_{exp}, of broken chain of the filler network (in black) and of the fracture energy, Γ_{exp}, (in red) as a function of the temperature after crack propagation in DAMAMA(2.3) at $\dot\lambda = 3 \times 10^{-3} \ s^{-1}$. Different symbols correspond to samples from different polymerizations. Values at 25 °C, 80 °C and 1 sample at 40 °C are underestimated (off-limit)
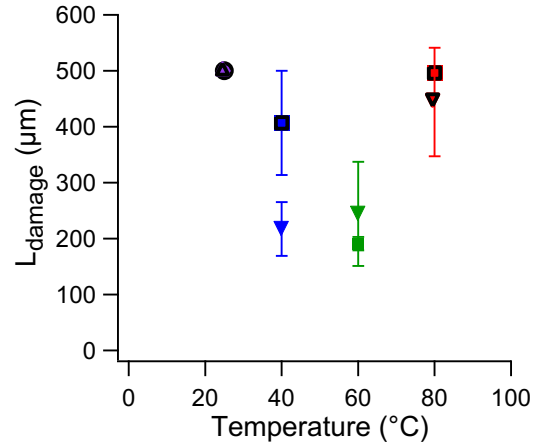
Figure 57: Evolution with temperature of the length, L_{damage}, over which damage is detected after crack propagation in DAMAMA(2.3) at $\dot\lambda = 3 \times 10^{-3} \ s^{-1}$. Different symbols correspond to samples from different polymerizations. Values at 25 °C, 80 °C and 1 sample at 40 °C are underestimated, they are identified by black edges(off-limit)

The component of the fracture energy, Γ_{damage}, due to bond scission was estimated by Eq 3. (U=64 kJ/mol) and divided by the macroscopically measured fracture energies, Γ_{exp}. $\frac{\Gamma_{damage}}{\Gamma_{exp}}$ was plotted as a function of the temperature, as shown in Figure 58.

The trend is not very clear: a slight decrease from 25 °C to 60 °C followed by a slight increase from 60 °C to 80 °C can be noticed. The contribution of energy dissipated by filler breakage is on average higher than 30 % (from about 36 % at 25 °C, to 31 % at 40 °C, to 28 % at 60 °C, to 45 % at 80 %). Energy dissipation by sacrificial chains scission represent a major contribution.
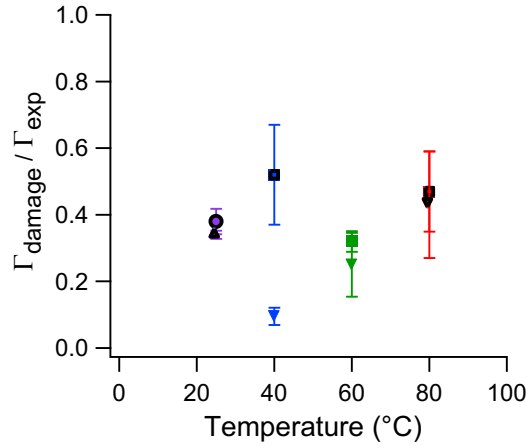
Figure 58: Evolution of $\Gamma_{damage}/\Gamma_{exp}$ with the temperature for crack propagation test on DAMAMA(2.3) at $\dot{\lambda} = 3 \times 10^{-3} \, s^{-1}$. Γ_{damage} calculated using U=64 kJ/mol. Average value calculated over 4 pictures, error bar correspond to the standard deviation. Different symbols correspond samples from different polymerizations. Values at 25 °C, 40 °C (1 sample) and 80 °C are underestimated, they are identified by black edges (off-limit)

The areal density, Σ_{exp}, of broken chains of the filler network was then normalized by a filler monolayer, Σ, to give the normalized areal density, $\bar{\Sigma}$. To be consistent we also plotted $\bar{\Sigma}$ as a function of the average crack velocity in Figure 59.

First, it is clear that in triple networks of poly methyl acrylate, the areal density of broken chains of the filler network is thousands of times higher than what would be expected from a filler monolayer.

A first reason for the decrease of the number of broken chains for similar crack velocity (around 1 mm/s) is attributed to the temperature. Indeed, by increasing the temperature, the friction between chains is reduced, the stress borne by each chain is reduced and the damage decreases.

However this explanation is not very valid at 80°C where dissipation is low and yet damage increases significantly; A possible explanation could be related to the fast crack propagation but it is not very convincing.
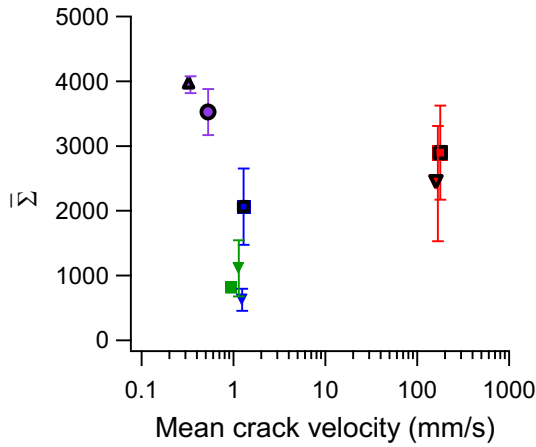
Figure 59: Evolution of $\bar{\bar{\Sigma}}$ as a function of the mean crack velocity after crack propagation in DAMAMA(2.3) at $\dot{\lambda} = 3 \times 10^{-3} \, s^{-1}$ and at different temperatures, 25 °C (in purple), 40 °C (in blue), 60 °C (in green) and 80 °C (in red). Different symbols correspond to samples from different polymerizations. Values at 25 °C and 80 °C are underestimated (off-limit).
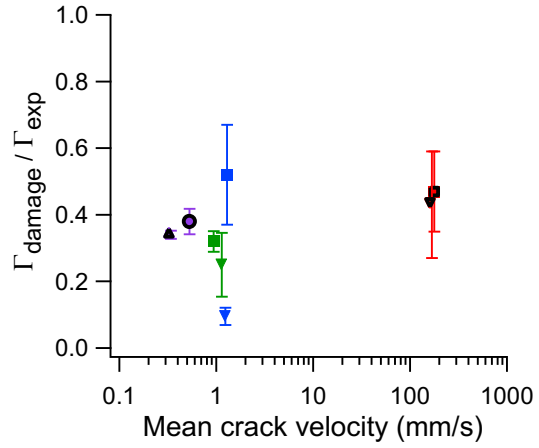
Figure 60: Evolution of $\Gamma_{damage}/\Gamma_{exp}$ with the crack velocity for crack propagation test on DAMAMA(2.3) at $\dot{\lambda} = 3 \times 10^{-3} \, s^{-1}$. Γ_{damage} calculated using U=64 kJ/mol. Mean value calculated over 4 pictures, error bar correspond to the standard deviation. Different symbols correspond samples from different polymerizations. Values at 25 °C, 40 °C (1 sample) and 80 °C are underestimated (off-limit)

To try a different path, we plotted in Figure 61, the evolution of $\bar{\bar{\Sigma}}$ as a function of the elongation at break. The number of broken chains increases clearly with the elongation at break without much difference between the low temperature regime and the case of 80°C.
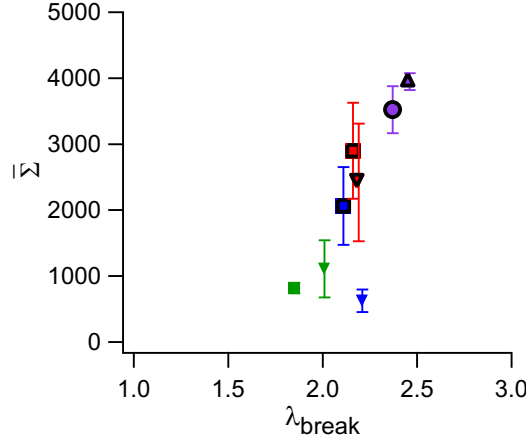
Figure 61: Evolution of $\bar{\bar{\Sigma}}$ with maximal strain before crack propagation in DAMAMA(2.3) at 50 µm/s and different temperature: 25 °C (in purple), 40 °C (in blue), 60 °C (in green) and 80 °C (in red). Means values calculated over 4 pictures, error bars correspond to the standard deviations. Different symbols correspond to sample from different polymerizations. Values at 25 °C and 80 °C are underestimated (off-limit).

The lack of correlation with crack propagation (a dynamic parameter characterizing stretch rate) and the better correlation with λ_{break} a static parameter characterizing strain, suggests that for these triple networks the dissipation is more related to the strain achievable at break than the stretch rate. An important general conclusion.

To summarize, from mechanical tests, SEM observations and damage analysis we observe that:

- From 25 °C to 60 °C, the fracture toughness and the level of bond scission decreases with increasing temperature. This decrease can be explained by the reduction of viscoelastic dissipation from chains friction at the Tg. The crack propagates at about 1 mm/s through crack bifurcations.

- At 80 °C, the initiation occurs at a higher stretch than at 60°C but once the crack starts to propagate it propagates fast, about 100 mm/s, as viscoelastic dissipation is low at this temperature. Important damage is caused by the fast propagation and higher strain.

The unsolved question is the reason why the crack initiation occurs at a much higher stretch at 80 °C. From experiments and analysis, we were not able to conclude on that point. It is possible that the fast relaxation processes occurring at high temperature favors equal sharing between strands and avoids therefore the correlated bond scission that is responsible for the nucleation of cracks. However, this does not explain why the fracture energy (and the bond scission during propagation) is non-monotonic with T.

3.3   Comparison of the effect of matrix viscoelasticity in double networks

From results of the previous sections, the role of the matrix viscoelasticity appeared crucial. Four double networks are now compared to summarize the influence of the nature of the matrix, but also of the nature of the filler and of the difference in temperature between the test temperature and the Tg of the polymer:

1. DAMAEA(1.6), a double network with a filler made of poly methyl acrylate, and a matrix of poly ethyl acrylate, tested at 25 °C.

2. DAEAEA(1.6), a double network with a filler made of poly ethyl acrylate, and a matrix of poly ethyl acrylate, tested at 25 °C, to compare the influence of the monomer used for the filler network.

3. DAMAMA(1.6), a double network with a filler made of poly methyl acrylate, and a matrix of poly methyl acrylate, tested at 60 °C. Comparing DAMAEA(1.6) and

> MAMA(1.6) will give information on the influence of the nature of the matrix monomer at about same distance to Tg.

4. DAMAMA(1.6), the same double network with a filler made of poly methyl acrylate, and a matrix of poly methyl acrylate, but tested at 25 °C, same tested temperature as DAMAEA(1.5) and DAEAEA(1.6).

Table 7 summarizes the materials composition and Tg as measured by DSC, the temperature at which the crack propagation test was done, the macroscopically measured fracture energy and the results from the LSCM quantitative analysis: L_{damage} and $\bar{\Sigma}$. These results were presented earlier in the chapter in different sections, except DAEAEA(1.6).

	DAMAEA(1.5)	DAEAEA(1.6)	DAMAMA(1.6)	DAMAMA(1.6)
Filler network	MA	EA	MA	MA
Matrix network	EA	EA	MA	MA
Tg (°C)	- 8	- 18	18	18
Test temperature (°C)	25	25	60	25
Γ_{exp} (J/m²)	744	1173 ± 226	624 ± 66	4849 ± 67
L_{damage} (µm)	30 ± 4	37 ± 6	22 ± 5	165 ± 67
Normalized $\bar{\Sigma}$	41 ± 10	64 ± 15	35 ± 13	373 ± 151

Table 7: Damage comparison in different double networks

First, DAMAEA(1.6) and DAEAEA(1.6) are compared. The nature of the filler is different but the matrix is the same. The fracture energy, areal density of broken chains and detected damage length are similar. In these conditions, the nature of the monomer of the filler network does not have drastic consequences on fracture of the double network. DAMAEA(1.6) is slightly less pre-stretched (as discussed in Section 2.2), slightly less tough and slightly less damaged. This seems to indicate that the choice of monomer of the filler network does not play a crucial role on crack propagation.

Second, DAMAEA(1.6) tested at 25 °C (33 °C above Tg) and DAMAMA(1.6) tested at 60 °C (42 °C above Tg) are directly compared. Both samples are tested at a temperature more than 30 °C above Tg where viscoelastic dissipation should be less important. The filler network is the same, the matrix is either polyethyl acrylate, either polymethyl acrylate. Fracture energy, number of broken chains and detected damage length are similar. If the matrix is at a comparable distance from Tg, the nature of the matrix monomer does not seem to have a major influence on fracture either.

Finally, the three previous samples were compared to DAMAMA(1.6) tested at 25 °C. The fracture energy, number of broken chains and damage length are much higher in this last case. The viscoelasticity of the matrix network plays a crucial role. More damage occurs in the filler network, enhancing the fracture energy. The molecular friction in the matrix dissipates the energy, makes it possible to slow crack propagation up to a much higher stretch and hence sacrificial bonds of the filler break in a larger extent before crack propagation. There is therefore a synergy between the viscoelastic dissipation in the matrix and the sacrificial bond breakage in the filler network.

To confirm and complete these results, triple network elastomers were also compared. The triple network fully made of poly ethyl acrylate tested at 25 °C (result presented in Section 3.1) was compared to the triple network fully made of poly methyl acrylate tested at 60 °C (result presented in Section 3.2.2). Table 8 summarizes the materials composition, Tg as measured by DSC, the temperature at which the crack propagation test was done, the macroscopically measured fracture energy and the results from the LSCM quantitative analysis: L_{damage} and $\bar{\Sigma}$.

	DAEAEA(2.3)	DAMAMA(2.3)
Filler network	EA	MA
Matrix network	EA	MA
Tg (°C)	-18	18
Test temperature (°C)	25	60
Γ_{exp} (J/m^2)	1647	3014 ± 846
L_{damage} (µm)	178 ± 42	218 ± 72
Normalized $\bar{\Sigma}$	788 ± 210	965 ± 343

Table 8: Damage comparison in different triple networks

For triple network elastomers at approximately the same distance to the glass transition temperature, the nature of the monomer does not have a drastic influence on molecular damage of the filler. The crack propagation test performed on the two samples of polymethyl acrylate suffered from poor reproducibility leading to large error bars. However, it is clear that L_{damage} and $\bar{\Sigma}$ are in the same range of value (considering the uncertainty), slightly higher ($\sim$ 20 %) for the poly methyl acrylate triple network.

Comparison of triple network confirm that the viscoelasticity of the matrix network plays a crucial role. When the temperature, at which the crack is propagated, is at a same distance from Tg, results from molecular damage analysis are comparable for the two different monomers.

Conclusions

In this chapter, the fracture of multiple network elastomers was investigated, with a focus on the analysis of the bond scission and dissipation mechanisms occurring at the crack tip.

In order to do so, cracks were propagated from single edge notched samples of multiple network elastomers deformed at different stretch rates and at different temperatures. Different sets of materials were tested to study the influence of the nature of the monomer, the temperature relative to the Tg and the level of pre-stretching of the filler network. After crack propagation, samples were unclamped, cooled down at room temperature and imaged 'post-mortem' with a Laser Scanning Confocal Macroscope. From the method presented in Chapter 3, quantitative results on bond scission near the fracture plane were obtained. The areal density of broken chains of the filler network was measured for different conditions of crack propagation.

The general pattern of crack propagation, straight or through bifurcations, depends on the material considered and the crack propagation conditions. In double networks of poly ethyl acrylate, many crack bifurcations occurred at 60 °C and 80 °C. Damage heterogeneities, caused by crack bifurcations, render impossible the quantitative analysis in that case. These crack bifurcations cost energy and are partly responsible for the material reinforcement. However, in the case of triple networks of poly methyl acrylate, at 80 °C, no crack bifurcations were observed. The initiation was delayed and the crack propagated fast and straight. The crack initiation and the propagation are two distinct phenomena but they are interdependent.

Different results were highlighted by the damage analysis following crack propagation:

- The dependence on stretch rate and temperature of the fracture energy decreases with increasing level of pre-stretching of the filler network.

- When the multiple network elastomer is far enough from its Tg, and the filler is sufficiently pre-stretched (triple network, of poly ethyl acrylate multiple networks at $\lambda_0 = 2.3$ and at least 40 °C from its Tg), the bond scission reinforcement mechanism seems nearly independent on temperature. In fact, the distance over

which damage was detected ranged from 80 to 180 μm and the areal density of broken chains was about 300 to 800 times the areal chain density. The multiple networks have drastically decreased their viscoelastic dissipation occurring at the crack tip in comparison to simple networks. This result confirms the interest of multiple networks: they can be used over a wide range of temperatures and stretch rates.

- Multiple networks become tougher as the testing temperature approaches the glass transition temperature and molecular friction is active in the matrix. This was the case for multiple network made from poly methyl acrylate tested from 25 °C or 60 °C. The coupling between bond scission and viscoelastic dissipation is high and complex. The energy transferred by the filler to the matrix by chain scission is dissipated. Thanks to this energy dissipation and stress redistribution, the crack propagation is delayed, allowing more chain scission. In addition to sacrificial chains scission, viscoelastic dissipation is enhanced at temperature close to Tg. However, the bond scission contribution increases with increasing rate or decreasing temperature. As viscoelasticity is rate and temperature dependent, these parameters still have an influence on fracture of multiple network elastomer. The areal density of broken chains goes from ~35 (at 60 °C) to ~370 (at 25 °C) times the areal chain density in double network and from ~965 (at 60 °C) to ~3740 (at 25 °C) time the chain areal density in triple network.

- The structure and the temperature relative to Tg are two key parameters to design multiple networks. For a same level of pre-stretching of the filler network and a comparable distance from Tg, the chemical nature of the filler and the matrix networks will not result in drastic changes. Indeed, for both double network elastomers with methyl acrylate filler and either an ethyl acrylate (tested at 25 °C) or a methyl acrylate (tested at 60 °C) matrix, the areal density of broken chain is ~40 times the areal chain density.

One condition was still puzzling: the triple network based on polymethyl acrylate at 80 °C. In this case, the crack propagation behavior was different. The initiation occurred at higher stretch but the crack propagated fast and straight leading to more damage.

However, this behavior was not observed for triple networks of poly ethyl acrylate at 40°C.

The evolution of molecular damage was explained by either temperature, crack speed or elongation at break. It would have been interesting to decouple the maximal strain (or stress) withstood by the sample before crack propagation from the rate and temperature effect. In order to do so, one can load an un-notched sample up to a certain strain, before breakage, and vary the conditions to reach that strain. The maximal macroscopic strain experienced by the material will be the same and the difference in terms of damage will only come from the temperature and the rate at which it was loaded.

It is interesting to note that the energy dissipated by viscoelasticity and by sacrificial bond scission can be complementary. In fact, when viscoelasticity is reduced, once initiated, a crack will propagate fast but a fast propagation will lead to high molecular damage and energy dissipation by bond scission.

References

1.   H. Furukawa *et al.*, Tear Velocity Dependence of High-Strength Double Network Gels in Comparison with Fast and Slow Relaxation Modes Observed by Scanning Microscopic Light Scattering. *Macromolecules* **41**, 7173-7178 (2008).
2.   P. Millereau, Large Strain and Fracture of Multiple Network Elastomers (Doctoral dissertation) UPMC (2017).
3.   E. Ducrot, Innovative tough elastomers: Designed sacrificial bonds in multiple networks (Doctoral dissertation) UPMC (2013).
4.   M. Rubinstein, R. H. Colby, *Polymer Physics*. (2003).
5.   S. Wang, S. Panyukov, M. Rubinstein, S. L. Craig, Quantitative Adjustment to the Molecular Energy Parameter in the Lake–Thomas Theory of Polymer Fracture Energy. *Macromolecules* **52**, 2772-2777 (2019).
6.   P. Millereau *et al.*, Mechanics of elastomeric molecular composites. *Proc Natl Acad Sci U S A*, (2018).
7.   E. Ducrot, Y. Chen, M. Bulters, R. P. Sijbesma, C. Creton, Toughening Elastomers with Sacrificial Bonds and Watching Them Break. *Science* **344**, 186-189 (2014).

Conclusions

General conclusion

Current vision of the chain scission contribution

The only molecular based model of fracture in soft materials adopted by the community is the Lake-Thomas theory (*1*). When viscoelastic dissipation tends towards zero, at very slow crack propagation rates or very high temperatures, the fracture energy tends toward a threshold value Γ_0. Lake-Thomas theory connects this threshold value to the network structure.

Closer to the glass transition, viscoelastic dissipation is not negligible. Its contribution to the fracture energy was estimated by linear viscoelasticity (*2-4*). This theory qualitatively predicts an increase in fracture energy with crack velocity but cannot quantitatively predict results for a broad variety of well-cross-linked elastomers.

The two models can be summarized in the classic equation describing the fracture energy of soft materials, Eq 1.

$$\Gamma = \Gamma_0\big(1 + f(v,T)\big) \qquad\qquad \text{Eq 1.}$$

Where $f(v,T)$ is a function representing viscoelastic energy dissipation in front of the crack tip. Currently this function cannot be predicted quantitatively from bulk mechanical properties of the soft materials.

In current theories, the molecular damage is too often limited to the Lake-Thomas threshold value. Neglecting molecular damage gives an oversimplified picture that cannot lead to a proper and realistic modeling.

A breakthrough methodology for quantitative results on molecular damage

First thesis objective: Developing and optimizing an investigation tool to examine chains scission at the crack tip.

The characterization of molecular damage in soft materials is the core of the thesis. In order to address this question, we took advantage of the latest advances in mechano-chemistry and developed a new method based on that field. Organic chemists designed molecules, that can be incorporated in polymer networks and which report for

chain scission, by optical changes, when specific bonds break. We specifically looked for a long lasting signal to quantitatively investigate damage near the tip of a crack at a high spatial resolution.

Among the variety of mechanophores available, we selected, for those reasons, the π-extended anthracene Diels-Alder adduct (*5*). We synthesized the mechanophore and incorporated it in the network structure as a cross-linker. No modification of mechanical properties by the mechanophore introduction was observed (at small and large extension). A mechanically driven retro Diels-Alder reaction releases a fluorescent π-extended anthracene. The high and stable fluorescence reports for chains scission. The fluorescent signal can be observed by a confocal microscope. Such confocal microscopes are broadly used in biology to identify at high resolution regions of the biological sample marked with fluorescent probes in water. Our methodological breakthrough couples a confocal macroscope with a mechano-fluorescent elastomer in order to map damage in 3D and at a resolution of a micron or so.

Transparency is required for confocal microscopy and conventional filled elastomers are not transparent. In order to analyze reinforced elastomers, the multiple network reinforcement strategy was adopted. Developed in our lab, multiple network elastomers are a combination of a sacrificial network, so-called filler network, highly cross-linked and pre-stretched which is diluted in a soft matrix network (*6*). Filler chain scission was proven to be a major source of energy dissipation leading to reinforcement. During our study, both classical elastomers and multiple network elastomers were under investigation.

The crack initiation was studied first. A tensile test device was incorporated to the stage of a confocal macroscope. Fluorescent signal observations were conducted on open cracks. Cyclic loading experiments on notched samples were punctuated by confocal observations.

This new method for examining spatial distributions of bond scission provides additional insights in the nature of dissipative mechanisms at the crack tip before propagation. The first objective of the thesis, which was to develop an investigation tool to examine chains scission at the crack tip, was achieved.

Second thesis objective: Developing a methodology to quantify chain scission.

The challenging quantification of fluorescence emission was implemented in the method. A calibration molecule (*5*) was synthesized and mixed with linear polymer chains at different concentrations. Calibration curves relating quantitatively the fluorescent intensity to the concentration of activated mechanophore were obtained. Assuming that the mechanophore is incorporated randomly in the network and that the fraction of mechanophore activation is the same as the fraction of chain scission, we can estimate the number of chains that break and normalize them by the area of crack plane. After different trials, the best strategy for quantification was identified as a crack propagation test followed by fluorescence observations 'post mortem' and image analysis. To the best of our knowledge, it is the first time quantitative results are obtained. This methodology fulfill requirements of the second objective. This methodology has limits that will be presented with suggestions for improvements in the perspectives.

The quantitative methodology was applied on multiple network elastomers to test its robustness, to confirm previous trends (*6, 7*) and to quantify results. We proved that after crack propagation in triple network elastomers (poly ethyl acrylate at 25 °C and $\dot{\lambda} = 3 \times 10^{-3} \ s^{-1}$) the damage of the filler network is one order of magnitude higher than in a double network. The damage was detected over about 180 μm away from the crack surface in triple networks and about 40 μm in double networks. In multiple networks, we confirmed that the damage zone is larger for more pre-stretched first networks, which is consistent with earlier studies but with a much better spatial resolution, sensitivity and quantification.

As the reinforcement mechanism is based on sacrificial bonds incorporated in the material, the damage detection in multiple network elastomers was a favorable case.

The methodology was also tested and validated on single networks of poly methyl acrylate. Poly methyl acrylate was chosen, instead of poly ethyl acrylate, to vary the viscoelastic properties of the material easily within a narrow range of accessible temperatures (related to objective 4). Since the glass transition temperature of polymethyl acrylate is close to ambient temperature, fracture occurs with significant viscoelastic dissipation We proved however that fracture surfaces of single networks (polymethyl acrylate at 25 °C and $3 \times 10^{-3} \ s^{-1}$) show molecular damage over 60 μm from the crack plane, i.e. 1000 times the mesh size. Furthermore the total amount of broken strands was 50 times higher than the Lake and Thomas prediction.

Molecular damage in multiple networks

Third thesis objective: Improving the comprehensive picture of fracture in multiple network elastomers.

In multiple networks, real time crack propagation observations showed that cracks do not necessarily propagate in a straight line but often propagate through bifurcations. A high level of damage was detected in the loaded fibril-like structure. We demonstrated the 3D nature of the damage by direct and fluorescence observations.

We also proved that filler damage occurred before crack propagation and was higher in the direction perpendicular to the crack propagation direction. The more pre-stretched the filler network, the broader appeared the damage zone. When incorporated in the second network, the fluorescent signal, reporting for molecular damage, was low and localized.

Previous works (*8-10*), direct observations and damage visualization, suggest a tentative picture of the fracture in multiple network elastomers:

1. First, random chains breakage occurs in the bulk in front of the crack
2. At some point, the breakage very close to the crack tip goes from random to correlated, creating a highly damaged region and stress transfer from the filler to the matrix, as shown by Yinjun Chen (*10*)
3. The crack propagates in the highly damaged region

Once the filler network breaks extensively, the elastomer becomes a heterogeneous material (we do not know at this stage at which length scale) with many microcraks in the filler network and matrix network bridging these cracks. The 'newly-formed' material has its own properties. The crack has now to propagate in this damaged material. The propagation will depend on the extensibility of this damaged material. In a highly pre-stretched filler network, many bonds can break which will dissipate a lot of energy. However, the extensibility of the highly damaged material formed by the broken filler network in the matrix will be limited. On the contrary, a less pre-stretched filler network will dissipate less energy by bond breaking but the 'broken material' will be more extensible. This argument explains why the crack front is more localized in triple than in

double networks. A higher level of pre-stretching prevents a large zone of crack bifurcation. The crack initiation is delayed by sacrificial bond breakage but once it is initiated, the crack propagates fast in the necked region.

Considering these results, the multiple network fracture mechanism is not yet fully understood yet, but this work gives important insights.

Coupling between molecular damage and viscoelasticity

Fourth thesis objective: Analyzing the coupling between viscoelasticity and molecular damage in single and multiple network elastomers

In order to separate energy dissipation due to molecular friction (classical viscoelasticity) from energy dissipation due to bond breakage, crack propagation tests were performed at different temperatures and different stretch rates on single networks of poly methyl acrylate. We highlighted that the molecular damage was not constant with temperature and loading rate. More damage was detected at high rate or low temperature (above Tg).

The comparison, at the same temperature difference from Tg, of a single network of poly ethyl acrylate and of a single network of poly methyl acrylate showed that the damage was more localized in poly ethyl acrylate. Both networks were designed to have the same molecular weight between crosslinks. Despite experiments and characterizations, we were not able to conclude on the origin of this interesting observation.

Multiple network elastomers were expected to be less temperature and loading rate dependent as conventional elastomers since the chains scission reinforcement mechanism is not based on viscoelasticity. P. Millereau verified this statement on multiple network of poly ethyl acrylate. We complete his investigation by molecular damage analysis. Cracks were propagated, at different speeds and different temperatures, in double and triple network elastomers of poly ethyl and poly methyl acrylate. When the matrix was made of poly ethyl acrylate and the tested temperatures were at least 30 °C above Tg, both fracture toughness and molecular damage were slightly rate and temperature dependent. However, when the matrix is viscoelastic, such as poly methyl acrylate close to its glass transition temperature, fracture toughness and molecular

damage in multiple network are markedly loading rate and temperature dependent. This dependence tends to decrease with increasing level of pre-stretching of the filler network.

In single and in multiple network elastomers, energy dissipation due to bond breakage is coupled with energy dissipation due to molecular friction (classical viscoelasticity).

The drawing given in Figure 1 summarizes the different steps where viscoelasticity influences chain scission in multiple network elastomers.

1. First, during loading, the viscoelasticity influences the friction between chains. The relevant strain rate is here controlled by the stretch rate applied by the operator.
2. Once a chemical bond is broken in a highly stretched chain, the chain relaxes fast to its random coil conformation. The relevant strain rate for this process is unknown but clearly much higher than the loading rate and dependent on the environment.

The friction between the broken filler network chain and the matrix must play a role in the load transfer from one bond to the next. Chain scission releases the energy stored by the loaded chain. This energy can be either transferred to the neighboring chains or dissipated.

1. In the first case (A in the drawing), the neighboring chains are overloaded by the stress transfer and preferentially break. The chains scission is correlated and leads to crack propagation.
2. In the second case (B in the drawing), the energy dissipation prevents the overloading of the neighboring chains. The chain scissions are random and shorter chains elsewhere break before longer chains in close proximity.
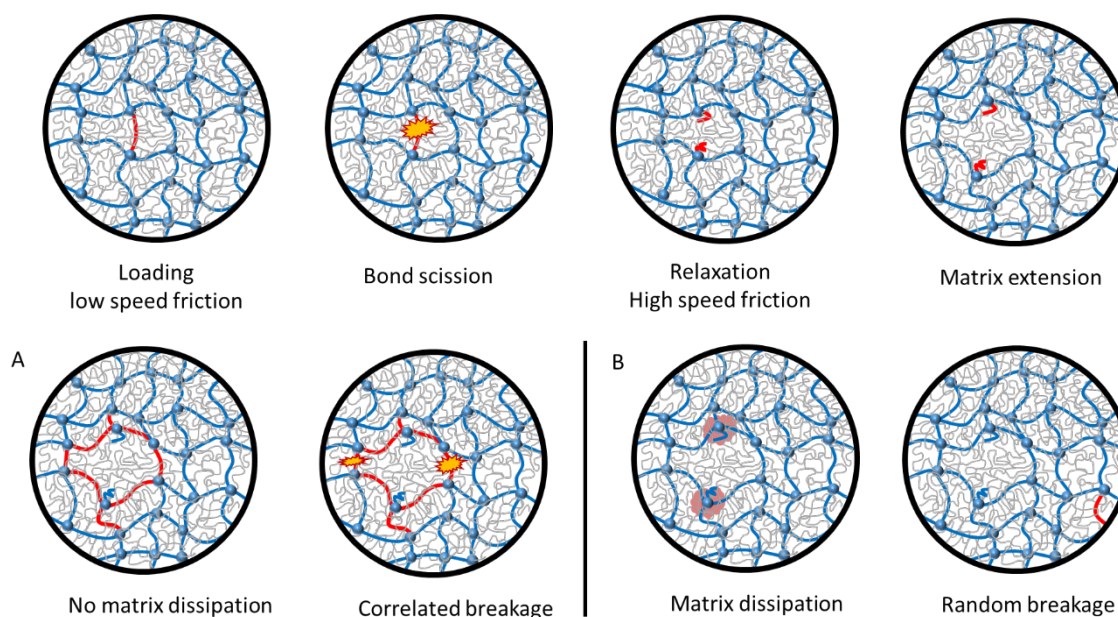
Figure 1: Schematic representation of coupling between viscoelasticity and chains breakage in multiple network elastomers.

The macroscopic crack propagates when the chain scission mechanism goes from random to correlated (and localized) (*7*). Viscoelasticity plays a crucial role in delaying the transfer from one mechanism to the other. Molecular friction is an intrinsic energy dissipative mechanism. It has two other consequences:

1. Energy dissipation prevents neighboring chains overloading and chain scissions are independent (non-correlated) events.
2. On the other hand, molecular friction increases the force borne by each individual chain and facilitates its rupture. This effect is loading rate dependent.

If the chain scission is facilitated and non-correlated, energy dissipation upon bond scission delays the nucleation of large enough defects to grow a crack. Fracture toughness and molecular damage increase with viscoelasticity, meaning with increasing loading rate and decreasing temperature.

There is a competition between both phenomena: the intrinsic energy dissipation due to molecular friction and the energy dissipation due to non-correlated bond breakage, facilitated by molecular friction. This argument is applicable to single networks and to multiple networks but to a different extent. In fact, depending on the materials and the tested conditions viscoelasticity dissipation or bond scission dissipation dominates the behavior.

In single network elastomers (poly methyl acrylate), the viscoelastic dissipation contribution increases faster than the bond scission contribution with increasing stretch rate (from $3 \times 10^{-4} \, s^{-1}$ to $3 \times 10^{-2} \, s^{-1}$, at 25 °C) or decreasing temperature (from Tg + 62 °C to Tg + 7 °C, at $3 \times 10^{-3} \, s^{-1}$).

In multiple network of poly ethyl acrylate (from 40 °C to 100 °C from Tg), fracture toughness is only slightly temperature and rate dependent. Reduced viscoelasticity decreases the coupling between energy dissipation due to molecular friction and the energy dissipation due to bond breakage. Chains scission appears slightly rate and temperature dependent. The behavior is dominated by the network structure more than by the viscoelasticity. This result is in good agreement with P. Millereau analysis showing that the level of pre-stretching of the filler network is directly linked to the fracture toughness (7).

In multiple networks of poly methyl acrylate (from 7 °C to 60 °C from Tg), fracture toughness increases with increasing rate and decreasing temperature. Enhanced viscoelasticity couples energy dissipation and the filler damage. The chains scission contribution increases with viscoelastic dissipation and appears as a very important contribution to the fracture toughness. There is clearly a coupling between both contributions

However, at 80 °C, in triple networks of poly methyl acrylate the fracture toughness and the molecular damage were higher than at 60 °C. The initiation was delayed at 80 °C and the crack propagation was faster. Despite experiments and characterizations, we were not able to conclude on the origin of this surprising observation.

Changing the vision of the chain scission contribution

To conclude, we developed an investigation tool to examine chains scission at the crack tip and a methodology to quantify bond scission. Thanks to this methodology, we were able to address specific questions, such as:

- The number of sacrificial bond that breaks in multiple network elastomer of poly ethyl acrylate and its evolution with the level of pre-stretching of the filler network.

- The number and the volume near the crack plane over which bonds break in a single network of poly methyl acrylate.

- The influence of the stretch rate and the temperature on molecular damage in different single networks and multiple network elastomers.

From the results obtained, the contribution of chain scission to fracture toughness of elastomers has to be clearly revised. This contribution cannot be limited to its lowest threshold, Γ_0, defined by the Lake-Thomas theory. In fact, this contribution was proven to be non-negligible and to vary with temperature and rate. As detailed above, the energy dissipation due to bond breakage is coupled with the energy dissipation due to molecular friction (viscoelasticity). Both contributions have to be incorporated in $f(v, T)$, the rate and temperature dependent term of Eq 1.

Now that the methodology is in place and data are available, the next step is the development of new physically-based models. Theorists in physics and solid mechanics can use this solid foundation to construct a better molecular model of fracture based on statistical physics of molecules and solid mechanics.

1. G. J. Lake, A. G. Thomas, The Strength of Highly Elastic Materials. *Proceedings of the Royal Society of London. Series A, Mathematical and Physical Sciences* **300**, 108-119 (1967).
2. A. N. Gent, J. Schultz, Effect of Wetting Liquids on the Strength of Adhesion of Viscoelastic Material. *The Journal of Adhesion* **3**, 281-294 (1972).
3. A. Ahagon, A. N. Gent, Effect of interfacial bonding on the strength of adhesion. *Journal of Polymer Science - Polymer Physics Edition* **13**, 1285-1300 (1975).
4. A. N. Gent, Adhesion and Strength of Viscoelastic Solids. Is There a Relationship between Adhesion and Bulk Properties? *Langmuir* **12**, 4492-4496 (1996).
5. R. Göstl, R. P. Sijbesma, π-extended anthracenes as sensitive probes for mechanical stress. *Chem. Sci.* **7**, 370-375 (2016).
6. E. Ducrot, Y. Chen, M. Bulters, R. P. Sijbesma, C. Creton, Toughening Elastomers with Sacrificial Bonds and Watching Them Break. *Science* **344**, 186-189 (2014).
7. P. Millereau *et al.*, Mechanics of elastomeric molecular composites. *Proc Natl Acad Sci U S A*, (2018).
8. P. Millereau, *Large Strain and Fracture of Multiple Network Elastomers* (Doctoral dissertation) UPMC (2017).
9. E. Ducrot, *Innovative tough elastomers: Designed sacrificial bonds in multiple networks* (Doctoral dissertation) UPMC (2013).
10. Y. Chen, *Quantitative mapping of stress in soft materials by mechanochemistry* (Doctoral dissertation) PSL (2018).

Future work and perspectives

Limitations and suggestions to overcome them

The quantification of bond scission is limited by the assumptions on which it relies:

1. The mechanophore activation is assumed to represent well chains scission. However, the retro-Diels-Alder reaction may occur at lower force level than the homolytic carbon-carbon bond scission. The assumption seems reasonable since the mechanophore reports for chains close to their limit of extensibility, so close to breakage.

2. A random and defect-free incorporation of the mechanophore is assumed. In reality, the network contains loop and dangling chains. If the mechanophore is trapped in these defects, the total number of activable mechanophore will be under-estimated.

3. The mechanophore was introduced as a cross-linker and not within the chain.

To verify the third assumption, the mechanophore can be introduced in the chain. A mechanophore bisinitiator (*1*) can be synthesized in order to form oligo-chains containing the mechanophore. Cross-linking oligo-chains in a second step will give networks with mechanophore inside chains. The comparison of results obtained with the mechanophore incorporated inside chains or as a cross-linker will confirm or refute the assumption.

The resolution of the quantitative analysis was limited to 2 μm (x and y axes). Higher resolution is available with a classic confocal microscope. Indeed, confocal microscope, as the Leica SP8 at *the Institut Pierre-Gilles de Gennes,* has objectives of higher magnification, up to 63 times. The objectives are inverted and the methodology needs to be adapted. Main modifications are:

1. The distortion correction slide should be changed (the Argo-LM reference slide bought from Argolight, to correct the distortion should be replaced by a Argo-HM reference slide)

2. The calibration samples should be prepared on glass slides and not into Petri dishes

3. Samples should be stuck to glass slides

261

4. As high magnification is obtain with oil objective, the refractive index of the oil objective should match the material refractive index

The quantification was limited when the damage was detected over a length longer than 500 μm. A first strategy to avoid this limitation is to record images at lower magnification. However, this solution will lead to higher optical aberrations that will have to be estimated and corrected. The second strategy is to stitch several images to get a mosaic and run the analysis on the large image obtained by stitching. Tuning the initial concentration of the mechanophore introduced inside the material is another way to broaden the window between under-saturated and over-saturated pixels.

Observations with the confocal macroscope at large deformations on un-notched sample was not possible because the tensile test device had a limited extension of 10 mm. In order to tackle this limitation, a new set up, with about 20 cm maximal extension, is under development. The study of the large deformation phenomenon, such as necking, will be accessible.

Finally, the following limitations are related to the 'post mortem' quantification.

1. Crack propagation temperature and rate were modified in order to tune viscoelasticity. However, depending on these settings, the crack propagated at different macroscopic strains. The temperature or rate effect was coupled with the highest extension experienced by the material. To decouple these parameters, uniaxial extension can be performed on un-notched sample, up to a fixed value of strain but reached at different temperature and rate. The difference in damage will come from the condition of elongation (temperature or rate) only and the macroscopic strain experienced by the material will be identical.

2. As the quantitative analysis was performed after crack propagation, the initiation and the propagation were coupled. We developed a cyclic loading strategy to evaluate qualitatively the damage before crack propagation. By comparing notch samples at a reference close position after increasing level of extension, we were close to quantification. However, the quantification of the evolution of damage through cycle was still challenging. The close position was not exactly identical because of sample slippage or large deformation. Taking images at the surface,

where few dusts can act as marks, can be a strategy to rescale images in order to get a fair and quantitative comparison.

3. After crack propagation test, samples were kept in the fridge. The time between crack propagation tests and the LSCM analysis was not constant for different set of experiments. The aging seems low by comparing overall averaged intensity of old and fresh calibration sample. Thus, a possible decay of signal with time was neglected. However, it is worthy to quantify the signal decrease with time (if any) in order to check that assumption. The movement of the pinhole prevented me from comparing old pictures (for which I do not have the flat field correction) and new pictures. A comparison of corrected images (using the pre-process MATLAB functions) at different time can give a fair and reliable comparison.

4. 'Post-mortem' analysis cannot distinguish damage ahead of the crack tip and damage during propagation. Quantitative cyclic loading can be a strategy to overcome this limitation. Another suggestion is to use the bis(adamantyl) dioxetane mechanophore that emits light upon breakage (*2*). This mechanophore will give dynamic and complementary information.

Recommendations for future research

Despite these limitations, the methodology in place to quantify chains scission is robust and can be largely used.

Poly ethyl and poly methyl acrylate were tested. Other change of monomer can be carried out, such as butyl acrylate to see the effect of entanglement density or butyl methacrylate to see the effect of chain transfer.

The method can be extended to any transparent material. During the last step of mechanophore synthesis, instead of two acrylate functions, the two hydroxyl moieties can be functionalized using a different chemistry to render it compatible with other materials. Gabriel Sanoja, a post-doc involved in the ERC project, is working on a water soluble version of the mechanophore to study hydrogels. The calibration samples also have to be adapted to the material under consideration.

Thanks to the ERC project, mechanochemistry competences were developed by different PhD students and post-docs. During his PhD, Yinjun Chen quantitatively mapped stress in multiple network elastomer by mechanochemistry using spiropyran. Both mechanophores are complementary as one is a stress sensor (the spiropyran) and the other a damage sensor (the Diels-Alder adduct). We proved that the damage of the matrix is very localized and Yinjun Chen proved that the matrix withstands stress when multiple network necked. Incorporating the Diels-Alder adduct in the filler network and the spiropyran in the matrix can be a strategy to visualize stress transfer from filler to matrix when the filler breaks during necking. One challenge of this study will be to handle on one side the UV excitation needed for the Diels-Alder visualization and on the other side the UV sensitivity of the spiropyran.

1.   R. Göstl, R. P. Sijbesma, π-extended anthracenes as sensitive probes for mechanical stress. *Chem. Sci.* **7**, 370-375 (2016).
2.   Y. Chen *et al.*, Mechanically induced chemiluminescence from polymers incorporating a 1,2-dioxetane unit in the main chain. *Nat Chem* **4**, 559-562 (2012).

RÉSUMÉ

L'utilisation de matériaux mous, tels que des ligaments de synthèse, est limitée par la propagation d'une fissure initiée par un défaut. Mieux comprendre les mécanismes de dissipation d'énergie en pointe de fissure, permettra de mettre au point des matériaux mous mais beaucoup plus résistants.

Nous avons développé une méthode permettant la visualisation en microscopie confocale de la rupture de liaisons chimiques grâce à une activation de fluorescence par rupture de liaison. Nous avons ainsi cartographié et quantifié l'endommagement moléculaire en 3D et à fort grossissement. Notre approche multi-échelle n'est possible que grâce à l'association de la chimie, de la mécanique et de la physique. Grâce à une calibration du signal fluorescent, c'est la première fois qu'une information quantitative est obtenue sur le nombre de liaisons cassées après la propagation de fissure. Les résultats obtenus par cette méthode remettent en cause la vision actuelle de la fracture des matériaux souples. En effet, nous avons montré que les ruptures moléculaires dans un élastomère se font sur une épaisseur de dizaines de microns et que cet endommagement moléculaire est couplé à la viscoélasticité et dépend donc de la température et de la vitesse. Ces informations sont indispensables et sont attendues par les modélisateurs pour le développement de modèles réalistes prédisant la fracture.

MOTS CLÉS

Fracture – Mécanochimie – Polymère – Fluorescence

ABSTRACT

Engineering applications of soft materials, such as prosthetic ligaments, are limited by crack propagation initiated by a defect. A better understanding of dissipative mechanism at the crack tip will be invaluable to guide materials chemists to design and develop better soft and tough materials.

We developed a method to visualize molecular chains scission based on mechano-fluorescence: fluorescence activation upon mechanically triggered bond scission. We mapped molecular damage in 3D and at high magnification by confocal microscopy. Chemistry, mechanics and physics were associated to give our multi-scale approach. With the help of a calibration curve we directly quantified and mapped chains scission inside a series of model elastomers, from brittle to tough. Results obtained from this method challenge the actual molecular picture of fracture in soft material. Indeed, we proved that chain scission in elastomers occurs over a thickness of tens of microns around the crack plane and depends on strain rate and temperature as they are coupled to viscoelasticity. Theorists in physics and mechanics can use this solid experimental foundation to construct better molecular models of fracture.

KEYWORDS

Fracture – Mechanochemistry – Polymer – Fluorescence